N° of Dissertation	

A DISSERTATION

Submitted to the Doctoral Research Programme on Climate Change and Energy

University Abdou Moumouni of Niamey, Niger

In Fulfilment of the Requirements for PhD

DOCTORAL SCHOOL OF EXACTS AND TECHNICS SCIENCES

Domain: Sciences and Technologies

Mention: Physics

Specialty: Climate Change and Energy

by

Boubou BAGRE

Development and characterization of Eco-materials for sensible heat storage in concentrating solar power plants

Thesis defence: On 22 June 2024 at 9:00 AM in Niamey, Niger

M. MADOUGOU Saidou Professeur Titulaire en Physique, Université Abdou Moumouni de Niamey-Niger	**Président/ Rapporteur**
M. KORGO Bruno Maître de Conférence en Physique, Université Joseph KI-ZERBO-Burkina Faso	**Rapporteur**
M. HALIDOU Ibrahim Maître de Conférence en Physique, Université Abdou Moumouni de Niamey-Niger	**Examinateur**
M. BOUKAR Makinta Professeur Titulaire en Physique, Université Abdou Moumouni de Niamey-Niger	**Directeur de thèse**
M. DAHO Tizane Professeur Titulaire en Physique, Université Université Joseph KI-ZERBO -Burkina Faso	**Co-Directeur de thèse**

Germany Benin Burkina Faso Cabo Verde Cote d'Ivoire Gambia Ghana Guinea Mali Niger Nigeria Senegal Togo ECOWAS

Federal Ministry of Education and Research

Dedication

To my daughter Yiépeni Cassandra BAGRE and her

Grand grandparents.

Acknowledgements

Writing acknowledgements is an exercise, not always easy, but essential, in order to thank all the actors who participated closely or from afar in this PhD thesis work. This thesis is the result of almost four years of very tough work that would not have been possible without the support and effort of many people. I will try not to forget any of you, just in case, I would like to thank in advance to all the people that has been direct or indirectly involved in this work.

I would like to thank ***Professor Makinta Boukar****, full Professor at Université Abdou Moumouni, my supervisor, for his scientific and human qualities. I thank him to be confident on me, for his ideas and his precious advice and support throughout my PhD thesis. You were not only my supervisor and professor but also a father, because your simplicity and modesty have affected me deeply.*

As for ***Professor Tizane Daho,*** *full Professor at Université Joseph KI-ZERBO my co-supervisor, I would like to express my deep gratitude to him, you are not only a scientist model or professor for me but also an elder brother and advisor who encouraged me to apply for the WASCAL programme scholarship when I myself was hesitating. I am grateful for everything.*

I would like to thank my co-supervisor, ***Dr.-Ing. Ibrahim Kolawole Muritala****, Adjunct Professor and project Engineer from Germany at Institute of Low-Carbon Industrial Processes, German Aerospace Center (DLR) Zittau, Germany for his scientific and human qualities. I am very grateful for all the support I got from him and wish a continuous collaboration with him during my scientific career.*

I am very grateful to ***Professor Saidou Madougou****, full Professor at "Université Abdou Moumouni" for serving as reviewer of this thesis and agreeing to chair the Jury of my defense.*

I would like also to thank ***Doctor Bruno Korgo****, Associate Professor at "Université Joseph KI-ZERBO", for giving time to honour me by reviewing this work.*

Many thanks to ***Doctor Halidou Ibrahim,*** *Associate Professor at "Université Abdou Moumouni" for serving as examiner of this work.*

I am very grateful to ***Professor Dungall Laouali****, the director of the "École Doctorale Sciences Exactes et Techniques (EDSET)." At University Abdou Moumouni and all his staff for everything they have done to make the defence of my PhD thesis possible. Many thanks also to* ***Professor Rabani Adamou****, Vice-Chancellor of University Abdou Moumouni and Director of WASCAL Doctorial Programme in Energy and Climate at Abdou University Moumouni. His advices were*

helpful for me during the different processes at my thesis. I am also grateful to all the staff of WASCAL-DRP-CCE and all the Lecturers who assisted us during the various courses in climate change and energy and all my stay in Niamey making me an expert in this area. To that I will say many thanks to my colleagues, PhD student at WASCAL-DRP-CCE and UAM for their collaboration and team spirit which were a way to achieve some milestones.

This PhD thesis reached at this level thanks to the financial support of ***Cuomo Foundation*** *through the* ***Intergovernmental Panel on Climate Change (IPCC)*** *Scholarship Program. I am very grateful for everything these International Programme have done for me. As agreement, "The contents of this document are solely the liability of Boubou BAGRE and under no circumstances may be considered as a reflexion of the position of Cuomo Foundation and/or IPCC".*

Many thanks to ***Professor Antoine Béré,*** *Director of "Laboratoire de Phyique et Chimie de l'Environnement (LPCE-UJKZ)" at Université Joseph KI-ZERBO for its willingness to collaborate with WASCAL-DRP-CCE and the city hall authorities which facilitated the completion of this thesis. The collaboration has help me to do my field work at LPCE-UJKZ and the "Centre de Valorisation et de Traitement de déchet" by having facilities for data collection, processing and analysis.*

I am grateful to the ***Director*** *of "Laboratoire National du Bâtiments et des Travaux Publique (LNBTP)" in Ouagadougou to receive me in his institution for the Geotechnical analysis of the raw materials.*

Many thanks to the ***Director*** *of the "Institut International d'ingénierie de l'Eau et de l'Environnement (2ie)". I am also grateful to the both Director of LNPTB and 2ie for granting me at least two internships during my data collection processes in their institutions.*

I would like to thank ***Professor Spiros Alexopoulos*** *and the all members of Solar Institute of Jülich (SIJ) at Applied Sciences University in Germany. Many thanks for sharing your knowledges during the four months I spent in your institution. It was a great experience and pleasure to meet all of you in Germany.*

I would like also thank ***Doctor Sié Zacharie Kam***, ***Doctor Moussa Sougoti*** *Associate Professors at "Université Joseph KI-ZERBO" and* ***Doctor Yomi Woro Gounkaou*** *at "Université Nazi BONI" for their moral and technical support during my field work.*

Being at LPCE during my fieldwork time was not only about research but also a process of well-being. So, I am very grateful to all the doctors and PhD students of LPCE for giving me not only the means to become but also the means to be.

To my wife ***Landrine Kanao****, I say thank you. Thank you for your support, your advices and your patience during these four years of struggle.*

Nomenclature and symbols

Abbreviation and Acronym	
A	Bottom Ash Sample
C	Clay sample from the deposit of Malgsombo in the commune of Saaba
C1	Clay sample the deposit of Ethouayou in the commune of Tcheriba
CBA	Coal bottom ash
CO0	Reference oil
CO1(720h)	Oil aged alone during I month or 720 h
CO2 (1440h)	Oil aged alone during 2 month or 1440 h
CO3(2160h)	Oil aged alone during 3 month or 2160 h
CODB1(720h)	Oil aged with Burkina dune sand ceramic ball during I month or 720 h
CODB2(1440h)	Oil aged with Burkina dune sand ceramic ball 2 month or 1440 h
CODB3(2160h)	Oil aged with Burkina dune sand ceramic ball 3 month or 2160 h
CODN1(720h)	Oil aged with Niger dune sand ceramic ball during I month or 720 h
CODN2(1440h)	Oil aged with Niger dune sand ceramic ball 2 month or 1440 h
CODN3(2160h)	Oil aged with Niger dune sand ceramic ball 3 month or 2160 h
COMB1(720h)	Oil aged with Burkina mining sand ceramic ball during 720 h
COMB2(1440h)	Oil aged with mining sand ceramic ball 2 month or 1440 h
COMB3(2160h)	Oil aged with mining sand ceramic ball 3 month or 2160 h
CONN1(720h)	Oil aged with Niger natural sand ceramic ball during I month or 720 h
CONN2(1440h)	Oil aged with Niger natural sand ceramic ball 2 month or 1440 h
CONN3(2160h)	Oil aged with Niger natural sand ceramic ball 3 month or 2160 h
CSP	Concentrating Solar Power
D	Dune sand sample in the ceramic ball
DMT	Dual medium thermocline
DNI	Direct Normal Irradiance (5.5 kWh. $\boldsymbol{m^{-2}.day^{-1}}$)
DS-B	Dune Sand from Burkina Faso
DS-N	Dune Sand from Niger
FP	Flash point (°C)
HTF	Heat Transfer fluid
IA	Index of Acid (mgKOH/g)
IEA	International Energy Agency

JCO	Jatropha Curcas Oil
JCCO	Jatropha Curcas Crude Oil
JCRO	Jatropha Curcas Refined Oil
LOI	Lost On Ignition
LTES	Latent Thermal Energy Storage
M	Mining sand sample in the ceramic ball
MS-B	Mining Sand from Burkina Faso
n	Total number of tests
N	Natural sand sample in the ceramic ball
NS-N	Natural Sand from Niger
Nu	Nusselt number
NFT 60–220:	Norme Française
ORC	Organic Rankine Cycle
P	Power, W
PCM	Phase Change Materials
PTC	Parabolic trough collector
PV	Photovoltaic
Sensitivity	Sensitivity
SE	Standard error [%]
SHS	Sensible heat storage
SONICHAR	Société Nigérienne de Charbon
TES	Thermal Energy Storage
TESM	Thermal Energy Storage Materials
VHC	Volumetric heat capacity
Greek	
$\boldsymbol{\sigma_t}$	Tensile strength, Pa
$\boldsymbol{\lambda}$	Thermal conductivity, $\boldsymbol{Wm^{-1}K^{-1}}$
$\boldsymbol{\varepsilon}$	Specimen or ceramic ball porosity, %
$\boldsymbol{\rho}$	Density, kg/m^3
$\boldsymbol{\alpha}$	Absorption factor
$\boldsymbol{\tau}$	Transmittivity factor
$\boldsymbol{\varepsilon}$	Emissivity factor
$\boldsymbol{\sigma}$	Stefan-Boltzmann constant, kg s^{-3} K^{-4}

$\boldsymbol{\eta}$	Efficiency
Subscript	
adv	Advection
abs	Absorber pipe
B	Ball
coll.	Collection
conv	Convection
diff	Diffusion
ext.	External
f	Fluid
g	Glass envelope
i	Number of tests
int	Internal
insul	Insulation
opt	Optical
p	Particle
rad	Radiation
s	Solid
$\boldsymbol{t}$	Tensile, threshold
r	Reference
w	Wall
Latin letter	
$\boldsymbol{C_p}$	Specific heat capacity, kJ/kg °C
D	Thermal diffusivity, $\boldsymbol{mm^2 s^{-1}}$
E	Irradiance coefficient, W.m^2
$\boldsymbol{T_{flash}}$	Temperature, °C
X value	The measured value
$\boldsymbol{\bar{X}}$	The mean value
m	Mass or weight, g
Q	Thermal energy or heat, W
$\boldsymbol{F_f}$	The peak load at failure of the sphere or the ceramic ball, N
h	Heat transfer coefficient, $\boldsymbol{W m^{-2} K^{-1}}$
T	Temperature, °C

$\dot{m}$	Mass flow rate, kgs^{-1}
h_{ext}	Heat exchange coefficient with ambient, $Wm^{-2}K^{-1}$
h_v	Interstitial heat transfer coefficient between particle and HTF, $Wm^{-3}K^{-1}$
a_s	Surface area of the solid, m^2
R_{th}	Thermal resistance coefficient of the tank, KW^{-1}
$r_{w,\text{ext}}$	External radius of the storage tank, m
$r_{w,int}$	Internal radius of the storage tank, m
$D_{w,\text{ext}}$	External diameter of the storage tank, m
$D_{w,int}$	Internal diameter of the storage tank, m
d_p	Particle diameter, m
m_0	Specimen mass after drying in the oven, g
m_1	Specimen mass after firing in the muffle furnace, g
D_{bed}	Diameter of the bed, m
H	Height of the tank, m
ΔH_{latent}	Latent heat of fusion, solidification, liquefaction or vaporisation of the correspondent material, $kJkg^{-1}$
u	Fluid velocity, ms^{-1}
U	Voltage, v
x	The axial distance along the collector, m

Contents

List of figures and pictures

List of tables

Abstract

Renewable energy is anticipated to play a vital role in the future to meet the global energy demand for low carbon transition. Solar energy presents the inherent characteristic given by the nature of the resource (intermittent availability). This observation highlights the need for thermal energy storage system. This PhD thesis was more focused on thermal energy storage for concentrating solar power plant, as well as its two essential components such as heat transfer fluid, storage materials and solar field. The analysis of the thermocline storage system and parabolic trough collector performance is achieved through the development of new thermal energy storage material, Direct normal irradiance data collection and numerical approaches. An innovative alternative solution for the storage materials consisted to use sand, clay and coal bottom ash to manufacture ceramic balls for thermal energy storage. The new material can store heat at temperature up to 610 °C. The new material showed good compatibility with Jatropha Curcas oil during 2160 h of heat treatment at 210 °C. After numerical analysis the new storage system (ceramic ball and JCO) can provide a discharge efficacy up to 94% depending on the storage tank size. In addition, Jatropha curcas oil is an innovative heat transfer fluid for parabolic trough collector (PTC) which can provide an average thermal efficiency up 83% to the collector. The connection of both TES system and parabolic trough collector (PTC) shows that a mass flow rate of 2 kgs^{-1} is necessary to charge a TES system of 2 MWh_{th} with a collection area of 460 m^2 before 3 pm under Ouagadougou and Agadez Climate condition. So, we propose, Jatropha curcas oil as heat transfer fluid (HTF) in medium-size (up to 1 MW_{el}) PTC plants using Organic Rankine Cycle power generation unit during 24h integrating the new TES system. It is a suitable technology in any region where the maximal DNI can reach 750 $W.m^{-2}$. The originality of the new composite material for thermal energy storage combines performance, materials availability at industrial scale and waste to energy approach while reducing environmental and financial impact.

Résumé

Les énergies renouvelables sont appelées à jouer un rôle essentiel dans l'avenir pour répondre à la demande mondiale d'énergie dans le cadre de la transition vers une économie à faible émission de carbone. L'énergie solaire présente une caractéristique inhérente à la nature de la ressource (disponibilité intermittente). Cette observation met en évidence la nécessité d'un système de stockage de l'énergie thermique. Cette thèse de doctorat s'est focalisée sur le stockage de l'énergie thermique dans les centrales solaires à concentration, ainsi que sur ses deux composants essentiels comme le système de stockage utilisant un nouveau fluide caloporteur et matériau de stockage et sur le champ solaire. L'analyse du système de stockage de la thermocline et des performances des collecteurs cylindro-paraboliques (PCT) est réalisée grâce au développement d'un nouveau matériau de stockage de l'énergie thermique, à la collecte de données sur l'irradiation normale directe et à des approches numériques. Une solution alternative innovante pour les matériaux de stockage a consisté à utiliser du sable, de l'argile et des mâchefers pour fabriquer des boules de céramique destinées au stockage de l'énergie thermique. Le nouveau matériau peut stocker la chaleur à des températures allant jusqu'à 610 °C. Le nouveau matériau a montré une bonne compatibilité avec l'huile de Jatropha Curcas pendant 2160 heures de traitement thermique accélérée à 210 °C. Après analyse numérique, le nouveau système de stockage (bille en céramique et JCO) peut fournir rendement de décharge allant jusqu'à 94 % en fonction de la taille du réservoir de stockage. En outre, l'huile de pourghère est un fluide de transfert de chaleur innovant pour les collecteurs cylindro-paraboliques qui peut fournir une efficacité thermique moyenne de 83 % au collecteur. La connexion du système TES et du PTC montre qu'un débit massique de 2 kg s^{-1} est nécessaire pour charger un système TES de 2 MW_{th} avec une zone de collecte de 460 m^2 avant 15 heures dans les conditions climatiques de Ouagadougou et d'Agadez. Ainsi, nous proposons l'huile de Jatropha curcas comme fluide caloporteur (HTF) pour faire fonctionner des centrales solaire thermodynamique de type cylindro-parabolique (PTC) de taille moyenne (jusqu'à 1 MW_{el}) utilisant une unité de production d'électricité à cycle organique de Rankine pendant 24h en intégrant le nouveau système de stockage d´énergie thermique TES. Il s'agit d'une technologie appropriée dans toutes les régions où le rayonnement direct (DNI) maximal peut atteindre 750 $W.m^{-2}$ pendant la journée. L'originalité de ces nouveaux matériaux composites pour le stockage de l'énergie thermique prend en compte l´efficacité, la durabilité, la disponibilité des matériaux à

l'échelle industrielle et l'approche de la transformation des déchets en énergie, pouvant reduire l'impact environnemental et financier.

General introduction

Energy is the fundamental essence that permeates everything in the known universe, and perhaps even beyond [1]. It has been present since the inception of time, spanning over 13.8 billion years, imbuing our vast cosmos with the brilliance of light, the presence of matter, and the warmth of heat. The swift evolution of these concepts has given rise to a novel scientific perspective, offering us a fresh understanding of the universe's intricacies. Whether the energy sources are familiar or not, humans have long utilized various forms of energy to improve their lives and carry out different activities. These energy sources can be broadly categorized into fossil fuels (such as coal, oil, and natural gas), renewable energy (including solar, hydro, geothermal, green hydrogen, biogas, biofuel, and wind turbine), and nuclear power. The consumption of this energy contributes to pollution. Fossil sources are the most contributing ones driving the climate change issues [2]. According to the International Energy Agency (IEA) CO_2 emissions from fossil sources combustion and industrial process accounted for close to 89% of energy sector greenhouse gas emissions in 2021 [3]. Within the framework of the objectives of reducing anthropogenic greenhouse gas emissions, a change in the energy production and consumption model is important. In addition to climate and environmental issues, energy transition is also likely to address economic and political issues such as the cost of energy, supply of energy, insecurity of supply, conflicts over access to resources, etc.[4]. In order to expedite the energy transition and address the challenges of climate change by reducing CO2 emissions, a crucial step is to prioritize the replacement of fossil fuels with renewable energy sources. Additionally, enhancing energy efficiency plays a significant role in achieving these goals [5]. Replacing of fossil fuels and energy efficiency enhancement should take into account the intermittence and variability of renewable energy in time and space for more adaptation of technologies from one region to another. In this context, systems that store and then restore energy are likely to be developed. Storage systems play an important role in facilitating the gradual integration and optimization of energy production and consumption. It enables energy to be used when it is needed. This characteristic allows to manage intermittency, whether it is linked to production or consumption. Thus, in discontinuous processes storage systems allow the temporary storage of excess energy for later usage. By acting as a buffer, they are also capable of making production and consumption more flexible, which makes it

possible to make the most of the energy produced and to optimize the sizing of the equipment since it operates more regularly in its nominal conditions. Energy can be stored based on several technics [6]. The main ones are of chemical process (fuels), gravity (hydraulic dams), thermal (heating or cooling), electrochemical (batteries), mechanical (compressed air), kinetic (flywheels) and magnetic. Thermal storage is particularly advantageous when the energy is produced or consumed in the form of heat because no conversion is required. Thermal energy storage (TES) is competitive when the quantities of energy involved exceed several hundred MWh. For these reasons, thermal storage is a particularly suitable solution for heat-based electricity production when sun is not shining using thermodynamic solar power. However, the main challenges for thermal energy storage systems are the cost of the storage system due to the used of mineral and synthetic oils as heat transfer fluids, the two tanks storage system. In addition to that, the high vapor pressure of thermal oil and the instability of molten salt make the storage systems complexes to manage and the oils have high risk of flammability.

This thesis deals with improving the performance of the TES system for concentrating solar power plants using local storage materials and heat transfer fluids in Burkina Faso and Niger. Also provides more information on the performance and sizing of parabolic trough collectors using Jatropha oil as a heat transfer fluid. It is structured into five chapters:

The chapter 1 will address the situation of concentrating solar power (CSP) plant potential in Burkina Faso and Niger and states of art on TES technologies. The chapter 2 will be focused on the formulation of the new sensible heat storage material, the chapter 3 on the compatibility between the developed specimens and innovative and available HTF (Jatropha curcas oil). In the chapter 4 the modelling and simulation to determine the performance of the new storage system will be addresses. As heat source is needed to filled the new storage tank, the chapter 5 will introduce the modelling and simulation of parabolic trough collector under Ouagadougou and Agadez climate conditions and its connection to the TES system before ending by a general conclusion.

Chapter 1: Concentrating solar power plant potential in Burkina Faso and Niger and state of art on thermal energy storage technologies.

Concentrating solar power (CSP) plants are mainly compound of a solar field, storage system and a power bloc. The solar filed produce heat for direct electricity generation or to charge the storage system. This chapter will introduce the context of thermal energy storage, the potential of CSP in Burkina Faso and Niger and state of art on thermocline energy storage.

I. Overview on energetic and storage context

The energy competition started since thousands of years, today, we remain searching more concentrated energetic sources able to provide the energetic demand of modern societies. That can be explained by the global demand growing of energy and the depleting of conventional resources like coal and petroleum**.** Renewable resources are expected to play a crucial role in the future. Among these sources we have solar energy, wind power, geothermal and hydropower. Furthermore, the development of clean and sustainable energy technology is imperative to avert and adapt to the impeding climatic crisis. Thermal energy applications are efficient in solar energy conversion through electricity generation, drying, cooling and cooking process. Concentrating solar power technologies are expected to produce about 7% and 25% of worldwide total electricity needs projected for the year 2030 and year 2050 respectively [7]. Although, this system is inherently transient as the available solar energy goes through diurnal cycles as well as short-term fluctuations due to intermittent and cloud cover [8]. Also, there exists some limitations in storing the huge energy produced like the short discharge time, the risk due to molten salt and synthetic oil use and the high cost of the global storage system linked to the two storage tanks use [9]**.** The hope in thermal solar area is the possibility to use local materials contrary to photovoltaic solar plants. And currently the aim is to use one tank to reduce the storage system cost thereby the cost of CSP. The use of local material as storage material is possible by using one tank for dual medium thermocline (DMT) storage [10],[11]**.**

I.1. Concentrating solar power plant potential in Burkina Faso, Niger and West Africa

The average rate of access to electricity in Sub-Saharan countries remains low. According to International Renewable Energy Agency (IRENA), it has grown from 33% in 2010 to 46% in 2019 [12]. However, 570 million of people remain in Sub-Saharan Africa without access to electricity [12]. According to World Bank, reports on Burkina Faso and Niger in 2020, the average electricity assess rate of 21% and 19.5% were recorded respectively [13],[12]. The two countries of West Africa have the lowest access to electricity while the direct normal irradiance (DNI) could exceeds 5.5kWh.day^{-1} [14] and [15].

The sun serves as the primary natural energy source for our planet, providing both heat and light. It fuels essential processes like photosynthesis and drives the water and wind cycle. Additionally, it contributes to shallow geothermal energy by heating the upper layers of the soil. However, solar energy is intermittent, and our society has evolved around more versatile but unevenly distributed energy sources. Reliance on conventional options like fossil fuels (oil, coal, natural gas) and nuclear energy comes with significant consequences for human life. For example, the emission of greenhouse gases (GHG), the risk of accidents (nuclear in particular) and the impact of these modes of energy production on health (air pollution) linked to human activities. In addition, we are witnessing a depletion of fossil and nuclear resources, the reserves of which are estimated in less than 150 years for coal, 53 years for oil, 55 years for gas and 120 years for uranium according to International Energy Agency [16]. This observation made in 1989 by the Intergovernmental Panel on Climate Change (IPCC) demonstrated that if nothing was done to reduce these harmful human activities, the greenhouse effect would lead to irreversible and unprecedented global warming [16]. And CSP technology is required to meet the world energy demand by reducing carbon emission. Global radiation reaching the ground is unevenly distributed in space and time. In Burkina Faso, there is a high density of sunshine in the north, especially towards Dori where maximum sunshine values of 6. 23 kwh /m² in April and 5.72 kWh /m² in August in the Dori station for the year 1996 according to a report of Gildas et al [17]. This maximum sunshine could be higher for Niger as illustrated in Figure. 1.1. With only 1% of the suitable (suitable for CSP installation) land area with daily DNI greater or equal to 5 kWh /m², a land slope (The slope refers to changes of the land elevation, orientation, and topography) less or equal to 5%, West Africa have a potential nominal capacity of 21.3 GW for only parabolic trough technology while the estimated electricity demand

is 17 GW for entire region [18] . This potentiality of CSP could improve when adding heliostat, Fresnel mirror and Dish technology.

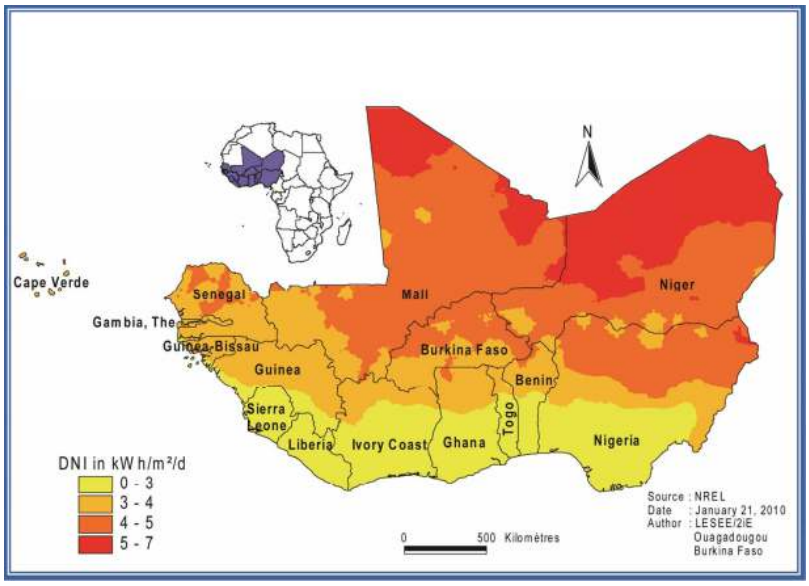

Figure. 1. 1. Annual average daily of Direct Normal Irradiance (DNI) for West Africa [18]

In Burkina Faso, CSP potentiality has been assessed based on satellite data. Because according to literature and survey no station in Burkina was found, equipped with pyrheliometers for DNI data monitoring. Based on SoDA dataset, Azoumah et al., [14] showed that the north part of Burkina Faso could be suited for CSP implementation [14]. The average daily DNI map since 2010 according to Azoumah et al., and the one according to World Bank are illustrated in Figure. 1.2.

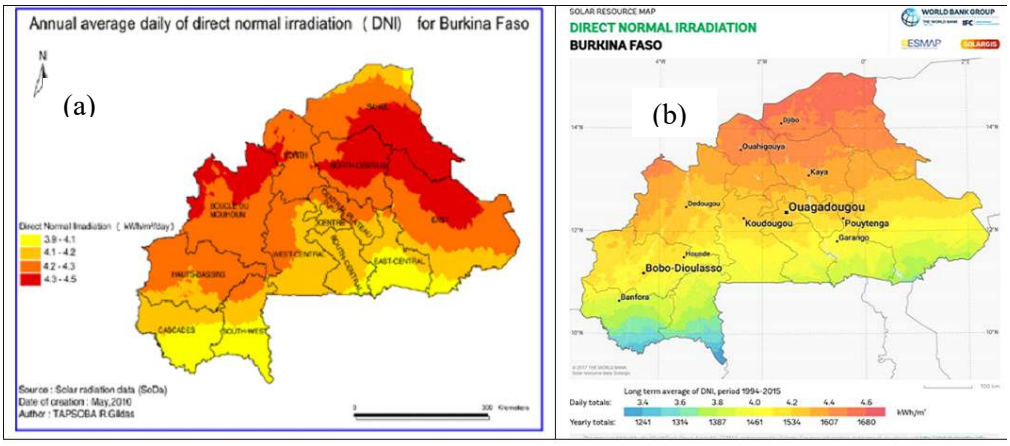

Figure. 1. 2. Direct normal Irradiation map in Burkina Faso according to Azoumah et al., 2010 (a) [14] and World Bank Group [19](b)

In Niger, there have so far been no studies on the potential of CSP apart from the one carried out by the World Bank Group as illustrated in the Figure. 1.3. Over this region a mean value of 2500 kWh/m^2 per year is available.

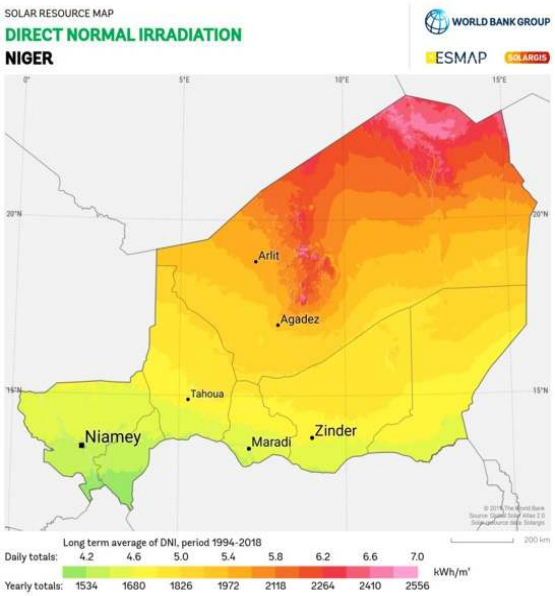

Figure. 1. 3. Niger DNI map according to World Bank Group [19]

I.2. Concentrating solar power technologies

Power generation from the solar radiation is currently achieved by two v different routes:

a. Photovoltaic technology, which is very popular, converts solar radiation directly into electricity;
b. The less known, thermal method which is based on an initial conversion of solar radiation (only the direct fraction) into heat to produce steam, which is used to drive turbines, as in all other thermal power plants [20].

The major advantage of thermal power plants is the fact that it is much easier (in term of implementation) and more affordable (low cost due the possible use of eco-materials) to store the energy at large scale in the form of heat than in the form of electricity. Therefore, the photovoltaic power stations produce rather erratic electricity to the grid inducing major risks of stability and the corresponding economic value of the product is necessarily low. In comparison, thanks to large scale thermal storage, concentrating solar power plants can produce 24 h/day a stable power levels to the grid. This is the case of Gemasolar (Spain 2011) or Crescent dune (USA 2015) power plants implemented recently which are able, thanks to 15 h of thermal energy storage duration (TES), to

produce 20 MW and 110 MW of constant power to the grid, respectively. Other CSP plants as ANDASOL [19],[20]and [22], Noor Ouarzazate with less extended storage unit (less than 8h), allow already the possibility to balance properly the solar radiation variation daily. Their production can be easily extended to the night by using fossil backup. Other CSP plants like the historic CEGS (USA), ran for several years without storage unit and using fossil backup [20]. However, the C.S.P has major flaws that currently limit its expansion [23] and [24]. Moreover, unlike photovoltaic panels, which are modular (installations ranging from a few kilowatts to several hundred megawatts), it is almost essential to build large plants to make CSP technology profitable, which requires very large investments. It is therefore necessary to develop low-cost solutions to promote its development in developing countries like Burkina Faso. All those CSP plants are based on two families of concentrating technologies: the first family is linear concentrators such as Linear Fresnel or solar trough mirrors and the second one is central receiver plants such as tower CSP or dish Sterling facilities. These concentrating systems (collectors) in CSP plants concentrate the sun's rays from a relatively large area (mirrors) to a smaller area (receiver).

I.2.1. Parabolic trough collector technology

This technology is the most mature industrially, representing nearly 90% of the world's installed solar thermodynamic capacity (5000 MW at the beginning of 2019) [25]. It uses semi-cylindrical mirrors that can be rotated along an axis, forming a line that can be up to 100 meters long, to concentrate the radiation on a receiving tube, as shown in Figure. 1.4. Several lines are assembled to form a collector field. The heat transfer fluid is usually synthetic oil, which limits maximum operating temperatures to around 400°C. However, some installations use molten salts or water. This focusing system makes it possible to reach concentration factors of the order of 70 to 100 suns, to reach temperatures in the receiver between 350 and 550 °C [26]. The first solar power plant using this technology was installed in Egypt in 1912 to power 73 kW agricultural water pump [4]. Currently, the two largest parabolic trough solar power plants, each with a capacity of 280 MW, are in the USA: Genesis and Solana (Figure. 1.4b) [27]. They both operate with therminol® (synthetic oil) at temperatures approaching 400°C. The first large CSP plant in Africa (160 MW) that operates with molten salt was inaugurated in February 2016 in Morocco (Figure. 1.4c).

(a) (b) (a)

Figure. 1. 4. Parabolic trough collector (a), Solana power plant [27](b), Noor Ouarzazate I power plant [12] (c).

I.2.2. Linear Fresnel Reflector

Linear Fresnel reflectors (LFRs) use an approximation of parabolic reflectors shape of trough systems with long rows of flat or slightly curved mirrors to reflect the sun's rays on to a downward-facing linear [28]. This allows the use of a fixed linear receiver to facilitate direct steam generation. Thus, eliminating the cost of using an auxiliary heat transfer fluid. Typical concentration factors are similar to those obtained with parabolic-cylinder technology, between 10 and 200 suns, allowing temperatures to reach up to 550 °C [26]. and [29]. This technology is less expensive than the parabolic trough technology but requires extensive work on sun tracking and the management of the different reflections. Indeed, problems of shading and blocking are recurrent [30], and the concentration being moreover imperfect, part of the flux does not reach the receiver directly and a secondary reflector is necessary. However, some drawbacks of parabolic trough sensors can be eliminated, based on the reduction of installation costs, thanks to cheap flat mirrors, better land use (up to 70% coverage compared to 30% to 35% for parabolic troughs) and mirrors that, by moving at the same angular velocity, allow less expensive tracking. The version with compact linear reflectors would produce the same amount of energy as the parabolic trough concentrators [31].

Despite its low installation cost, this technology is not very well represented on an industrial scale, with about 216.4 MW installed worldwide [32] (2019), or 1% of the total capacity. The most extensive installation is Dhursar plant located in India (Figure. 1.5) with a capacity of 125 MW. The second largest installation is Dacheng Dunhuang plant, with a capacity of 50 MW, located in China [32].

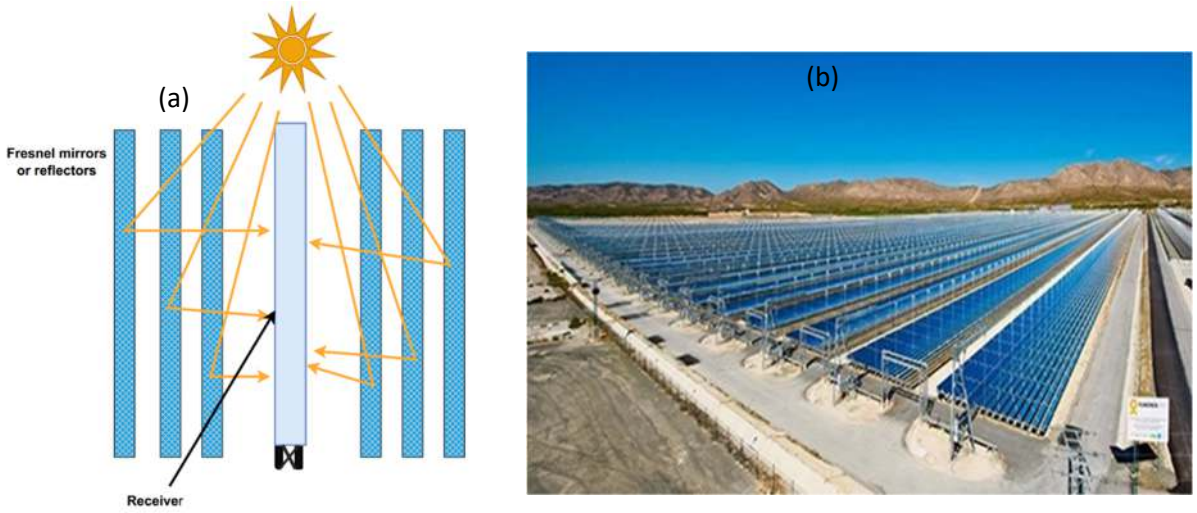

Figure. 1. 5. Linear Fresnel reflector (a) and Puerto Errado 2 plant in Spain [26] (b)

I.2.3. Solar tower power plants technology

Solar tower power plants use flat or slightly concave unit mirrors mounted on independent orientation systems that are controlled along two axes (azimuth and elevation), the whole forming a heliostat. The radiation is concentrated at the top of a tower, on a receiver, thanks to a sun tracking system that manages the whole heliostat park, as described in the Figure. 1.6. It is at the receiver that the energy of the radiation is absorbed and transferred to the heat transfer fluid, which can be water, water vapour, molten salt, pressurized hot air, etc**.** [33]. Tower power plants have been developed for installations for high production volumes scale, developing strong powers and working at high temperature [34]. One of the major advantages of such a process is a concentration factor which can be between 300 and 1000 [35], which allows to reach high temperatures, from 800 to 1000°C. The possibility to combined cycles in this type of plant increases the overall efficiency of the plant. Among the industrial scale projects, we can mention the Planta Solar 10 (PS10) [36] and Planta Solar 20 (PS20) installations of Abengoa Solar in Spain, which operate with direct steam generation [37], [27]. The Gemasolar plant of Masdar and Sener in Spain uses the same technology of concentrating radiation with a molten salt heat transfer fluid. After the Gemasolar plant comes the Noor Ouarzazate III plant (see Figure. 1.7) with a thermal capacity of 150 MW inaugurated at the end of 2018 in Morocco.

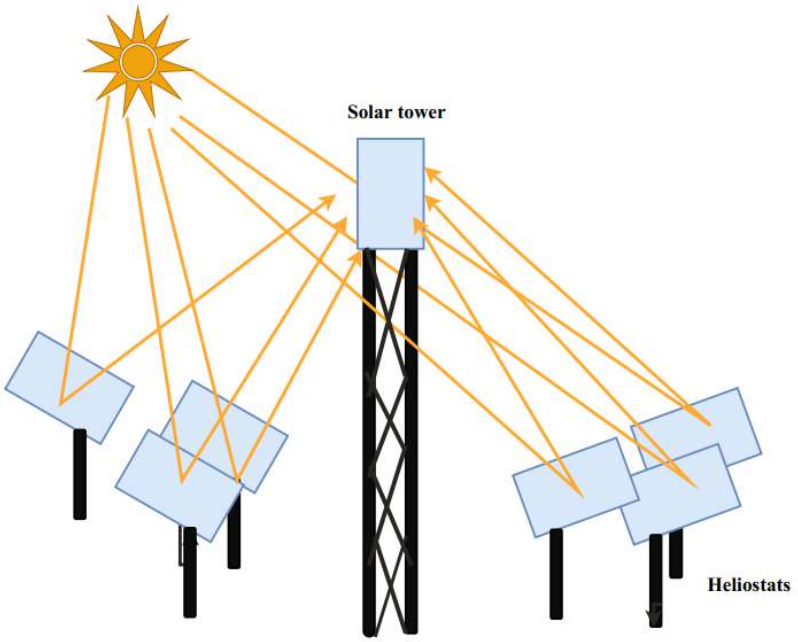

Figure. 1. 6. Solar tower [26],[38]

Figure. 1. 7. Gemasolar [33] (a) and Noor Ouarzazate III [39] (b) solar tower power plants

I.2.4. Parabolic or dish technologies

Among the four technologies presented here, parabolic reflector technology is the one that achieves the most important concentration factors - from 1000 to 3000 suns [26]. A parabolic reflector with a surface area of up to 400 m² [26] was used for demonstration, mounted on a sun tracking system similar to a heliostat of a tower power plant. The receiver, located at the focal point of the parabola, is usually an independent power generation system - a Stirling engine or a compact gas turbine [28], as shown in Figure (1. 8a). In theory, it provides the best efficiency

(thanks to a very high concentration factor) but the installation of storage is very difficult, they are the most expensive collectors and are not adapted to large powers. These concentration systems have reduced sizes compared to the other three technologies. The most industrially mature realization is the Maricopa solar power plant in the United States (Figure. 1.8b). It consists of 60 parabolas each equipped with a Stirling engine with a power of 25 kW, thus constituting a demonstration plant with a capacity of 1.5 MW [40]. Unfortunately, the Stirling Energy System company behind this project went bankrupt, condemning the larger projects it was planning. Nevertheless, this technology is still under study for the realization of decentralized energy production systems.

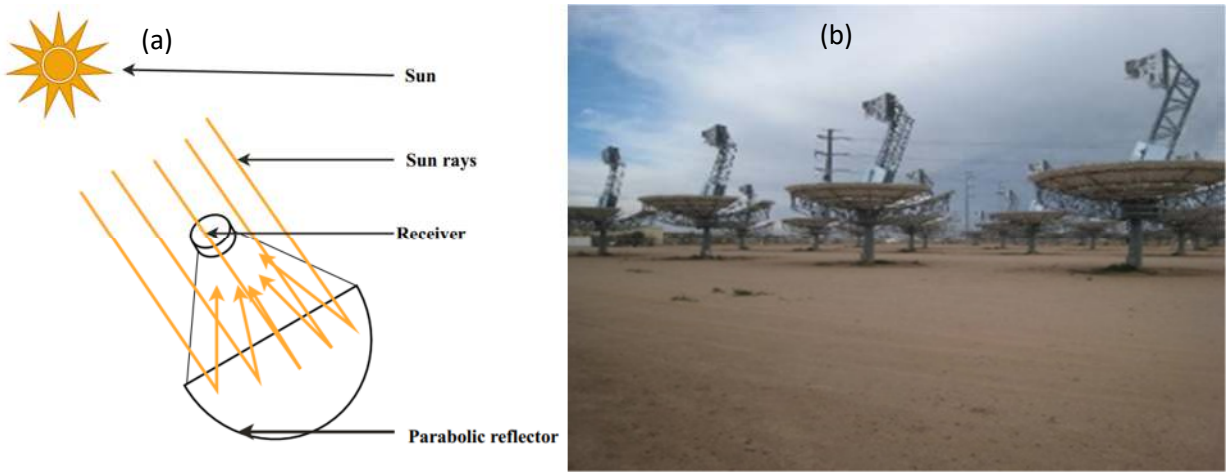

Figure. 1. 8. Parabolic dish collector (a)[28] Maricopa dish solar power plant (b) [40]

To Conclude, parabolic cylinder technology has the most maturity of several decades of industrial experience (significant development following the first oil crisis in the 1970s). On the other hand, current developments are more oriented towards tower power plants. However, much of the research carried out on one of the technologies can be applied to the others, since many elements of the power plant are similar (storage, power unit, etc.).

CSP plants are mainly defined by concentrating factor and global efficiency. These parameters or indicator are defined as follows:

- **Concentrating Factor**

The geometrical concentration factor corresponds to the ratio between the total collection surface of the mirrors and the reception surface of the concentrated rays. The concentrating Factor can be written in equation (1.1)

$$F_c = \frac{A_{collected}}{A_{received}} \quad (1.1)$$

Higher is the concentration factor, the flux density impacting the receiver highly, and therefore the temperature reached by the receiver can be high.

- **Efficiencies**

A high temperature makes it possible to achieve theoretical thermodynamic efficiencies close to the Carnot efficiency when converting heat into electricity. This Carnot efficiency is given by equation (1.2).

$$\eta_{carnot} = 1 - \frac{T_{cold}}{T_{hot}} \quad (1.2)$$

Where T_{cold} is the cold temperature, T_{hot} the hot temperature and η_{carnot} for the Carnot efficiency.

The efficiency of the power plant is well below this theoretical limit: optical losses occur in the heliostat field or collectors, thermal losses in the receivers, pipes, heat exchangers (if present), and mechanical thermal losses in the power unit. In the end, the total efficiency of the power plant is defined as the ratio between the electrical output power and the solar input power of the collector system equation (1. 3).

$$\eta_{global} = \frac{P_{elec}}{P_{sol}} = \frac{P_{elec}}{DNI.A_{coll}} \quad (1.3)$$

Where P_{elec} is the electrical output power in W, P_{sol} is solar input power of the collector system in W and η_{global} the global efficiency of the plant.

The Table 1.1 Illustrates the characteristics of the different concentrating solar power technologies. Each technology has concentration factors, operating temperatures, overall theoretical efficiencies, as shown in the table below. The highest concentrator is achieved by the dish technology, follow by solar tower. Currently, solar dish has the best annual solar-to-electric efficiency (%) demonstrated (d) follows by parabolic trough collector, linear Fresnel and solar tower. In the future (p) solar tower is expected to reached the best annual efficiency follows by dish technology. The

different technologies have similar thermal cycle efficiency expected the solar tower that can reach a thermal efficiency between 45% to 55% due to the possibility to combined different cycles (CC).

Table 1. 1. Characteristics of the different concentrating solar power technologies [26]..

Characteristics	Parabolic trough	Linear Fresnel	Solar tower	Parabolic or dish
Capacity (MW)	10-200	10-200	10-200	0.01-0.04
Concentration factor	70-80	25-100	300-1000	1000-3000
Thermal cycle efficiency (%)	30-40	30-40	30-40	30-40
			45-55 (CC)	
Annual solar-to-electric Efficiency	10-15 (d)	9-11 (d)	8-10 (d)	16-18 (d)
(%)	17-18 (p)		15-25 (p)	18-23 (p)
Cost: capital (Dollars/kW)	3972		4000+	12,578
(Dollars/m2)	424	234	475	
Land use ($\boldsymbol{m^{-2}.MWh^{-1}.y^{-1}}$)	6-8	4-6	8-12	8-12

II. Thermal energy storage and its applications

This section looks at thermal energy storage technologies and their applications in solar power plant systems [8].

II.1. Storage media

There are mainly three types of TES systems, sensible, latent storages and thermochemical storage. In this thesis, the sensible heat storage is studied. The thermochemical storage, still under deep research but worth to be mentioned.

II.1.1. Sensible thermal energy storage

Sensible TES consist of a storage medium which stores energy in the change of temperature of the substance. The most important parameters when considering sensible heat storage are density and specific heat; however other important factors are operational temperatures, thermal conductivity and diffusivity. The quantity of energy stored during the charging process can be calculated by equation (1.4).

$$Q = \int_{T1}^{T2} V \rho c_p \, dT \qquad (1.4)$$

Where V, ρ, C_P, and dT are respectively the storage material volume, density, specific heat and the temperature gradient suffered by the material.

Therefore, the main focus of sensible TES (STES) is put on the choice of suitable storage materials and their characteristics in fulfilling desired purposes [41]. Usually, sensible thermal energy storage materials are sub-grouped into two main categories: solid and liquid materials. Solid storage materials are mainly preferred for building applications but also in some cases of high temperature solar applications. The main advantages of such materials are reduced risks of leakage and viability at very high temperature. In CSP applications the most used material are castable ceramic, concrete and natural rock within a packed bed system [8],[41],[42] and [43]. Especially concrete and rocks as rhyolite are cheaper and interesting material for high specific heat, good mechanical properties, with thermal expansion coefficient like the one of steel for concrete. But rocks are not well shape (low sphericity) and size (big size) driving to the reduction of the storage performance (affect discharge efficiency, discharge time, increase of thermocline thickness) [44]and [45].

Liquid media have been favourable for better performances and for the possibility of stratification which enhances the performance of the storage tank. Water is the most used liquid for low temperature applications (25 - 90 °C). For a temperature variation of 60°C, water stores 250 kJ/kg, and is therefore widely used in solar applications for heating buildings and domestic hot water[46]. On the other hand, its use in high temperature applications is conditioned by its high vapour pressure which presents a major disadvantage. For this purpose, the use of large storage tanks is recommended. In CSP application molten salts, mineral and synthetic oils are mainly used. Liquid phase media have several advantages such as higher heat capacity, which makes it more suitable for applications at nearly any temperature level [41],[8],[47]**.** Molten salts are the universal or popular materials for storage in CSP applications for a number of reasons.

- they are liquid at atmospheric pressure;
- they can be used as HTF;
- their working temperatures are suitable for high temperature steam turbines.

In addition to this, experience with this kind of media existed already in chemical and metal industries as HTF. The most common salt is the HitecXL, which consist of a mixture of $NaNO_3$ and KNO_3(60/40 %).

Table 1.2 illustrate the different sensible heat storage materials and their properties. All the materials are characterized by their density (ρ), specific heat capacity (c_p), volumetric heat capacity (ρc_p), thermal conductivity and operating temperature (O.T). It shows that the ρc_p on the different materials depends on their density and specific heat capacity. For example, cast iron is the solid material that has the highest ρc_p with the highest ρ but limited in operating temperature. For the liquid, carbonate salts present the highest ρc_p with a density of 2100 kgm^{-3} and c_p of 1.8 kJ$kg^{-1}°C^{-1}$ with a possibility to reach 850°C as operating temperature. Oils present good specific heat capacity but their density is greatly reduced at high temperatures. Vegetable oils present the lowest operating temperature.

Always conditioned by safety and stability problems, the use of these molten salts and oils from petroleum (synthetic and mineral oils) requires very sophisticated installations from a control point of view.

Table 1. 2. Sensible heat storage material and their properties [44],[48]- [49]

Material	ρ $\boldsymbol{kg.m^{-3}}$	$\boldsymbol{c_p}$ (kJ/kg°C)	$\boldsymbol{\rho c_p}$ (kW/$\boldsymbol{m^3}$.°C)	$\boldsymbol{\lambda}$(W/m.K)	O.T(°C)	References
High temperature concrete	2750	0.915	0.7	1	Up to 350	[48],[44]
Reinforced concrete	2200	0.85	0.5	1.5	200-400	[50]
Heat Crete	N/A	N/A	0.5-1	1.7-2.5	20-450	[1]
NaCl	2160	0.85	0.5	7	200-500	[50][1]
Cast iron	7200	0.56	1.1	37	200-400	[50][1]
Cast steel	7800	0.6	0.9	40	200-700	[50][1]
Silicate fire brick	1820	1	0.5	1.5	200-400	[50][1]
Ceramic						
Clay ceramic		1.2-1.49			Up 500	[51]
Clay and ash Waste ceramic (fire Temp>1125°C)	1800-2140	N/A	0.27-0.54	<1	N/A	[52][53]
Alumina ceramic	3750	0.780	0.81	30	N/A	[44]
Silicon carbide ceramics	3210	0.750	0.67	120	N/A	[44]
Coal Fly ashes	2600	0.735-1.3	0.53-0.94	1.3-2.1	N/A	[54]

Rocks						
Desert sand	2612-2660	0.9261			650	[55][56]
River sand		1.041			RT. >1087	[57]
Silicate sand		1.3		2.5	550	[58][59]
Rhyolite	2720-2736			2.3		[43][60]
quarzitic	2656	0.831-1.054		5-3.7	RT. 650	
Quartzite rock	2500	0.830	0.58	5.69	->370	[44]
River pebble						
Liquide						
Solar salt			0.75	0.5	260-565	
HITEC			0.78	0.6	142-454	
Therminol VP1	904	2.075	0.52	0.1	12-400	[61]
HitecXL			0.85		133-500	
Syltherm800			0.4	0.1	R.T-400	
Delcoterm Solar E15			0.5	0.12	R.T-320	
Nacl	2160	0.56	0.5	7	200-400	[50]
Liquid sodium	850	1.3	0.31	71	270-530	[50]
Mineral oil	770	2.6	0.55	0.12	200-300	[50]
Synthetic oil	900	2.3	0.57	0.11	250-350	[50]
Nitrate salts	1870	1.5	0.83	2	265-565	[50]
Nitrite salts	1825	1.5	0.76	0.57	250-450	[50]
Carbonate salts	2100	`1.8	1.075	2	450-850	[50]
Vegetal oils						
Jatropha curcas oil	802	2.509	0.56	0.11	160-≥ 210	[62][63]
Rapeseed oil					160-≥ 210	[49]

II.1.2. Latent thermal energy storage (LTES)

In addition to the sensible variation of the internal energy of a material associated to temperature change, isothermal or quasi-isothermal internal energy involving mechanisms can also be exploited to store heat. In this frame, heat can be exchanged with a thermal system maintaining

constant any of the thermodynamic variable magnitudes such as temperature, pressure or volume. This exploitation of physical mechanism leading to the exchange of the internal energy of the material under isothermal condition is based on its phase change. In this process, the internal energy of a thermodynamic system is not used to promote a temperature variation, but to rearrange its internal structure at molecule or atomic level [1]. Substances which can be used to store thermal energy during the phase change are called Phase Change Material (PCMs). Examples of transition with an associated heat latent able to exchange thermal energy, and exploited in TES application are presented as follows:

- Melting-Solidification (solid ↔ liquid): This phase change usually occurs in a temperature range between -100 and 1500°C, depending on the material. the volume variation between the solid phase and liquid phases presents a controllable and predictable behaviour. The associated operation pressures also show controllable values, suitable for the practical implementation.
- Evaporation-Condensation (liquid ↔ gas): These phase changes involve higher latent enthalpies when compared to solid-liquid transformations. The huge volume change between liquid and gaseous phase involves the implementation of very complex practical devices. As consequences, this transition mechanism does not show a strong attractive for LTES applications.
- Structure transition (solid ↔ solid): Usually present a limited latent heat value compared to the rest of phase change mechanism [1].

In all the mentioned phase change mechanism, the stored or exchange heat can be calculated using equation (1. 5).

$$Q=m\Delta H_{latent}. \quad (1.\ 5)$$

Where m is the mass of the material stress from the phase change and ΔH_{latent} represent the latent heat of fusion, solidification, liquefaction or vaporisation of the correspondent material.

In addition to the standard requirements applicable to any storage material, a PCM shall be selected based on the following criteria:

- The reversibility of the phase transition must be guaranteed to obtain a successful cyclic operation of the storage.

- The transformation temperatures, both on the heating and cooling processes, must meet the requirements of the selected storage application.

As a consequence of the last requirement the thermal hysteresis (separation of the melting and freezing), subcooling or superheating effects suffered in the transition must be limited, controlled and reproducible.

Many materials have been proposed as PCM in the last years as show in Table 3:

Table 1. 3. Example of some PCM materials [64]and [65]

compound	Melting temperature (°C)	Heat of fusion ($kJ.kg^{-1}$)
Water-salt solutions	-100 to 0	200 to 300
water	0	330
Clathrates	-50 to 0	200 to 300
Paraffins	-20 to 100	150 to 250
Salt hydrates	-20 to 80	200 to 600
Sugar alcohols	20 to 450	200 to 450
Nitrates	120 to 300	200 to 700
Hydroxides	150 to 400	500 to700
Chlorides	350 to 750	550 to 800
Carbonates	400 to 800	600 t0 1000
Fluorides	700 to 900	>1000

Between STES and LTES principles, LTES present two main advantages. On one hand, LTES systems show higher energetic density than STES, based on the usually large latent heat values. On the other hand, considering the isothermal nature of the mentioned phase transitions, PCM

materials can supply or absorb thermal energy at constant temperature. However, some drawbacks like the highest cost of the PCM (compare to current sensible materials such as molten salts, concretes or ceramic Material), the flexibility in the operating temperature can limit the implementation of this technology.

II.2. Storage concepts

The implementation of heat storage system requires the development of suitable storage concept for its deployment in real applications. As detailed in STES and LTES sections, each alternative presents a particular problematic which makes necessary a customized design (specific). Taking into account, the detailed requirements of each TES alternative, in this section, a general heat storage conceptual implementation survey is provided.

II.2.1. Active storage

In this concept the storage medium (molten salt for example) moves through the TES unit. As an example of active TES concept, in the CSP environment these systems typically use a double-tank solution (one for the hot fluid and other for the cold fluid [66] and [67]) or a single-tank (thermocline concept without filler material [68]) to contain the storage medium. Currently two different configurations can be found in commercial systems:

II.2.1.1. Direct active storage

In the direct systems, the storage medium works also as HTF, no intermediate heat exchangers are required and the energy is directly transferred to the working fluid [69] and [70]. In this configuration, the hot fluid coming from the heat source, i.e., industrial process, solar field, etc. is directly fed to the hot tank (Figure. 1.9a). From this tank, it is sent to the particular heat demanding application, i.e., power block, industrial process, etc. and once cooled down, it is introduced back into the cold tank. When the heat is available again the process can restart.

A second example of direct active storage is a single fluid solution (Figure. 1.9b), which shows a thermocline TES concept. Under this configuration, the heat from heat source is introduce through the upper part of the tank and released cold from the bottom. Inside the storage tank coexist, hot and cold, fluids separated by a temperature stratification region called thermocline [71]. When it is necessary to take the heat back from the tank, the hot fluid leaves the storage system through the upper part to the heat application system where it gets cold after use and goes back to the tank

from the bottom. The main advantage is the cost reduction due to the elimination of the intermediate expensive heat exchanger.

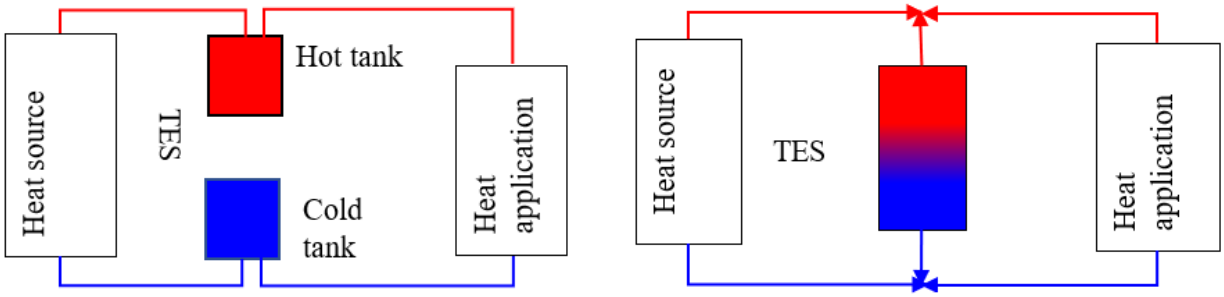

Figure. 1. 9. TES configuration: a) active direct storage; b) active direct storage with thermocline [1].

II.2.1.2. Indirect active storage

Two different fluids are used, one as heat transfer fluid and other as storage medium. Heat exchanger is required in this configuration (Figure. 1.10). In this case, a heat exchanger is fed with hot fluid coming from the heat source (solar field) to heat up the secondary fluid used as storage medium or directly consumed in the heat demanding application. When the heat source is not available (during the night, cloud cover, etc.) the fluid from the hot tank is fed in the second heat exchanger to heat up the working fluid or to produce steam.

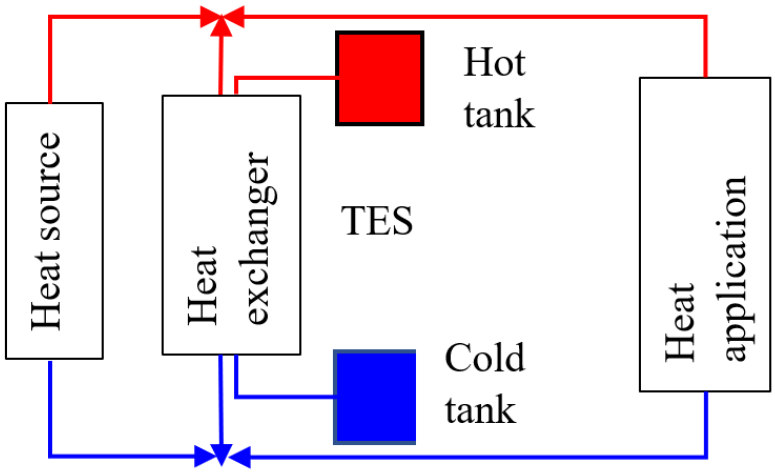

Figure. 1. 10. Active indirect storage TES configuration [1].

II.2.2. Passive storage

In this configuration (Figure. 1.11) the heat transfer fluid is passing through the storage medium during charging and discharging time. The storage medium is fixed and does not move through the TES unit. This is the case of thermocline storage when using filler materials [8]

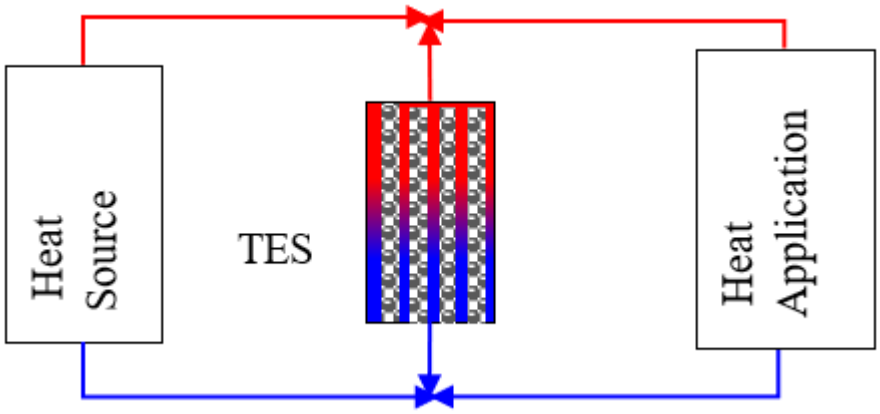

Figure. 1. 11. Thermocline energy storage system configuration

III. Thermocline storage

The accessibility of CSP technology suffers from the unavailability of solar energy at night and during periods of cloud cover. For more flexibility when using CSP technology for electricity generation, it is necessary to use an energy storage system to distribute electricity during these periods, which requires significant investment. The cost of the two-tank storage system, for example, represents 15-20% of the initial investment.

Added to this is the high price of the heat transfer fluid (HTF), such as mineral oil and synthetic oil, use as storage medium since 1984 at SEGS plant [72]. Another problem of mineral oil is the high risk of flammability, for example in 2009 , Andasol CSP plant solar field in Spain took fire [49]. To face these challenge in 2004 an engineering study shown the possibility reduction of 10% of levelized cost of electricity (LCE, price at which the generated electricity should be sold) cost using molten salt in the storage medium [72]. Becoming the most effective TES material, most of CSP plant like Andasol, Ouarzazate have molten salt as storage medium material [68][39]. The molten salt is also compromise because of it high melting temperature and the complex management of its thermal stability [73],[74] and [49]. A part from the high cost, low thermal stability of mineral oil and molten salt, these materials have negative impact on the environment.

Though, according to previous studies, there is a possibility to have a broad reduction of CSP cost (33% to 35%) by cancelling one tank of the storage system and using eco-materials(natural rocks, industrial waste etc.) as filler materials [68] and [11]**.** A thermocline storage is one that uses a single tank to store thermal energy. As example of thermocline tanks in experimentation, there is one at Solar One at university of Bayreuth at Ait Baba at Jülich etc.[75],[59],[42] and [76]. In this tank a thermal gradient separates the hot zone from the cold one. The word thermocline is from oceanic language. It corresponds to the thermal transition zone between the superficial waters and the deep waters. At the top and the bottom of thermocline zone, temperatures are quasi-uniform, while the different of temperature is important in the width of thermocline [49]. There are two types of thermocline system:

- Single-medium thermocline (SMT); When the tank uses only fluid as storage medium such as molten salt (Figure. 1. 12a)
- Dual medium thermocline (DMT) (Figure. 1. 12b); It is obtained by adding filler materials to reduce the amount of molten salt or thermal oil required. It offers economic and technical advantages over SMT tanks [77].

The single-medium thermocline is active storage system while the DMT can be both active and/or passive also called regenerators [78] and [76]. When the thermal capacity of the heat transfer fluid (HTF) is significant, the thermocline storage system is a dual-medium system (active-passive) [78] and [67]. When gas is used as HTF, the storage system is passive.

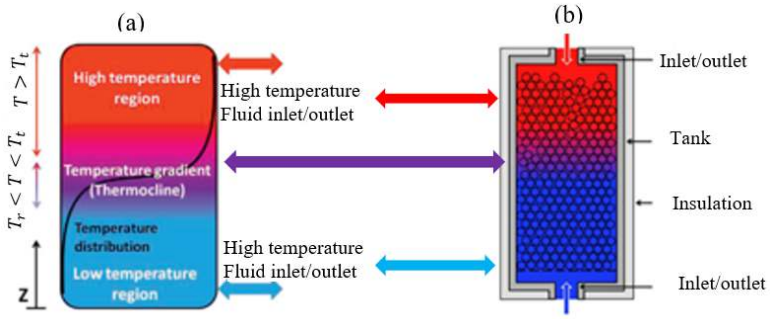

Figure. 1. 12. (a) Single-medium thermocline (SMT), (b) Dual-medium [68] and [49]

In the following section the effectiveness of the different type of thermocline storage system is presented. With more focused on DMT system an overview is carried out on the different

parameters (fluid, filler material and tank) influencing the thermal performances of the thermocline TES.

III.1. Single-medium thermocline storage system.

Most of SMT systems are usually used for industrial refrigeration systems and domestic solar thermal devices. To assess under static and dynamic conditions a thermocline performance, Abdouly et al studying in 1982 the static and dynamic properties of a water thermocline carrying out a possibility degradation of the thermocline due to heat mechanism losses through the insulation. Also, the tank should have an optimal size (length>3.048m, diameter>0.4572m and insulation resistance>113.566 W$m^{-2}K^{-1}$) [79]. Water has an excellent specific heat (4.19 kJ/kg K) but the system need to be pressurized at above 100°C, which adds tremendously to cost, increase accident risk [80]. Assessment based on numerical simulation has shown a higher thermal performance of molten salt SMT than the DMT one because there is absence of thermal ratcheting. But molten salt SMT tank is more sensitive to flow disturbances, internal mixing and have less cost-effectiveness [77]. The main equations governing the SMT behaviour consider the motion of the fluid inside the tank that obeys the mass and momentum conservation principles as expressed in the following laminar flow equations (1.6) and (1. 7).

$$\frac{\partial \rho}{\partial t} + \vec{\nabla}(\rho\vec{u}) = 0 \qquad (1.\ 6)$$

$$\frac{\partial \rho}{\partial t} + \vec{\nabla}(\rho\vec{u}) = \Delta\rho + \nabla\tau + \rho\overrightarrow{Ig/} \qquad (1.\ 7)$$

For the energy balance in the storage system, one equation is required for a SMT tank and is writing in equation (1. 8).

$$\frac{\partial(\rho C_p T)}{\partial t} + \vec{\nabla}\left(\vec{u}\rho C_p T\right) = \vec{\nabla}(\lambda\vec{\nabla}T) + \mu\emptyset \qquad (1.\ 8)$$

Where ρ is the density, c_p the specific heat, T fluid temperature, λ thermal conductivity, μ the viscosity of the fluid and ∅ viscous dissipation function; ∇ defines the dimension of the model (1D, 2D or 3D).

Based on these models, researchers have carried out the influence of the ratio height over diameter (H/D) and tank position on thermal stratification. In 2017 Burak et al have found optimal values of 0.5 and 45° respectively for the tank ratio and tank position angle for water thermocline storage tank with 93% of stratification efficiency [81]. Bent inlet geometry design is required to have a

good stratification for the Reynolds number between 7500 to 20500 and for HTF velocity between 0.11-0.16 mm/s [82].

III.2. Dual medium thermocline system (DMT)

Most of CSP pilot and laboratory scale projects for thermocline storage studied are dual-medium thermocline [83],[76],[84],[85],[59],[9] and [42]. DMT tanks are favored because they have economical and technical advantages. The solid material reduces the quantity of the liquid material (oil, molten salt) which is often the most expensive. But, to have a good thermal stratification, many parameters need to be considered. Such as thermocline extraction during charging and discharging time. Solar One CSP pilot plant is one of the first plants where DMT system has been experimented since 1982. The storage system was sized to generate 7MWe for four hours. The storage system uses dual liquid (Caloria HT-43) and solid (quartzite and sand) storage media in a thermal storage tank with 13.8m of height, 18.3m of diameter and 0.304m of external insulation. The HTF (Caloria HT-43) was heat from 218°C to 304°C and was heated indirectly by the steam from the receiver through heat exchanger [1]. Thermal-to-electric efficiency was 25% from thermal storage steam instead of 35% because of the limitation to use oil more than 304°C (avoid vaporization) and the indirect storage method [1]. In 2012 the thermos mechanical performance simulation (infinite rigidity approach for the solid filler) of the Solar One thermocline storage tank by Scott et al linked the stresses along the tank wall to some finite amount of solid filler volume change due to thermal expansion and mechanical interactions; because the measured horizontal stress reached 190 MPa again 177 MPa from numerical investigation (6.8% of deviation) [75]. Moreover the thermal performance of the molten salt packed-bed investigated in 2013 [44] carried out the impact of solid particles size on the thermocline performance. The efficiency is the highest for the particle's diameter smaller than 1.9 cm. The discharge time increases with thermal capacity (energy density) trough different solid particle material. And also the particle should have an optimal thermal conductivity [45] to easier release heat during discharge time [44]. Solid particles like cast iron and ceramics have long discharge time but are not abundant and are expensive, while rock like quartzite rock has a good discharge efficiency and available with effective cost. That explains the use of quartzite/sand in the first thermocline storage tank (solar one) and why rocks are being experimented on thermal energy storage materials. But the uncontrolled shape and size of rocks affect the thermocline efficiency (big size, not well shape) [49]. In addition, the configuration of the storage tank impacts the storage efficiency through insulation, its size and

wall. The heat losses have to be taken into account for small tanks to correctly predict outlet temperature, but can be negligible for large-scale tank, also the tank wall may exert non-negligible effect on temperature profile inside the tank [86].The thermal storage efficiency increases with the ratio height over diameter (H/D) and should have a minimum value of 2.3948 [87] because resulting in higher velocities of the HTF. That drives to a better heat transfer with the solid particles [45]. The optimal height of tank could be 30 m according to Angelini et al.,[68]. Also, different HTFs may influence the thermal performance of the thermocline through the porosity of the tank. The increasing of the tank porosity from 0.1 to 0.7 decreases the effectiveness of the storage tank and could be more suitable with therminol oil compare to molten salt like solar salt [88]. Table (1.4) illustrates a state of art on some DMT projects:

Table 1. 4. Parameters of some thermocline energy storage systems in the literature [89]

Particles	Fluids	D_{bed} [m]	H [m]	d_p [mm]	ε	D_{bed}/d_p	T [°C]	u	Temperature measurements processing
River pebbles (granite) and silica sand	Caloria HT 43 (oil)	3,2	12,2	25 / 1,5	0,25	128	218 - 302	0,3 – 3,3 mm/s	Fluid Longitudinal / Transversal
Rocks and sand (NC)	Caloria HT 43 (oil)	18,3	13,7	25 / NC	0,22	732	200 - 290	NC	Longitudinal fluid
Rocks (NC)	HP Hytherm 500 (oil)	2,2	2,0	50	0,30	44	230 - 247	0,4 mm/s	Fluid / Solid Longitudinal / Transversal
Quartzite rocks and silica sand	$NaNO_3$-KNO_3, 50-50 %m	3,0	6,1	19 / 1,5	0,22	158	290 - 390	2,6 mm/s	Fluid Longitudinal / Transversal
Rocks (NC)	CALFLO^{TM} LT (oil)	0,29	0,3	5	0,42	58	20 - 240	0,04 – 0,12 mm/s	Longitudinal fluid
Silicate glass balles	Shell Thermia Oil B (oil)	0,035	0,45	3	0,42	12	30 - 160	10 – 19 mm/s	Fluid Longitudinal
Ceramic spheres	Hitec® (KNO_3-$NaNO_2$-	0,263	0,55	30	NC	8,8	280 - 355	3 mm/s	Fluid Longitudinal

	$NaNO_3$, 53-40-7 %m)								
Silica rock and silica sand	Therminol® 66 (oil)	1,0	3,0	30 / 3	0,27	33	50 - 250	0,7 – 1,9 mm/s	Fluid / Solid Longitudinal / Transversal
Quartzite rocks	Rapeseed oil	0,4	1,8	40	0,41	4,5	160 - 210	0,5 mm/s [a]	Fluid Longitudinal / Transversal
Alumina beads	Jarysol® (huile)	1,28	2,64	20	0,485	64	220 - 300	1,7 mm/s	Fluid Longitudinal / Transversal

D_l diameter of the bed, L la the bed height, D_c the particle diameter, ε, the bed porosity, Temperature and u the fluid velocity.

III.2.1. Governing equation for DMT system performance analysis

To evaluate the effect of tank parameters (size, shape, porosity, position), filler material and HTF properties on the performance or the behaviors of packed-bed thermocline system; most of the models developed in the literature are based on Schuman equations developed since 1929 [90]. This one-dimension model was used for porous medium modelling and combines two energy equations. One for the fluid equation (1.9) and one for the solid particle's equation (1.10).

$$\varepsilon\rho C_{p,f}\left(\frac{\partial T_f}{\partial t} + u\frac{\partial T_f}{\partial z}\right) = h.a_s(T_s - T_f) \quad (1.9)$$

$$(1-\varepsilon)\rho C_{p,s}\frac{\partial T_s}{\partial t} = h.a_s(T_f - T_s) \quad (1.10)$$

Where a_s is representing solid surface per volume unit of the bed in m^2m^{-3},T_s solid temperature, T_f fluid temperature in °C, h convective heat capacity coefficient in Wm^2K^{-1}, u the velocity of the fluid in m/s, c_{pf} the specific heat capacity of the fluid in J$kg^{-1}K^{-1}$,

ρ_s the density of the soild in kgm^{-3}, c_{ps} the specific heat capacity of the solid in J$kg^{-1}K^{-1}$.

For better understanding thermocline behaviors, the thermal losses, the effective conductivities of the fluid and solid and tank thermal capacity have been added to Schuman model [89]and [9]. And energy balance for the tank wall has been considered. Through the years to better analyze temperature distribution based on continuous solid phase assumption and fluid flow the two and

three dimension model respectively have been developed [91],[92],[75],[85]and [93]. The general description of these models with three equations are presented in equation (1. 11), equation (1. 12) and equation (1. 13) respectively for the fluid, particle and tank wall.

- Energy equation for the fluid

$$\rho C_{p,f}\left(\frac{\partial T_f}{\partial t}+\nabla u\frac{\partial T_f}{\partial z}\right)=\nabla\left(\lambda\nabla T_f\right)+h_{v,s}\left(T_s-T_f\right)+U_{u,fw}\left(T_w-T_f\right) \qquad (1.\ 11)$$

- Energy equation for the solid particles

$$(1-\varepsilon)\rho C_{s,p,s}\left(\frac{\partial T_s}{\partial t}\right)=\nabla(\lambda\nabla T_s)+h_{v,s}\left(T_s-T_f\right)+U_{u,fw}\left(T_w-T_f\right) \qquad (1.\ 12)$$

- Energy equation for the tank wall.

$$\rho C_{p.w}\left(\frac{\partial T_s}{\partial t}\right)=\nabla(\lambda_w\nabla T_w)+h_{v,w}\left(T_s-T_f\right)+h_{v.ext}(T_w-T_{ext}) \qquad (1.\ 13)$$

Where h_v is the convective heat transfer coefficient per unit bed volume in W$m^{-3}K^{-1}$, T_w the tank wall temperature, $U_{u,sw}$ overall heat transfer coefficient between the tank wall and the solid, $h_{v,ext}$ convective heat transfer coefficient per unit bed volume in W$m^{-3}K^{-1}$ with ambient air.

In addition energy equations, continuity equation and momentum equation should be considered [44]. According to the model dimension and the size of the tank, several numerical methods like finite volume, finite element and different finite have been used to resolve these energy balance equations and assess the performance of thermocline storage system during thermal cycles. The important of numerical model is to have data from an ideal system and use it for experimental data validation. The three equation model provide an effective thermal performance study of a storage system than one equation [9]. Two equations model can study thermocline behaviors[94] like three equations model by reducing 18% the computing time [89].

III.2.2. Thermal stratification

Stratification in the storage tank results from buoyancy effects caused by density differences in the storage system. The hot fluid rises to the top and the cold fluid falls to the bottom [95]. This thermal stratification is among the key factors that can sensibly affect the performance of the TES system: the thinner of the thermocline, the thermodynamic quality of the energy stored

is better. The thermal stratification efficiency into packed bed can be compute based on equation (1.14)

$$\eta_{MIX} = 1 - MIX \quad (1.14)$$

Where MIX is the number which determines the energy level in the storage tank weighted by vertical location and range between 0 and 1 [96] and [97]. MIX is expressed in equation (1.15).

$$MIX = \frac{M_{str} - M_{exp}}{M_{str} - M_{mix}} \quad (1.15)$$

Where M_{exp} is the moment of the energy real TES, M_{str} (largest moment of energy) the moment of the ideally stratified TES and M_{mix} (smallest moment of energy) fully mixed in the TES system. The moment of energy M accounts for energy location in the tank. In a vertical tank the moment of energy can be computed using equation (1. 16) [97].

$$M = \int_0^H z dE \quad (1.16)$$

Where H is the tank height and E energy.

Into a packed bed as DMT system using gravel as filler material and air as HTF, the thermal stratification efficiency enhances with starting-up of thermal cycles (pre-charge). Based on moment of energy and one equation model for energy balance resolved with finite volume approach and 3D CFD simulations software, Simone et al [96] have shown a stable thermal stratification after 30 cycles with 93% as efficiency as showed in Figure. 1.13 and Figure. 1.14. This shown the important to do pre-charging of the TES system before the first cycles to reduce the long time required to achieve a stable thermal stratification [98]. Similar results was achieved by Ortega et al using air as HTF and rocks as filler materials with energetic efficiency more than 95% after the 10th cycle [98].

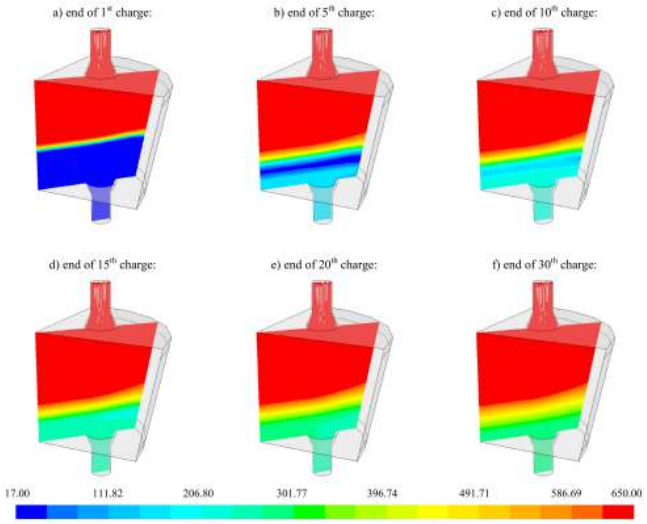

Figure. 1. 13. Thermal stratification enhancement with thermal cycles (end of each charge) [96]. Temperature value in (°C)

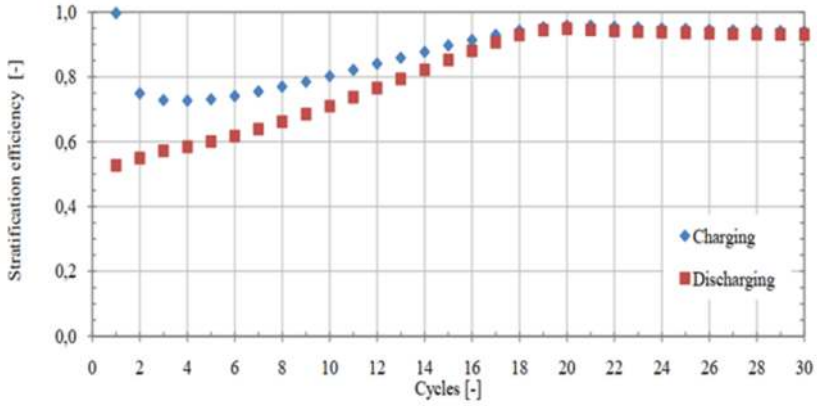

Figure. 1. 14. Average transient stratification efficiency for consecutive [96].

III.2.3. DMT thermal cycle effectiveness

From the Figure. 1.14 it can be assumed that the stratification efficiency could depend on the charge and discharge efficiency which is influenced by porosity of the tank, particles size, and storage capacity [45]. The thermocline thickness is defined as the covering length of the thermocline region and depends on charging and discharging cycle and can be defined according to Chang et al [99] by equation (1. 17) and equation (1. 18):

$$dX = min\{H(T_{out}, T_{crit,h})\} - H(T_{crit,c}) \quad \text{in discharge cycle.} \qquad (1.\ 17)$$

$$dX = H(T_{crit,c}) - max\{H(T_{out}, T_{crit,h})\}-) \text{ in charging cycle.} \qquad (1.\ 18)$$

Where $T_{crit,h} = T_h - 5$ and $T_{crit,c} = T_c + 5$ Represent the critical low and hot temperature for evaluating the thermocline thickness respectively. $min\{H(T_{out}, T_{crit,h})\}$ is the minimum height comparing the one of T_{out} and $T_{crit,h}$. $max\{H(T_{out}, T_{crit,h})\}$ the maximum height comparing the one of T_{out} and $T_{crit,h}$. $T_{crit,h}$ is the hot critical or threshold temperature, $T_{crit,c}$ is the cold critical or threshold temperature, T_h is the hot temperature and T_c is the cold temperature.

From there it can be seen that a thin thermocline can be achieved with an effective thermal stratification and thermal cycle. A thin thermocline thickness can conduct to a good cycle efficiency defined in equation (1. 19).

$$\eta = \frac{Q_{dish}}{Q_{chg}} = \frac{\int_0^{t_{dish}} \dot{m} c_{p,f} (T_{out} - T_{min}) dt}{\int_0^{t_{chg}} \dot{m} c_{p,f} (T_{max} - T_{min}) dt} \quad (1.\ 19)$$

Where η is the effective discharge efficiency, $t_{dis} = t_{dis,ref}$ is the time at which the HTF temperature drops to a threshold value. The threshold value is usually determined by the application of the interest and is arbitrary chosen like $T_h - 5$, $T_h - 20$ etc. as threshold values

An effective thermal storage depends on the discharge efficiency and the discharge time.

III.3. DMT performance during discharging cycle

Dual medium thermocline performance depends on the filler material properties, fluid properties and velocity and tank parameters and configuration.

III.3.1. Particles effect on discharge effectiveness.

Based on transient two-dimensional dispersion-concentric (D-C) model for heat transfer and fluid dynamics in a packed-bed molten salt thermocline thermal storage system xu et al [44] have shown the possibility reduction discharge efficiency [44] with large particles confirmed by numerous other authors [44],[45] and [100] . The Figure. 1.15 illustrates how the particle diameter can influences the discharge efficiencies for a laboratory (Nadine 2018) and industrial scale TES system [45]. In addition to the particle diameter the highest discharge efficiency is obtained with the highest storage capacity TES system (industrial) regardless of the particle size.

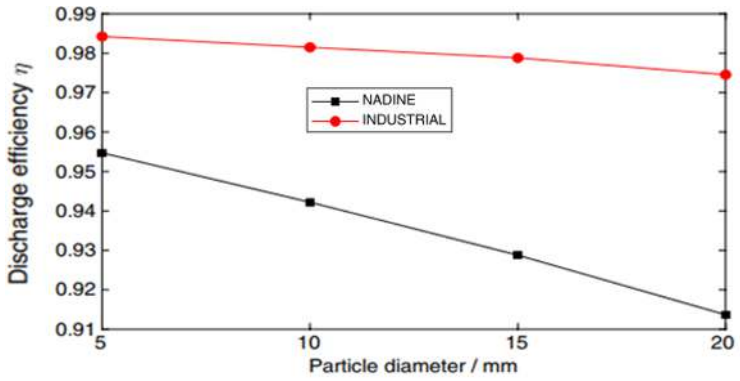

Figure. 1. 15. Effect of particle size on discharge efficiency [45].

To obtain a thin thermocline with an effective discharge efficiency and good discharge time, small particle diameter is required (less than 2cm) to avoid bad thermal distribution in the particle and provide a good heat transfer process between the fluid and the particle. However, when the particle diameter is too small, the influence of particle diameter on thermal performance becomes negligible [44] . Figure. 1.16 illustrates the effect of particle diameter on thermocline thickness.

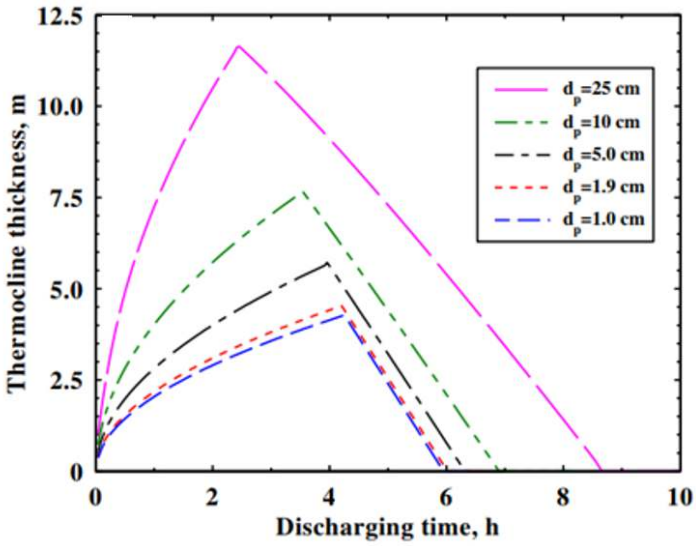

Figure. 1. 16. Effect of discharge time on thermocline thickness when using quartzite as filler materials [44].

In addition, the thermal performance of a thermocline is also influenced by the properties of the particles. The density, volumetric heat capacity, and thermal conductivity of a filler material are the primary characteristics that determine its thermal performance. The primary elements controlling these mechanical and thermal characteristics of natural rocks are quartz and calcite

[43]. The filler material's thermal conductivity affects how heat is distributed within the tank. High solid particle thermal conductivity, which results in poor thermal distribution and low thermal cycle efficiency, could be the cause of greater thermal diffusion (increasing heat loss) in DMT systems [77]. This hypothesis can explain better the different results achieved by Keilany et al., in 2018 using cofalit rock and aluminum sphere as filler materials than based on particles shape [101]. The thermal conductivity must be optimum to ovoid heat increasing between adjacent particles when it is too high and heat discharge rate reduction when it is too low [44]. The different types of filler materials properties useful for DMT storage tank are noted in Table 1. 5. It is observed that sand and developed ceramic have better specific heat capacity compare to stone such as sandstone, quartzite etc. But sand, clay ceramic and concrete have lower thermal conductivity.

Table 1. 5. Thermal properties and discharge efficiency of some storage materials [43],[44], [53],[57], [91],[93], [102]- [103].

Material properties	λ $Wm^{-1}K^{-1}$	ρ (kgm^{-3})	c_p $Jkg^{-1}K^{-1}$	ρc_p $kJm^{-1}K^{-1}$	η_{dchg} (%)	T_{max} (°C)
1.Rocks						
River pebble [102]		2713.6	N/A	N/A	N/A	N/A
Pea pebble [102]	1.2	2506.3	N/A	N/A	N/A	N/A
Sand and Quartzite [104]	5.5	2600	973	N/A	N/A	N/A
Quartzite [44]	5.69	2500	830	2075	90.43	650
Dune sand [105],[103] and [93]	1	2600-2660	926		N/A	600
River sand [57]	N/A	N/A	1041	N/A	N/A	<1100
Quarzitic sandstone [43]	5	2733	652	1783		650
Rhyolite[43]	2.3	2601	785	2045	N/A	650
2.Developed materials						
HighTemp Concrete [44]	1	2750	780	2519	91.69	≥370
From ash and clay ceramic	0.75-0.96	1720-2140	N/A	1700-1995	N/A	1000
From laterite Aluminium ceramic [44]	30	3750	916	295	90.03	≥ 370

S.C ceramic [44]	120	3210	750	2407.5	90.70	
Den stone ceramic pebbles [91]			700	1300		900
Laterite ceramic [53]	1.1-2.5		700	1300		900
Industrial waste Cast iron [44]	29.3	7900	837	6612.3	89.7	≥ 370

III.3.2. Heat transfer fluid effect on DMT performance

Heat transfer fluid must be compatible with the containment materials, storage media and be able to operate in the required temperature range. The HTF defines the maximal temperature at which the heat is store in the packed bed and the range temperature of the power block (thermodynamic cycle) especially for liquids. To have a large temperature range the HTF must be stable at high temperature. The main HTFs are mineral oil, air, molten salt and vegetal oils and liquid metal. A HTF impacts the thermal energy storage performance through its velocity, inlet temperature and properties.

III.3.2.1. Effect of fluid velocity on DMT performances

Several studies have shown the impact of the fluid velocity or inlet Reynolds number on thermal performance. Using molten salt as HTF, Xu et al [10] have pointed out the increase of effective discharging time and discharging efficiency at low velocity of the fluid, and shown the possibility to achieve :

- 9.1h as discharging time at fluid velocity of $3.0085\times 10^{-4} m\, s^{-1}$, with a discharge efficiency of 89.76%
- 0.91h as discharge time at fluid velocity of $6.017\times 10^{-3} m\, s^{-1}$ with a discharge efficiency of 89.41%

Figure. 1. 18 shows the effect of HTF velocity on the thermocline thickness and discharging time. At high fluid velocity the thermocline thickness increases faster, reaches it maximum and leaves the TES system. At the same time a short discharge time is observed.

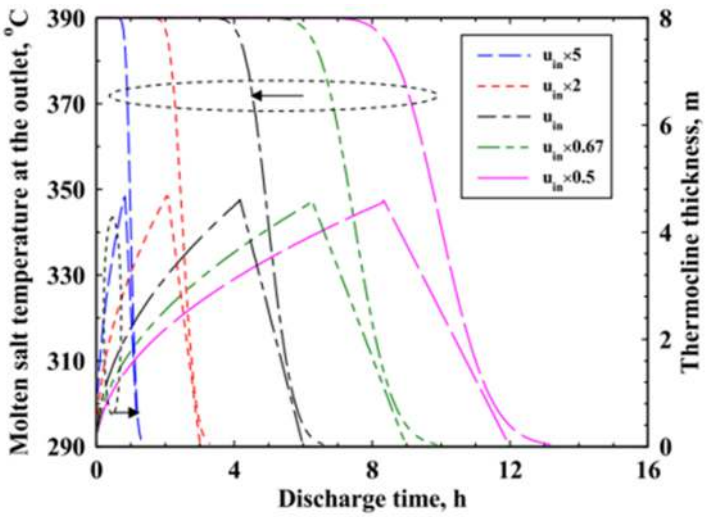

Figure. 1. 17. Variations in the fluid (molten salt) temperature at the outlet and the thermocline thickness with the discharging time using different fluid inlet velocities [10]

III.3.2.2. Effect of fluid inlet temperature on DMT performances

The inlet temperature or difference between inlet temperature and outlet temperature influences slowly the thermocline thickness and the discharge efficiency and discharge time [10]. However when the hot temperature (maximal temperature) of the storage system is too high it can reduce the charge and discharge time, making the storage less effective due to increase of thermal losses at high temperature [106] .

III.3.2.3. Effect of fluid thermal properties on DMT performances

The main properties of HTF influencing the performance of thermal energy storage are specific heat, density, kinetic viscosity, and thermal conductivity. As these properties differ from one fluid to another, the thickness of the thermocline, the thermal cycle efficiency (charge/discharge) and the stability of tank storage capacity may be also different as shown in Figure. 1.18. The figure presents a lower storage capacity for the therminol oil and higher storage capacity with molten salt (Figure, 1. 18b). Thus, the higher specific heat capacity or volumetric heat capacity of molten salts (table 1. 6) increase the storage capacity of the TES system.

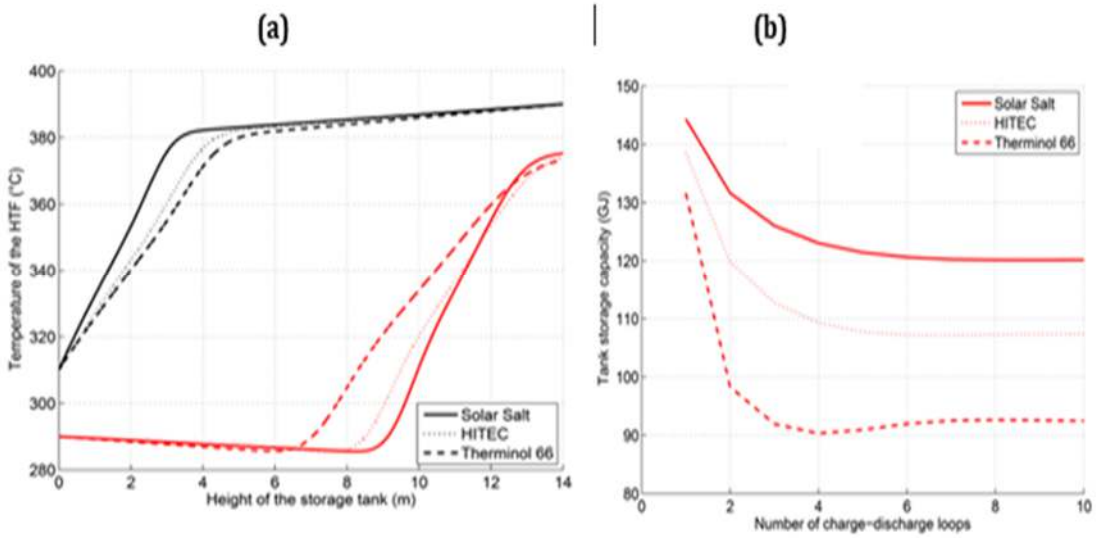

Figure. 1. 18. (a)Temperature profile for different HTFs during charging (curves in black) and discharging (curves in red) periods , and (b) tank storage capacity for different HTFs [106].

The volumetric heat capacity ($\rho.c_p$) enables to assess the heat storage density of materials, while the thermal effusively E enables to assess their ability to exchange heat. Liquid HTFs like molten salt and oils have heat capacity and thermal conductivity higher than the one of gas. This enables liquid/solid systems to operate at low HTF velocity while keeping a good heat transfer coefficient (HTC), which improves thermal stratification [107]. Comparison study between a synthetic oil and rapeseed oil of thermocline performance base on the same sizing condition gave a better thermal performance for the synthetic oil showing thus the depending of thermal storage efficiency on thermal and thermo-physical properties, but rapeseed oil has given a better cost effectiveness[108]. The influence of fluid properties like viscosity and thermal conductivity is responsible for maintaining thermocline thickness within the tank. Higher is the viscosity, faster the thermocline moves and may reduce the discharge time thereby the operation time [88]. Moreover, a HTF with very low thermal conductivity is not required because limiting the heat transfer between HTF and solid particle. Also, a HTF with very high thermal conductivity increases heat losses due to increasing of thermal diffusion. This shows whether the presence of an optimal value of thermal conductivity for better heat transfer between solid and HTF and internal heat diffusion [45]. In addition the storage utilization factor and the exergy efficiency may be better for liquid HTFs (molten salt and oil) than air due to their higher thermo-physical properties [109]. Table 1. 6 presents the thermo-physical properties of several fluids for thermal energy storage and heat

transfer within a DMT storage tank. Molten salts like Na2CO3–K2CO3 Li2CO3 present the higher volumetric heat capacity followed by vegetable oils. Regarding the temperature operating range, air has the highest range followed by metal liquids and molten salts.

Table 1. 6. Comparison of thermo-physical properties of some HTFs [45], [45], [63], [49], [83], [88], [110]- [111].

TFS/properties	ρ $kg.m^{-3}$	c_p $J.kg^{-1}.K^{-1}$	ρc_p $kJ.m^{-1}.K^{-1}$	μ $(Pa\ s)$	λ $W.m^{-1}.K^{-1}$	$T_{min-}T_{max}$ (℃)
1.Molten salt						
Solar salt[88]	1899	1495	N/A	0.00326	0.57	221/600
MgCl2–KCl [45]	1660	1150	1909	0.005	0.5	426/>500
Na2CO3–K2CO3 Li2CO3 [45]	1848	1612	2979	5.9	0.00047	398/>500
ZnCl2–NaCl–KCl [45]	1977	900	1779.3	0.0042	0.29	204 / >500
HITEC[88][99]	1640	1560	N/A	0.00316	0.38	142/538
2.Vegetable oil						
(NC)(210°C)						
Rapeseed oil [49]	787.7	2492	1963	0.003155	0.143	-21/250
Jatropha curcas oil [49] [63]	778.2	2400-2509	1953	0.001781	0.139	3 />200
3.synthetic oil						
$\boldsymbol{Therminol^{\mathbb{R}}}$ $\boldsymbol{66oil}$[110]	885 (200°C)	2195 (200°C)	1942.57	N/A	0.113 (200°C)	/400
$\boldsymbol{Therminol^{\mathbb{R}}}$ $\boldsymbol{VP-1}$ [112]	757.7	2464.5	1867.35	0.000185	0.0865	12/400
sylthermXLT(210°C)[113]	660	2171	1433	0.00023	0.23	-11 /260
Coloria [83][111]	867	2200				
Xceltherm 600 [113]	736	2643	1945	0.00055	0.13	-29/316
4.Liquide Metals						
(700°C) [45]						
Sodium	798	1256	1002.3	0.00018	57.5	
Lead-bismuth Eutectic	9807	138	1353.4	0.0011	16.8	125/ >600
Tin (Sn)	6650	282	1875.3	0.0011	32	232/ >600
Pure lead (Pb)	10196	141	1437.6	0.0014	19.9	327/ >600
5.Gasses						
Air(450°C)[110]	0.448	1080/1190	N/A	N/A	0.053	0-infinite

III.4. Effect of tank parameter on DMT thermal performance

The primary component of the thermal energy storage system, the tank contains the filler materials. The tank can impact the storage performance through its size (ratio of height and diameter H/D and height), porosity, insulation, position and shape. So, these parameters must be chosen appropriately to ensure and optimal operation and to satisfy the required energy. The total energy needed, the length of the discharge process, the HTF's high and low temperatures, the tank's porosity, and the thermophysical characteristics of the filler materials and HTF all play a role in determining the tank size [108].

When the solid filler material is ignored, the tank volume is optimal and may be computed using equation (1. 20)

$$V_{ideal} = \frac{Q_{total}}{\rho_f C_{p,f}(T_h - T_c)} \quad (1.\ 20)$$

Where Q_{total} is the total storage capacity, T_h the hot temperature and T_c the cold temperature ρ_f the fluid density and $C_{p,f}$ the volumetric heat capacity of the fluid.

When taking considering the solid filler material, the real volume of the tank should be calculated by equation (1. 21) [87].

$$V_{real} = \frac{\rho_f \times C_{p.f}}{\varepsilon \times \rho_p \times C_{p.f} + (1-\varepsilon)\rho_s \times C_{p.s}} \times V_{ideal} \quad (1.\ 21)$$

Where ρ_s is the density of the solid or particle $C_{p.s}$ the specific heat capacity of the particle.

The quantity of useable energy that the tank can deliver throughout the discharging process is determined by the performance of the thermal storage system, which is dependent upon the effective discharge efficiency.

III.4.1. Effect of the tank ratio H/D on the thermocline effectiveness.

The thermal energy storage efficiency increase with the ratio H/D, because high ratio result in higher velocities of the HTFs and consequently a better heat transfer with the solid particles [45][112][108]. However when the ratio is higher than around 2.4, the ratio effect becomes negligible [87]. In addition, the discharge and collection efficiency increase with the height of the

vessel[114]. And when the tank is taller than 30m there is no more improvement and heat loss become more significant [68]. Figure.1.19 shows how the ratio H/D and height of the tank can affect the thermocline storage efficiency.

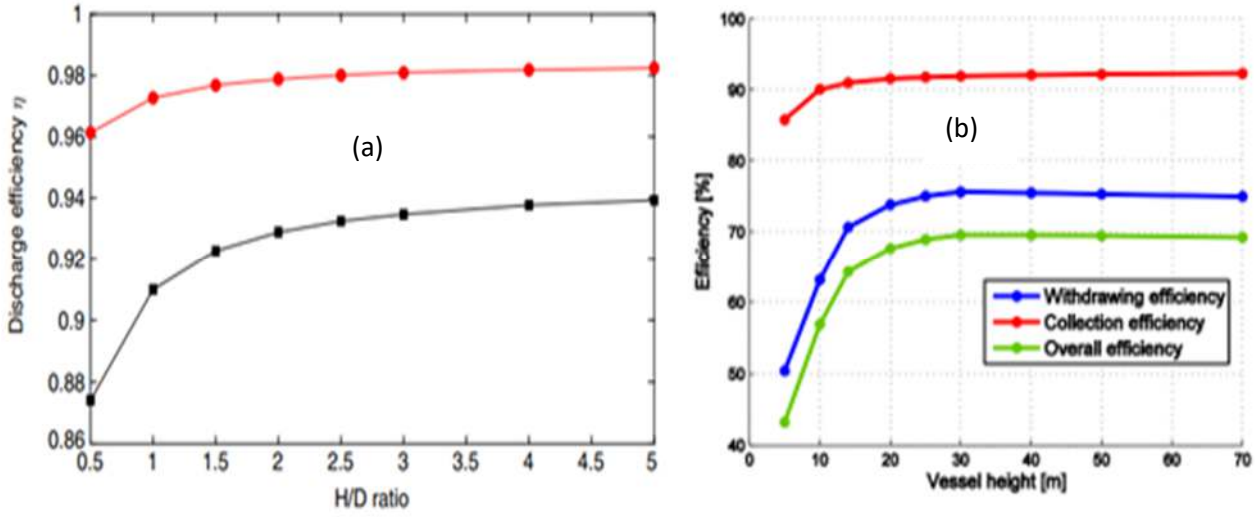

Figure. 1. 19. effect of the ration H/D on discharge efficiency (a) and the variation of discharge, collection and overall efficiency with the tank height (b) [45] [45].

III.4.2. The effect of tank porosity, geometry, position, and wall configuration on DMT performance

A porosity between 0.15 and 0.35 is desirable without compensating much on the effectiveness of the storage system [88].

Most of the storage tanks studied in the literature are cylindrical [115],[99],[104] and [86][1]. Also the rectangular shape [76] and [59] and truncated cone shape [116] and [98] effect on TES performance has been addressed. Mao et al. (2019) suggested a shell-and-tube thermoelectric storage tank (TES tank) utilizing the enthalpy technique, based on a 2D physical and mathematical model of a new truncated cone [117]. With regard to DMT storage (sensible heat storage), Ortega et al. 2017, have showed that, the cylindrical tank has a better thermal performance than truncated cone tank for particle diameter equal 1 cm and mass flow rate equal to 0.3kg/s [118]. However, the conical geometry performs better mechanically and has lower thermal performance.

There is a lack of data in the literature regarding the DMT thermocline tank position on thermal performance. However a CFD simulation to analyze thermal stratification in domestic hot water

storage tank (SMT) have given a better results (stratification) for the vertical tank than the horizontal one [115] as presented in figure. 1.20. In addition, a discharge efficiency of 79% is obtained for the vertical tank against 59% for the horizontal tank after 30 minutes of discharging time. In horizontal tank, mixing forces are more pronounced due to the existing of two recirculation zones (cold and hot) at lower Richardson number [115].

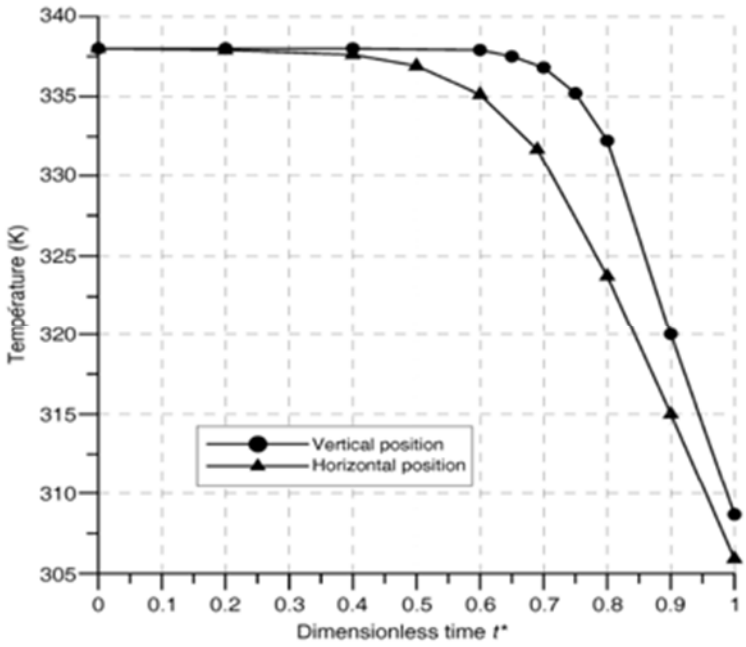

Figure. 1. 20. Effect of tank position on thermal energy storage performance [115].

Regarding the tank size, Hoffman et al., observed more heat losses through the tank wall for small tanks. But these heat losses are negligible for large tanks like solar One storage tank [86]. This can explained why discharge efficiencies for a laboratory (Nadine) TES system is lower compared to industrial TES system [45].

IV. Thermal energy storage and their applications

IV.1. DMT storage for concentrating solar power.

State-of-the art in CSP plants is currently the indirect sensible-heat two-tank concept with oil as HTF and molten salt as storage medium. However, molten salt has crucial disadvantages such as high cost and restricted operating temperatures due to relatively high freezing points of the molten salts (120-240°C) and relatively low maximum operating temperatures (<600°C). Therefore, with

thermocline energy storage system higher CSP plant efficiencies with high temperature and low cost can be reached [119].

IV.2. Solar thermochemical fuel and green hydrogen

Liquid fuels can be produced from H_2O and CO_2 by using a reactor at elevated temperatures to thermochemically dissociate H_2O and CO_2 [120]. Elevated temperature can be reached by using concentrated solar technology and by storing heat in a TES system. That heat can also be used to produce syngas ($CO+ H_2$) from biomass using pyrolysis, and gasification process with steam and/or oxygen [113] and [114]. To reach high solar-fuel efficiencies, heat storage and heat recovery are essential. Several concepts of heat recovery have been suggested[119] with a possible sufficiently high heat recovery rates and efficiencies with the concept of high temperature solar thermochemical process using ceramic spheres as solid heat transfer medium (DMT)[123]. The high surface area of the spheres favours the mixing of redox particle and heat transfer during that process. A pilot-scale reactor for this propose was successful conducted at Odeillo, France in the 1MW solar furnace (MWSF) [124]. A pilot plant for direct solar synthesis is in operation in China at Lanzhou, the capital city of northwest China's Gansu Province. Hydrogen can also be obtained from solar energy through solar thermochemical processes or electrolysis using electricity. The efficiency of heat recovery can be also improved with a TES system.

V. Problem statement, Research question and objective

The contribution of this thesis consists to use sand, clay coal bottom ash (CBA) to develop eco-material for sensible heat storage material. The main question to answer in this thesis is how to develop an effective and sustainable TES materials using abundant and available eco-material? A spherical shape will be given to the new filler material, which will contribute to reduce the effect of thermal ratcheting due to the reduction of contact between filler material and the tank wall. With spherical shape the convective heat transfer between the HTF and the storage material will be improved. In addition to that, sand used as the major material in the formulation will increase the thermal inertia and volumetric heat capacity of the filler material driving to the limitation of thermocline degradation.

This new material will contribute acing the major challenges of DMT mentioned previously. The major drawbacks of thermocline storage system are thermal ratcheting and thermocline degradation. Thermal ratcheting is of concern, which occurs due to uneven expansion and

contraction of the tank structure and filler particles [72], [77], [79] and [131]. To address this problem, the spherical shape will reduce the normal force on the walls during thermal expansion of the filler materials [116]. Several methods were proposed in previous works to reduce thermocline degradation and its consequences. In this thesis passive solutions are suggested. Passive methods consists to reduce thermocline degradation or mitigate at least some of its negative consequences: The increasing of tank ratio H/D; Combination of sensible and latent heat storage by adding a relatively small amount of phase change material (PCM) to the top of the bed to stabilized the outflow temperature [126]. Therefore, the development of the new storage material by shaping the storage material and increasing it volumetric heat capacity and thermal conductivity will reduce the thermocline degradation and increase the discharging time of the TES system.

As conclusion, in this chapter a literature review was conducted on the different CSP technologies and potential in West Africa and on thermal energy storage systems and material. For the storage system, a cylindrical configuration is more suitable for TES system. A spherical shape of the filler material allows reducing thermal ratcheting and increasing the heat transfer surface between the particle and the fluid. Thus, spherical ceramic ball is developed from sand, clay and CBA to face these challenges. The chapter 1 assesses the potentiality of the new storage material developed to address passively some challenges of the TES system.

Chapter 2: Development of sensible heat storage materials using sand, clay and coal bottom ash.

Introduction

A thorough review was conducted in chapter 1 on the main parameters of filler material and heat transfer fluid, which influence the performance of DMT. This chapter will be more focused on the development and characterization of new storage materials. Firstly, a state of art will be conducted on rocks, industrial waste and different ceramic formulated potentiality as TES. The different raw materials and mould useful for ceramic manufacturing will be also carry out. The main question to answer in this chapter is: Sand clay and industrial waste like coal bottom ash (CBA) could be used to developed thermal energy storage materials (TESM)? Before processing, we must keep in mind that, the new storage material should respect the criteria establish by International Energy Agency (IEA).

I. State of art on filler material for DMT

As introduce previously, DMT system has potentiality to have a broad reduction of CSP cost from 33% to about 35%. To improve this system, thus enable the use of a single tank system instead of two, the use of eco-materials such as natural rocks, industrial waste, concrete, ceramic etc. as filler materials [68],[9],[127] and [125] inside one tank calls thermocline tank. Eco-materials such as Rhyolite and Quarzitic sandstone (rocks) with good thermal capacity of around 2800 $kJ.m^{-3}K^{-1}$ and 2250 $kJ.m^{-3}K^{-1}$ respectively at 600 °C are likely to be the most effective eco-material for typical thermocline tank [43]. However, a main demerit is that such eco-material could possess low sphericity and irregular size (big size) which may reduce the thermal storage efficiency as discussed in [44] . To achieve a more effective storage efficiency as reviewed in [125], the thermocline should be thin, and an optimum thickness would be achieved with particle dimeter less than 3cm. This optimum point reached was as result of the heat transfer process that existed between the heat transfer fluid and the particle surface, which depends on the particle size [44] and [118]. To overcome challenges due to shape and size, material formulation is required. Thus, several studies have employed material formulation as a required process to overcoming issues relating to shapes and sizes in heat transfer processes in raw material [43], [126] and [127]. More studies have employed the use of ceramics from clay and ash for sensible heat storing, which

include: Lopez et al., [52]made pressed plates ceramics from incinerator bottom ashes and waste clay using sintering method at different temperature level. Results achieved by Lopez revealed a preferred and sustainable mechanical performance (more than 30MPa) and with thermally stable specimens. However, the volumetric specific heat capacities were limited. Similarly, based on X-ray pair distribution function analysis, differential scanning calorimetry, Nigay et al have shown the possibility of achieving more than 1.49 kJ. $kg^{-1}K^{-1}$ as specific heat capacity with flexural strength of 11.1 MPa for ceramic made with clay and 30 wt.% of biochar using sintering method up to 950°C [51]. Sane et al., buttressed by showing that the clay ceramic thermal conductivity can increase with the wt.% of silicon-carbide [131]. By mixing slaked lime with bottom ash or laterite from Burkina and Niger, Kenda et al., have developed ceramic ball by melting the raw materials with concentrating solar technology. These ceramics were estimated to have good thermal properties and cost effective than industrial ceramics [53], but need important energy. The table 1 presents state of art of some developed ceramic with their properties.

Table 2. 1.Thermal properties of some developed ceramic for thermal energy storage [51], [52], [53], [132] and [133].

Ceramic	$\boldsymbol{\rho}$ ($kg.m^{-3}$)	$\boldsymbol{C_p}$ ($J.kg^{-1}K^{-1}$)	$\boldsymbol{\sigma}$ ($\boldsymbol{MPa}$)	$\boldsymbol{\rho C_p}$ ($MJ.m^{-3}K^{-1}$)	cost
Clay ceramic+ organic additive [51]		1200-1490	11.1	N/A	N/A
Clay ceramic+ SiC [131]	3160	620	19.6	1.96	N/A
Pressed plat ceramic [52]			40	1.08-1.92	N/A
Ceramic made bottom ash and laterite [53]	N/A	700-1300	2-11	N/A	N/A
Sand-clay ceramic [132]	1650-1800	1020	7.9-12.8	N/A	N/A
Coal fly ceramic [133]	2600	735-1300	N/A	N/A	N/A
Cofalit [133]	3120	800-1034	N/A	N/A	N/A

In addition, other researcher have proposed to used directly sand as heat transfer fluid and storage medium due to it good thermal properties and inertia [46] and [95] and its ability to behave like a fluid, solid and even a gas. However the agglomeration can occur during the use of sand at high

temperature making it flow to be impossible [105]. The Figure. 2.1 illustrates the effect of heat treatment temperature on natural sand.

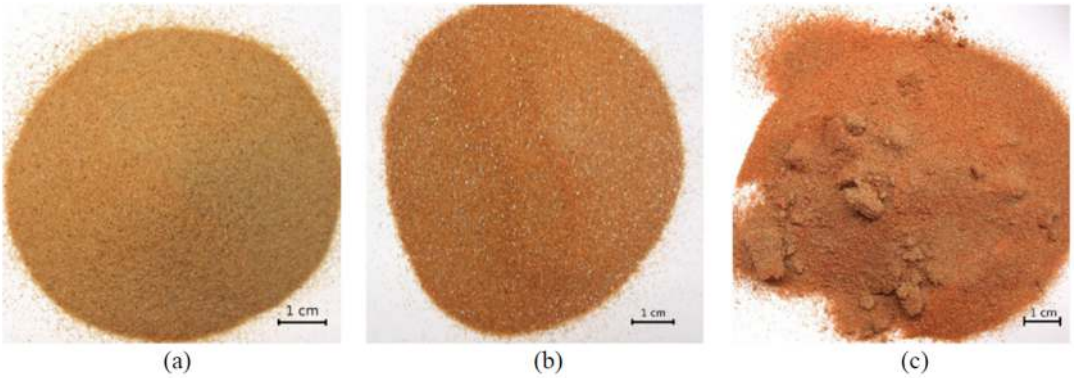

Figure. 2. 1. Reference sample (a), after heat treatment at 800 °C (b) and after [105].

In addition, sand potentiality as storage material and heat transfer fluid could be affected by it chemical composition [55]. Dune and mining sand of Burkina Faso potent assessment as TESM or raw material to formulate sensible heat storage material showed a great potential [134]. The two different sand sample were heated at 1000°C during two hours without any agglomeration as illustrated in Figure. 2.2.

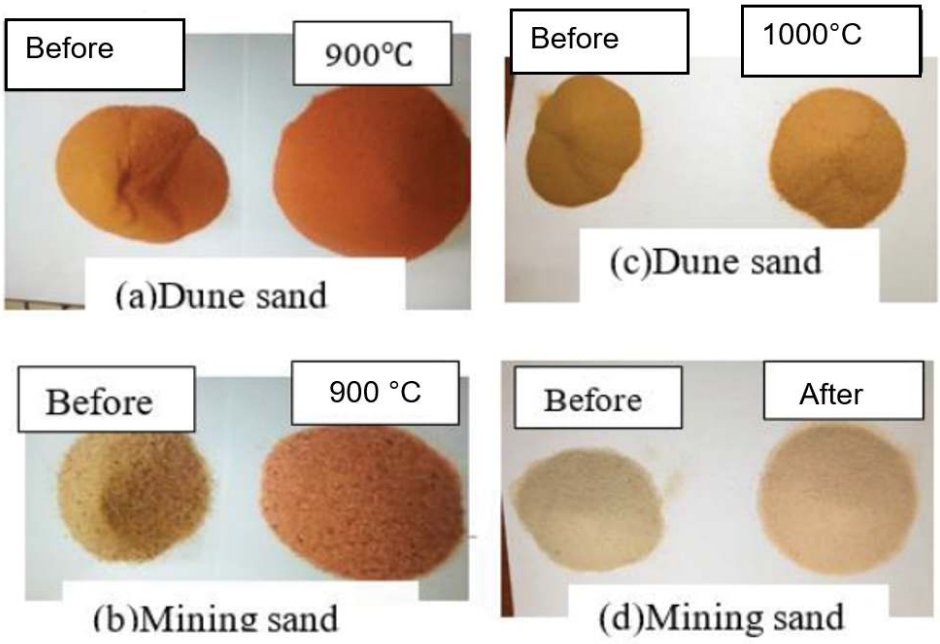

Figure. 2. 2. Effect of heat treatment on dune and mining sand [134]

In this chapter, two additional samples dune and natural sand from Niger will be added to formulate the new storage material. This will include: 1) Material formulation by mixing different percentage weight (wt.%) of sand, clay and CBA. 2) assessment and selection of the2 best ceramics based on thermos-mechanical properties and thermal stability analysis.

II. Materials and methods for the storage material development

II.1. Raw materials and their processing

II.1.1. Raw material

West Africa has a huge potential for raw material resources that could be used to manufacture thermal energy storage material [53]. In addition to laterite potential and industrial waste such as bottom ash and lime, dune and mining sand have high thermal stability (up to 1000°C) to be used as TESM or to shape TESM [53] and [134]. In this chapter sand, clay, and coal bottom ash (CBA) from different region in West Africa (Burkina and Niger) are mined and used to formulate ceramic for sensible heat storage. The main mineral composition of sands studied in Burkina Faso and Niger is up to 80% of quartz (SiO_2), 9% of Alumina (Al_2O_3) and some other oxide [135] and [136]. Clay is an argillaceous material usually composed of complex natural mixtures of minerals presenting very variable grain size and physicochemical properties. Clay is an argillaceous material usually composed of complex natural mixtures of minerals presenting very variable granulometry and physicochemical properties [137]. The different clays studied in Burkina Faso contain mainly kaolinite (>40 wt%), illite (>13 wt%), quartz (>18 wt%) and rutile (1 wt%) [137]. Table 2 illustrates the chemical composition of the CBA used and size distribution of dune and mining sand [55] and [125].

Table 2. 2.Chemical composition of CBA [53],[138]

Composition(%wt)	SiO_2	Fe_2O_3	Al_2O_3	MgO	TiO_2	CaO	K_2O	LOI
CBA	35.63-62.12	3.93-5.58	19.43-27.13	1.24	2.62	0-0.5	2.05	15

II.1.2. Sampling sites

In addition to the sand study in our previous work[134] from Oursi and Borgodougou in Burkina Faso, two other samples were collected in Niger. The dune sand was collected around Agadez

(16.966686°N, 7.9833353° E) and the natural sand around Ingall (16.7855571°N, 7.9322241°E). For the clay samples, one was collected from the deposit of Malgsombo (12.4527288°N, 1.4050814°E) in the commune of Saaba (C) and the second one from the deposit of Ethouayou (12.0587723°N, -3.03435°E) in the commune of Tchériba (C1) in Burkina Faso. The main different between both, is the colour (brown (C) and green (C1)), also in terms of use, the first one is used to make brick or fired brick for building and the second one is used to make pottery also by firing. Both have been obtained by digging. The CBA was gathered straight from the bottom of the incinerator at the Niger State Company (SONICHAR) coal power plant, as opposed to a landfill, where 150,000 tons of waste are disposed of annually and over 2 million tons of material are already available. [53] as illustrated in figure. 2.3 (important to use a map).

Figure. 2. 3. Location of CBA landfill of SONICHAR in Niger near Agadez [129].

II.1.3. Raw material processing

Sifting and milling

For the size distribution analysis, dune, mining and natural sand samples were separated through a series of wire mesh sieves. The chosen standard was NFP 18-560 and the sieves used had nominal aperture sizes in mm of 16, 12.5, 10, 8, 6.3, 5, 4, 3,15, 2.5, 2, 1.6, 1.25, 1, 0.8, 0.63, 0.5, 0.4, 0.315, 0.25 0.2, 0.1, 0.16, 0.125, 0.1, and 0.080. Between each set of sieves, the particles were halted, and their weight was noted. The Sauter mean diameter was computed using equation (2. 1) as follows:

$$SMD=\sum_i(m_i d_{av})/M \qquad (2.\ 1)$$

Where m_i is the mass stopped by a given sieve i; d_{av} is the mean size between the stopping sieve i and the immediate larger one; and M is the total mass sieved for a given sample. Table 3 shows the calculated SMD for each sample.

Table 2. 3.The Sauter mean diameter of the different sand samples.

Samples	Dune sand	Mining sand	Natural sand
SMD (mm)	0.26	0.91	0.93

The idea of grain size distribution analysis and the mean diameter is to assess the effect of sand particle size on the formulated material mechanical properties. During the formulation a sieve of 1 mm was used to sift the different sand samples. This operation was not necessary for dune or desert sands due to their small (< 0.3mm). The clay samples (binder) were sifted with sieve of 0.5 mm after milling them with a porcelain miller. About 7 kg of the CBA sample was milled for about 10 minutes into powered form in an electrical miller and used directly for the formulation. The different samples after processing are presented in Figure. 2.4.

Figure. 2. 4. Raw materials: (a)-Dune sand from Burkina (DS-B) and Dune sand (DS-N) from Niger, mining sand from Burkina (MS-N), Natural sand from Niger (NS-N); (b)-clay (C) from Malgsombo, Clay (C1) from Tchériba and coal bottom ash from Agadez.

II.2. Formulation description

II.2.1. Thermal energy storage material (TESM) shaping

It's crucial to shape the solid materials used to fill thermocline storage systems. A spherical shape is desirable to achieve better contact between the heat transfer fluid and the filler material [60]. In this chapter a mould with six spherical elements of 3 cm diameter was designed and made locally to shape the material. During the manufacture of the sample mixture, the percentage weight of clay (binder) is first set equal to the porosity of the sand. The porosities of the sand samples were 42% for mining sand from Burkina, natural and dune sand from Niger and 45 wt.%. for dune sand from Burkina [134] and [55].The formulas were obtained with 58 wt.% or 55 wt.% of sand and 42 wt.%. or 45 wt.% of clay. For the second formulas, 12 wt.% of clay ratio was replaced by ash to check out the effect of the ash on the ceramic mechanical performance. The composition of these formulas becomes 58 wt.% or 55 wt.% of sand, 12 wt.% of bottom ash and 30 wt.% or 33 wt.% of clay. Finally, the ratio of the ash was increase to 30%wt to obtain pellets with 40%wt of sand, wt.% clay and 30 wt.% of ash. Each component of the mould was pressed with human force once water had been combined. The clay fraction is supposed to provide the shape by providing plasticity and dry mechanical strength during processing. During firing, clay and kaolinite has a role in mulita recrystallization and in the formation of a vitreous phase. Feldspars contribute in the quantity and behaviour of the liquid phase at temperatures above 1050°C [139][137]. Thirty-six (36) different formulations were done with nine (9) formulas per sand sample. The Table 4 illustrates samples of some formulations with their nomenclatures used in this work.

Table 2. 4.Different weight of raw materials and water used for ceramic balls formulation.

Formulas	Sand weight (g)	Clay weight (g)	Ash weight (g)	Water weight (g)	M_{water}/m_{binder}
D55C45-B	99	81	0	19.5	0.241
D55A12C33-B	99	59.4	21.6	23.9	0.295
D40A30C30-B	72	54	54	25.8	0.239
M58C42-B	104.6	75.6	0	23.3	0.308
M58A12C30-B	104.4	54	21.6	22.5	0.297
M40A30C30-B	72	54	54	27.8	0.257

D58C42-N	104.4	75.6	0	21.2	0.280
D58A12C30-N	104.4	54	21.6	20.5	0.271
D40A30C30-N	104.4	54	21.6	24.1	0.318
N58C42-N	104.4	75.6	0	19.1	0.253
N58A12C30-N	104.4	54	21.6	21.9	0.290
N40A30C30-N	72	54	54	25	0.231

A minimum of six replications of each formulation were conducted to verify the repeatability of the experimental outcomes. Clay C1 (green clay) was used in the same formulation and replication. The balls were shape following the process illustrates in figure. 2.5:

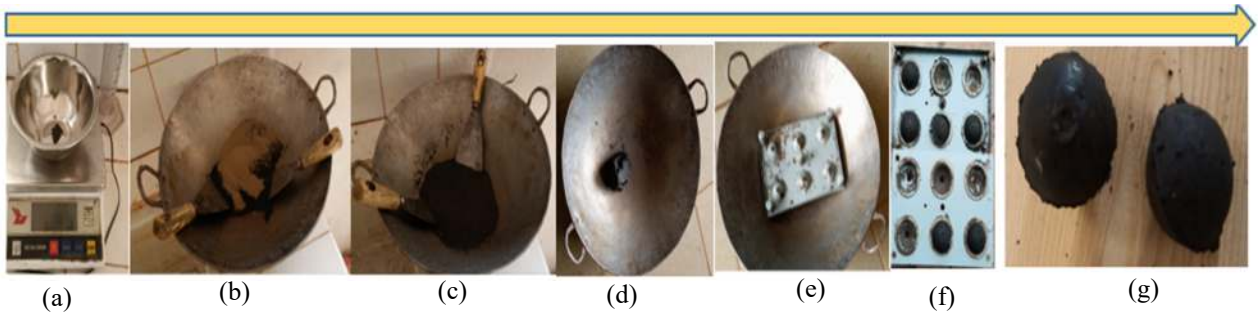

Figure. 2. 5. Formulation and shaping process: (a)-precision balance, (b) and (c)-mixing of the raw materials, (d)-mixing with water, (e)-mould filled with Mortar, (f)-ball withdraw process from the mould, (g)-balls after withdrawing from the mould.

II.2.2. Drying and sintering process

After shaping the different specimens were dried at 105°C within an oven for 24 hours to remove all water from the specimens. Then, the weighted specimens (m_0) were put within a muffle furnace and fired with heat rate of 3°C from room temperature to 500°C, 2°C heating rate from 500°C to 1000°C and held at 1000°C during 4hours after being cold down to 50°C with cooling rate of 2°C. The same process was repeated for the pellets obtained at 1060°C. After firing the specimens were weighted (m_1) and the lost-on ignition (LOI) was computed using the equation (2.2). It represents the rate of organic element or volatile element in the formulated specimen.

$$LOI = \frac{m_0 - m_1}{m_0} \times 100 \qquad (2.2)$$

Drying and firing process is illustrated in figure. 2.6.

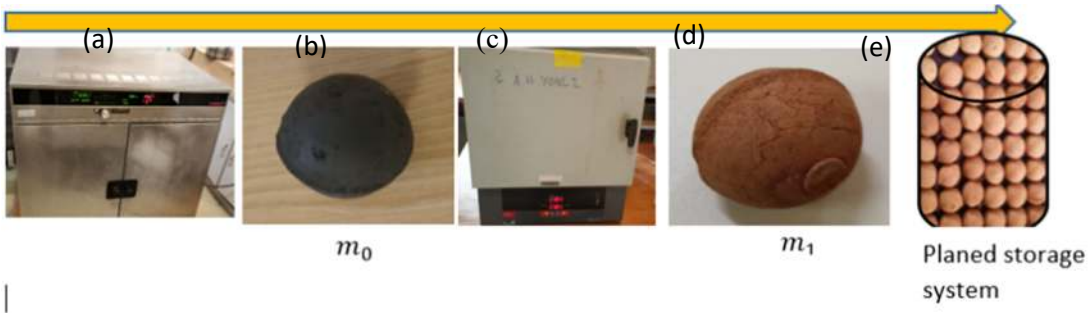

Figure. 2. 6. Drying and firing process: (a)-oven, (b)-mortar balls after drying, (c)-muffle furnace, (d)-ceramic ball and (e)-overview of the planed storage system.

II.3. Characterization of the sintered specimens

II.3.1. Mechanical properties

II.3.1.1. Bulk density

To store thermal energy, the filler materials density, play a crucial role because it influences TES capacity or energy density. Higher is the density of the storage material, better is the volumetric heat capacity. It is an important input data for sensible heat storage system modelling [9]. In order to determine the bulk density of the various specimens (ceramic balls), Archimedes' method was applied. This method is useful to determine the bulk and apparent density of any regular or irregular material, including ceramic. The test specimens were dried out at 105°C for 12 hours to ensure total water loss. Their dry weights ($m_{\,dry\ in\ air}$) were measured in air in suspended condition and recorded. After letting them cool, they were submerged in a beaker of water. As the specimens' pores filled with water, bubbles were seen. Their soaked weights were measured in air ($m_{\,soacked\ \ in\ air}$) and in water ($m_{soacked\ in\ water}$) in suspended condition and recorded. The soaked weights were measure also after 15 hours in water in suspended condition to compute the porosity. Bulk density (ρ_b) and porosity (ε) of the samples were calculated using equations (2.3) and (2.4):

$$\rho_b = \frac{m_{\,dry\ in\ air}}{m_{\,soacked\ \ in\ air} - m_{soacked\ in\ water}} \times \rho_w \qquad (2.\ 3)$$

$$\varepsilon = \frac{m_{\,soacked\ in\ air} - m_{\,dry\ in\ air}}{m_{\,soacked\ \ in\ air} - m_{soacked\ in\ water}} \times 100 \qquad (2.\ 4)$$

II.3.1.2. Mechanical properties

Compressive strength can be defined as the capacity of a material to withstand load before failure. When a material has spherical shape, its tensile strength and compressive strength are similar [140] and [141]. Because cracks can propagate more quickly, a material's tensile strength is often substantially lower than its compressive strength [140]. The determination of mechanical strength is not an easy thing, especially when the size of the specimen is small and the shape is spherical. In the literature several models are proposed for irregular and spherical material mechanical strength determination. Based on the value of tensile strength obtained by the Brazilian test with flat platens (plaster of Paris, coal and cement) [141], JAEGER, developed a model to compute (equation 2. 5) the tensile strength of four spherical rocks [142].

$$\sigma_t = k\frac{F_f}{R^2} \qquad (2.\ 5)$$

Where k is a numerical constant, F_f the peak load at failure of the sphere and R the radius of the sphere.

The next year, 1967, HIRAMATSUS and OKA used a compression test on an uneven test piece to ascertain the tensile strength of rock. They showed that, the theoretical peak tensile is considerably greater than below validated equation (2.6) with experimental results [143]

$$\sigma_t = 1.4\frac{F_f}{\pi R^2} \qquad (2.\ 6)$$

Many experimental studies have used these expressions to evaluate the strength of spherical or irregular particles tested in uniaxial compression [144], [143] and [145].

In this study the quasi-static method was used. A particle is squeezed between two parallel platens of a compression machine in a uniaxial compression test until it fails. Following the test, the peak load was noted, and using equation (2. 6) as described in [143], the axial tensile strengths for three specimens for each formulation were calculated. The sand-clay and CBA ceramic balls were tested as showed in Figure. 2.7.

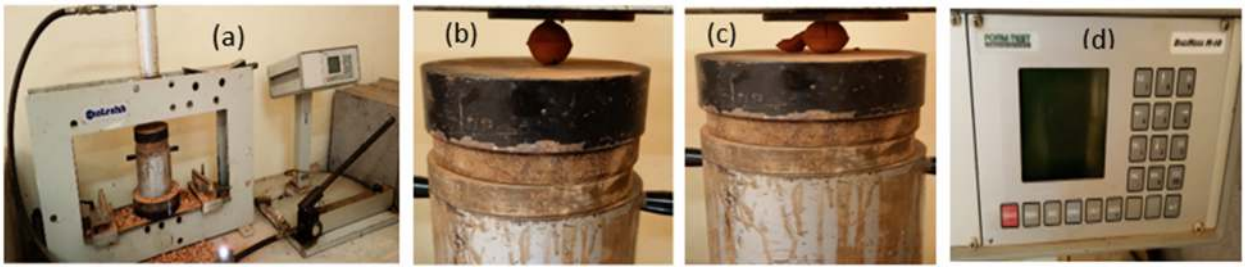

Figure. 2. 7. Compression test process: a) compression machine, b) Insertion of specimen between the two parallel platens, c) Fail of the specimen under the maximal load and d) the display screen.

For the different mechanical properties, the standard errors [146] were computed using the equation (2. 7)

$$SE=\frac{\sqrt{\sum(x_i-\bar{x})^2}}{\bar{x}\times n}\times 100. \qquad (2.\ 7)$$

For the bulk density, porosity, loss on ignition, and axial tensile strength, the formulation yields maximum standard errors or uncertainties of 6%, 2.94%, 4.91%, and 10%, respectively, for the various mechanical properties have been obtained.

II.3.2. Thermal properties measurement method

Thermal conductivity, thermal diffusivity, and volumetric specific heat capacity were measured using the battery-powered, portable KD2 Pro Thermal Properties Analyzer with dual needle sensor. The dual-needle SH-1 sensor (1.3 mm diameter 30 mm long for a needle) was chosen to perform the tests as the producer recommends [147] it for porous material and other material like granular material (soil, sand) and rocks. Pilot hole was drilled using a drilling machine with a drill bit of 1mm and 1.5mm. Measuring range is 0.5 to 4 $MJm^{-3}K^{-1}$ for volumetric heat 0.02 to 2 $Wm^{-1}K^{-1}$ for thermal conductivity and 0.1 to $1mm^2s^{-1}$ for thermal diffusivity with accuracy of ±10% for the sensor. Prior to any testing, the sensor was calibrated using the dual sensor calibration specimen. The read time was chosen to minimise the error on the results (<0.01) and the measurements were replicated at least three time on two different pellets of the same formulation. The Figure. 2.8 illustrates the materials and the process for thermal properties data collection.

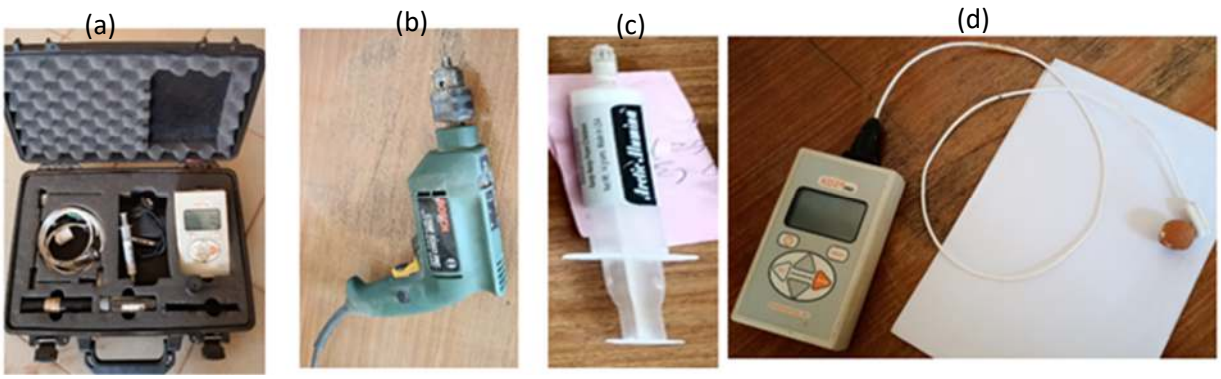

Figure. 2. 8. Thermal properties analysis process: (a)-Thermal analyser, (b)-drilling machine, (c)-thermal paste and (d)-the connection of the sensor and sample to the controller.

II.3.3. Thermal stability analysis process

An average CSP plant is expected to last at least 10–30 years, which could require thousands charge–discharge cycles [43],[129] and [148]. To reduce the number of cycles performed for each sample, the rate of heating and cooling was increased during the charge–discharge cycles. When the ceramic balls will have thermal stability at high heating rate, their thermal properties will be even better for low heating rates [43] (In the storage system). The thermal cycles were carried out in a programmable muffle furnace at 610°C with a heating rate of 20 °C/min (less than 1°C/min in normal operation), the temperature was hold during one hour at 610°C and a discharge cycle was carried out in ambient air to100°C for thirty-three minutes with a cooling rate of 14°C /min. A multimeter with thermocouple was used to control cooling rate by tracking the time. The thermal stability study process is presented in figure. 2.9. After the 60 cycles the specimens were weighted for mass loss appreciation. The examined ceramic balls have a similar mean diameter of around 2.88 cm.

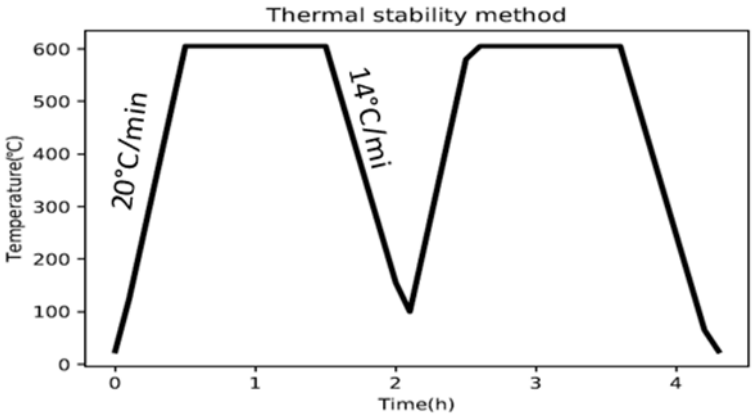

Figure. 2. 9. Thermal stability study method.

II.4. Selection process of the ceramic balls with the required properties for sensible heat storage (SHS) at medium and high temperature.

Keeping in mind the criteria established by the IEA, the formulated material must meet certain requirements to be used as TESM in solar power plants. The filler material needs to have sufficiently high compressive strength so that the bottom most layer does not crush under the load of the ceramic ball piled above it. For a packed bed 25m high, the average load at the bottom would be below 1MPa for a particle density of 3000 kgm^{-3} [148]. For any formulated or filer material (ceramic or rocks) that weathers rapidly and forms dust or sand (disintegrates) that fills the heat transfer fluid passages in the bed is undesirable [148]. The filler material must have a high storage capacity ($\rho c_p > 2\ MJ.m^{-3}K^{-1}$) to reduce the volume of thermal storage tank and this will result in lower material costs and also lower tank costs. In order for heat to be transferred from the particle's outside to its centre with only a slight temperature difference, the thermal conductivity must be high enough. In this investigation, the ceramic ball's axial tensile strength was analysed in the first phase, its thermal characteristics were analysed in the second, and its thermal stability was examined in the last step. The selection of SHS materials base on thermal cycling is not yet standardized. In 2019, Sane et al. produced a suitable ceramic for TES made of clay and 20 weight percent SiC (silicate carbide) after 20 cycles at 700°C under air environment with a heating rate of 5 °C/min and based on mass losses observation [131]. based on mass loss and fracture observation In 2014, Allen et al. demonstrated that after 950 cycles at mean temperatures of 350°C and 500°C -530°C with heating rate of 2 °C/min, rock types such as igneous and high-grade metamorphic are suitable for sensible heat storage (SHS) application [148]. In 2017, Tiskatine and colleagues proved that quarzitic was suitable for SHS based on crack observation following 120 thermal cycles at 650 °C in an air atmosphere with a 25 °C heating rate, a 1-hour isotherm, and a 20 °C cooling rate [43]. After three cycles at 1000 °C with heating rate of 10 °C /min and in a TMA/TG-ATD device (TMA Setsys, from Setaram, TG-ATD Labsys from Setaram), Ferber et al.,2020 have come out with suitable SHSM ceramic made with 20 wt.% and 30 wt.% clay an Municipal Waste Incineration Bottom Ash (MWIBA) [52].

III. Results and discussion

III.1. Mechanical Properties analysis

Figure. 2.10 to Figure. 2.12, present the results (illustrated cases) of the bulk density for each ceramic developed at 1000 °C and 1060 °C.

The bulk density values obtained range from 1730 kg/m³ to 2050 kg/m³ (±6%) and are similar to the one developed in the literature [132]. With the exception of the pellets developed with NS-N and C1 at 1060 °C, the overall bulk density of the pellet drops when the CBA ratio increases and the sand ratio decreases. For example, it decreases 9.71%, 6.21%, 1.12%, 7.82% respectively for dune and mining sand from Burkina and dune sand and natural sand from Niger for the pellet fired at 1000°C. Taking into count the measuring error ((±6%), the density decreases can be neglected for the dune sand ceramic from Niger compare to the uncertainty. The volatile elements, which affect the LOI in the different sand can explain the different in decrease ratio specially for MS-B, DS-N and NS-N. Since the fine sand ratio increases the clay-sand ceramic density, this decrease might also be accounted by the reduction in the sand ratio [132].

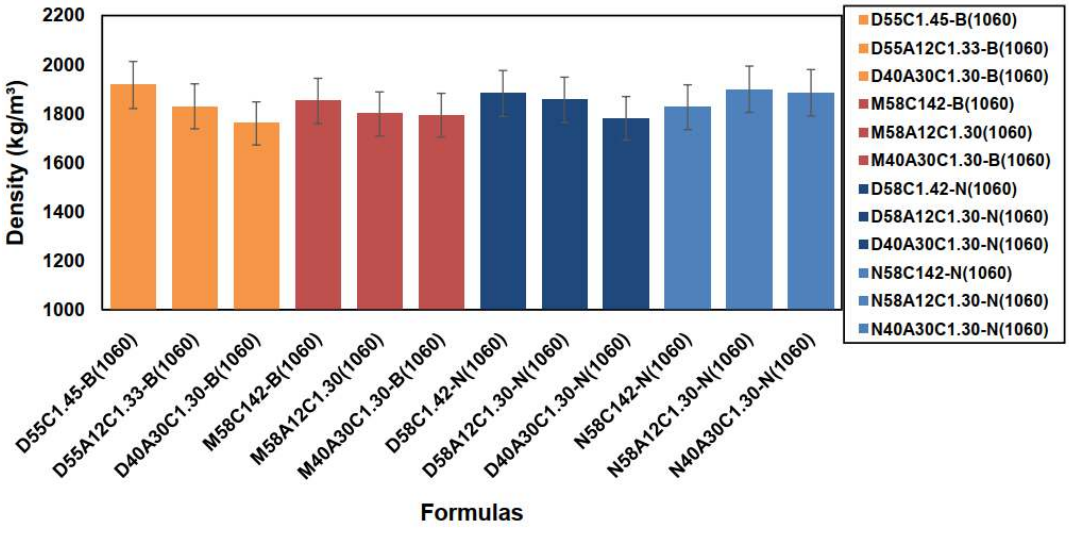

Figure. 2. 10. Bulk density of some specimens made using various sand CBA formulations.

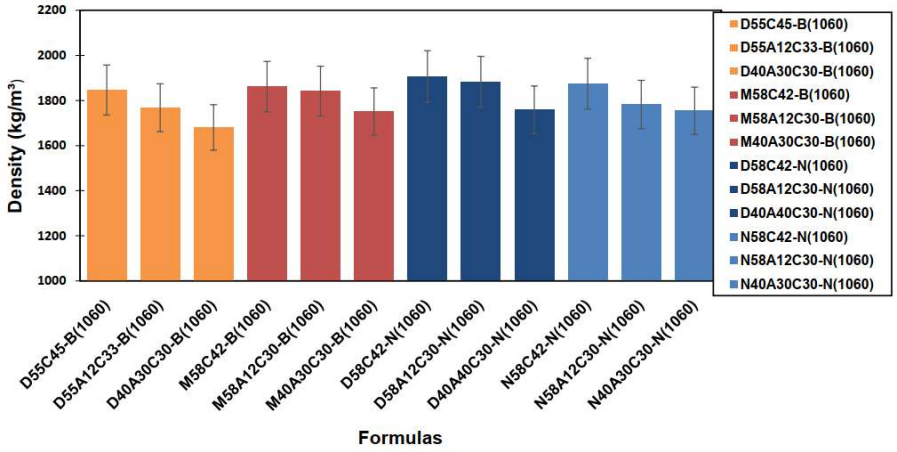

Figure. 2. 11. Bulk density of certain specimens made using various sand compositions, CBA

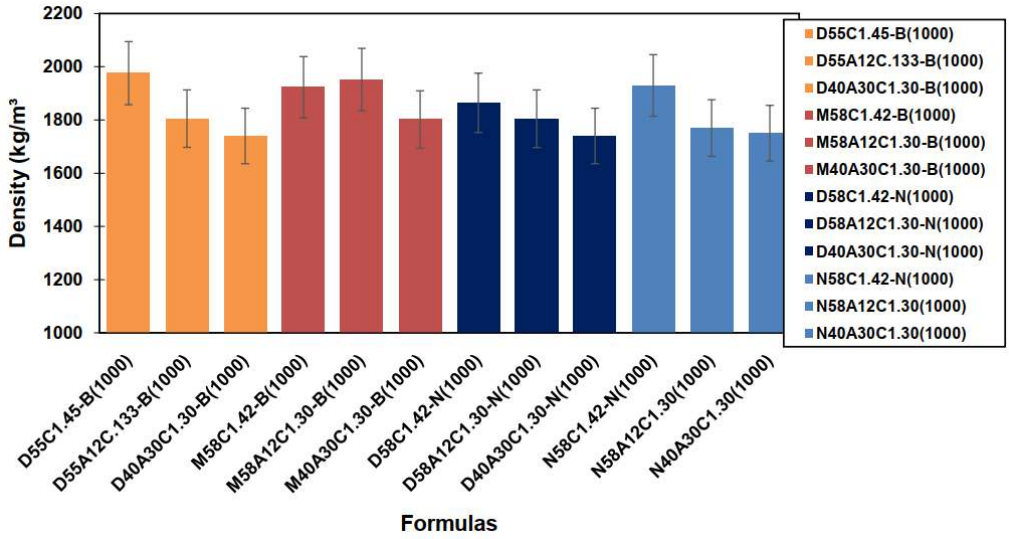

Figure. 2. 12. Bulk density of some specimens made using various sand CBA formulations.

The porosity and LOI results during the formulation of the different ceramic balls range respectively from 20.8% to 28.57% (±2.94%) and 2,08% to 5.71 % (±4.91%) according to the formulas.

The ceramic ball density results show a slight decreasing of the bulk density with increasing of CBA %wt. as illustrated in figure. 2.10 to figure. 2.12 The trend of bulk density as function of porosity and the one of porosity as function of loss on ignition are illustrated in figure. 2.13 and figure. 2.14. This increasing of the porosity with CBA ratio (Table. 5) could justify the decreasing of the density due to the increase of mass loss, which increases the void volume due to loss on

ignition. Most of the ceramic ball loss on ignition values are below 6% (figure. 2.14). However, these values increase slightly when the mass of CBA increases (table.2. 5). Thus, with high loss in ignition (15%wt.) [53] [138], compare to sand [134], the increase of ash, increase the ceramic LOI driving to the increase of the specimen porosity (Figure. 2.14 and Table. 2. 5). The following correlation between the density and the porosity and between the porosity and LOI of the ceramic ball can be written:

$$\rho = -25.453\varepsilon + 2448.4 \quad (2.\ 8)$$

Where ρ is the specimen density in kg.m^{-3} and ε its porosity in (%).

$$\varepsilon = 0.3601LOI + 22.447 \quad (2.\ 9)$$

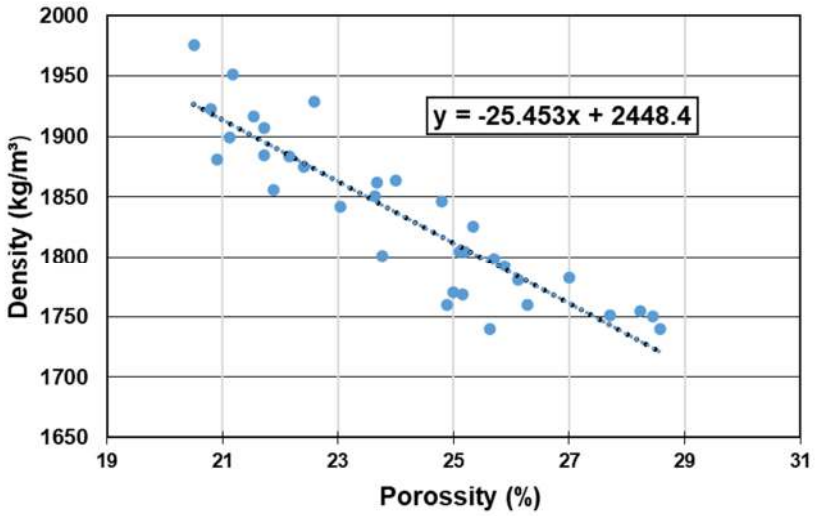

Figure. 2. 13. Effect of porosity or ash percentage weight on the ceramic balls bulk density.

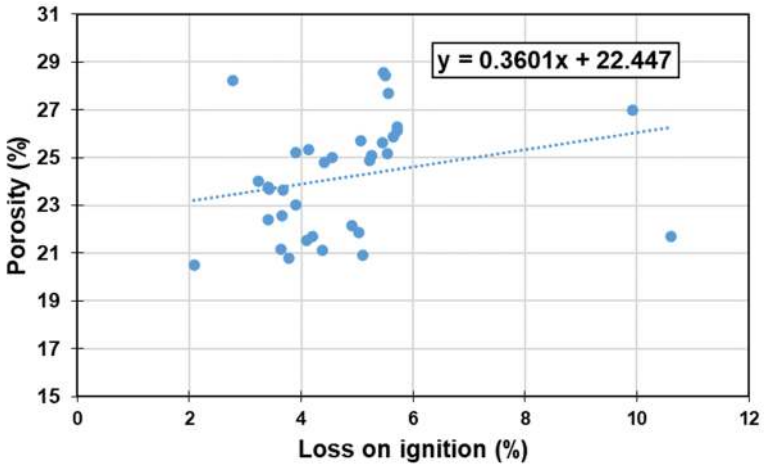

Figure. 2. 14. Effect of CBA wt. % increasing on the porosity and the loss on ignition of some specimens.

Table 2. 5.Effect of CBA percentage weight on loss on ignition and porosity at 1060°C of the different ceramic developed with clay C1.

Ceramic		Loss on Ignition (%)	Porosity (%)
DS-B	CBA (0%wt.)	3.795	21.538
	CBA (12%wt.)	4.092	23.653
	CBA (30% wt.)	5.223	25.331
MS-B	CBA (0% wt.)	3.680	23.631
	CBA (12% wt.)	5.065	25.703
	CBA (30% wt.)	5.646	25.882
DS-N	CBA (0% wt.)	4.296	20.899
	CBA (12% wt.)	5.030	21.887
	CBA (30% wt.)	5.718	26.114
NS-N	CBA (0% wt.)	4.1263	24.896
	CBA (12% wt.)	4.369	21.117
	CBA (30% wt.)	10.595	21.724

For the axial tensile strength, illustrate from figure 38 to 40 their values ranged from 350kPa to 3500kPa with standard error of ±10% according to the formulation. An improvement with the CBA ratio in all the formulations (ceramic ball) has been observed. The results are similar to the flexure strength obtained by Balogun *et al en 2021* [132] with sand-clay ceramic. The goal of this study is to improve the thermal properties of TESM by combining sand particles. All ceramic balls

containing ash waste, with the exception of N58A12C30-N and N58A12C1.30-N, have acceptable tensile strengths. The axial tensile strength of sand and clay ceramic is improved by an increase in the CBA ratio. While this increase in ash ratio leads to more voids in the ceramic in relation to the increase in LOI during the firing process (Table. 6), an improvement in compressive strength is observed. This shows that the ash plays a rule of binder like clay. Even though, the porosity of the specimen increases with CBA wt.% (table. 6), an increasing of the tensile strength is observed (figure. 2.15 to figure. 2.18). This can be explained by the chemical composition of the CBA given in [53] and the other raw material (clay and sand) . Generally, raw materials for ceramic pastes containing CaCO3 is liable to form crystalline phases at relatively low temperatures from 950 °C to 1000 °C [149]. In addition alkaline contribute to the formation of liquid phases at low temperature [150]. As the ratio of alumina (Al_2O_3) is enough in the CBA, it could contribute to increase the quantity of kaolinite. Therefore, during heat treatment, the major component of kaolinite is transformed into meta kaolinite between 550°C to 600°C, with a dehydrated metastable amorphous structure. It very gradually changes into an alumina spinel phase and amorphous silica between 950°C and 1000°C. A viscous liquid is created when feldspar grains combine with meta kaolinite and amorphous silica at temperatures just above 1000 °C. The finest quartz grains gradually dissolve into the liquid phase during this procedure [137] and [151]. Since the highest firing temperature of the current ceramic was 1060°C, and the dissolution of larger quartz grains—the primary component of the raw materials—begins at temperatures as high as 1100°C, the final process may be restricted during the firing process (particularly so for natural sand with 0.93mm mean grain size) [137] and [151]. This could account for the specimens' high porosity since the dissolution of quartz causes a decrease in ceramic pores. These phenomena could be difference from one clay to another because the highest tensile strength ceramics are obtained with pottery clay or green clay (figure. 2.15 and figure. 2.16). In the end, we can conclude that CBA was successfully integrated in a ceramic manufacturing, potentially providing an end-use for this waste at temperature less than 1100°C.

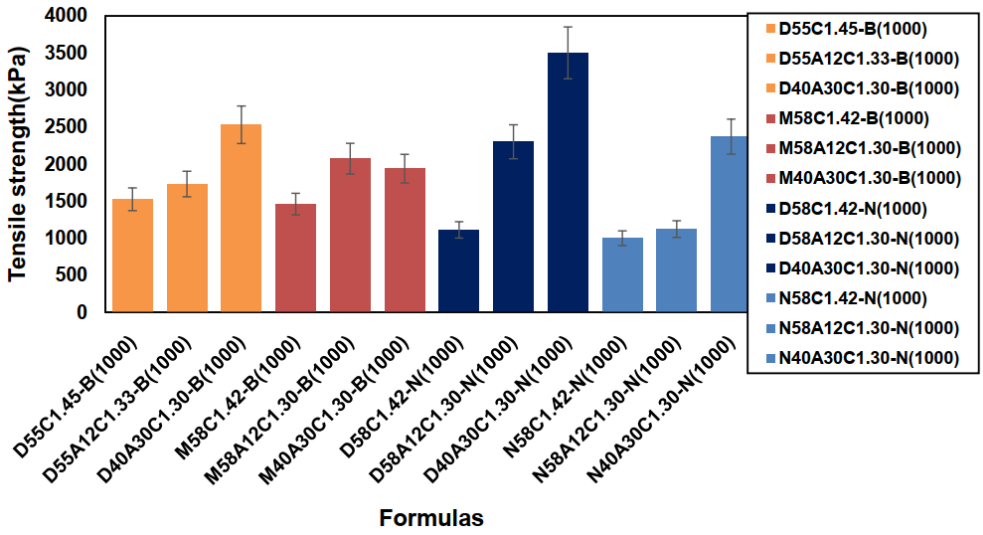

Figure. 2. 15. Uniaxial tensile strength of several specimens made with various sands, clays, and CBA compositions.

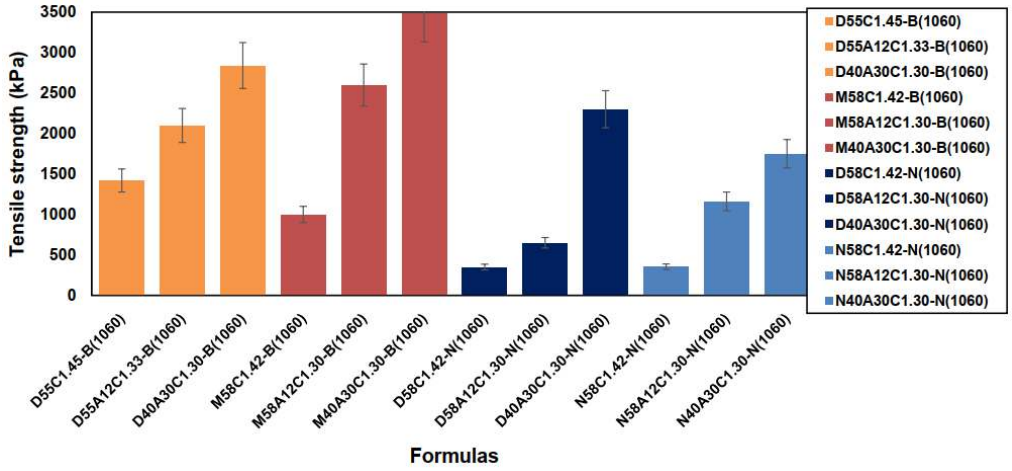

Figure. 2. 16. The uniaxial tensile strength of the various specimens made with various combinations of sand, clay, and CBA.

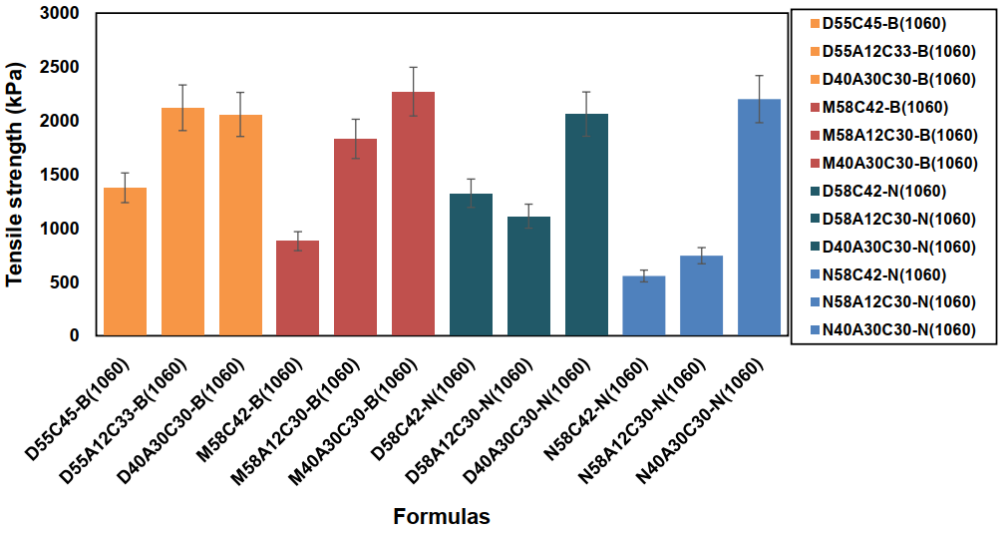

Figure. 2. 17. Uniaxial tensile strength of several specimens made with various %wt of sand, clay, and CBA.

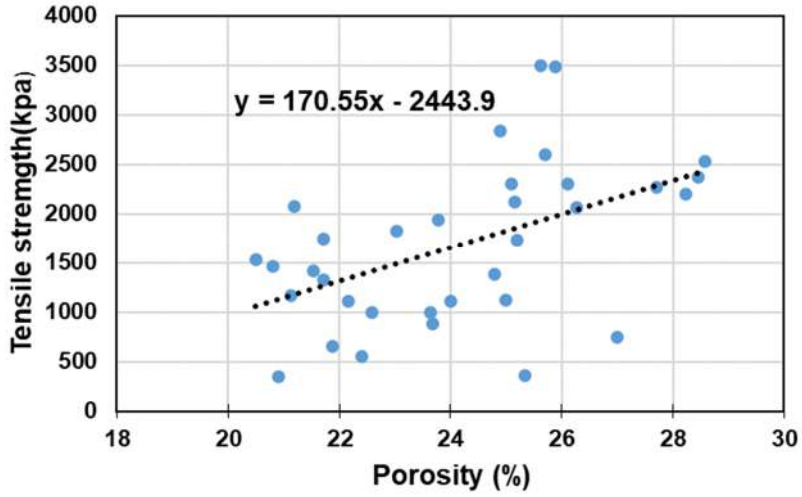

Figure. 2. 18. Impact of ash % weight or porosity on the tensile strength of ceramic balls.

Table 2. 6. Effect of CBA percentage weight on loss on ignition, porosity and tensile strength at 1060°C of the different ceramic developed with clay C1.

Ceramic		Loss on Ignition (%)	Porosity (%)	Tensile strength
DS-B	CBA (0%wt.)	3.795	21.538	1420
	CBA (12%wt.)	4.092	23.653	2100
	CBA (30% wt.)	5.223	25.331	2840

MS-B	CBA (0% wt.)	3.680	23.631	1000
	CBA (12% wt.)	5.065	25.703	2600
	CBA (30% wt.)	5.646	25.882	3480
DS-N	CBA (0% wt.)	4.296	20.899	350
	CBA (12% wt.)	5.031	21.887	650
	CBA (30% wt.)	5.718	26.114	2300
NS-N	CBA (0% wt.)	4.126	24.897	354
	CBA (12% wt.)	4.369	21.117	1162
	CBA (30% wt.)	10.595	21.724	1750

It is crucial to consider the compressive strength loss during heat treatment when choosing the optimal TESM based on tensile strength. Depending on the operating temperature, this reduction in compression strength for rocks like granite might range from 30% to 60% [152]. Because of this, specimens made of ceramic or porcelain may have a lower mechanical performance decline because of their refractory nature, which is defined as the material collapsing under its own weight at high temperatures [153]. As mentioned earlier in the IEA criteria for the selection of a thermal storage material, the minimum strength for compression should be at least 1MPa to avoid any ball crushes in the storage system [148]. Therefore, all samples made from sand, clay and bottom ash are usable with the exception of N58A12C30-N and N58A12C1.30-N and will be considered in the following work for thermal analysis.

III.2. Thermal properties analysis

All ceramic balls with a compressive strength of more than 1MPa were selected for analysis of their thermal properties. Their thermal properties were evaluated with an accuracy of ±10%. Their values and standards errors, at room temperature (Temp) and at firing temperatures 1000°C and 1060°C are presented in table 2. 7 and table 2. 8.

Table 2. 7.Thermal properties of the ceramic balls sintered at 1000°C.

Formulation	$\boldsymbol{\lambda}$ ($\boldsymbol{Wm^{-1}°C^{-1}}$)	D ($\boldsymbol{mm^2s^{-1}}$)	$\boldsymbol{\rho c_p}$ ($\boldsymbol{MJm^{-3}°C^{-1}}$J)	Temp (°C)
D55A12C1.33-B (1000)	0.397 (±1.63%)	0.156 (1.27%)	2.539 (±2.21%)	30.8 (±5%)
D40A30C1.30-B (1000)	0.366 (±3.2%)	0.134 (±1.63%)	2.736 (±1.63%)	31.885 (±0.77%)
M58A12C1.30-B (1000)	1.014 (±0.28%)	0.135 (±0.165%)	2.906 (±0.19%)	31.48 (±1.86%)

M40A30C1.30-B (1000)	0.383 (3.2±%)	0.137 (0.4±%)	2.789 (±0.84%)	26.41 (±0.34%)
D58A12C1.30-N (1000)	0.382 (±3.67%)	0.152 (±3.72%)	2.624 (±8.2%)	34.12 (±9%)
D40A30C1.30-N (1000)	0.373 (±%0.15)	0.148 (±0.38%)	2.513 (±0.20%)	30.51 (±2.58%)
N40A30C1.30-N (1000)	0.407 (±2.06%)	0.164 (±1.405%)	2.476 (±3.476%)	31.073 (±5.17%)

Table 2. 8.Thermal properties of the different ceramic ball sintered at 1060°C.

Formulation	$\boldsymbol{\lambda}$ ($\boldsymbol{Wm^{-1}°C^{-1}}$)	D ($\boldsymbol{mm^2s^{-1}}$)	$\boldsymbol{\rho c_p}$ ($\boldsymbol{MJm^{-3}°C^{-1}}$J)	Temp (°C)
D55A12C1.33-B (1060)	0.456 (±0.33%)	0.177 (±3.72%)	2.596 (±1.32%)	34.62 (±2.71%)
D40A30C1.30-B (1060)	0.411(±0%)	0.173 (±4.08%)	2.407 (±5.72%)	29.76 (±2.18%)
M58A12C1.30-B (1060)	0.418 (±0.5%)	0.167 (±1.27%)	2.509 (±1.54%)	36.55 (±2.47%)
M40A30C1.30-B (1060)	0.47(±0.12%)	0.174 (±0.57%)	2.70 (±0.7%)	24.783 (±1.46%)
D58A12C1.30-N (1060)	0.416 (±0%)	0.155 (±1.5%)	2.693 (±1.39%)	27.257 (±6.16%)
D40A30C1.30-N (1060)	0.414 (±1.53%)	0.148 (±3.59%)	2.798(±2.53%)	35.5 (±4.93%)
N40A30C130-N (1060)	0.41(±0.54%)	0.138 (±0.36%)	2.971 (±0.18%)	27.92 (±10%)
D55A12C33-B (1060)	0.371 (±0.38%)	0.121 (±0%)	3.054 (±0.44%)	32.17 (±0.13%)
D40A30C30-B (1060)	0.402 (±0.2%)	0.135 (±0%)	2.551 (±0.47%)	29.37 (±7.8%)
M58A12C30-B (1060)	0.473 (±0.32%)	0.138 (±2.17%)	3.426 (±1.51%)	30.505 (±3.58%)
M40A30C30-B (1060)	0.436 (±0%)	0.167 (±0.32%)	2.612 (±0%)	27.065 (±0.16%)
D58A12C30-N (1060)	0.42 (±0%)	0.15825 (±0%)	2.776 (±0.076%)	30.9375 (±0.38%)
D40A30C30-N (1060)	0.331(±7.4%)	0.123 (±6.19%)	2.713 (±4.34%)	34.78 (±5.1%)
N40A30C30-N (1060)	0.411(±0.24%)	0.141 (±0.82%)	2.916 (±1.15%)	25.66 (±7.28%)

In general, the minimum thermal conductivity value recommended by the IEA is 1 $Wm^{-1}K^{-1}$for a heat storage material. However, the effect of the effective thermal conductivity on the performance of the TES could be negligible. The thermal conductivity of the different specimens developed ranges from 0.331 $W.m^{-1}.K^{-1}$. to 1.014 $W.m^{-1}.K^{-1}$ with standard error less than 10% for each formulation. Thermal conductivity is not significantly affected by the CBA ratio or the firing temperature. Therefore, below 1050 °C, the clay ceramic is not properly fired, that strongly reduced its thermal conductivity as demonstrated in [154] where a value less than 0.3 $W.m^{-1}.K^{-1}$ was measured for kaolin clay ceramic fired at 1050°C. As the effect of thermal conductivity on TES performance is negligible [155], it will not hinder the use of ceramic balls as a heat storage material.

The thermal diffusivity of the different pellets ranges from 0.123 $mm^2.s^{-1}$ to 0.177 $mm^2.s^{-1}$ with standard error less 10% for each formulation. The pace at which warmth spreads across a material and the amount of heat transferred from a hot material to a cool one is measured and characterized as thermal diffusivity, which is the ratio of thermal conductivity to volumetric heat capacity. Thermal diffusion can cause the thermocline energy storage to deteriorate at a high thermal diffusivity value [21].

The volumetric heat capacity or volumetric specific heat (VHC) of the different ceramic ball's ranges from 2.407.$MJ.m^{-3}°C^{-1}$ to 3.426 $MJ.m^{-3}°C^{-1}$ with standard error less than 10% for each formulation as presented in table 13 and table 14. The results are better for the composition with 58 wt.% or 55 wt.% sand, 12 wt.% ash and 33 wt.% or 30 wt.% clay. Thus, the highest VHC is obtained with M58A12C30-B (1060). This can be explained by the sand particle size effect on the specific heat capacity which is around 0.26 mm, 0.91 mm and 0.93 mm respectively for dune sand, mining sand and natural sand. The mean particle size in the ceramic may decrease as a result of increasing and decreasing the weight percentages of ash powder and sand, respectively. As a result, the volumetric heat capacity may decrease, as shown by Bwayo et al., 2014 study on the specific heat capacity of burnt brick made from sawdust and clay, which increases with particle size [156]. However, all the ceramic balls developed in the present study met the required VHC (up to 2.$MJ.m^{-3}.°C^{-1}$) to be used as sensible heat storage materials in the CSP plant according to Fernandez et al., [157] . Some ceramic balls have a volumetric heat capacity higher than 3 $MJ.m^{-3}°C^{-1}$ at room temperature (table 3 and 4) and can become better at high temperature. Therefore, the ceramics developed could compete with the best stable rock (Rhyolite and quarzitic sandstone) in terms of heat storage capacity [43] and with molten salt at high temperature because the favoured molten nitrate salt has a volumetric heat capacity of 3 $MJ.m^{-3}°K^{-1}$, and limited to a temperature change at approximately 300°C [8].

III.3. Thermal stability analysis

The thermal stability qualifies the sample loss of mass with temperature or under heat treatment. A material with a high thermal stability shows a high resistance to thermal decomposition. If after 20 cycles the material did not loss enough mass and did not crash under heat treatment rate higher than 5°C/min, the material can be considered thermally stable [131]. Forty-two (42) ceramic balls (numbered from 1 to 42 before the test) have been treated during 60 cycles as demonstrated in the

figure 8 including those with lowest tensile strength like numbers 1, 4, 6, 7, 10, 17, 20, 21, 23, 26, 29, 32, 35, 38 made only with sand and clay. After each 20 cycles the specimens were photographed and illustrated by the figure. 2.19 as follows.

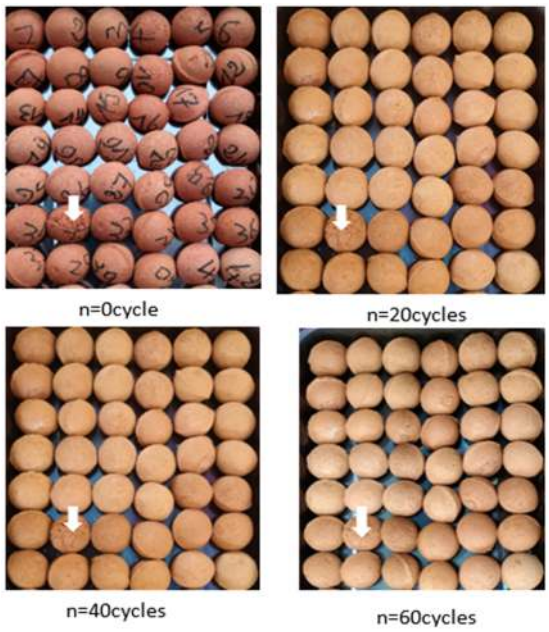

Figure. 2. 19. Photographed of the different specimens after each 20 cycles.

For each of the several ceramic balls, there has only been a noticeable colour shift. After 60 cycles, not even the one with the lowest tensile strength cracked. After 60 heat cycles, not even the most delicate porcelain in this investigation showed any signs of cracking. In addition, the figure. 2.20 present the mass loss obtained with the selected specimens base on tensile strength after 60 cycles. The maximum mass loss registered is 0.87% compare to 0.6% obtained by [131]. The type of raw materials used, their mechanical characteristics, the number of cycles—60 in this study compared to 20 in the previous one—and the rate of heating and cooling might all contribute to this discrepancy. Therefore, based on the evaluation of the axial tensile strength, thermal characteristics, and thermal stability analysis, it can be said that all of the ceramic balls composed of sand, clay, and CBA may be suitable for SHS.

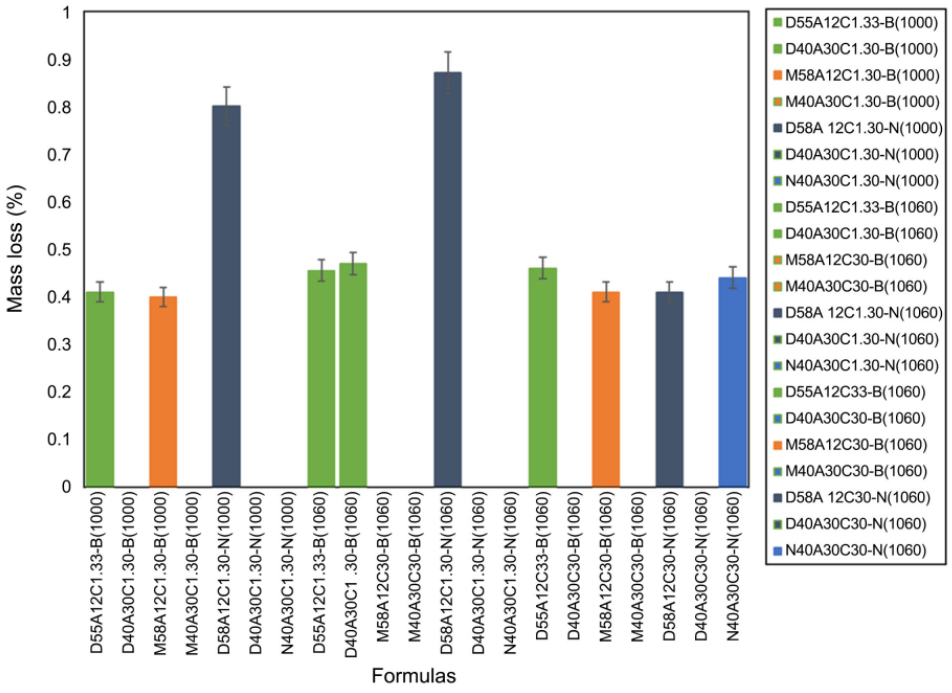

Figure. 2. 20. Mass lost by the different ceramic balls during heat treatment.

III.4. Manufacturing cost approach of the new thermal energy storage material

The developed ceramic ball can be produced within local furnaces where the temperature can reach 1000°C [129]. The figure. 2.21 illustrate the local furnace of Malgsombo used for fired bricks manufacturing for building purpose. The cost of these brick is around 300 FCFA per brick of 2.25kg. Using this approach, the ceramic balls can be formulated 134 FCFA/kg which is around 0.204 euro per kg.

Figure. 2. 21. Local furnace used for fired bricks manufacturing at Malgsombo.

Conclusion

As demonstrated previously [134]., sand have a high potentiality to developed effective TESM. In this chapter, the technical feasibility has been demonstrated. Sand particles have been combine using clay and coal bottom ash waste from incinerator of Niger coal power plant giving a spherical shape to the material. After formulation and firing at 1000°C and 1060°C, the obtained ceramics were mechanically and thermally analysed. From the tensile strength analysis, the results have shown that only the formulation with ash waste have the required tensile strength for SHS excepted N58A12C30(1000) and N58A12C1.30(1060) due to the large grains of natural sand. All the ceramic selected from the axial tensile strength have the required VHC for SHS and could even compete with the one of molten salt for high TES application. Based on the thermal conductivity, only the formulation M58A12C1.30-B (1000) have the required thermal conductivity. However, the thermal conductivity of the selected ceramic is closed or higher than the thermal conductivity of molten salt and thermal oil use in CSP plant. The thermal cycling shown that all the selected material could have a higher thermal stability due to the refractory (presence of silicate and alumina) character of the ceramic [158], the absence of crack and the low mass loss observed. In conclusion the selected materials are the one compose with 40 wt.% to 58 wt.% of sand (dune sand and mining sand), 12 wt.% to 30 wt.% ash and 30 wt.% to 30 wt.% clay and N58A12C30 (1000).

Chapter 3: Compatibility study between Jatropha curcas oil and ceramic balls

Introduction

The new material has been developed successfully and those meeting the criteria of IEA have been selected. At mean thermal energy storage temperature, oil has better thermal properties than air. In this chapter the selected ceramic will be put in contact of jatropha curcas crude oil (JCCO) and jatropha curcas refined oil (JCRO). This process is called thermal compatibility study. Two material liquid and solid are compatible if they can stay together for long time without destroy themselves. In term of cost JCCO has low cost than JCRO. The refining process drives to additional cost. Nevertheless, given its cleanliness, this oil (JCRO) will be taken into account in this study in order to compare the evolution of its thermal properties with those of crude oil (JCCO). Because, for the both oils JCCO and JCRO their thermal performance is not yet addressed in the literature. This study will be more focused on JCCO. The effect of jatropha curcas oil (JCO) on the new TESM under long time heat treatment and vis versa will be addressed. The advantage to study JCO is due to its low cost. In addition, JCO has no food conflict. A part from that JCO has good thermal properties compare to others vegetal oils (rapeseed oil, cotton oil soya oil etc.) [159]. To address assessing the compatibility between JCO and the ceramic ball, a state of art will be conducted in the next paragraph.

I. State of art on compatibility study between HTF and TESM for DMT application

In West Africa, there is only one pilot CSP plant (CSP4AFRICA) of 8.8 kW_{el}. The plant is installed at 2ie designed to work with the conventional two tank storage system using Jatropha curcas oil as HTF and storage material [130]. Numerous investigations on the thermal stability of JCCO and RJCO in steel reactors over extended periods of time were conducted in order to implement this system or technology in the area [63] and [113]. In this work, developed ceramic balls are put in contact with JCCO for three months to develop an effective cost TES system using JCCO as HTF and TESM and ceramic balls as filler materials (TESM). The approach of accelerating aging of the TES system is to assess the life time base on indicators evolution such as oil acidity at short time without being in real plant working conditions. For example, an accelerating aging of 500

hours corresponds to 1.4 year in real working condition [160]. Compatibility evolution issue between HTF and TESM is also another drawback of thermocline storage when the storage is direct. Several types of thermal oils are available nowadays. Among these oils we have mineral and synthetic oil which are respectively from hydrocarbon mixture produced from the distillation of crude oil and synthesised from chemical compounds [161]. Mineral oils, in addition to sources limitation have several other drawbacks such as, non-biodegradability (not more than 30%), low flash point, non-renewable and could cause a serious problem if there is a spillage[162]. Synthetic oils are also used as thermal oils because of their good properties like high flash point and excellent oxidation resistance[163] and [164], but are expensive. Vegetable oils have been the focus of numerous studies in an effort to address these problems and replace mineral or synthetic oils in a variety of applications [163] and [164]. Vegetable oils are well-known for their dependable usage as insulating fluids at high temperatures in the transformer sector, as are solar oils in solar cookers [161]. However, the use of vegetable oils as HTF and TESM in CSP is totally a new field. Therefore, studies have shown their potentiality in this area. For this propose, seven vegetable oils thermophysical and rheological (like steady flow behaviour, yield stress, transient flow behaviour, thixotropy behaviour, and viscoelastic behaviour [158]) properties were investigated in [159]. Among them we have rapeseed, soybean, sunflower, palm, copra, cottonseed and Jatropha oils. Their thermo-physical properties are on average 13% higher than the one of Therminol VP1® and are influencing by temperature and fatty acid [159]. The main different of JCO from the others, it is a non-edible oil and could be presented as the most suitable HTF and TESM for CSP application in developing countries avoiding food conflict. In the framework of CSP4AFRCA, Kenda et al. 2017 have investigate the thermal stability of JCCO in steel reactors. JCCO presents good thermal stability up to 210 °C with good energy storage density. To prevent oil oxidation, however, the reactor's oxygen renewal should be kept to a minimum [62]. In addition, the high present of free acid in JCCO can lead to corrosion of some metals (Zink , iron) and accelerate oil oxidation [62] and [165]. The heat stability of refined Jatropha Curcas oil has been tested for 2160 hours (an isothermal test) in order to combat these oxidation and corrosion issues [164]. After 2160h, RJCO still had a good specific heat capacity and kinematic viscosity at 100°C confirming jatropha curcas oil stability at 210 °C. However, a drop of flash point to 175°C occurred [164]. The Table 3. 1 present the properties of some HTF.

Table 3. 1.Thermal properties of mineral, synthetic and vegetable oil used as HTF [159],[62],[161] and [166]

Parameter	Mineral oils	Synthetic oils	Silicone oil	Vegetable oils	JCCO
Composition	Complex mixture of hydrocarbons	Pentaeryhritol tetra ester	di-alkyl silicone polymer	Plant-based natural ester	Plant-based natural ester
Flash point	160-193	47-124	>300	220-330	220-240
Fire point	110–185	300–310	340-350	300–360	275°C
Pour point at 1013mbar	-29	-11 to 12		- 11 to 20	
Total acidity	0.015–1.2	<0.01	N/A	0.015-23.82	11-23.82
$\boldsymbol{v}$ at 40°C	3–16	14-29	35–40	16–37	30-35
$\boldsymbol{\mu}$ at 40°C					
$\boldsymbol{v}$ at 100°C	2–2.5	4-6	15–17	4–8	1.73 at 210°C
$\boldsymbol{\mu}$ at 210°C					
$\boldsymbol{\rho\ at\ 210\ °C}$ $(\boldsymbol{kg.m^{-3}})$	736.4	649.8-904	N/A	771.6-805.5	778.2
$\boldsymbol{\lambda\ at\ 210}$ $(\boldsymbol{W.m^{-1}K^{-1}})$	0.13	0.062-0.121	N/A	0.128-0.143	0.139
$\boldsymbol{C_p(kJ.kg^{-1}K^{-1})}$ at 210°C	2.643	2.075-2192	N/A	2.440-2.677	2.509
$\boldsymbol{\rho \times C_p(MJ.m^{-3}.K^{-1})}$		5.5-25	N/A	N/A	N/A
Cost $(€.\boldsymbol{t^{-1}})$		N/A	N/A	0.4-1.2	N/A

In this chapter the compatibility between JCCO and ceramic balls developed using clay, coal bottom ash and sand [167] will be investigated. This approach will reduce the cost of the system while using local materials, with no negative impact on the environment. As vegetal oil, it constrains the working temperature to a lower value (250 °C) than the one that is obtained with conventional thermal oil (400 °C)[168]. The use of vegetable oil as HTF drives to direct heat production or the use of an Organic Rankine Cycle to produce electricity [169]. Jatropha oil should therefore be an alternative to mineral and synthetic oil. As the HTF could be in contact with TESM during several thermal cycles without destroy themselves, it is important to know the compatibility between HTF and filler materials. The compatibility means the capacity of an element to be well matched with another one. Several studies have been conducted on oil compatibility with filler material or TES tank wall material to select the best couple (HTF, TESM) for thermal energy storage. Some are illustrated in Table. 2

Table 3. 2. Effect of aging time and temperature on oil stability.

		New oil				Oil after aging			
PROJECTs	oils	FP (°C)	acidity mgKOHg^{-1}	Water content (ppm)	Kinematic viscosity mm^2·s^{-1}	FP (°C)	acidity mgKOHg^{-1}	Water content (ppm)	Kinematic viscosity mm^2·s^{-1}
Kenda et al[113] aged at 210°C(500h)	JaCCO+Iron	236	17.1	508	36	236	18.2	273	39
hoffmann et al[168][49] Vegetaloils aged at 210°C(720H)	Rapeseed+ quartzite	285	0.08	N/A	N/A		10.25	N/A	N/A
	Jatropha+ quartzite	236	23.82	N/A	N/A		21.82	N/A	N/A
	Palm+ quartzite	280	13.72	N/A	N/A		25.21	N/A	N/A
	Soybean+ quartzite	330	0.13	N/A	N/A		12.67	N/A	N/A
FASQUELLE ET AL 2017 synthetic oil aged at 330°C(500H)	Jarytherm®DBT +CFA	230	0.05	39		224	<0.01	112	
	Jarytherm®DBT +cofalit	230	0.05	39		224	<0.01	160	
	Jarytherm®DBT +Alumina	230	0.05	39		226	<0.01	176	

The table 3.2 shows that, the main parameters track for thermal oil as HTF or TESM (when being in contact with filler material) are flash point and acid index under temperature treatment. The flash point and thermal stability drops with aging time, which are a function of acidity. This drop depends on the compatibility study method and the aging temperature. The isothermal test method influences less the flash point than the thermal cycles test [113] and [63]. In addition, the flash point thermal stability of several vegetable oils can be function of acid index as correlated in equations (3. 1) and (3.3).

$$T_{flash} = 327.589 - 11.504 \times IA + 0.481 \times IA^2 \quad (3.\ 1)$$

$$T_{stab} = 385.942 - 3.455 \times IA \quad (3.\ 2)$$

Where IA is the acid index in mg.KOH.g^{-1}, T_{flash} is the flash point in °C and T_{stab} the stability temperature in °C.

Synthetic and mineral oil use in CSP plant is more known than vegetal oils. However, due to the low thermal instability and the high environmental hazard (negative impact on environment),

vegetable oil could be an alternative as mentioned by several authors [168],[113],[63] and [159] as HTF and TESM.

II. Materials and methods

Several processes for thermal compatibility between HTF and filler material or tank wall are available in the literature [113],[160],[168] and [170]:

Dynamic process consists of to submit together the system oil and filler material under dynamic heating and cooling process within a reactor.

The semi dynamic process is similar to the dynamic process. However, during a thermal cycle there is a holding of temperature after heating up at the working point during some hours to be more closed to CSP working conditions.

The static process is an accelerating aging process which consists of to hold the system oil and filler material at the working temperature for at least 500 hours [160].

In this work the static method was used during three months for the system Jatropha curcas oil and ceramic balls. This approach is to accelerate the degradation process of both JCO and ceramic balls thermo-physical and chemical properties to carry out the best indicators to track the performance of the new storage system during its lifetime.

II.1. Materials

II.1.1. Jatropha curcas oil (JCO)

Jatropha curcas L is known as a physic nut. It is a large shrub or small tree that belongs to the genus Euphorbiaceous, which produces oil-containing seeds. In addition to its use as a biofuel and for soap production [171] and [172], Jatropha curcas oil can also be used as HTF and TESM for thermal applications[113] and [161]. The jatropha curcas crude oil (JCCO) and JCRO supplied by the Belwet Company in Burkina Faso (Belwet 2019) was used in this work. The extraction of the crude oil is done in an AISO bar press and after direct filtration with an adapted AISO plate filter (Belwet 2008) [173]. Without any addition processing the JCCO oil is cheaper than the refined where the process of neutralisation of the free fatty acid could increase the cost of the oil. The extraction methods are available in [174]. The main composition of JCCO is fatty acid like acid oleic (38%-40%), linoleic (37%-38%) and palmitic (13%-16%) [175]. The initial characteristics

of the oil were determined at the beginning of each test because the physical and chemical properties of the oil may be impacted by the quality of the feedstock, the processing production and storage conditions.

II.1.2. Ceramic balls

The solid materials use in this study in contact with JCO are the ceramic balls developed with the same formulation in the chapter 2. After the development of the ceramic balls including, their thermal stability assessment with air at 610°C [167], their compatibility with JCO is carried out for 2160h for JCCO and 1440h for JCRO. The choice of 1440 h for refined oil is to be able to compare its degradation over two months with that of crude oil regarding to the facilities available on ground.

II.2 Corrosion or compatibility test process

Twelve (12) different pellets developed with dune sand from Burkina Faso and Niger, Mining sand from Burkina Faso and Natural sand from Niger were put in contact of JCCO and two (2) in contact with RJCO. Seventeen (17) waterproof glass containers of 100ml were used as reactors. One sheet of ball was put in a container filled with JCCO and JCRO and closed with glass cover avoiding any contact between air and oil. Twelve reactors with balls and three without pellet were prepared. The fifteen containers were put in stainless steel box and the box in turn put in an oven as presented in Figure. 3. 1. The two containers of JCRO on stainless flat plat and put also in the oven. The first 24 hours are not taken into account as this is the time needed for the temperature to be uniform in the oven. The objective is to study pellet corrosion maintaining the materials at 210 °C, which is close to the maximum temperature that jatropha curcas oil can handle (250 °C) and which can be the target temperature for a later use in a solar power plant or a thermal energy storage system [49]. After each month, every type of sample was removed and analysed.

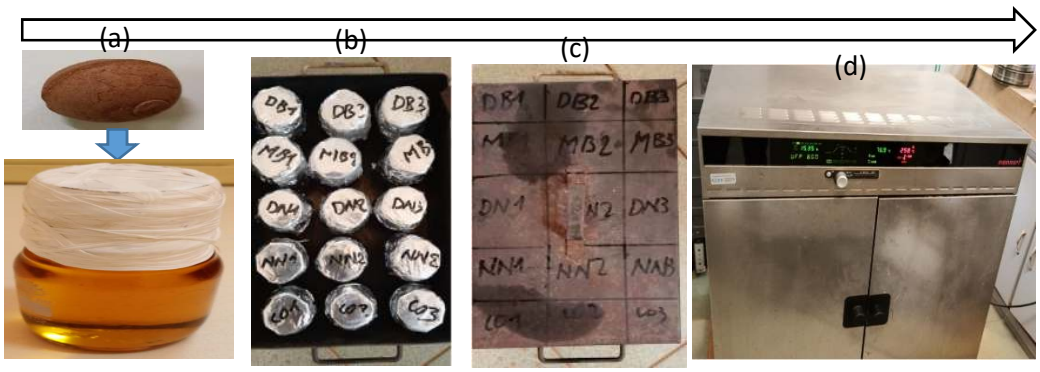

Figure. 3. 1. Corrosion and heat treatment test process: (a)-sample placing in the container, (b)-container placing in the reactor, (c)-close of the reactors, (d)-placing of the reactor in the oven.

II.3. Measurement of the different properties providing the best indicator for compatibility assessment.

In this work, physical, rheological and chemical properties of oil samples were assessed including Index of Acidity (IA); Peroxide value, Thermal conductivity; kinematic viscosity; Density; Flash point; Thermal stability and ceramic balls coloration.

II.3.1. Chemical properties

II.3.1.1. Index of acid

Acidity is defined as the amount of potassium hydroxide in mg needed to neutralize free fatty acids in a one-gram oil sample. Free fatty acids have smaller molecular weights than the triglycerides from which they are derived, making the acids more easily flammable. In addition, free fatty acids can cause corrosion and deposits in the piping circuit of facilities. Free fatty acids are indicators of vegetable oil, quality since they are partly generated during production process as well as during ageing process. In this chapter the oil samples acidity has been assessed using potentiometric titration according to the ASTM D974 standard method. This consists of to measure the need of potassium hydroxide (in mg) mass to neutralize the free fatty acid that are contained in a gram of oil. As oil acid value increase with time and temperature, tracking the acidity during aging time is important because an elevate acid value can affect the TES vessel (tank and pipe) due to corrosion [176].

II.3.1.2. Peroxide value

The peroxide value (PV) is a measure of the peroxides formed during the oxidation process. It is usually composed of primary oxidation products, such as various peroxides and hydroperoxides. It thus indicates the tendency of vegetable oil to oxidize or polymerize, which can lead to the formation of insoluble particles such as gums, sediments or other deposits especially under the action of light, high storage temperature or oxygen if the oil contains high levels of polyunsaturated fatty acids. For JCO, the refining process can also lead to the increasing of PV. The oxidation stability of the oil is directly related to its peroxide value. In addition, it influences different parameters of the oil, such as its density, viscosity etc. The PV of oil samples was assessed by the potentiometric titration method according to the NFT 60–220 standard methods.

II.3.2. Thermophysical properties

II.3.2.1. Density

The density as a function of temperature. is an important parameter for the oil volumetric heat capacity computation thereby an important data for the TES performance simulation. It is very often influenced by oxidation due the polymerization produces at high temperature. The formation of insoluble sediments or heavier molecules by polymerization drives to the increasing of oil density. Density is therefore an easily measurable indicator of possible degradation of oil[129]. In this study the density has been assessed at room temperature by using an analytical balance of 0.1mg of accuracy and a flask of 10 ml. The density has been computed basing on equation (3. 3).

$$\rho = \frac{m}{v} \qquad (3.\ 3)$$

With m oil sample mass, v the flask volume and ρ the density of the substance

II.3.2.2. Thermal conductivity

The thermal conductivity is a fundamental thermal parameter that determines heat transfer inside a fluid. The thermal conductivity is a function of temperature. A significant drop in this physical quantity would result in a decrease in the efficiency of the transfer. In this study, the thermal analyser KD2PRO has been used to assess the thermal conductivity. The KD2 Pro is a handheld device used to measure thermal properties. The base KD-2 Pro package consists of a handheld controller and one sensor kit of your choice. There are several sensors available for purchase that operators can insert into almost any material. The single needle sensors measure thermal

conductivity and resistivity; while the dual-needle sensor measures thermal conductivity, resistivity, volumetric specific heat capacity and diffusivity. The principle of thermal conductivity measurement is based on a transient line heat source method. Typically, a probe for this measurement consists of a needle with a heater and temperature sensor inside. A current pass through the heater and the system monitors the temperature of the sensor over time. Analysis of the sensor temperature determines thermal conductivity [147]. KD2 Pro device has been designed to optimized thermal properties measurement by minimizing thermally induced water movement and lower the time required for a measurement and limiting heat input. The small single needle KS-1 sensor (6 cm long, 1.3 mm diameter) was used to measure the thermal conductivity as recommended for liquid samples and insulating materials by the constructor. Before starting any measurement, the device was calibrated using the calibration oil. Measure the oil thermal conductivity of oil with aging time will provide information on the vulnerability of oil thermal properties to heat treatment. The figure. 3. 2 and figure. 3. 3 illustrate the KD2-PRO device, its various accessories used in the measurement of thermal conductivity and the measurement process of oil samples.

Figure. 3. 2. The KD2-PRO device and its various accessories used in the measurement of thermal conductivity.

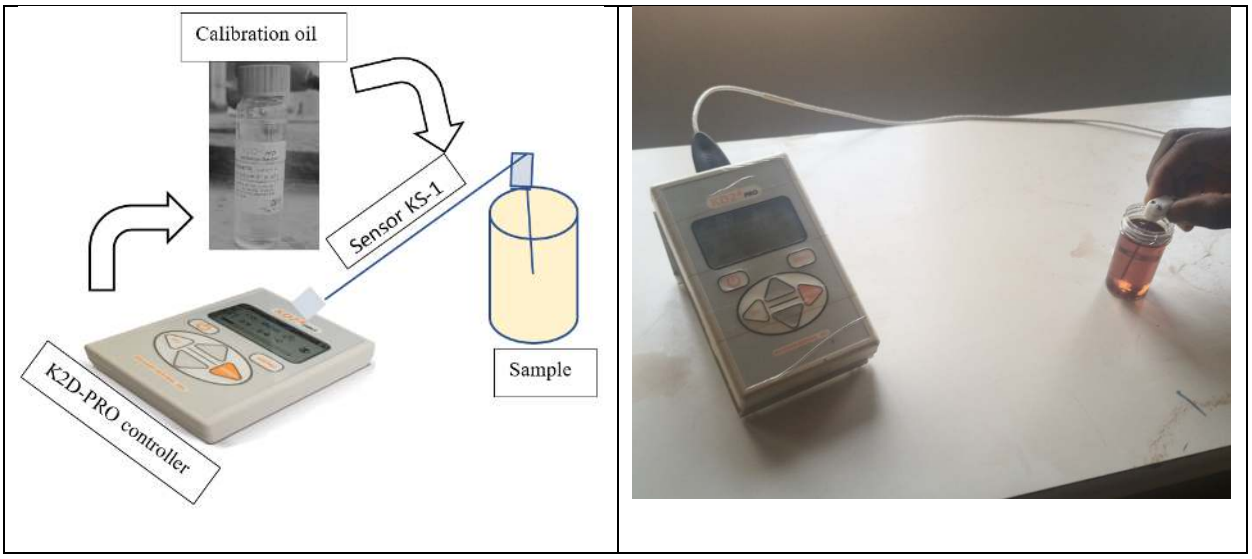

Figure. 3. 3. Oil samples thermal conductivity measurement process.

II.3.2.3. Kinematic viscosity

The kinematic viscosity (rheological properties) is the ratio of the dynamic viscosity and density, which can be, define as the ratio of shear stress to the velocity gradient perpendicular to the shear plane. It is a parameter that allows to assess the evolution of oil motion ability during aging time. High kinematic viscosity increases the pumping system pressure drop increasing then its cost. Vegetable oils are highly viscous at room temperature. On the other hand, at high temperatures, viscosities decrease very rapidly due to the decrease in intermolecular forces [177]. However, the oxidation process increases the viscosity of oil which could have direct economic impact on heat pumps necessary to circulate the fluid. The kinematic viscosity was measure at 40°C and 100°C with a viscometer. The kinematic viscosity was then, predicted at any temperature ranging from 40°C to 210°C using the power function correlation given in (3. 4).

$$\upsilon = AT^{B} \qquad (3.\ 4)$$

With T temperature in °C, A and B constants determine with data obtained at 40°C and 100°C

The figure. 3. 4 illustrate the device used to measure the kinematic viscosity of oils sample at 40°C and 100°C.

Figure. 3. 4. Viscosimeter.

II.3.2.4. The flash points

The flash point is a parameter related to the vapour pressure of a flammable liquid and is defined as the minimum temperature at which it can form a combustible mixture with air. When the flash point (or "flash" point) is reached, a simple priming source is able to cause the flammable liquid to burn. It is an important parameter to assess the fired risk in CSP and some others thermal applications. In this work the flash point was measured with an open-cup Seta flash 3′Plus′model 33000–0 analyser from STANHOPE-SETA according to the ASTM D93A standard method.

Figure. 3. 5. Seta flash 3′Plus′ series device

II.3.2.5. Thermal stability

In addition to the flash point, the thermal stability has been assessed by measuring the sample's mass loss with temperature. This process is called thermogravimetric analysis (TGA). During the aging of the vegetable oils tested, the thermal stability characteristic makes it possible to assess the evolution of decomposition or denaturation temperatures. A decrease in thermal stability can lead to an increase in the hazard factor [49]. To confirm the thermal stability of the different samples, after the measurement of the flash point, 7 samples were chosen for thermogravimetric analysis (TGA) according to the facilities available in the ground. The reference oil, three samples aged alone and three put in contact with the pellet developed with dune sand from Burkina Faso. Thermogravimetric analysis and differential thermal analysis of oil samples was investigated by thermogravimetric analyser (SETSYS Evolution 1750, Setaram Instrumentation) under inert environment (N_2). The samples were analysed under nitrogen (50 ml min−1) using aluminium pans with heating rate of 10°C per min in the 24–1000°C temperature range. The thermogravimetric analysis process is illustrated in figure. 3. 5.

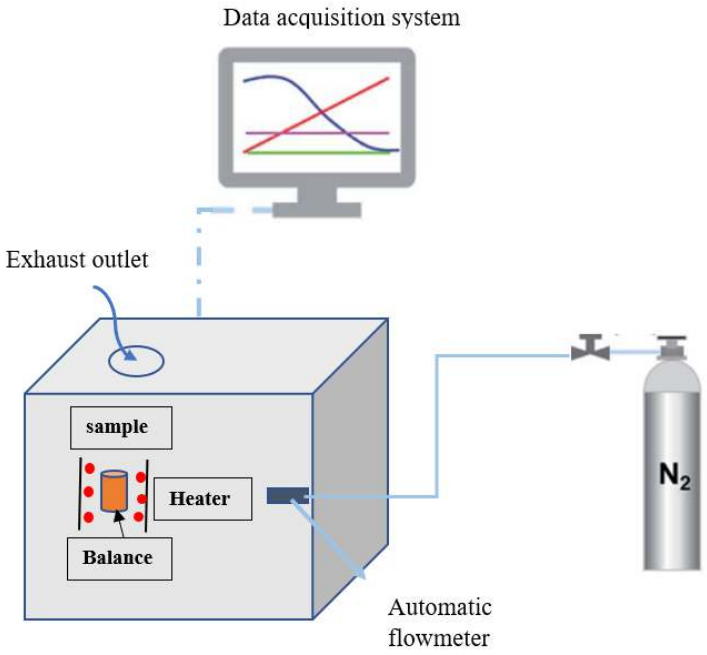

Figure. 3. 6. Thermogravimetric analysis process

III. Results and discussion

III.1. Aspect of oil samples and ceramic ball after heat treatment

The different oils samples and ceramic balls were photographed and present in figure. 3. 6. Regarding the oil samples, there is colour degradation turning to black after the third month. This colour change may be explained by the long-time heat treatment at 210°C driving to the decomposition of peroxide. The residues resulting from these decompositions have settled to the bottom of class centenaries and could they be polymers. However, the change in colour should not affect the HTF quality. It may be a qualitative parameter of the oil deterioration state or due to metallic oxides migrating from ceramic ball (TESM) to oil (HTF)[160]

For the ceramic balls, there structure did not change anymore after the three months according to macroscopically observation. Also, the balls have not softened or crushed. This well holding of the ceramic can be explained by their porosity[11], oil wicked into the pellets, but this did not seem to affect them. Apart from oil residues, there were not production of any other fine particles of material from ceramic pellets.

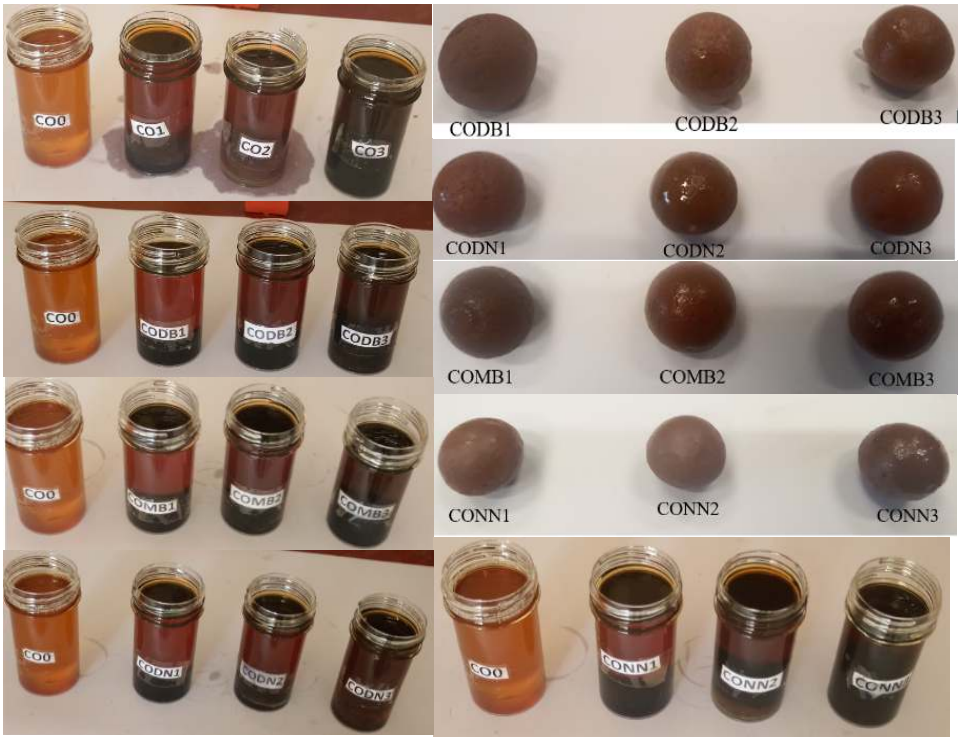

Figure. 3. 7. Oil and ceramic balls before or after heat treatment. Co is crude oil, the number 0, 1, 2, 3 indicate the reference oil and the oil after the first, second and third month. The same labelling

was used for the oil and ceramic put in contact: Oil with dune sand ceramic from Burkina (CODB), Niger (CODN), mining sand from Burkina Faso (COMB), Nature sand from Niger (CONN).

III.2. Effect of heat treatment on JCCO chemical properties

III.2.1. Acid index

Potentiometric titration analysis enables to assess the acid index with uncertainties of 5.03%. The figure. 3. 7 presents the different results. The total acid value increases respectively 54.38%, 39.68%, 41.72%, 40.73%, 40.42% as illustrated in table. 3 for the oil aged alone, the one put in contact with Dune and mining sand from Burkina and dune and natural sand from Niger after the third month compared to reference crude oil (CO0). However, all the oil samples have an acid index lower than the critical value (25 mg. $KOH.g^{-1}$) [160].

Table 3. 3.The reference and 2160 h acid index for the different oil samples.

Oil and ceramic ball	Reference acidity (mg $KOHg^{-1}$)	Acidity (mg $KOHg^{-1}$) after 2160h	Increasing percentage after 2160h
Oil aged alone (CO)	8.8460	13.657	54.38%,
Oil in contact with Burkina dune sand (CODB)	8.8467	12.355	39.68%,
Oil in contact with Burkina mining sand (COMB	8.846	12.537	41.72%,
Oil in contact with Niger dune sand (CODN)	8.846	12.449	40.73%,
Oil in contact with Niger natural sand (CONN)	8.846	12.422	40.42%

The acid value of oil put in contact with ceramic ball is less than the one aged alone. Regarding the overall results obtained, the increasing of the acidy results from the combined action of peroxide thermal decomposition, hydrolysis reactions and thermal oxidation [63] and [176]. However, these actions on JCOO under heat treatment could be low in presence of ceramic balls. Compare to the results found by Hoffmann et al., acid value increase quickly with the other vegetal oils in contact with filler material than refine jatropha curcas oil [49] and [160]. It can be assumed that jatropha oil would be more compatible with filler materials despite its high acid value.

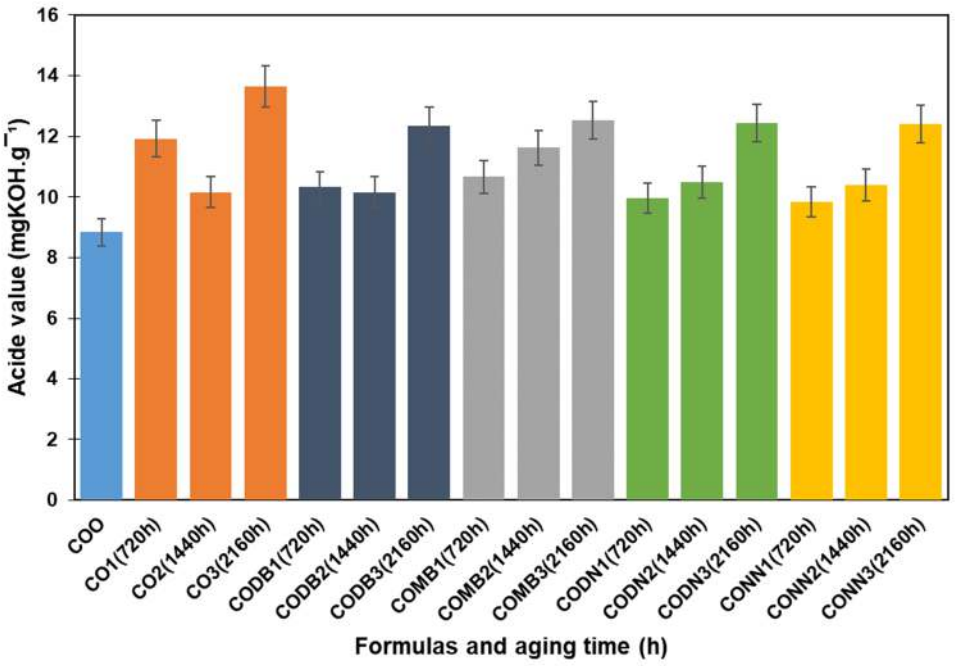

Figure. 3. 8. Acidity of the JaCCO aged with or without different type of ceramic balls.

III.2.2. Peroxide value

The peroxide value has been also assessed using potentiometric titration with uncertainties of 8.26%. The figure. 3. 8 present the results of PV obtained each month. A decrease of PV is observed for all the samples. This drop of PV is due to its thermal decomposition at high temperature and the absence of air leader of oil oxidation [178]. This decrease is about 90.61%,75.80%,86.82%,89.04% and 86.64% respectively for CO2, CODB2, COMB2, CODN2 and CONN2 compared to the reference new oil. These results are similar to the results found in the literature [63]. The degradation of PV value could be explained by Peroxide decomposition to volatile and non-volatile products and the absence of air in the different reactors [179]. The peroxide decomposition drives to oil colour change and the increase of kinematic viscosity due to continuous heating. It is observed that, the decomposition rate is different from a sample to another. The highest rate is obtained with the oil aged alone and the lowest with the oil in contact with ceramic developed with dune sand from Burkina Faso (CODB2). The ceramic balls reduce the destruction of peroxide. As the ceramic is porous, air in the pores of ceramic could contribute to

the oxidation of oils. The difference in porosity could explain the difference in peroxide decomposition of oil in contact of ceramic balls.

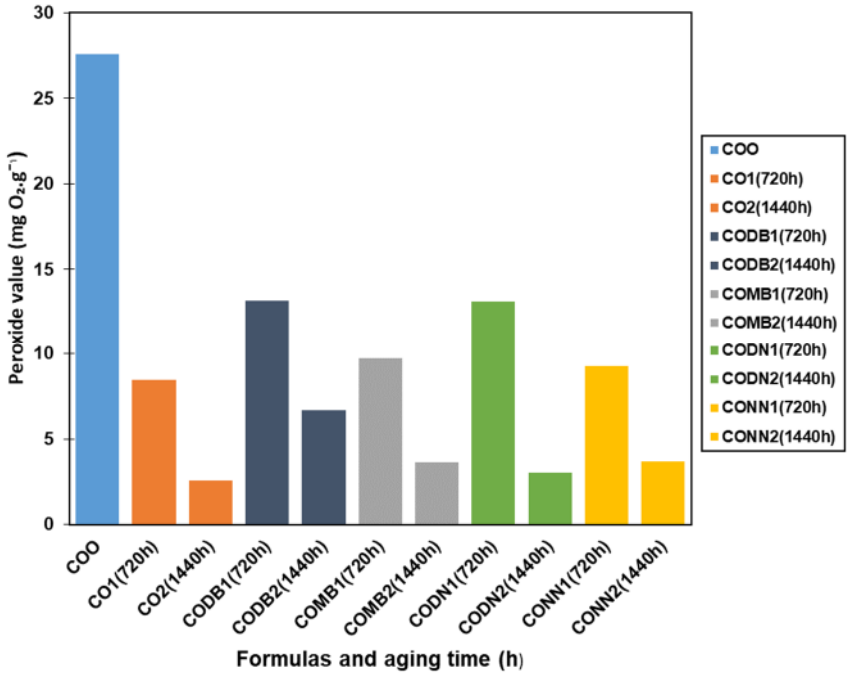

Figure. 3. 9. Peroxide value of JaCCO aged with or without different type of ceramic balls.

III.3. Effect of heat treatment on JCCO thermal properties

III.3.1. Density

The density of the different aging oil measured at room temperature is plotted in figure. 3. 9. The density values of the different samples measured range from 901.23 $kg.m^{-3}$ to 905.4 $kg.m^{-3}$ with uncertainty of ±2.25%. The density variation is low and shows a slightly decreasing in density of 2.7 kgm^{-3}, and 2.97 $kg.m^{-3}$ than new oil respectively for the oil aged alone and the one put in contact with Niger dune and natural sand ceramic ball. However, after 740 h (1 month) a slightly increasing in density of 1.53 kgm^{-3} and 1.26 $kg.m^{-3}$ than the one-month aged oil was observed for the oil put in contact respectively with Burkina dune and mining sand ceramic balls after decreasing of 2.07 $kg.m^{-3}$ and 2 $kg.m^{-3}$ respectively. From the second month the dune and mining sand ceramic balls could release suspended solid particles in the fluid. Thus, taking into count the measuring error (±2.25%), no sensible modification of density with ageing or contact with TESM at 210 °C and during 2160 h. Therefore, the aging effect on the oil is negligible.

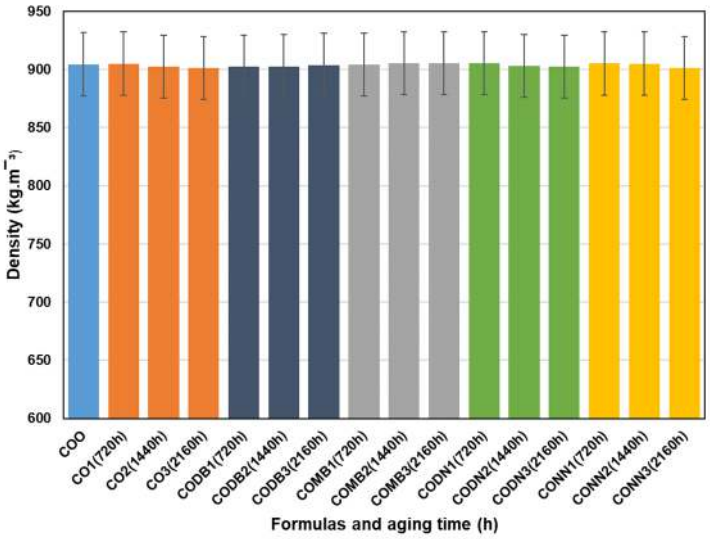

Figure. 3. 10. Density of JaCCO aged with or without different type of ceramic balls.

III.3.2. Thermal conductivity

Figure. 3. 10 represents the evolution with aging time of the thermal conductivity of the jatropha curcas crude oil (JCCO) samples that have been aged with or without ceramic balls. The maximum measurement relative error was ±6%. A slight increase of the JCCO thermal conductivity is observed with the oil samples aged alone and the one put in contact with balls. JCCO sees its thermal conductivity increase to 0.8% and 3.125%, 1.875% respectively for the one aged alone and the one put in contact with mining sand and natural sand ceramic balls after 2160h. The inverse is observed with decreasing of 1.25% for the JCCO put in contact with Niger sand ceramic ball. All these variations are less than the uncertainties. Considering these uncertainties and the accuracy of the device (10%), it seems that the oil deterioration does not significantly affect oil thermal conductivity for compatibility tests with the developed TESM at 210 °C and during 2160h.

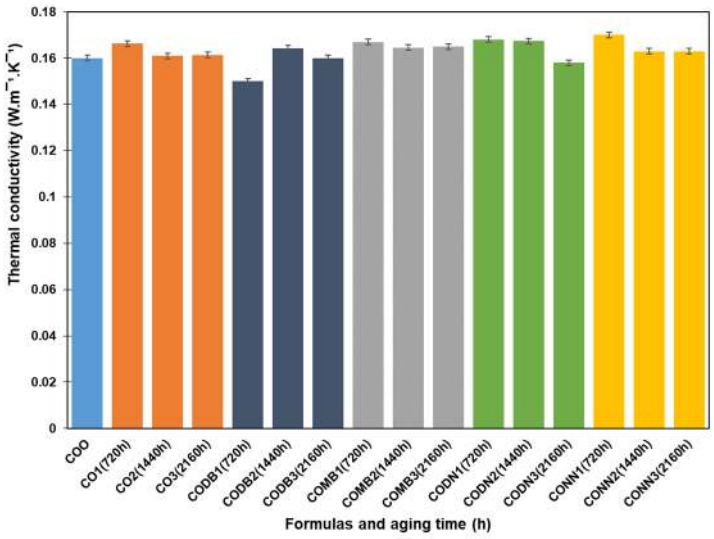

Figure. 3. 11. Thermal conductivity of JaCCO aged with or without different type of ceramic balls.

III.3.3. Kinematic viscosity

The table 3. 10 shows the kinematic viscosity of the different oil sample at 40°C and 100°C. As this parameter on temperature, the constant A and B were computed and used to predict the kinematic viscosity at temperature up to 210°C using equation (3. 4). The profile of the overall oil sample as a function of temperature are presented in figure. 3. 11. The viscosity remained stable after 2160h of thermal treatment at 210°C. After three months, only the maximal kinematic viscosity is 2.83mm^2/s which is closed to the one of reference oil (mm^2/s). However, an increase of 54.4% ,50.8%, 48.35%, 47%, 47, 34% (table. 4) respectively for the oil aged alone or aged with Burkina dune (D40A30C1.30-B) and mining (M40A30C1.30-B) sand ceramic balls, Niger dune (D40A30C1.30-N) and natural (N40A30C1.30-N) sand ceramic balls was observed with the different oil sample.

Table 3. 4. The reference and 2160 h kinematic viscosity for the different oil samples.

Oil and ceramic ball	Reference oil kinematic viscosity (mm.s^{-1})	Kinematic viscosity (mm.s^{-1}) after 2160h	Increasing percentage after 2160h
Oil aged alone (CO)	33.94	52.4	54.4%
Oil in contact with Burkina dune sand (CODB)	33.94	51.18	50.8%,
Oil in contact with Burkina mining sand (COMB	33.94	50.35	48.35%,
Oil in contact with Niger dune sand (CODN)	33.94	49.89	47%

Oil in contact with Niger natural sand (CONN)	33.94	50.01	47, 34%

The viscosity of the oil aged alone is higher than the one put in contact with TESM after 2160h. This increase is the consequence of vegetable oil polymerization by thermal oxidation [63] due to peroxide degradation leading to polymeric material. The presence of TESM mitigates the increase of the viscosity making it more stable than the viscosity of the one aged alone.

Table 3. 5. Kinematic viscosity of the different JCCO and the constant A and B values to correlate the kinematic viscosity as function of temperature ($A \times T^B$) in $mm.s^{-2}$.

Oil samples	40°C	100°C	constant B	constant A
CO0 (reference oil)	33.94	7.574	-1.63689632	14227.15123
CO1(720)	44.44	8.898	-1.75524359	28825.68116
CO2 (1440)	42.23	8.778	-1.71439285	23560.32479
CO3(2160h)	52.4	10.34	-1.77114825	36042.67618
CODB1(720h)	45.28	9.009	-1.76214961	30128.38191
CODB2(1440h)	46.75	8.898	-1.81054731	37186.64769
CODB3(2160h)	51.18	10.34	-1.74543833	32018.22055
COMB1(720h)	41.39	8.135	-1.7754884	28929.06228
COMB2(1440h)	44.61	8.824	-1.76852467	30388.89062
COMB3(2160)	50.35	9.783	-1.78802685	36857.49026
CODN1(720h)	40.89	8.41	-1.72594135	23805.57581
CODN2(1440)	43.82	8.896	-1.74015576	26884.76831
CODN3(2160h)	49.89	9.966	-1.7577841	32665.48332
CONN1(720h)	39	7.983	-1.73116164	23146.71732
CONN2(1440h)	44.24	8.775	-1.76551233	29803.81036
CONN3(2160h)	50.01	9.97	-1.75996804	33008.91383

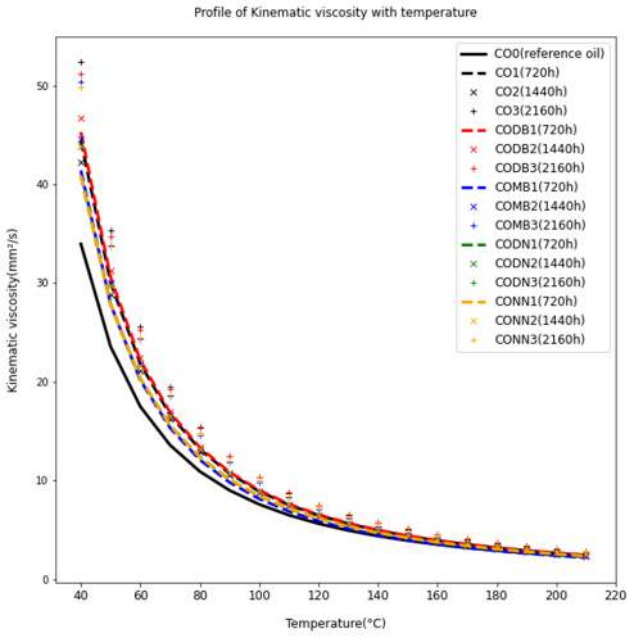

Figure. 3. 12. Kinematic viscosity of the oil aged with or without different type of ceramic balls.

III.4. Effect of heat treatment on JCCO thermal stability

III.4.1 Flash point

After the 2160h of heat treatment the flash point of the oil aged with or without TESM remain stable around 220°C because no flash was observed at 210°C (The maximum calibration temperature of the device) for all the samples. This is highlighting that there is no degradation at this temperature level. Using the same method (static method) of heat treatment, similar results was found in [113]. To confirm the stability of the overall oil samples, the oil aged alone and the one put in contact with Burkina dune sand ceramic which had the highest kinematic viscosity after three months thermogravimetric analysis (TGA) was conducted.

III.4.2. Thermogravimetric analysis

Figure. 3. 12 and Figure. 3. 13 show the non-isothermal thermogravimetric (TG) and derivative thermogravimetric (DTG) analysis of JCCO aged with or without TESM under nitrogen (N2) environment up to 500°C. A significant degradation peak is observed between 421.36°C and 427.61°C on the DTG curve (figure. 3.12) depending on the oil. In the same range of temperature, the TGA (figure. 3.12) curve shows a mass loss of around 70% for the overall sample. This can be attributed to the thermal decomposition of fatty acid (up to 90%) in JCCO which could occurred from 280°C [180]. However, the curves show a thermal stability of JCCO up to a temperature of

287.1 °C and 261.93°C respectively for the reference oil and the one aged with or without TESM for three months. After three months CO3 has a thermal stability temperature of 261.93°C against 263.41°C for CODB3 (2160h) at 3% of oil mass loss. As demonstrated previously, the TESM mitigates the degradation of JCCO thermal stability. As the ceramic ball is made from sand, these ball could release some sand particle in the oil which could improve the thermal stability of JCCO as demonstrated in [181] where 2 wt.% of sand increase the thermal stability temperature of molten salt from 682°C to 694°C.

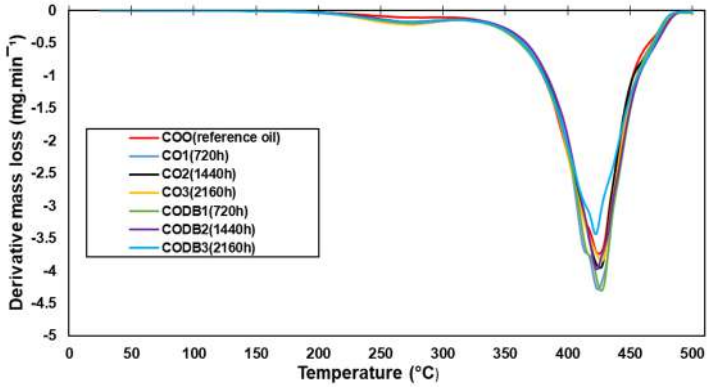

Figure. 3. 13. DTA profile of the different JaCCO aged with or without different type of ceramic balls

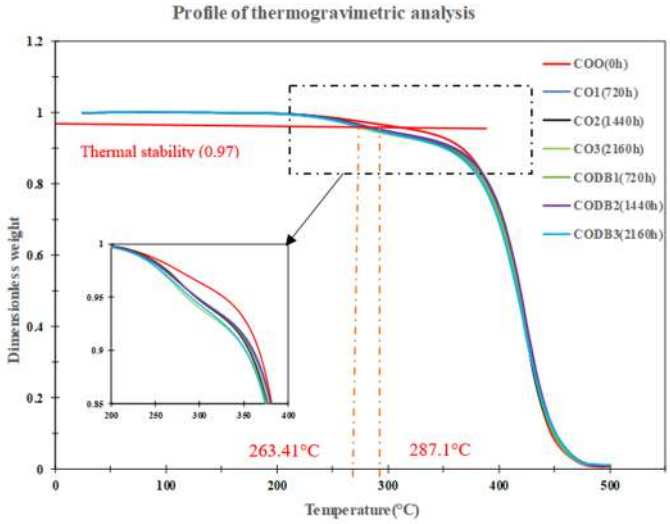

Figure. 3. 14. TGA profile of the different JaCCO aged with or without different type of Ceramic balls.

III.5. Comparative thermal stability study of JCCO and RJCO in contact with the ceramic balls

Figure. 3. 14 illustrate the profile of TGA and DTG of JCCO and JCRO in contact with ceramic balls for 2 months (1440h). The result show that for the new oils the JCCO has thermal stability temperature of 281.1°C against 261.1°C for JCRO. The low thermal stability of refine oil is explained by the refined process. During the refined process, vegetable oil is put under heat treatment. To eliminate the free fatty acid, the first process after extraction is the neutralization process, which consists of mixing the degummed oil with potassium hydroxide (KOH) aqueous solution to eliminate the free fatty acid. The degumming process consists of removing the phosphorus-based compounds, mainly lecithin and cephalin from the fresh oil. The removed substance was called "gums.". During this process the oil is heated to 55-60 °C after adding a de-ionized water. After neutralization the neutralized oil is washed with the de-ionized water (second step). To separate oil and water, decantation can be used at small scall, otherwise centrifuge is requested. The last step of oil refining is to remove waxes to avoid cloud forming. During this process 5% of NaOH and 5% of deionized water have to be mixed with the neutralized oil and placed in a chiller setting at 5^{o}C during 4 hours [182]. All these process have low effect on thermophysical properties but could impact highly the melting point as discussed in [183]. As the melting point decreasing during refining process, it may also decrease the thermal stability temperature as observed in this study. In contact with ceramic ball, a continuous decreasing of the thermal stability temperature has been observed with JCCO during the two months (Figure. 3.15), while for the JCRO the thermal stability temperature become better than the reference oil after being dropped to 253.45°C, it has raised up to 262.39. As mentioned previously, the ceramic ball used in the JCRO reactor may release more sand particles in the JCRO which have increased more its thermal stability compare to the one of JCCO. Also, JCRO could be more mitigated by the ceramic balls compare to JCCO. After 720 h in contact with ceramic a drop of 18°C and 7.65 for JCCO and JCRO respectively. However, after 1440 h this drop was very low for JCCO and always higher than the one of JCRO even if it has increased.

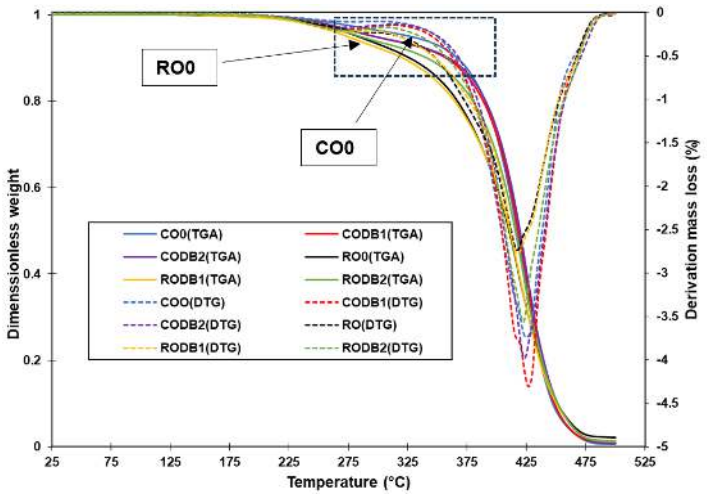

Figure. 3. 15. ATG and DTG profile of JCCO and JCRO in contact with ceramic ball during 1440h

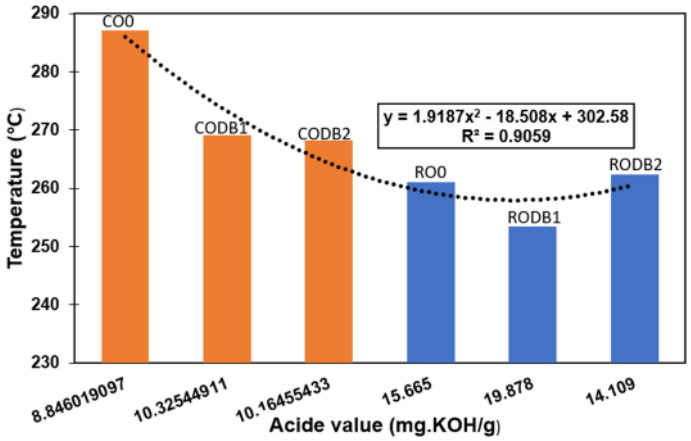

Figure. 3. 16. Thermal stability temperature (°C) of JCCO and JCRO under heat treatment in contact with ceramic balls.

This study showed that JCCO have better thermal stability and cost effectiveness than JCRO. However, the refining process provides a clean oil which could reduce the corrosion effect on filler material as illustrated on Figure. 3. 16

Figure. 3. 17. Aspect of JCRO (a) and ceramic balls (c) before or after heat treatment.

Conclusion

The present compatibility study evaluates the behaviour of several JaCCO with temperature and put in contact with potential solid filler materials due to its good thermal stability. Jotropha curcas crude oil has been aged during a period of 2160 h and at 210 °C in contact with ceramic balls made with clay coal bottom ash and various sand (dune sand, mining sand and natural sand). From the compatibility study between the oil and the ceramic balls, three conclusions can be done:

- The thermal properties (density, thermal conductivity, and Kinematic viscosity) of the oil are not significantly modified by ageing and contact with solids.
- The oil flash point remains higher than 220 °C. However, the oil thermal stability temperature decreases with ageing time with low decrease for the one in contact with filler materials. In addition, no solid has been crushed for the testing period.
- This result may help to evaluate the quality of the heat transfer fluid when used in a concentrated solar power plant. Measurement of the index of acidity informs about the possible partial replacement of the oil to avoid any risk of fire. An index of acidity higher than 25 mg KOH.g−1 corresponds to a thermal stability lower than 300 °C [168]. Therefore, during the study period the maximum acid value was 13.657 mg KOH.g−1 and 12.355mg KOH.g−1 respectively for the oils aged alone and the one in contact with the filler material.
- The comparative study between JCCO and JCRO in contact with ceramic balls show that JCCO have better thermal stability than JCRO.

Numerous solutions are available worldwide to provide an efficient, cost-effective and environmental-friendly thermal energy storage system. This study confirms that natural products and industry wastes could be estimate as resources for the future of energy. However, there is still a need for process investigations like the structure and chemical composition analysis of ceramic balls. In addition, to perform the process a thermocline energy storage system should be designed for heating and cooling (thermal cycles) behaviour assessment.

Chapter 4: Modelling of a thermocline energy storage system using JCCO as HTF and TESM and ceramic balls as filler material

Introduction

DMT system are expected to be a better option compare to the conventional two tank TES due to its capability to reduce CSP cost of about 33% to 35%. Thats involves removing one reservoir from the two tank storage system and using eco-materials such as natural rock and industrial waste as filler materials in a single reservoir [68]. An effective cost analysis of the new DMT system using ceramic balls made from sand, clay and CBA and JCO as storage medium is important before any investment is made. Before that, it is crucial to know the performance of the system to facilitate decision regarding the development of the new TES. In the literature there is no data on DMT systems using ceramic and JCO as storage medium and JCO as HTF. However, DMT system data using rapeseed oil and quartzite or molten salt and quartzite are available in [86] and [184]. In addition the thermal properties data of JCO as function of temperature are available in [159]. In this chapter the main question to answer is: What is the thermal performance (storage efficiencies, thermocline thickness) or behavior (temperature profile, the discharge time) of a DMT system using the couple ceramic ball and JCO as storage medium and JCO as HTF?

To answer this question, a model will be first descripted. And after the validation of the model the sensitivity analysis or performance analysis of $2MWh_{th}$ storage system will be carried out, followed by the sizing and behavior analysis of a storage system capable of generating 2 MW_{el} of electricity using an organic Rankine cycle (ORC).

I. Model Description

I.1. Working principle

The aim of this thesis is to achieve an effective thermal energy storage efficiency based on the concept of DMT. The working principle of a DMT energy storage system integrated in a CSP plant can be describe as illustrated in Figure. 4.1. During the day and the charging time the cool fluid leave the tank from the bottom, go to the solar field. The solar collector heats up the fluid. And the hot fluid flow back in the tank. As the fluid and solid are in contact, the heat is directly exchange with the solid and the whole system is heated up after several cycles. During cloud time or the night, the heat is discharge to continuous electricity generation. The hot fluid leaves the tank to the

boiler where it exchanges heat with the working fluid and returns cooled in the tank to start a new discharging cycle. The heat is used to produce steam at high pressure to run turbine for electricity generation. This chapter thus aims to assess the thermal performances and behaviour of the new storage system under thermal cycling.

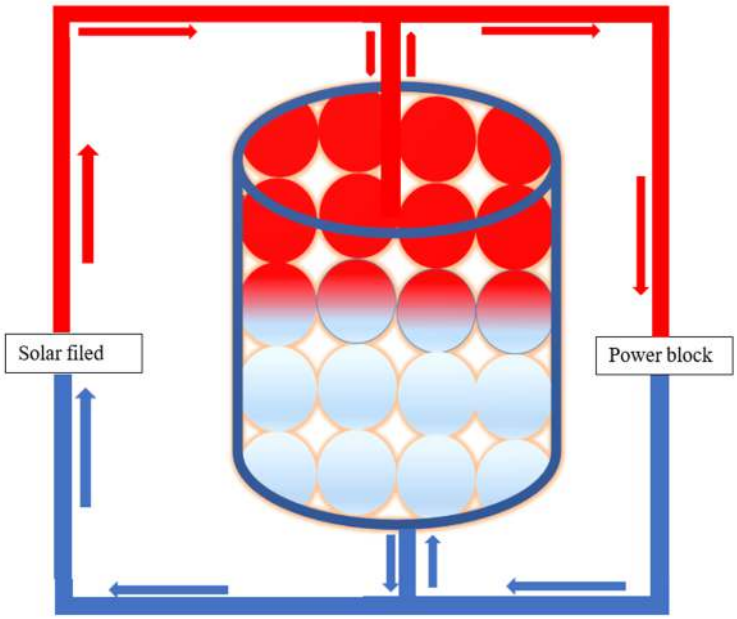

Figure. 4. 1. Working principle of DMT.

I.2. Model description

Different numerical models are often used to assess the performance of storage systems. Most of these models have been developed based on the Schuman model since 1929 [14] depending on assumptions and the number of dimensions as described in the first chapter. Depending on whether a notable heat gradient inside the solids is taken into account, there are two main groups. Then, differentiation can be made according to the number of phases (fluid, solid, walls) accounted for or the number of dimensions (1D or 2D) [107] and [125]. These models are all designed to either improve experimental result prediction or decrease calculation time. One-dimension 1D-2P without conduction and 1D-2P models are two examples of models that calculate more quickly than the 2 D-1phase model. The last two model give better results accounting for the overall heat exchange between solids and fluids and for increasing conduction resistance inside solids [107]. In this study we assessed the performance of the ceramic ball –JCO packed bed TES system using

the 1D-2P model because that model can predict the TES behaviour (temperature profiles) with better accuracy compare to 2D models [49][107] which required longer computation time.

In literature, vegetable oil like rapeseed oil and quarzitic thermocline systems have been numerical analysed and implemented [86]. The thermal stability of Jatropha curcas has been evaluated in numerous investigations. Up to now, we did not see any study addressing the thermal performance assessment or thermocline storage experimental setup. In this study, a new TESM has been developed and has undergone 2160 hours (90 days) within JCCO without any crush and without enough degradation of the oil. To sensitivity analysis, the effect of the different parameters like fluid velocity, particle diameter, tank porosity and volumetric heat capacity on the new storage system performance must be access. The TES model is illustrated in Figure. 4.2. The TES cross-section (Figure. 4.2) shows the ball inside the tank, the insulation thickness, the internal (D_{wext}) and external ($D_{w,int}$) diameters and the tank height. The different heat transfer modes which occur inside and around the TES are illustrated in Figure. 4.3.

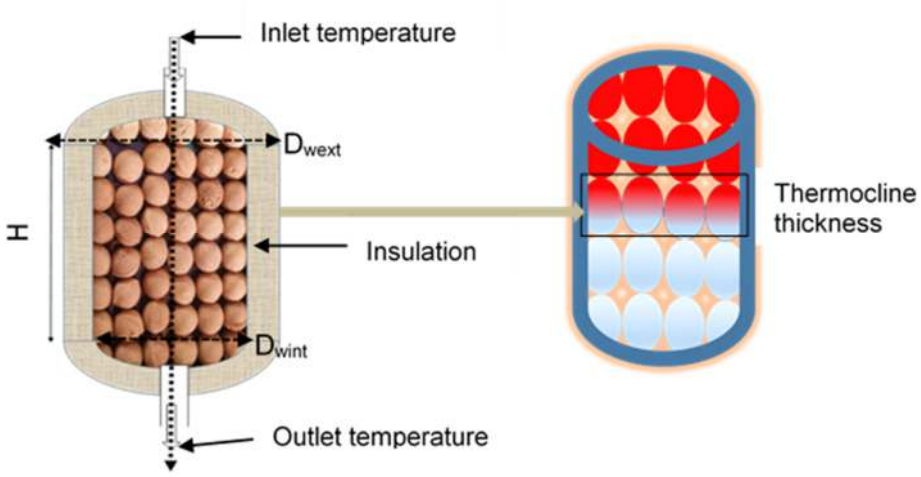

Figure. 4. 2. Ceramic balls and JCCO thermal energy storage model.

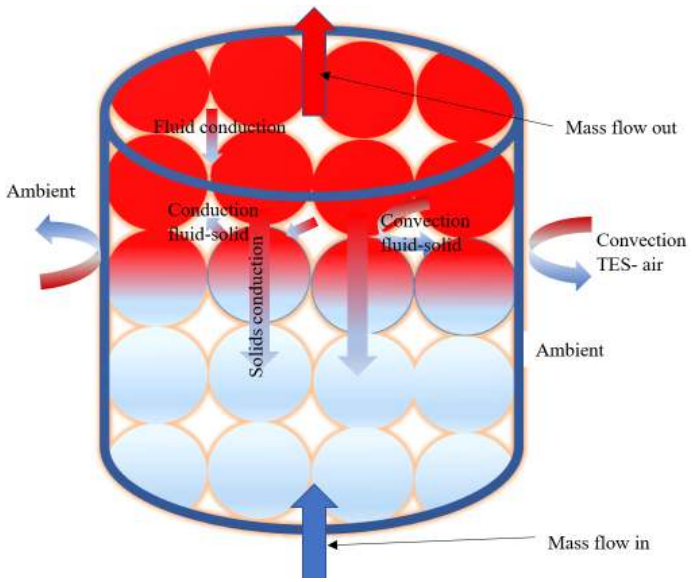

Figure. 4. 3. The different phenomena impacting the performance of the storage.

I.3. Mathematical model

The energy balance or conservation describing the system can be write as follow:

For the liquid phase, the energy balance can be written by equation (4. 1) [86] and [185] :

$$\dot{Q}_{store,f} + \dot{Q}_{adv,f} = \dot{Q}_{diff,f} + \dot{Q}_{conv,f\to p} + \dot{Q}_{losses,amb} \quad (4.\ 1)$$

$\dot{Q}_{store,f}$ is the quantity of heat stored in the oil within the TES system can be expressed in equation (4. 2)

$$\dot{Q}_{store,f} = \varepsilon(\rho c_p)_f(\frac{\partial T_f}{\partial t}) . \quad (4.\ 2)$$

$\dot{Q}_{adv,f}$ is the advection flow of the oil within the TES system which transports the fluid substance and heat (energy) by bulk motion and can be expressed in equation (4. 3).

$$\dot{Q}_{adv,f} = \varepsilon(\rho c_p)_f \mathrm{u}\frac{\partial T_f}{\partial z} \quad (4.\ 3)$$

$\dot{Q}_{diff,f}$ is the thermal diffusion flux within the fluid in the TES system and is expressed in equation (4,4)

$$\dot{Q}_{diff,f} = \lambda_{feff}[\frac{\partial^2 T_f}{\partial z^2}] \ . \quad (4.\ 4)$$

$\dot{Q}_{conv,f\to p}$ is the convection flow between the fluid and the particle expressed in equation (4. 5)

$$\dot{Q}_{conv,f\to p} = h_v\left(T_p - T_f\right) . \quad (4.\ 5)$$

The energy balance for the fluid become

$$\varepsilon(\rho c_p)_f(\frac{\partial T_f}{\partial t}+u\frac{\partial T_f}{\partial z})=\lambda_{feff}[\frac{\partial^2 T_f}{\partial z^2}]+h_v(T_p-T_f)+\frac{U_W}{V_{total}}(T_{ext}-T_f). \quad (4.\ 6)$$

For the solid phase energy balance is expressed in equation (4. 7) [86] and [185].

$$\dot{Q}_{store,p}+\dot{Q}_{adv,p}=\dot{Q}_{diff,p}+\dot{Q}_{conv,p\to f} \quad (4.\ 7)$$

$\dot{Q}_{store,p}$ is the quantity of heat stored in the particle and expressed in equation (4. 8).

$$\dot{Q}_{store,p}=\lambda_{peff}[\frac{\partial^2 T_p}{\partial z^2}]\ . \quad (4.\ 8)$$

$\dot{Q}_{conv,p\to f}$ is the convection flow between the particle and the fluid written in equation (4. 9)

$$\dot{Q}_{conv,f\to p}=h_v(T_f-T_p) \quad (4.\ 9)$$

The energy balance for the particle becomes:

$$(1-\varepsilon)(\rho c_p)_p(\frac{\partial T_p}{\partial t})=\lambda_{peff}\frac{\partial^2 T_p}{\partial z^2}+h_v(T_f-T_p)\ . \quad (4.\ 10)$$

Where T_f is the fluid temperature, T_p the filler material or particle temperature, ε the tank porosity, ρ the density, c_p the specific heat capacity, f for the fluid, p for the solid, λ_{eff} the effective thermal conductivity, h_v Interstitial heat transfer coefficient, U_W is the heat loss coefficient.

Thes equations for the energy balance were obtained after taking into account the following assumption:

- Fluid velocity and temperature distribution is only in axial direction.

$$\vec{u}_r=\overrightarrow{0},\ \ \frac{\partial T}{\partial r}=0 \quad (4.\ 11)$$

- HTF mass flows through the packed bed in laminar regime
- Particle bed porosity in the tank is homogenous.
- Properties of the solid particle are independent from temperature.
- Inlet temperature and velocity is constant.
- For solid, filler material is spherical with a very small contact surface, so that there is no. heat conduction between particles.
- Heat conduction occur in fluid phase in axial direction.
- The properties of the fluid are computed at the film temperature.
- The pressure is constant in the hole vessel of the tank.

The porosity is an important parameter for packed bed TES performance analysis. The pressure drops across the bed and HTF mass flow are affected by the tank average porosity [186]. The porosity can be affected by the packing mode, the tank diameter, the particle diameter. the particle shape, the particle size distribution, the roughness of the particle surface and also by the bed heigh [187]. The porosity of the new ceramic ball packed bed has been determined using a cylindrical beaker of 1l.

$$\varepsilon = \frac{V_{pores}}{V_{totat}} \quad (4.\ 12)$$

Several models are available in the literature to predict the porosity of a packed bed [187]–[191]. The model of Furnas given in the following equation was the most accurate one to validate the experimental results.

$$\varepsilon = 0.375 + 0.34 \times \frac{d_{particle}}{D_{tank}}. \quad (4.\ 13)$$

With the bed of 1L, diameter of 6.5cm a porosity of 60% has been obtained against 52.56% for the model. Therefore, Furnas correlation can be used to compute accurately the TES system porosity with standard error of 4.671%. These results account also for the ceramic ball porosity.

The velocity of the fluid inside the filler bed is calculated from the density of the fluid, the tanks cross-sectional area and the mass flow rate data as in equation (3. 14).

$$u = \frac{\dot{m}}{\rho_f \times (\varepsilon\pi\left(\frac{D}{2}\right)^2)} \quad . \quad (4.\ 14)$$

The key thermo-physical properties use to estimate the heat transfer inside the packed bed system are the effective thermal conductivities of HTF and solid fillers, respectively $\lambda_{f,eff}$ and $\lambda_{p,eff}$. The various effective thermal conductivities models that have been set up over the past years and are presented in [192]. In this work the effective thermal conductivity equation (3. 15) is considered to study the impact of different effective thermal conductivities.

$$\lambda_{feff} = \varepsilon \times \lambda_f, \lambda_{peff} = (1 - \varepsilon) \times \lambda_p \quad . \quad (4.\ 15)$$

The interstitial heat transfer coefficient between HTF and solid fillers, hv, and the effective thermal conductivities of HTF are of great importance for the developing process of thermocline

region [44]. Several correlation for hv, exists, depending on flow type and if the fluid is incompressible or not[192],[193] and [194]. Some of these correlations were tested by Xu et al., in 2011 [192]. In this study, a laminar flow is considered and the interstitial heat transfer coefficient between particle and HTF h_v is calculated using equation (4. 16)

$$h_v = \frac{6(1-\varepsilon)k_f(2+1.1\times {Re_p}^{0.6} Pr^{\frac{1}{3}})}{{d_p}^2} \quad (4.\ 16)$$

U_w is the global heat transfer coefficient for the evaluating thermal losses to the environment W/K

$$U_w = \frac{1}{R_{th}} \quad (4.\ 17)$$

The rank wall thermal resistance can be computed using equation (4. 18)

$$R_{th} = \frac{1}{h_{ext}\times A_{w,ext}} = \frac{\ln(\frac{r_{w,ext}}{r_{w,int}})}{2\times\pi\lambda_{insul}\times H} + \frac{1}{h_{air}\times A_{wext}} \quad (4.\ 18)$$

Where h_{ext} is the heat exchange coefficient with ambient, $A_{w,ext}$ the external surface of the tank, λ_{insul} the thermal conductivity of the insulation, H the tank height, $r_{w,ext}$ the external radius of the tank $r_{w,in}$ the internal radius of the tan and h_{air} the heat exchange coefficient of air

I.4. Boundary and initial conditions

Initial conditions of discharge are given in equation (4. 19)

$$T_f(t=0) = T_p = T_{exp}(t=0) \quad (4.\ 19)$$

Since the numerical model consider one dimensional media, the boundary conditions during a discharge considers only one on the top and one on bottom of the tank. The hot heat transfer fluid exits the tank at the top and flows towards the boiler where it is discharged. The cooled fluid leaves the boiler and heads for the tank, where it re-enters at the bottom. This means an inlet temperature and velocity for the fluid conditions and an adiabatic condition for the solid and the wall. On the bottom:

$$T_f(z=0) = T_L \quad (4.\ 20)$$

$$\frac{\partial T_f}{\partial z}(z=0) = \frac{\partial T_p}{\partial z}(z=0) = 0 \quad (4.\ 21)$$

Hot heat transfer fluid leaves the tank, an adiabatic condition for the solid and for the fluid occurred at the top of the tank.

$$\frac{\partial T_f}{\partial z}(z = H) = \frac{\partial T_p}{\partial z}(z = H) = 0 \quad (4.\ 22)$$

II. Numerical method

The difference finite method was used to numerically discretised different equations. For the first order derivative term, an implicit scheme was employed, for time discretization, the central differencing scheme was utilized, and for the second order derivative terms, the backward differencing scheme. Partial differential equations (PDEs) of 1D systems and issues can be easily solved with finite difference methods (FDMs), which are accurate, stable, fast convergent, and straightforward [195]. Especially when using Gauss-Seidel method for solving. An iterative method based on the Gauss-Seidel computational method was used to find the answer, which involved computing one or two temperature vectors (particle and fluid) simultaneously for each time step. Equations (4. 23) - (4. 25) provide examples of the discretization techniques.

$$\frac{\partial^2 \mathrm{T}}{\partial z^2} = \frac{T_{i+1}^{N+1} - 2 \times T_i^{N+1} + T_{i+1}^{N+1}}{\Delta z^2} \quad (4.\ 23)$$

$$\frac{\partial T}{\partial z} = \frac{T_i^{n+1} - T_{i-1}^{n+1}}{\Delta z} \quad (4.\ 24)$$

$$\frac{\partial \mathrm{T}}{\partial t} = \frac{T_i^{n+1} - T_i^{n}}{\Delta t} \quad (4.\ 25)$$

The convergence criterion was 10^{-3} and is illustrated on the flowchart for a loop (figure.4.4). However, the system divergent can be predicted using Courant-Friedrichs-Lewis coefficient which can be assessed using equation (4. 26) [49]

$$\mathrm{C}=u\frac{\Delta t}{\Delta z}. \quad (4.\ 26)$$

To simplify the model and reduce the computational time, the fluid properties was computed at the mean temperature. The numerical model was coded using an open access software FORTRAN force 2 for computation.

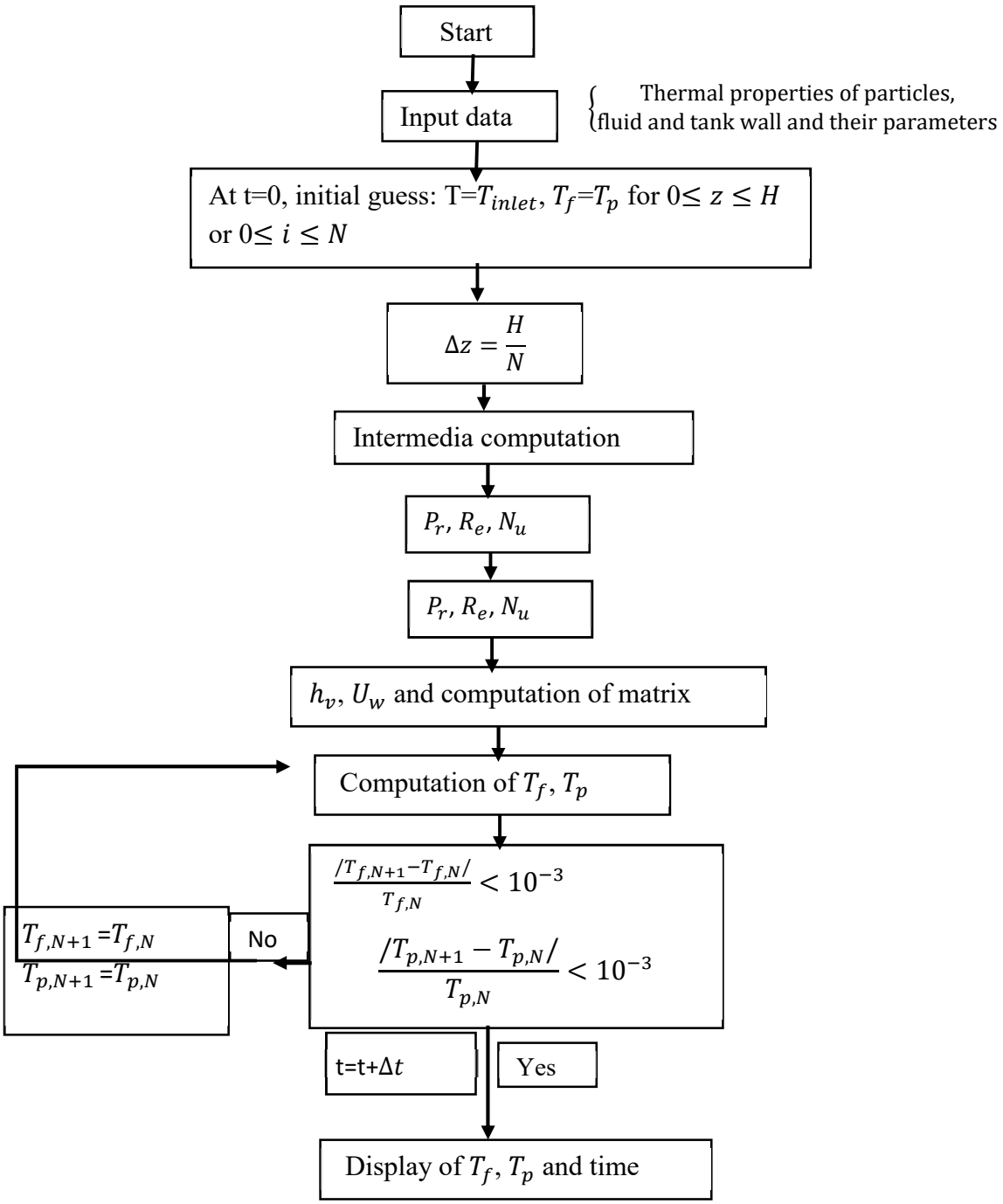

Figure. 4. 4. Flowchart use during the computation process for a loop.

Figure. 4. 5 illustrates the data collection process during experimentation. The black dots show the location of the thermocouples. The temperatures along the tank axial are collected at each time step and recording by the data acquisition system.

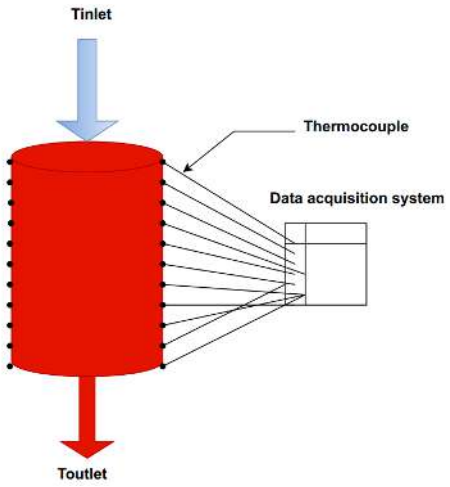

Figure. 4. 5. Overview of TES data collection process during a discharge time.

III. Results and discussion

III.1. Model validation

To assess the ability of the 1D-2P model to provide reasonable predictions of the model described above, we compare with experimental results. The numerical results are validated using the experimental results of Hoffmann et al., [49][86] and Pacheco et al.,[184] [11] based on lab scale 8.3kWh$_{th}$ packed bed quartzite rapeseed oil TES and 2.3 MWh_{th} pilot scale packed-bed molten salt thermocline storage systems [11], [86]. Figure. 4. 6 and Figure. 4. 7 show the axial temperature profiles of the rapeseed oil and molten salt in storage tanks of the experimental and numerical results and table. 1 and table. 2 the model uncertainties. For the both thermal energy storage systems rapeseed oil-quartzite and molten salt-quartzite, the thermocline is well illustrated after the 0.5h. The cold fluid (at 160 °C and 290°C respectively for the oil and molten salt TES) occurs at the bottom and the hot fluid (210°C and 400°C) at the top during the discharging process. When the energy stored in the particle (quartzite) is not enough to keep the outlet temperature at the maximum temperature, it starts reducing after 1h and 1.5h respectively for rapeseed oil and molten salt.

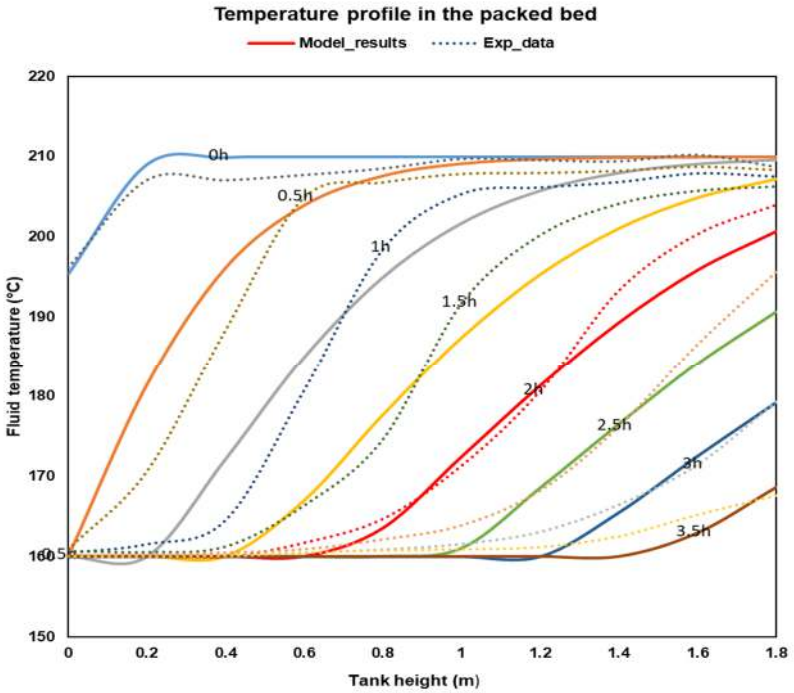

Figure. 4. 6. Temperature profile for the model and experimental results for the 8.3kWhth TES during the discharge process from 0 to 3.5 h using rapeseed oil and quartzite as storage material.

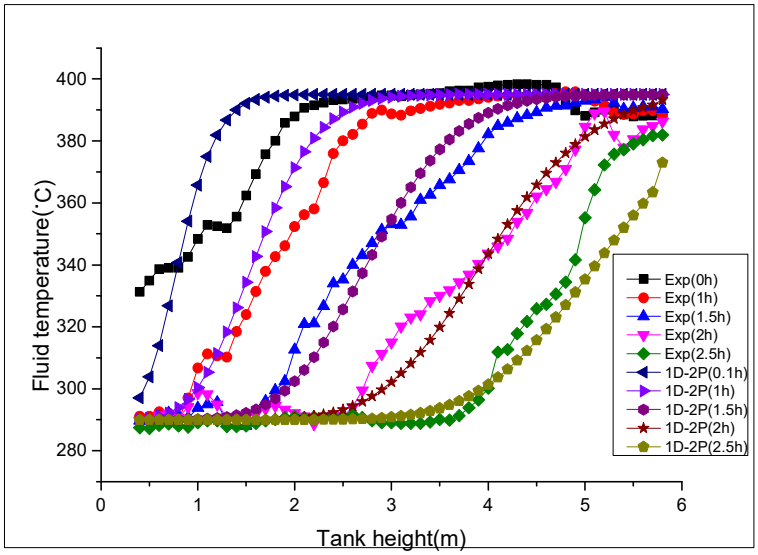

Figure. 4. 7. Temperature profile for the model and experimental results for the 2.3MWhth TES during the discharge process from 0 to 2 h using molten salt and quartzite as storage material.

The model error (relative error) is computed using the f equations (4. 27) and (4. 28) [49].

$$\text{Rmse}=\frac{1}{n}\times\sum\left(\frac{T_{exp}-T}{T_{exp}}\right)^2 \qquad (4.\ 27)$$

$$\text{Relative error}=\frac{experimental\ value-model\ value}{experimental\ value}\ . \qquad (4.\ 28)$$

Table 4. 1.Different errors of the model for rapeseed oil and quartzite thermocline thermal energy storage system [196].

Experimental data sources	1D-2P model	Mean error (°C)	Maximum error (°C)	RMse
Hoffmann experimental data (temperature profile)	Hoffman model	3.58	13.77	$1.4x10^{-4}$
Hoffmann experimental data	present model	3.59	6.44	2.10^{-4}
Hoffmann experimental data (Outlet temperature)	Hoffman model	2.11	4.52	1.910^{-4}
Hoffmann data	Our model	3.59	6.45	1.510^{-4}

Table 4. 2.Different errors of the model for molten salt and quartzite thermocline thermal energy storage system [11].

Experimental data sources	1D-2P model	Mean error (°C)	Maximum error (°C)	RMse
Pacheco et al., experimental data (temperature profile)	present model	1.79	2.41	$3.4.10^{-4}$
Pacheco et al., experimental data (outlet temperature	Present model	1.75	2.33	$3.2.10^{-4}$

For the sensitivity analysis or optimisation of the new storage system, the most unfavourable conditions are taken into account. Thus, the lowest values of the thermal properties of the ceramic balls manufactured were first considered as input data. To evaluate the effect of a parameter, the others are fixed and the value of the parameter studied is varied from the smallest to the largest obtained during the characterisation of the ceramic balls. Table 4. 3 presents the thermal properties

of ceramic ball with the lowest thermal properties And table 4 the thermal properties of Jatropha curcas oil from [159]. The correlation for the dynamic viscosity has been developed from the results of the chapter 3.

Table 4. 3.Thermal properties of the ceramic ball with the lowest thermal properties.

Properties	$\boldsymbol{\lambda_p}$ (W/m K)	D (mm^2s^{-1})	ρC_p (MJ m^{-3} K^{-1})	d_b (m)
Ceramic balls	0.347	0.143	2.429	0.028

Table 4. 4.Thermal properties of Jatropha curcas oil [159] and author.

Dynamic viscosity (Pa.s.K^{-1})	μ_f= (14227.1512293829×$(T_f)^{-1.63689632357044}$)/1000000))× ρ_f
Density(kg.m^{-3})	$\rho_f = -0{,}7392 \times T + 933{,}47$
Specific heat capacity (J.kg^1.K^1)	c_{pf} = (2.262× $10^{-9}T^4$- 10,423× $10^{-7}T^3$+12,947× $10^{-5}T^2$+0,441× 10^{-3}T+1,9608)× 1000.
Thermal conductivity	λ_f=2,80× $10^{-7}T^2$- 2,258× 10^{-4}T+0,1736

The thermal performances analysis was carried using a total storage capacity of $2MWh_{th}$ with tank ration of HD_w^{-1}= 2.5. The characteristics of the tank are presented in table. 5.

Table 4. 5. Different characteristic of the storage tank.

Tank characteristics	H	$D_{w,ext}$	$D_{w,in}$	ε	HD_w^{-1}
Values	7.98	3.59	3.19	41%	2.5

III.2. sensitivity analysis of the new TES system

III.2.1. Effect of JCO velocity on the new TES performance

Perfectly segregated hot and cold areas prevent heat loss, and all thermal energy (Q) charged into can be discharged at the same temperature in idealized storage systems. In practice however, performance degradation can occur due to heat losses to the environment as well as internal thermal diffusion inside the tank. To represent these effects threshold or cut off temperature of 200°C has been chosen because that temperature is between 150 °C and 210°C, range where an

ORC power block can generate electricity effectively with an efficiency equal to 15.81 % [197]. The discharge and storage efficiencies were computed using equation (4. 29) and (4. 30).

$$\eta_{discharge} = \frac{Q_{discharge}}{Q_{charge}} = \frac{\int_0^{t_{dischg}} \dot{m} C_{p,f} (T_{out} - T_{\min}) dt}{\int_0^{t_{chg}} \dot{m} C_{p,f} (T_{max} - T_{\min}) dt} \quad (4.\ 29)$$

$$\eta_{storage} = \eta_{discharge} \times \eta_{charge} \text{ with } \eta_{charge} = \frac{Q_{charge}}{Q_{total}} . \quad (4.\ 30)$$

In addition to the discharge and storage efficiencies, the development of the thermocline zone is assessed by its height variation. This value allows to appreciate its thermal behaviour and the performance of the thermal storage [198]. The thickness of the thermocline is evaluated using the following equation (4. 31).

$$H_{thermocline} = H_{high\ threshold} - H_{low\ threshold} \quad (4.\ 31)$$

$H_{high\ threshold}$ corresponds to the layer in the tank where the temperature is equal to the temperature corresponding to the selected high threshold. It represents the temperature above which the hot zone of the thermocline occurred. The high threshold temperature is computed in equation (4. 32).

$$T_{high\ threshold} = T_{low} + 0.9 * (T_{hot} - T_{cold}) \quad (4.\ 32)$$

$H_{low\ threshold}$ corresponds to the layer in the tank where the temperature is equal to the temperature corresponding to the selected low threshold. It represents the temperature below which the cold zone of the thermocline occurred. The low threshold temperature is computed using equations (4. 33), (4. 34), (4. 35) [49].

$$T_{low\ threshold} = T_{low} + 0.1 * (T_{hot} - T_{cold}) \quad (4.\ 33)$$

If $T_{Z=H_{tank}} < T_{high\ threshold}$ then, $H_{high\ threshold} = H_{tank}$. (4. 34)

If $T_{Z=0} > T_{low\ threshold}$ then, $H_{low\ threshold} = 0$. (4. 35)

The figure. 4. 8a and figure. 4. 8b presents the effect of fluid velocity on thermocline storage performance, respectively the thickness and the efficiencies. At any speed, the fig Figure. 4. 8a shows that the, thermocline thickness increases from 0 m (start of the discharge) to a maximum value when the outlet temperature tends towards the threshold temperature (200°C) and start decreasing after that value. The maximum fluid velocity study in this (u=5 mm/s) has been chosen to be higher than the maximum velocity (3 mm/s) of Caloria HT 43 used as HTF in the 10 MW_{el}

thermocline thermal energy storage system [83] and [107]. This option is to enable consideration of all different scales of thermocline TES for electricity generation. At higher velocity (u), JCO flows faster through the packed bed, indicating a larger heat discharging rate with discharging time less than 1.5h. The thermocline thickness reaches faster it maximum and decreases to 0 m for a total extraction of the thermocline. Chang et al., observed similar behaviour during the simulation of 2 MWh_{th} molten salt [99]. Faster increased in thermocline thickness and the higher thermocline thickness were observed at higher molten salt velocity [99]. However, when the velocity decreases, the thermocline is gradually established. Lower is the velocity, slower is the establishment of the thermocline and the maximum is reach at different time affecting also the discharge time. In addition, the thermocline become more thinner when the fluid velocity decreases making the TES system more effective. When the inlet velocity decrease, the discharging time increases significantly for higher than 9 h for fluid velocity low than 6.25×10^{-4} m.s^{-1} (see figure. 4. 8c). However, the effect of fluid velocity on TES efficiencies is low (figure. 4. 8b). A slight decrease of around 2.59% and 2.08% respectively for the discharge and storage efficiencies have been observed for a variation of the velocity from 5×10^{-4}m.s^{-1} to 5×10^{-3} m.s^{-1} (figure. 4. 8b).

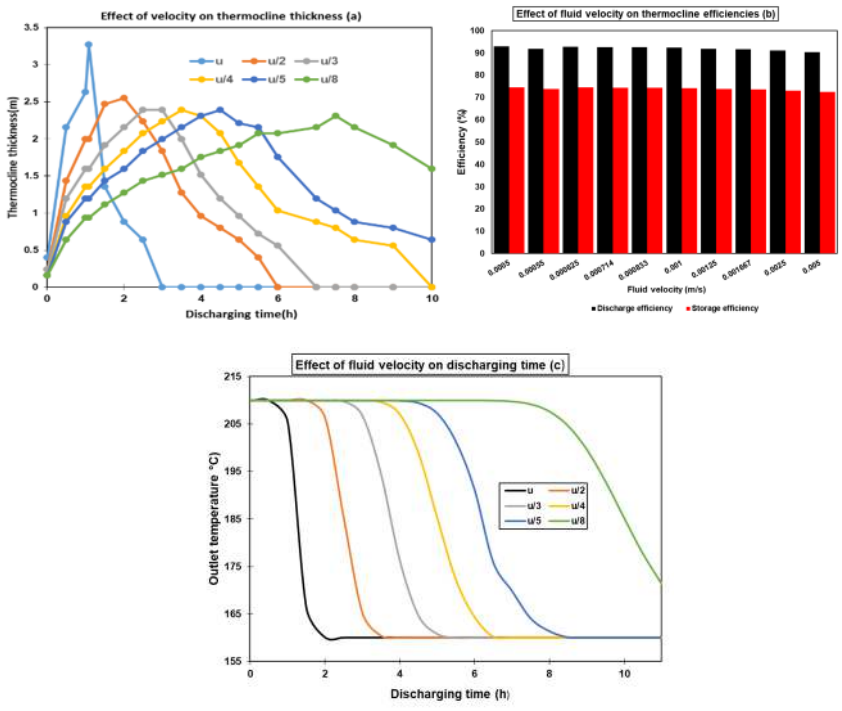

Figure. 4. 8. Effect of fluid velocity on thermocline thickness (a), efficiencies (b) and discharge time (c).

The thermal power during discharge cycle can be define as follows:

$$P_{th} = \frac{E_{total}}{t_{dchg}} \quad (4.\ 36)$$

Where E_{total} is the total energy stored in Joule (J) and t_{dchg} the discharge time in second (s).

As the discharge time depends on the HTF velocity, the TES system thermal power depend highly on the fluid velocity (mass flow) which should account for the sizing of the storage tank. This is highlighted in Figure. 4.9. High fluid velocity increases the thermal power of the storage system driven to faster degradation of the thermocline thereby making the discharging time very short as illustrated in figure. 4.9.

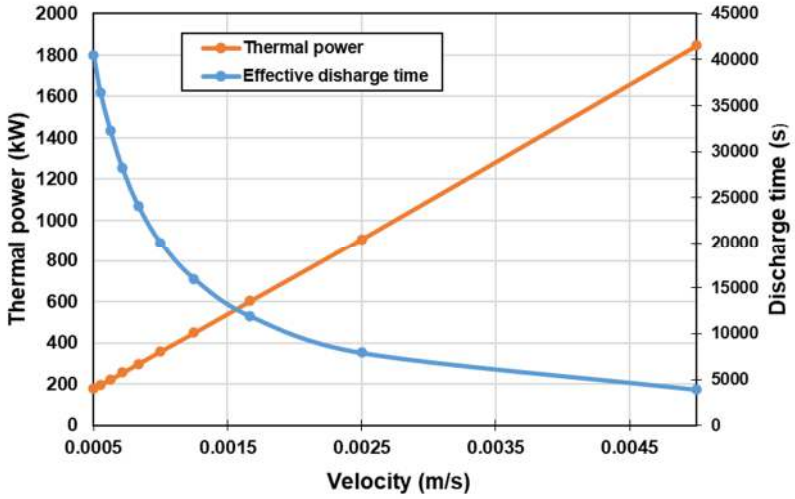

Figure. 4. 9. Effect fluid velocity on thermal power and discharge time of the storage system.

III.2.2. Effect of the oil aging time on the TES thermal performance

During the aging time, an increasing of the kinematic viscosity has been observed. From the literature there is no study carrying out the effect of oil properties behaviour during aging time on the performance of the TES. Even if the thermal properties of thermal oil do no change enough under heat treatment, the kinematic viscosity has increase 48.35% at 40°C for the oil put in contact with dune sand ceramic. In addition, the heat exchange coefficient between the ceramic ball and the HTF depend on the Reynolds and Prandtl number[192]. These numbers depend highly on the dynamic viscosity that is the product of the kinematic viscosity and the density. The Reynolds and Prandtl number can be written using equations (4. 37) and (4. 39)

$$\mathrm{Re}=\frac{\rho_f d_p u}{\mu_f}. \quad (4.\ 37)$$

with ρ_f the fluid density, d_p the particle diameter, u the fluid velocity and μ_f the dynamic viscosity of the fluid and is given by equation (4. 38)

$$\mu_f = \nu_f \rho_f. \quad (4.\ 38)$$

With ν_f the kinematic velocity.

$$\mathrm{Pr}=\frac{C_{p,f}\mu_f}{\lambda_f}. \quad (4.\ 39)$$

With $C_{p,f}$, the specific heat capacity and λ_f the thermal conductivity.

Figure. 4. 10 to Figure. 4.11, illustrate respectively the effect of ageing time on the TES thermocline thickness, efficiencies, Reynolds number and HTF outlet temperature. The thermocline thickness, TES efficiencies, Reynolds number and HTF outlet temperature did not change enough after the three months. However, a slight increase of the thermocline thickness and HTF outlet temperature for a total discharge can be observed after the third month. While the efficiencies are 89.72% and 71.77% against 89.62% and 71.70% respectively for the new oil and the oil after three months under heat treatment in contact with dune sand ceramic. Base on the conclusion done by Fasquelle et al.,[160], the ceramic ball-JCO TES would lose around 0.1% and 0.07% respectively for the discharge and storage efficiencies after 6 years of working. Therefore, the system can continue perfectly working 6 years without any changing or renewing of oil.

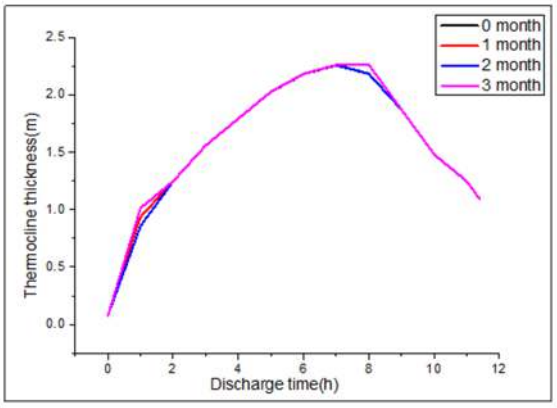

Figure. 4. 10. Effect of JCO ageing time on thermocline thickness

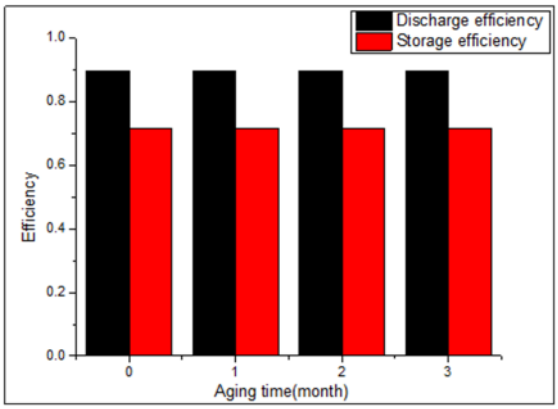

Figure. 4. 11. Effect of JCO ageing time on discharge and storage efficiencies

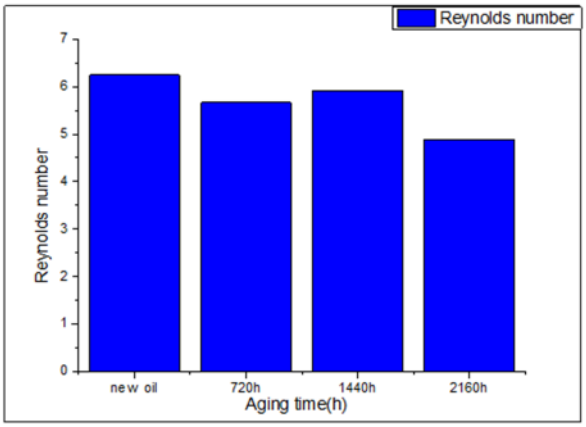

Figure. 4. 12. Effect of JCO ageing time on Reynolds number.

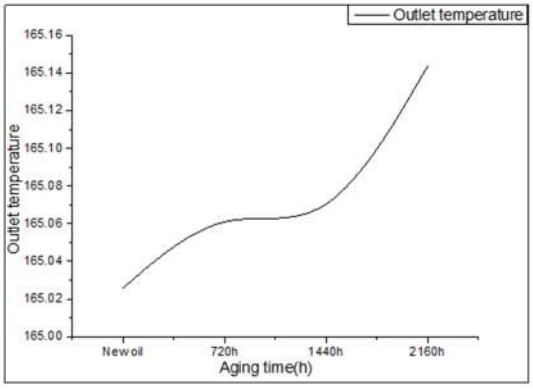

Figure. 4. 13. The effect of ageing time on HTF outlet temperature for a complete discharge cycle.

III.2.3. Effect of the tank porosity on TES performance

The mass flow of the HTF is function of its velocity through the packed bed porosity as written in equation (4, 14). Based on Furnas model, the minimum storage tank porosity is 37.8% for water flow through the bed as theoretical value. The average porosity of the ceramic ball is 26%. So, a minimum porosity of 40% as been chosen taking into account the relative error which is 4.671%. To control the mass flow and avoiding faster thermocline degradation or low thermocline extraction, the fluid velocity was fixed at 8.33×10^{-4} m/s (u/6) to assess the effect of bed porosity on the TES performance. Figure. 4. 14a and figure. 4. 14b illustrate the effect of tank porosity respectively on the thermocline thickness and efficiencies. It is observed in figure. 4.14a that the thermocline thickness reaches a similar maximum value for the for any porosity value but not at the same moment. A longer discharge time can be reach for a low porosity compared to the higher porosity. For a porosity value higher than 50% there is faster degradation of the thermocline. In the figure. 4.14b, when the porosity values increase from 40% to 50%, it can be observed that the energy delivery and storage efficiencies consistently drop from 90.07% to 86.53% and 72.50% to 68.37% respectively. Therefore, there is no loss in exergy during charging and discharging for and ideal thermocline tank which is a conceptual tank consisting of hot and cold fluid separated by a fictitious barrier without any filler material ($\varepsilon = 1$) [88]. Hence for a DMT, at a low porosity range, with an increase from 40% the energy storage efficiencies are actually getting diminished in the tank, affecting the energy capability. Thus, in the present thermocline thermal energy storage system, the ceramic balls have a higher energy storage density $\rho_p C_{p,p}$ than that of fluid $\rho_f C_{p,f}$ (at least 2.4 $MJ.m^{-3}K^{-1}$ for the developed ceramic balls at room temperature against 1.953 $MJ.m^{-3}K^{-1}$ at 210°C for JCO [49]). So, at low porosity most of the energy is stored in the solid material. However, when the porosity is very higher than 50%, the thermal storage tank behaves like an ideal thermocline tank, which will have high energy storage efficiencies. That means that the TES density is led by the fluid.

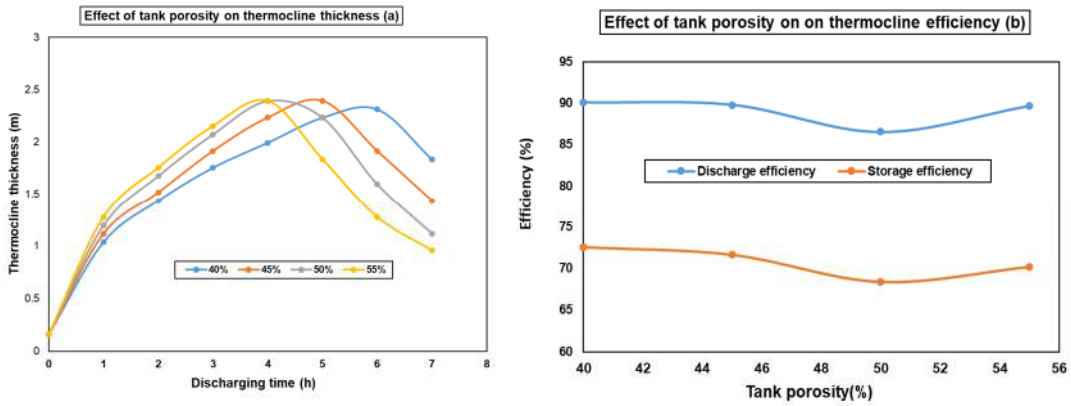

Figure. 4. 14. Effect of tank porosity on thermocline thickness (a) and TES efficiencies (b).

III.2.4. Effect of particle diameter of the TES performance

The effect of spherical particle diameter on the system performance is investigated in this section through testing different diameters of ceramic balls varying from 1.0 to 3 cm figure.15. A tank porosity of 41%, a fluid velocity of $8.33x10^{-4}$m/s has been chosen. The thermocline thickness and the TES efficiencies are illustrated in figure. 4.15a and figure. 4.15b.

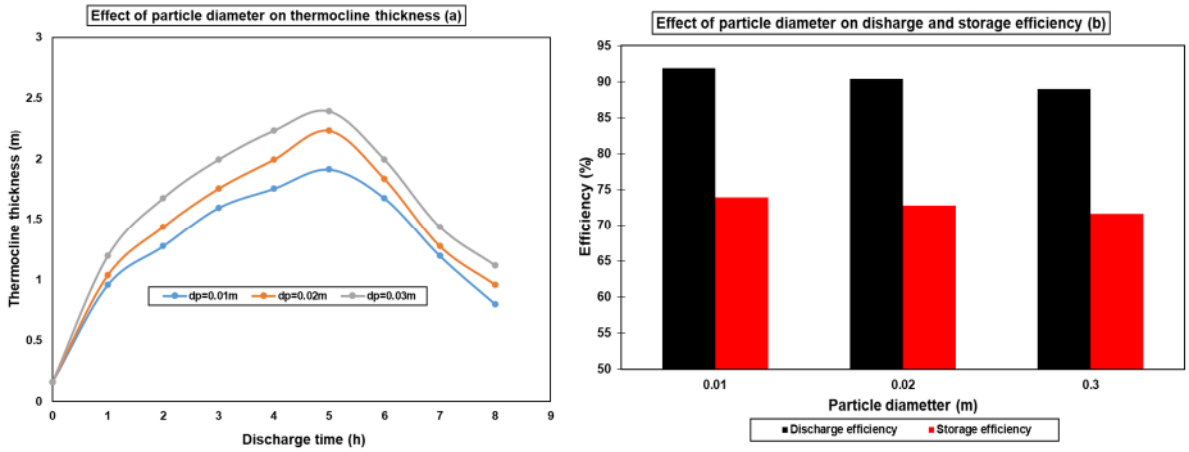

Figure. 4. 15: Effect of ceramic ball diameter on the thermocline effectiveness (a) and TES efficiencies (b).

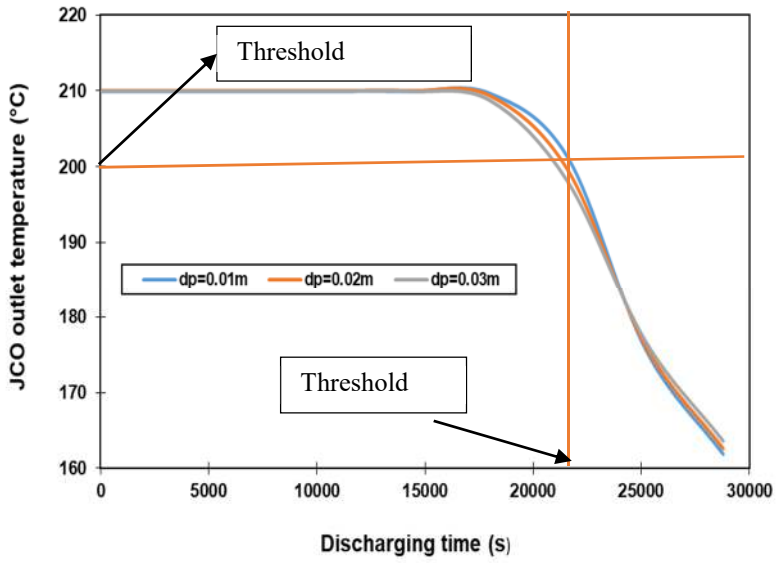

Figure. 4. 16: Effect of ceramic balls diameter on discharge time.

A better energy can be delivered and stored with small filler material because a thin thermocline can be achieved (figure. 4.15a). When the particle dimeter increase, the thickness is getting increasing. Increasing in thermocline drives to a low energy delivery capability and storage as illustrated in figure. 4.15b. The energy storage efficiencies decrease from 91.84% to 88.92% and 73.93% to 71.58% respectively for the energy delivery and store capability. The energy delivery time is longer for the smallest particle (figure. 4.16) at a threshold temperature of 200°C. During the discharging time, the small particle takes more time to cool down from inside to the surface compare to larger particle as illustrated in figure. 4.16 for a fluid. However, for a total extraction of the thermocline with a threshold temperature close to 160°C the discharge time is longer for the biggest particle, but the delivered energy may not be useful to run the power block.

III.2.5. Effect of ceramic ball volumetric heat capacity on the TES performance

The effect of the volumetric heat capacity on the storage efficiencies is carried out in this point for values varying from 2.5 MJ.m^{-3}. K^{-1} to 3.25 MJ.m^{-3}. K^{-1}. These values have been choosing to be within the range values obtained in chapter 2. The effect on the thermocline thickness, the TES efficiencies and discharge time are investigated and illustrated on Figure. 4.17, Figure. 4. 18 and Figure. 4. 19. The Figure. 4. 17 shows that, when the volumetric heat capacity ($\rho_b c_{p,b}$) increases from 2.5 MJ.m^{-3}. K^{-1} to 3.25 MJ.m^{-3}. K^{-1} it impacts slightly the thermocline thickness at the

biggening of the discharge, but increased to reach a maximum value (thermocline establishment). At low volumetric heat capacity (2.5 MJ.m^{-3}. K^{-1} and 2.75 MJ$m^{-3}K^{-1}$) the thermocline thickness reach faster its maximum value (2.391m after 5h) and starts leaving the tank during the discharge cycle. While for high value of $\rho_b c_{p,b}$ ($\geq$ 3 MJ.m^{-3}. K^{-1}) the total establishment of the thermocline delay for 1h. As illustrated in figure. 4. 17, the $\rho_b c_{p,b}$ impact highly the thermocline leaving time in the storage tank and delay more when the $\rho_b c_{p,b}$ is increasing. For example, after 8h the thermocline thickness reduces to 1.12m, 1.275, 1.435 and1.674 m respectively for 2.5 MJ.m^{-3}. K^{-1}, 2.75 MJ.m^{-3}. K^{-1}, 3 MJ.m^{-3}. K^{-1} and 3.25 MJ.m^{-3}. K^{-1}. Higher $\rho_b c_{p,b}$, drives to the retention of the thermocline in the tank due to the high capacity of heat storage which can take advantage to increase convective heat transfer. Similar results have been carried out by Fernando et al., during a charging cycle [199]. This confirm that high volumetric heat capacity of the ceramic balls drives to high heat retention capacity in the ceramic balls and high discharging time of the storage system.

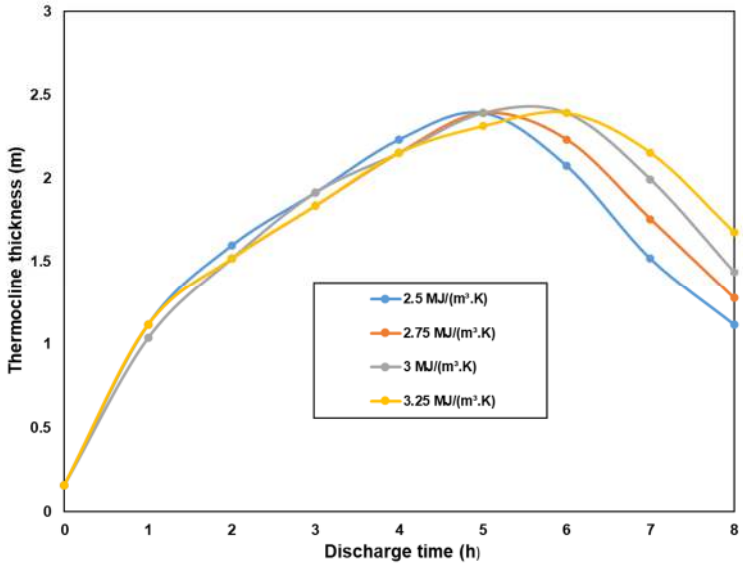

Figure. 4. 17. Effect of volumetric heat capacity on thermocline thickness.

For the effect of $\rho_b c_{p,b}$ on the discharge and storage efficiencies (Figure. 4. 18) of the TES system the discharging efficiency is slightly affected while the storage efficiency is highly affected. As illustrated in figure. 4. 18 storage efficiency increases from72.78% to 85.581when $\rho_b c_{p,b}$ increases from 2.5 MJ.m^{-3}. K^{-1} to 3.25 MJ.m^{-3}. K^{-1} throughout a cycle. This shows that the increasing of

ceramic balls volumetric heat capacity increases their heat retention capacity providing more efficiency throughout the cycle.

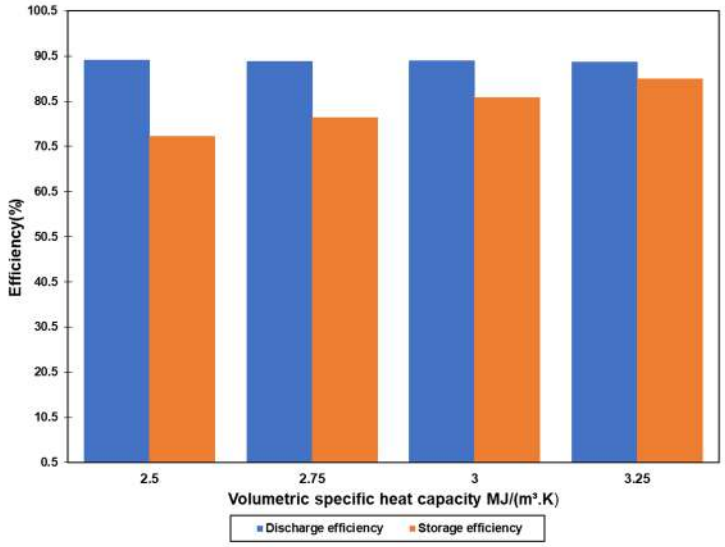

Figure. 4. 18. Effect of volumetric heat capacity on the TES discharge and storage efficiencies.

The Figure. 4. 19 illustrate the effect of $\rho_b c_{p,b}$ on the HTF outlet temperature variation. A constant outlet temperature (around 210°C) is observed for all the values of $\rho_b c_{p,b}$ for the first five (5) hours. After that time the outlet temperature decrease faster for low value of $\rho_b c_{p,b}$ compare to high value of $\rho_b c_{p,b}$. For example, around the threshold temperature (200°C) the discharge time is 6h for $\rho_b c_{p,b} = 2.5\ MJm^{-3}K^{-2}$ against 7h for $\rho_b c_{p,b} = 3.25\ MJm^{-3}K^{-2}$. This shows that the amount of heat stored in the ceramic balls is higher when their volumetric heat capacity is higher. So, during a discharging cycle, the TES will discharge faster for ceramic balls with low volumetric heat capacity compared to the one filled with ceramic balls with high volumetric heat capacity.

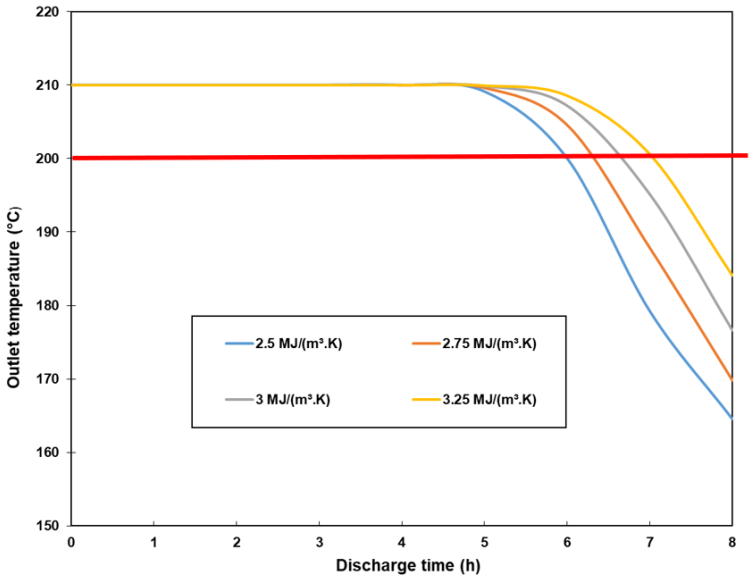

Figure. 4. 19. Effect of the volumetric heat capacity on TES outlet temperature and discharge time.

III.2.6. Charging and discharging process analysis

The figure. 4. 20 illustrates the effect of fluid velocity on the 2 MWh_{th} charging time. The profile of the different curves are the same. These profile show the increasising of the temperature from the bigining of the charge (t=0, T=160°C) to the end of the charging process (t=t_{chg}, T=210°C). Thus, the final temperature is reached faster when the fluid velocity is increasing reducing significantly the charging time. This is due to the effect of fluid velocity on Renolds number. High fluid velocity increase the Reynolds number increasing the confective heat transfer between the JCO and ceramic balls.

However, the the total charging time should be closed to the available sunshine duration of the study area where the CSP plant should run during a day. For example, the sunshine duration is around 8h.day^{-1} in Burkina Faso [200] and around 9h.day^{-1} for Niger [15]. In addition, in real time plant working conditions the JCO outlet temperature cannot reach 210°C during all the sunshine duration due to solar radition fluctuation. Also, high fluid velocity drives to the mixing of cold and hot fluid mixing dealing with bad thermal stratification. For these proposes, a maximum fluid velocity of $1.66710^{-3} m.s^{-1}$ could be suited to charge fully the $2MWh_{th}$ TES for around 7h as illustrated in figure (4. 20).

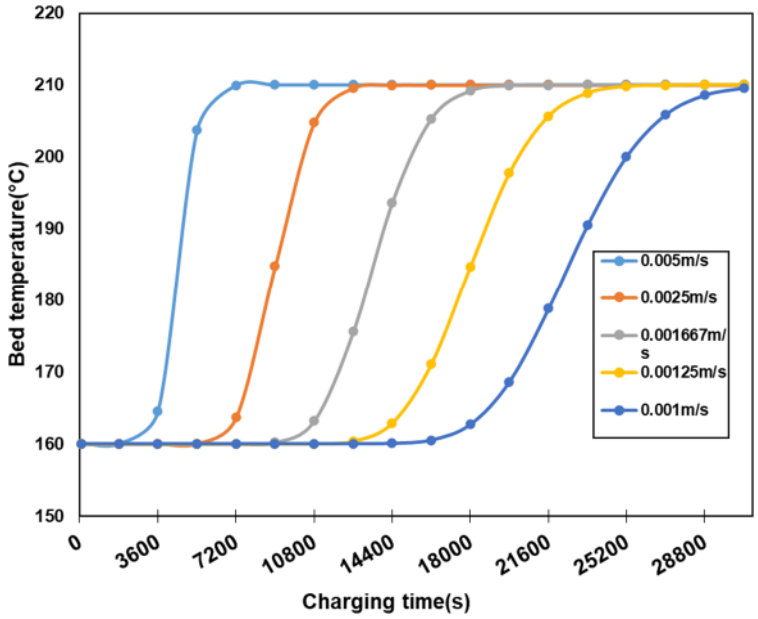

Figure. 4. 20. Effect of fluid velocity on charging time.

The figure. 4. 21 illustrates the temperature profiles in the TES system during a charging cycle for a JCO velocity of $1.66710^{-3} m.s^{-1}$. These profiles have been plotted by reversing the orientation of the tank. It shows that the temperature is humogen in the TES tank at the beginning (T=160°C) and at the end of the charging process. During the charging cycle it can be seen that the temperature within the TES is high at the entrance (top) of the tank and lower at the outlet (bottom) after 1h. Therefore, the thermocline is established and starts leaving the tank after three (3) hours when the JCO outlet temperature is higher 160°C. During that process, the JCO outlet temperature is increasing and reach the final temperature (210°) after 7 h when the thermocline leaves ($T_{inlet} = T_{out}$) completely the storage tank.

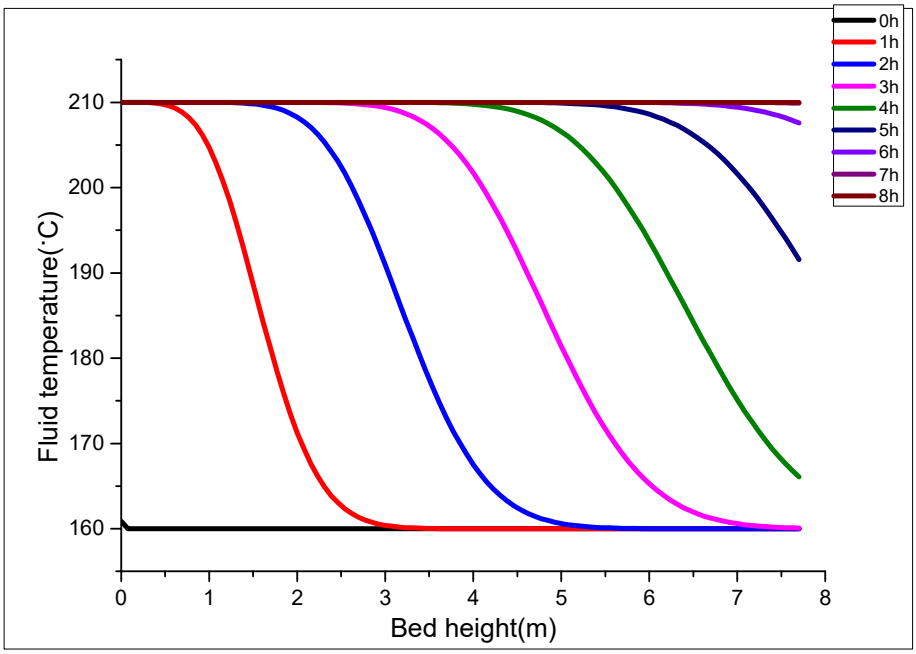

Figure. 4. 21. Axial fluid temperature in the packed bed during charging cycle.

The figure. 4. 22 illustrates temperature profile in the TES system at the ends of charging (upper curve) and discharging (lower curves) cycles for a fluid velocity of $1.66710^{-3} m.s^{-1}$ and threshold temperature of 20%. The calculation shows that when the charging or discharging process is ending the temperature profiles are getting tighter as result of an increase in thermocline region. This is due to the phenomenon of thermal diffusion in this zone where thermal gradients are significant. So, it can be seen that the thermocline is still high at the end of the discharge. This shows that when the set temperature is imposed, the thermocline cannot be extracted. Because the exchanger which supplies the power block will not accept temperature lower than the threshold temperature [49]. To face this challenge the threshold temperature can be fixed according to the type of power block used to generate electricity. For example, a threshold temperature of 50% (185°C) to 60% (180°) can be fixed to generate effectively electricity using Organic Rankine Cycle (ORC) in temperature range of 150°C to 210°C[201],[197]. However, for a Steam Rankine Cycle (SRC), the threshold temperature should be higher than 10% (205°C) because the electricity generation capacity is better between 210°C and 350°C [197]. Therefore, using JCO may not be suitable for a CSP generating electricity using SRC.

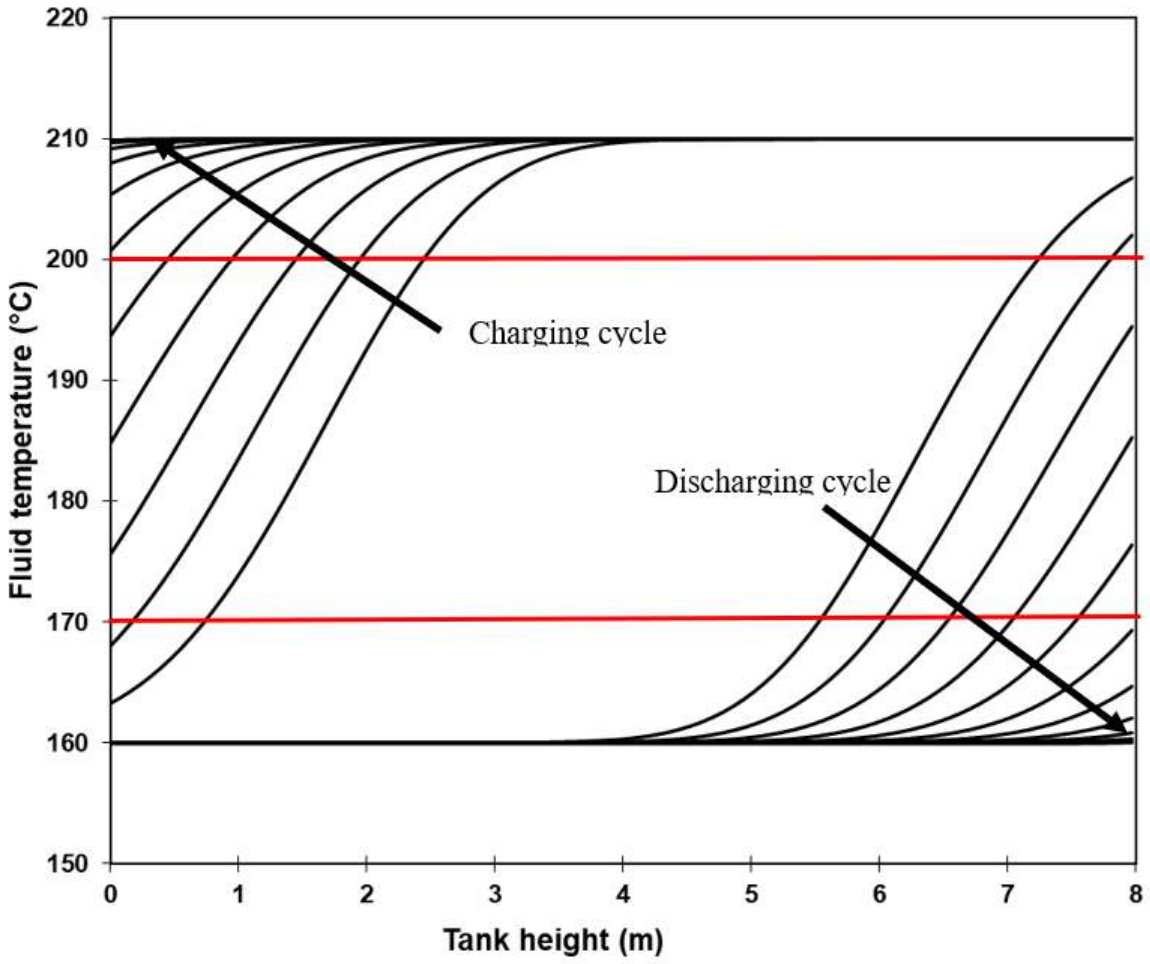

Figure. 4. 22. Fluid temperature profile in the packed bed during charging and discharging cycle.

III.3. Heat transfer behaviour for the fluid and the particle in the packed bed

This section presents the general behaviour of heat transfer between JCO and spherical ceramic during the discharging process for a fluid velocity of 6.25×10^{-4}m.s^{-1} and packed bed porosity of 41%. The solid Ceramic ball developed and used is of diameter of 2.88 cm. Figures 4.23 and 4.24 show how the fluid temperature profile and the fluid and solid temperatures at the particle surface vary with the discharge time, respectively, and figure 4.25 shows (iii) how much the temperatures differ for 2MWh$_{th}$ ceramic balls-JCCO Testing Equipment. The results confirm the accuracy of the model based on the different temperature profiles in the hypothetical 2 MWh$_{th}$ TES system. However, a difference temperature of 2°C has been observed during discharging process after 2h (figure. 4. 25). The thermal properties of the fluid vary easily with temperature while in this study the properties have been considered at mean temperature.

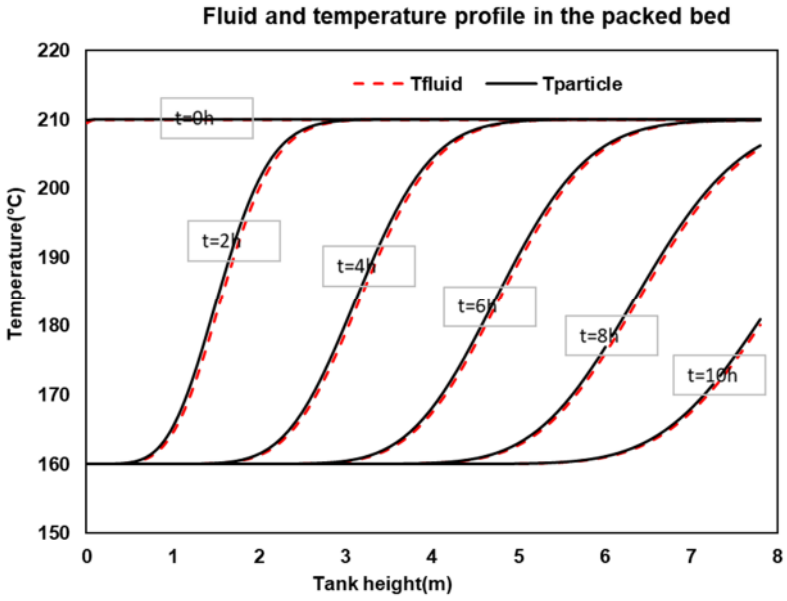

Figure. 4. 23. Fluid and particle temperature profile in the bed.

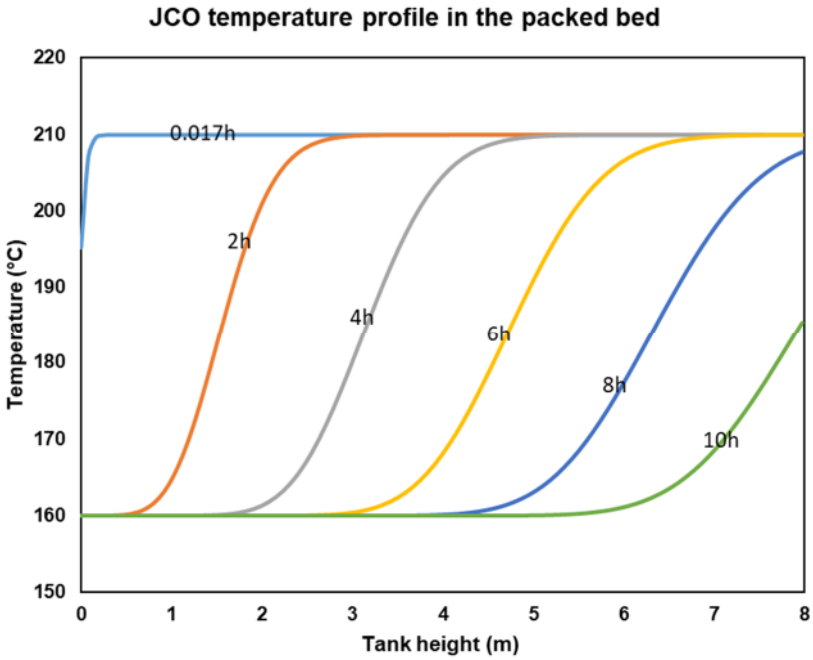

Figure. 4. 24. JCO temperature profile during discharge time.

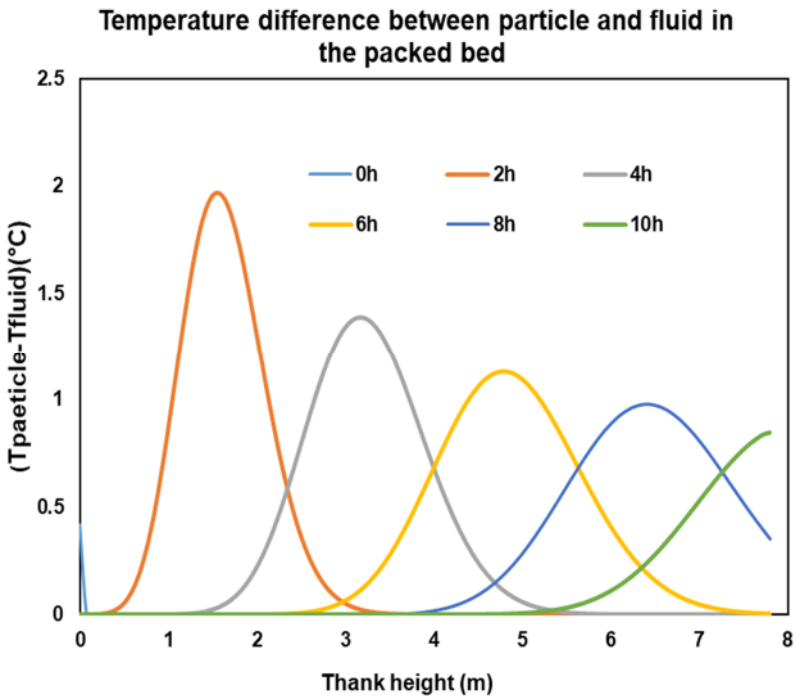

Figure. 4. 25. Temperature difference between JCO and ceramic ball surface temperature during discharging time.

III.4. Comparative performance assessment of the four types of ceramic balls used as filler material in the 2 MWh_{th}.

The performance of the 2 MWh_{th} TES system in this part is going to be assessed by fixing only the tank porosity at 45% and fluid velocity at $6.10^{-4} m.s^{-1}$. The objective is to check if the thermocline efficiency can be improved when using ceramic ball with known thermal properties. The properties of the four ceramic balls are illustrated in table. 6 as follows:

Table 4. 6.The properties of the four ceramic balls and volumetric heat capacity and thermal conductivity ration of the TES system.

Formulation	λ_p $(W.m^{-1}.K^{-1})$	$\rho_p C_{p,p}$ $(MJm^{-3}K^{-1})$	$\frac{\rho_p C_{p,p}}{\rho_f C_{p,f}}$	λ_p/λ_f	η (%)
M58A12C130-B (1000) or (MS58 (1000)	1.012	2.907	1.445	7.16	89.81

M40A30C30-B (1060) or MS40(1060),	0.437	2.618	1.353	3.09	90.02
D40A30C130-B (1060) or DSB40(1060),	0.411	2.505	1.246	2.91	90.065
D40A30C130-B (1000) or DSB40(1000),	0.367	2.74	1.363	2.595	89.72

The tank volume computed using the equation (1. 20), depends highly on the volumetric heat capacity of the ceramic balls as illustrated on figure. 4. 26. The difference in tank volume is related to $\boldsymbol{\rho_b C_{p,b}}$ of ceramic balls which can be used to store the same amount of energy ($2\ MWh_{th}$). From the diagram analysis, the M58A12C130-B (1000) is the most suitable filler material because it reduces the volume of the tank due to the high volumetric heat capacity of the ceramic ball.

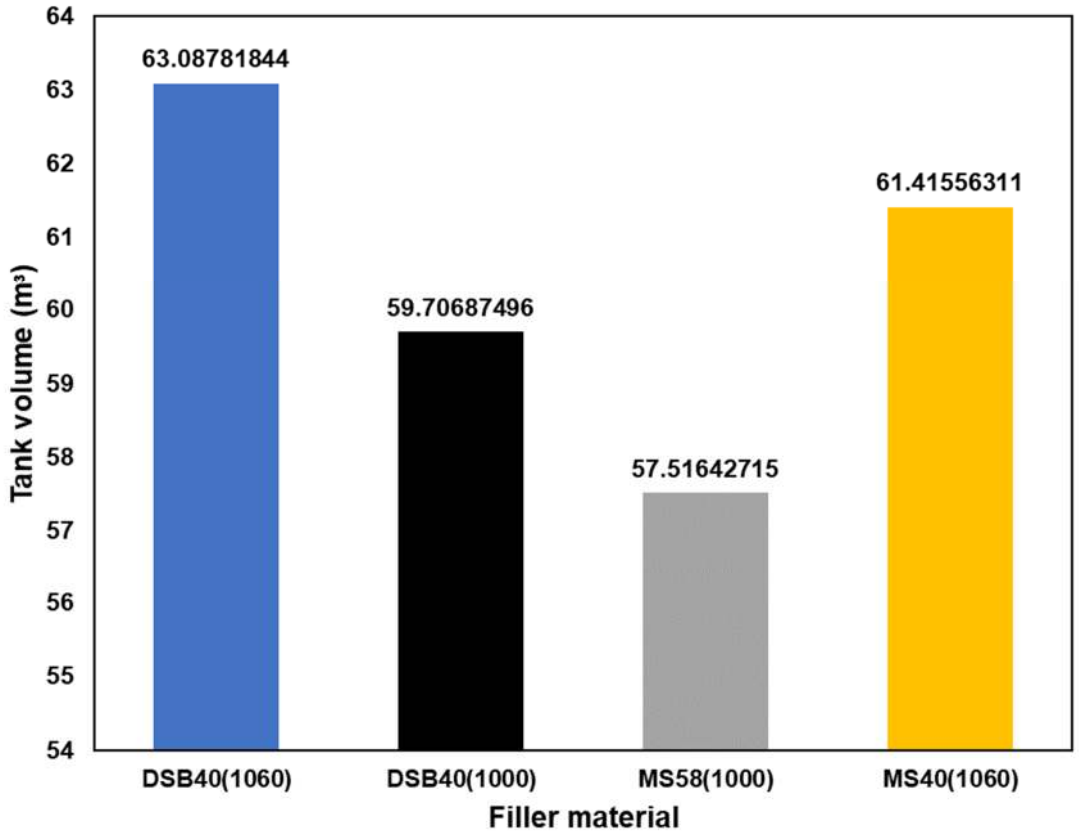

Figure. 4. 26. The volumetric heat capacity effect of filler material properties on tank volume.

Figure. 4. 27a and Figure. 4. 27b illustrates the discharging time profile for dune and mining sand ceramic balls. Similar profiles or behaviours to the effect of volumetric heat capacity on

discharging time is observed. It can be observed that, for a threshold temperature of 200°C, the TES system using ceramic ball developed with 58 wt.% of mining sand 30% wt.% of clay an 12% wt.% of CBA (MS58 (1000) takes more time to discharge compared to MS40(1060), DSB40(1060), DSB40(1000) ceramic balls. The volumetric heat capacity of these ceramic balls is respectively 2.907 MJ. m^{-3}. K^{-1}, 2.721 MJ. m^{-3}. K^{-1}, 2.50 MJ. m^{-3}. K^{-1}, 2.74 MJ. m^{-3}. K^{-1}. This shows that longer discharge time is obtained with the ceramic ball which has the higher volumetric heat storage capacity which increase the heat retention ability. The effect of aging time on the discharge time, storage efficiency and Reynolds number are negligible for the four types of ceramic balls. However, the discharge time could be reduced faster with dune sand ceramic compared to mining sand ceramic as illustrated on figure. 4. 28.

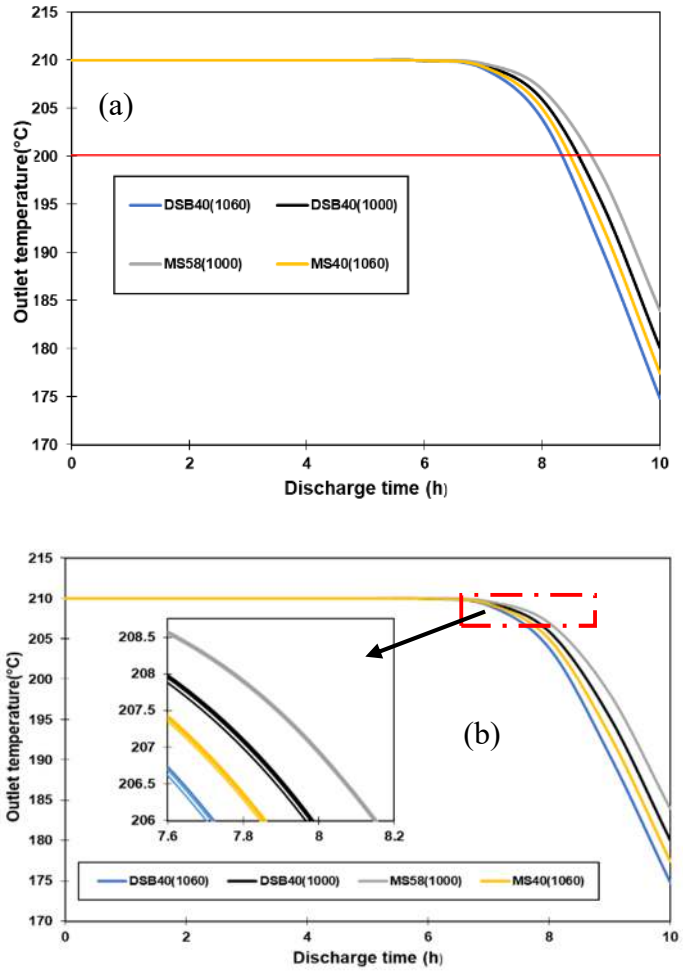

Figure. 4. 27. Discharging time for four different formulations of ceramic balls (a) and zoom in (b).

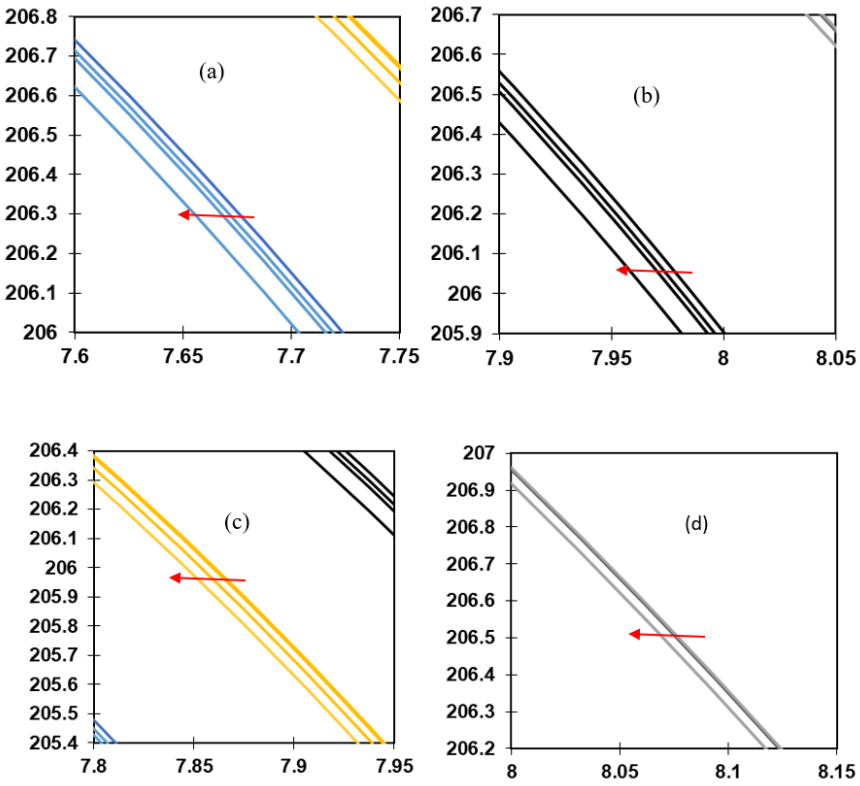

Figure. 4. 28. Clear view of discharging time evolution for four different formulations of ceramic balls with aging time.

For the thermocline thickness of the different storage systems, the different profiles are illustrated in figure. 4. 29. The thermocline thickness increases during the discharging process and reach it maximum almost at the same time (after 7 h) for MS40(1060), DSB40(1060), DSB40(1000) and after 8h for MS58 (1000). This is due to the high $\rho_b C_{p,b}$ of MS58 (1000) which increases the TES storage capacity and efficiency. After 7h and 8h, the thermocline decreases for the different TES system and reach almost the same lower thickness value (1 m) after 11.4 h. It can be observed that the effect of volumetric heat capacity on the thermocline extraction becomes. While DSB40(1060) has the lowest value of $\rho_b C_{p,b}$, the thermocline is leaving faster with MS58 (1000) TES system compare to DSB40(1060) TES system. This is due to the high thermal conductivity of MS58 (1000). The high thermal conductivity of MS58(1000) enhance the effective thermal conductivity of the storage system which improve thermal diffusion, and thus lead to faster extraction of the thermocline. Between 9h and 11h the thermocline thickness of DSB40(1060) TES is the most important showing that other parameters can affect the performance of thermocline storage system.

These parameters are the volumetric heat capacity ($\frac{\rho_b C_{b,p}}{\rho_f C_{p,f}}$) and thermal conductivities ($\frac{\lambda_p}{\lambda_f}$) ratio of the ceramic ball and the heat transfer fluid.

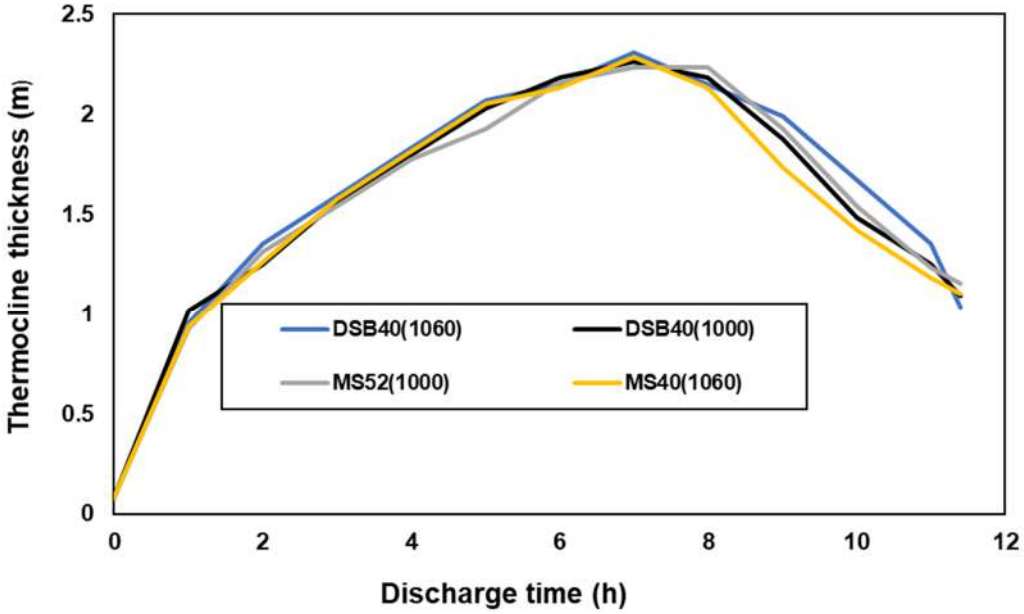

Figure. 4. 29. Thermocline thickness for four formulations of ceramic ball.

The figure. 4. 30 illustrates the efficiencies of the different TES system. No change has occurred due to the aging effect showing that the effect of aging is negligible. However, a slight difference can be observed and the best discharge efficiency (90.06%) and storage efficiency (72.05%) is achieved with DSB40 (1060) follows by MS40(1060) with discharge efficiency of 90.02% and storage efficiency of 72.01%. Indeed, better thermal efficiency is achieved at low thermal conductivity ratio λ_b/λ_f while increasing in thermal capacity ratio ($\rho_b C_{p,b}/\rho_f C_{p,f}$) can reduce the discharging efficiency as mentioned by Fernando et al., in 2020 and 2022 [199]. The thermal conductivity ratio for the different storage system is 7.157, 3.324, 2.906, 2.595 respectively for MS58 (1000), MS40(1060), DSB40(1060), DSB40(1000) while their thermal capacity ratio is 1.446, 1.353, 1.246 and 1.3623. As mentioned by Fernando et al., in 2022, in this study the best thermal performance is obtained with DSB40 (1060) which has the lowest thermal capacity ratio (1.246). After the first month the thermocline discharging efficiency slightly increased for the three types of ceramic balls respectively of 0.147%, 0.02% and 0.019% for DS40(1060), MS58(1000), MS40(1060) and decrease of 0.13% for DS40(1000). Thus, these differences are

unsignificant during the aging time shows its low effect on the storage efficiency as illustrated in figure (4.30).

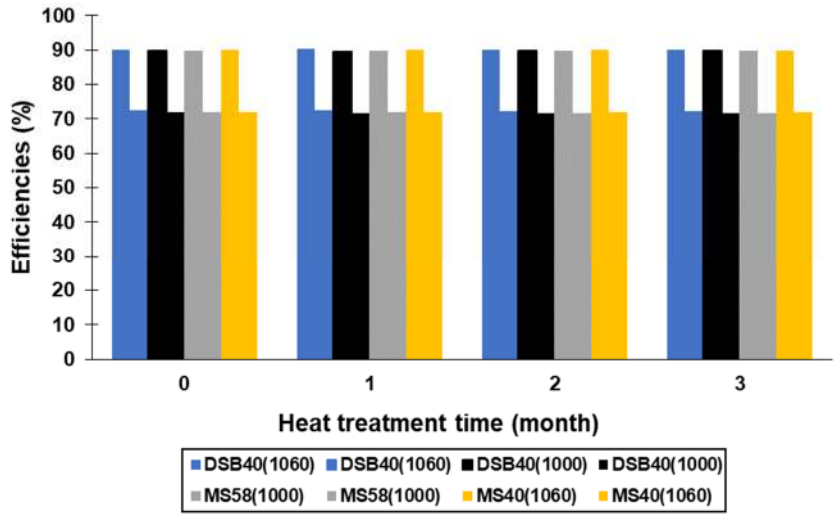

Figure. 4. 30. Discharging and charging efficiency for different ceramic balls.

The figure. 4. 31illustrates the effect of ageing time on Reynold number. It can be observed that the Reynolds number is the same for the different TES systems for the new oil of JCO. After the first month of heat treatment, the Reynolds number decreases (for dune sand) or increases (for mining) in the same way for ceramic ball developed with the same type of sand. From the second month the same behaviour is observed, but this time the Reynolds number increases with dune sand ceramic and decreases with mining sand ceramic. At the end of aging time, a large and low reduction of Reynolds number is observed respectively for dune sand ceramic and MS40(1060) while no change has been observed with MS58 (1000). These results show that, the Reynolds number could be an indicator to monitor the performance of TES system during its operation. Moreover, the Reynolds number change in the same way for the same raw material excepted the one of mining sand after third month. Having the same refractory character [202], it may be difficult to link the variation of Reynolds number to the ceramic composition. As the Reynolds number depends on mass flow rate and kinematic viscosity, it can be affected by the both thermal capacity ratio and thermal conductivity ratio of filler material and HTF in the TES system. High thermal conductivity ratio will increase the thermal diffusion driving to high heat losses in the TES system. Therefore, the effect of heat treatment increases the kinematic viscosity of oil, driving to

low effect on Reynolds number (slight decrease) and energy (slight increase) used for the pumping system.

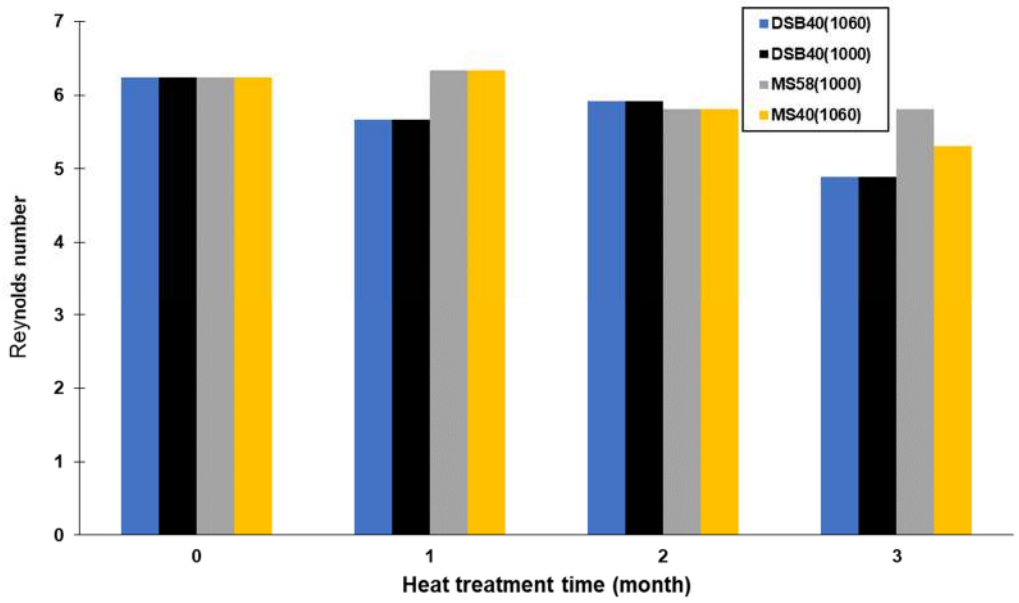

Figure. 4. 31. Effect of heat treatment time on Reynolds number.

In general, the effect of aging time on the TES performance is negligible for the four types of ceramic balls used as filler materials. The axial temperature profile and difference temperature in the TES system are plotted for dune and mining sand ceramic as illustrated from figure (4. 32) to figure (4. 35) in the packed bed for a discharge cycle.

Figure. 4. 32 and figure. 4. 33 show a homogenous temperature (210°C) for Jatropha Curcas Oil and ceramic ball in the TES system at the beginning of the discharging process. After that, the diffusion effect increases the thermocline zone showing the cold zone and hot zone. The thermocline reaches its maximum thickness between 6h and 8h and start leaving the TES system. As mentioned previously, if there is no temperature setpoint the thermocline will completely leave the TES system for a deep discharge.

The temperature profile for the oil and ceramic balls surface are almost similar during the discharging process. To reveal the temperature difference, the variation in the temperature difference between the ceramic ball and oil are shown in the figure. 4. 34 and figure. 4. 35. There

is a relatively large temperature different (1.97°C) at the beginning of the discharging cycle. The temperature difference decreases very sharply with the discharging time and reaches 0.85°C after 10h. As mentioned by Xu et al., in 2013 [44] the maximum temperature difference is not a constant for particles at different heights but due to the entering of cold oil at the entry. Thus, the farther is the particle from the cold-oil entry, the lower is the maximum temperature difference.

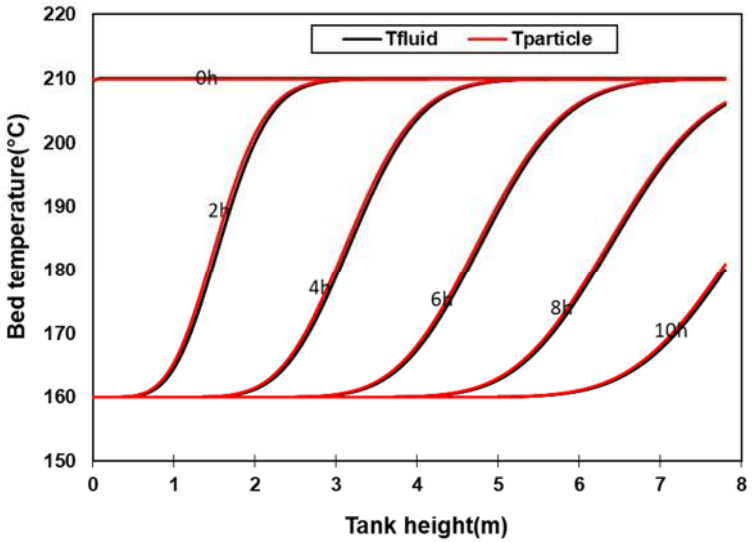

Figure. 4. 32. Temperature profiles in the packed bed when using dune sand ceramic balls as filler materials.

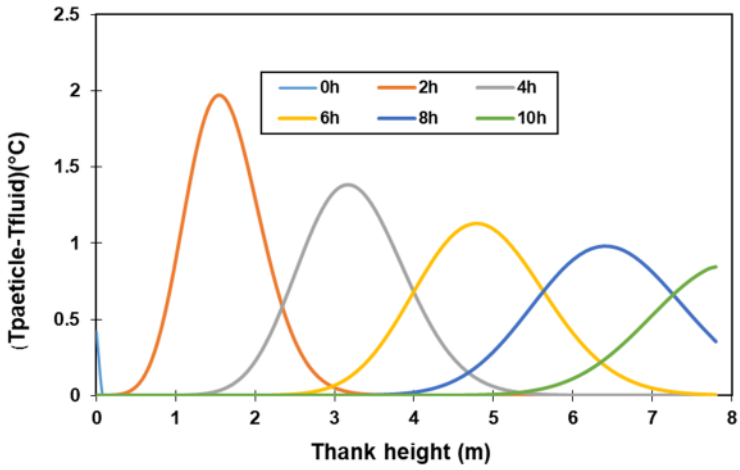

Figure. 4. 33. Dune sand ceramic and JCO temperature difference profile in the tank during discharging time.

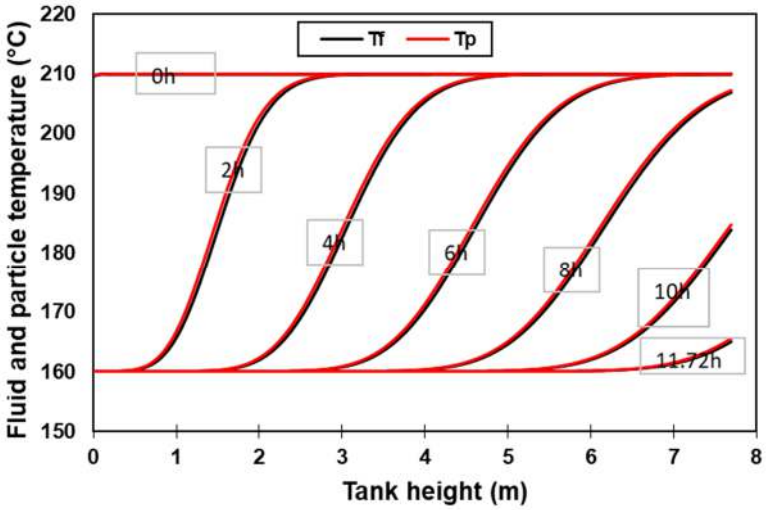

Figure. 4. 34. Temperature profiles in the packed bed when using mining sand ceramic balls as filler materials.

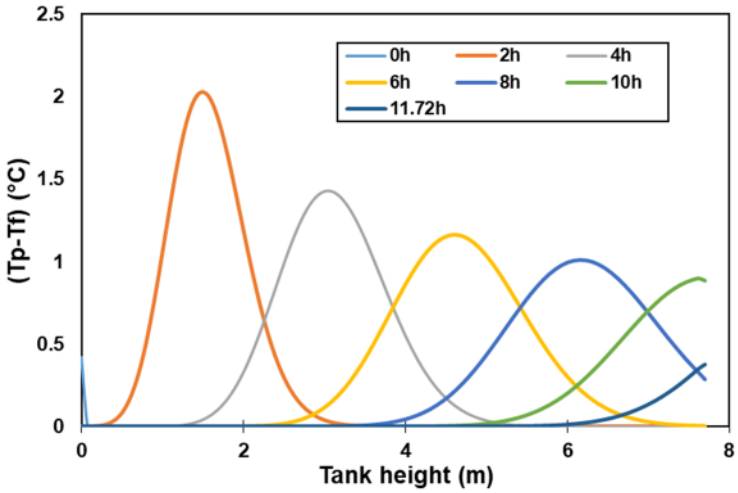

Figure. 4. 35. Mining sand ceramic and JCO temperature difference profile in the tank during discharging time.

IV. Sizing and behaviour analysis of Thermal energy storage system for 2 MW_{el} electricity power output CSP plant

For the sizing of a thermal energy storage system, specifications are needed. In this work storage duration is assume to be 12 hours to expected the plant working during at least 23 hours a day. For a clear sky the discharging process should start at around 4 PM or 5 PM and the plant should be shut down at around 6 AM the next day. As the jatropha curcas oil has a temperature limitation, ORC turbine is the best power block require to achieve better electricity generation efficiency of 15.81 % ($\eta_{power\ block}$ [197]. The working temperature range is 210° to 160°C.

The required total mass flow to run the turbine can be computed using equation (4. 40).

$$\frac{\dot{Q}_{el}}{\eta_{disch}\eta_{power\ block}\eta_{alternator}} = \dot{Q}_{th} = \dot{m}_{total} \times C_{p,f} \times \Delta T \qquad (4.\ 40)$$

Where η_{disch} is the discharge efficiency of the TES system. It is assumed equal to 90%, $\eta_{power\ block}$ is the ORC power block, which is equal to 15.81 % between 210 °C and 150°C [197], $\eta_{alternator}$ is the electricity generation efficiency by the alternator. In this work it is assume to be equal to 95% [203]. $C_{p,f}$ is the specific heat capacity of Jatopha curcas oil computed at the average

temperature using the corelation available in [159] and ΔT (T_H-T_L) the difference between hot and low fluid temperature.

The thermal energy stored is given by:

$$Q_{stored} = \dot{Q}_{th} \times n_{SD}. \quad (4.\ 41)$$

n_{SD} is the storage duration

The mass of the ceramic ball useful as filler material is given by equation (4. 42).

$$m_{particle} = \left(\frac{Q_{stored}}{((\rho C_{p,p})_p \times \Delta T + ((\rho C_{p,f})_f \times \Delta T)/(1-\varepsilon)) - (\rho C_{p,f})_f \times \Delta T)} \right) \times \rho_p \quad (4.\ 42)$$

Where $\rho C_{p,p}$ and $\rho C_{p,f}$ are respectively the volumetric heat capacity of the particle and the fluid, ε the tank porosity assume to be equal to 45%, and ρ_p the particle bulk density

The tank volume is given by equation (4.43)

$$V_{total} = \frac{V_p}{1-\varepsilon} \quad (4.\ 43)$$

And the hot fluid volume is given by equation (1. 44)

$$V_f = V_{total} - V_p\ . \quad (4.\ 44)$$

The tank ratio (H/D) is assumed to be 2.5.

The volumetric heat capacity of the difference ceramic balls is illustrated in table 22.

The required oil volume can be obtained by equation (4. 45)

$$V_{f,amb} = \frac{V_f \rho_f}{\rho_{fluid,amb}} \quad (4.\ 45)$$

$V_{f,amb}$ is the oil volume required at ambient temperature (around 25°C) and $\rho_{fluid,amb}$ the oil density at ambient temperature.

A small code has been written in excel to compute the TES tank different parameters and presented in Table 7 for four (4) ceramic ball with different thermal properties.

Table 4. 7. Characteristic of the TES tank to generate 2 MWel electricity power as output.

Formulation	$\dot{Q}_{th}(MW_{th})$	$\dot{m}_{total}\ (kgs^{-1})$	$V_{total}\ (m^{-3})$	$D_{inner}\ (m)$	$H_{inner}\ (m)$
M58A12C130-B (1000)	14.8	117.256	5107.055	13.755	34.385
M40A30C30-B (1060)	14.8	117.256	5459.757	14.064	35.161
D40A30C130-B (1060)	14.8	117.256	5735.267	14.297	35.743
D40A30C130-B (1000)	14.8	117.256	5300.387	13.926	34.815

The commercial tank has been sized with the thermal efficiency of the 14.8 MWh_{th}. With the four (4) types of ceramic balls the tanks height is higher than 30m, the desirable height to avoid heat loss [125], for a tank ratio of 2.5 . With a particle diameter of 2.88 cm and threshold temperature of 200°C, the effective heat extraction time can reach 11.15 h and 13.27 h for 75% of extraction as illustrated in figure. 4. 36. This is similar for the various ceramic balls with different volumetric heat capacity. Regarding the discharge time the model performs well. However, the discharge efficiency has been underestimated (Table. 8). Thus, a large tank minimizes heat losses compared to small tank as mention in [49]. However, the tank volume is high to generate a maximum electricity of 26.54 MWh_e a day compare to the Solar One storage tank volume (30603.4 m^3) which store 28 MWh_e a day [83]. This is due to the limitation of JCO working temperature at 210°C.

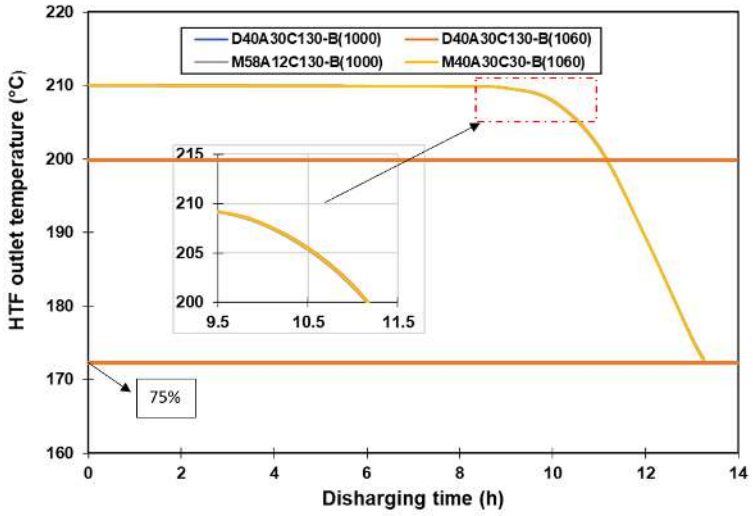

Figure. 4. 36. Discharge time of the storage 14.8 MW_{th}.

Table 4. 8.Discharge efficiency of the 14.8 MW_{th} storage tank.

Ceramic	η_{disch}(%)
D40A30C130-B (1000)	94.05889
D40A30C130-B (1060)	94.55009
M40A30C30-B (1060)	94.24685
M58A12C130-B (1000)	94.06919

To reduce the tank height, the effect of tank ratio on discharge efficiency has been accesses and illustrated as follows:

Table 4. 9.Effect of tank ratio on discharge efficiency.

Ceramic	H/D=1			H/D=1.5			H/D=2			H/D=2.5		
	η_{disch}(%)	D_i(m)	H_i(m)	η_{disch}(%	D_i(m)	H_i(m)	η_{disch}(%	D_i(m)	H_i(m)	η_{disch}(%	D_i(m)	H_i(m)
D40A30C130-B (1000)	93.30	18.9	18.9	93.70	16.51	24.76	93.95	15	30	94.06	13.93	34.81
D40A30C130-B (1060)	93.83	19.40	19.40	93.97	16.95	25.43	94.25	15.40	30.80	94.55	14.3	35.74

M40A30C30-B (1060)	93.27	19.08	19.08	93.92	16.67	25	93.94	15.15	30.30	94.25	14.06	35.16
M58A12C130-B (1000)	92.97	18.67	18.67	93.40	16.31	24.46	93.76	14.82	29.63	94.07	13.75	34.38

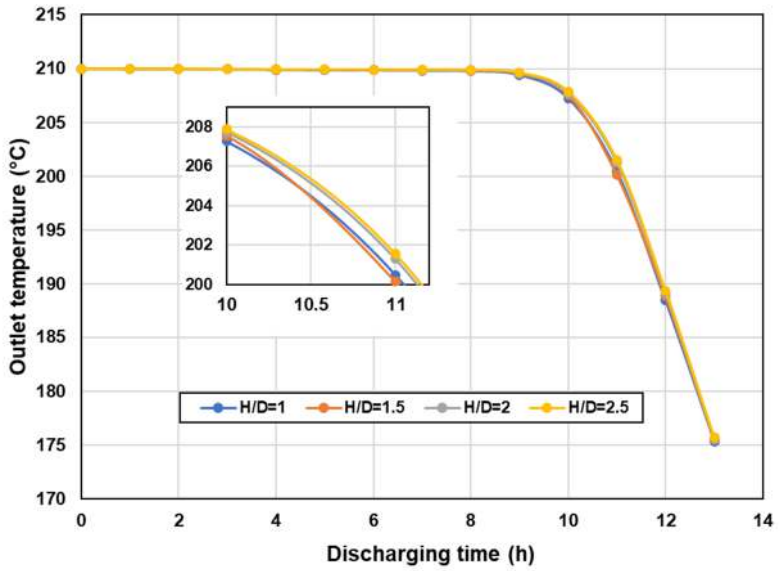

Figure. 4. 37: Effect of tank ratio on discharging time.

The effect of tank ratio on discharge efficiency, tank dimension and discharging time are illustrated respectively on table. 9 and figure. 4. 37. It can be observed that more heat losses occurred at low tank ration driving to discharging efficiency and effective time reduction. For a tank ratio from 1 to 2.5 a gain of 0.76%, 0.72%, 0.98% and 1.1% respectively for D40A30C130-B (1000), D40A30C130-B (1060), M40A30C30-B (1060) and M58A12C130-B (1000) occurred. So, a thin and tall vessel is more suitable to avoid heat losses. However, it will be complexed to build up to 30 meters tall tanks [68]. Therefore, a tank ratio of 1 or two tanks in series with the required vessel volume can be built with maximum 1.1% reduction of discharge efficiency.

Conclusion

An analysis of the performance of a packed bed thermal energy storage system has been conducted in this chapter using a one-dimensional, two-phase basic model. The model validation shows a maximum relative error of 6.44% and 2.41% respectively for rapeseed-quartzite oil and molten

salt-quartzite thermocline storage system. After the validation of the model the new thermocline energy storage sytem (ceramic balls-JCCO) performance has been assessed. The findings indicate that in order to prevent a higher heat discharge rate and a quicker rate of thermocline thickness deterioration, low fluid velosity is necessary. For a tank porosity of 41% of a 2 MWh_{th} tank, the fluid velocity should be less than $6.2510^{-4} m.s^{-1}$ to achieve an effective discharge time of 9 h. For a fluid velocity of $8.3310^{-4} m.s^{-1}$, particle diameter did not affect enough the discharging time while increasing the tank porosity by 10% reduce the discharging time by 0.8 h . And increasing the volumetric heat capacity of the filler material increase by 0.75 $MJ.m^{-3}K^{-1}$ can increasies by1h the discharge duration. However, for the particle diameter an effective thermocine thickness and efficiency can be achieved with particle diameter less than 2 cm. Morever, a tank porostiy less or equal to 45% is required for the new storage system. The analysis of the TES performance using different filler material shows that the thermal conductivity ratio and volumetric heat capacity ratio of the filler material and HTF can affect the TES effectiveness. Because there is a slight improvement of the dicharge efficiency with low thermal conductivity ratio. The ceramic balls developed from sand clay and coal bottom ash could be used as filler material for thermocline energy storage with disharge efficiency of 90% for fluid velocity less than $8.3310^{-4} m.s^{-1}$ and tank porosity less than 45%. For fluid velocity less than $6.10^{-4} m.s^{-1}$, a minimum effective disharge time of 8 h is achievable with total discharge time of 10 h for 2 MWh_{th} thermal storage tank. Regarding the size of the 14.8 MWh_{th} storage tank, two tank should be put in series, reducing the storage time to 6h or reducing the storage capacity to 7.4 MWh_{th} to avoid complex manufacturing of the tank and risk during the management of the plant. These solutions will reduce the tank height to a value less than the maximum height which is limiter to 14 m in engineering studies [204]. In the other hand, the tank radius can be incresed up to 22.08 m [204].

Chapter 5: Thermal performance analysis of parabolic trough collector using a vegetable oil as heat transfer fluid under different climate conditions

Introduction

To store thermal energy, a heat source is needed. This source can come from the combustion of coal, natural gas, hydrocarbons, biomass, waste heat, underground and solar energy. Solar energy is used in this study. Using solar energy to produce heat and generate electricity requires a solar concentrator whose output temperature depends on its configuration and concentration factor [29], [205]–[207]. Those collectors are parabolic trough collector (PTC), linear Fresnel, heliostat and parabolic collector. Among these collectors the PTC is most mature (95% of CSP installed) and attractive for electricity generation [208]. PTC has been long term proved durability and reliability with modular components and compatible with combined cycle. This chapter will be focused on the performance analysis of PTC under Ouagadougou and Agadez climate conditions using Jatropha curcas oil as HTF.

I. Reminder on some heat transfer fluid used as heat transfer fluid in PTC including vegetable oils.

A parabolic trough solar collector consists of a group of reflectors that are curved in one dimension in a parabolic shape to focus sun rays on to an absorber tube mounted in the focal line. In most cases of PTC plant it is fitted with an integrated sun-tracking system which allows the reflectors and the absorber tubes to track the sun from sunrise to sunset [29]. These reflectors are usually mirroring metals made of iron-poor glass. They are covered with a silver film on the underside and a special protective coating. The figure. 5. 1 illustrates first industrial PTC system in Cyprus [205].

Figure. 5. 1. Collector of the first industrial PTC system in Cyprus [205], [209]

In an ideal case, the PTC reflector receives light rays all perpendicular to its optical axis. They are then all reflected by the mirrors towards the receiver. They then pass through the envelope and reach the absorber, which increases its temperature and transmits the absorbed energy to the transfer fluid. In this configuration (ideal), the efficiency of the collector is assumed to be 100% [198]. However, there are obviously optical and thermal optical losses and thermal losses, which reduce this value significantly [198].

In real condition, the sun has a finite size. The light radiation at a point cannot be modelled by a single ray but by a cone. The reflection is of the same form. Even in a case where the sun can be facing the collector, there are errors in tracking the sun. The light rays are therefore not perpendicular to the optical axis. The reflector has many imperfections, such as global or local curvature errors, which lead to reflection errors. Thus, not all the flux reaches the receiver [198]. Considering these conditions, the collector efficiency cannot reach 100%. In addition, the thermal performance of the PTC could depend on HTF. Synthetic oil such as therminol oil gives better performance than water (67.8% against 63.01%) [210]. And can better extracts energy compare to molten salt and water [211]. Economically, water is a better candidate because it has many advantages such as low cost and good thermal performance for small needs in the case of low temperatures [198]. The thermal performance of TES system using vegetable oils as thermal energy storage material in a DMT system has been demonstrated trough experimentations and simulations [86] and [212], but till now there is few study on PTC performance using vegetable oil as HTF. In 2008, Khan and Islam have investigated experimentally the performance of a

parabolic trough collector using Canola vegetable oil and waste vegetable oil as HTF [213]. Canola oil is food grade oil used in Canada. It is the most widely grown crops in Canada. With Canola oil, a thermal efficiency of 77.8% is achieved with the PTC of 1.8m length, width of 2.25 m and mass flow of 0.0176 kg/s against 37.67% for the waste vegetable oil [213]. This efficiency could be better because in a PTC demonstration or commercial plant the mass flow in a collector loop could be higher than $1kg.s^{-1}$ [205]. Also, the PTC thermal efficiency increases when the HTF mass flow increases [214] and [215], but the HTF inlet temperature increasing could lead to the decrease of the PTC efficiency [215]. Considering weather conditions, the direct normal Irradiance (DNI) is the main parameter which heat up the HTF and affects the PTC efficiency [216], [217]. Especially when a new heat transfer fluid needs to be used. So, it is important to address the performance of the PTC according to the climate conditions before implementing a PTC project. Especially if a new HTF have to be used. In addition, high ambient temperature could improve the PTC thermal efficiency [215]. But, the effect of wind speed could be low on PTC thermal performance whatever the type of fluid [210]. From the literature, till now there is no study on the PTC performance using Jathopha curcas oil as heat transfer fluid. The present chapter will be focused on dynamic modelling and simulation of PTC performance under Ouagadougou and Agadez climate conditions respectively in Burkina Faso and Niger using JCO as heat transfer fluid. Due to the limitation in temperatures, the most effective steam generation cycle is Organic Rankine cycle. In a solar power plant two different types of Rankine cycle can be used: Steam Rankine cycle (ORC) and Organic Rankine Cycle (ORC).

A Steam Rankine cycle (SRC) use water as working fluid. For direct steam generation, water, the heat transfer fluid, is heated in the solar field and transformed into steam to run a steam turbine. It is possible to other types of heat transfer fluid, e.g., molten salts, thermal oil when the stem generation is indirect to transfer the stored heat to water by means of a heat exchanger. Systems using SRC offer 37-42% efficiency at temperatures between 300°C and 565°C [47] because SRC is the best option for medium/high temperature large heat sources. In large-scale power plants with a power range greater than 100 MW, SRC performs well [169]. SRC can be used for thermochemical storage with reactive storage material operating in this temperature range, but is not suitable for high temperature thermal storage (~1000°C). The SRC system requires the use of pipes supplied with water at high pressure, implying possible corrosion problems.

Organic Rankine cycle gives possibility to use plenty of fluids at medium/low temperature (150°C to 210°C) and it is suitable for waste heat recovery and the use of vegetable oils as heat transfer fluid. SRM and ORC share the same principle [169]. In ORC system organic fluids are used as working fluids efficiently at temperature less 300°C[197]. The four stages of a conventional Rankine cycle are:

- 1→2: adiabatic and reversible compression of water

- 2→3: isobaric and irreversible water vaporization

- 3→4: adiabatic and reversible steam expansion

- 4→1: the isobaric and irreversible liquefaction of steam

The figure illustrates the main component of a parabolic trough collector plant including the steam generation system

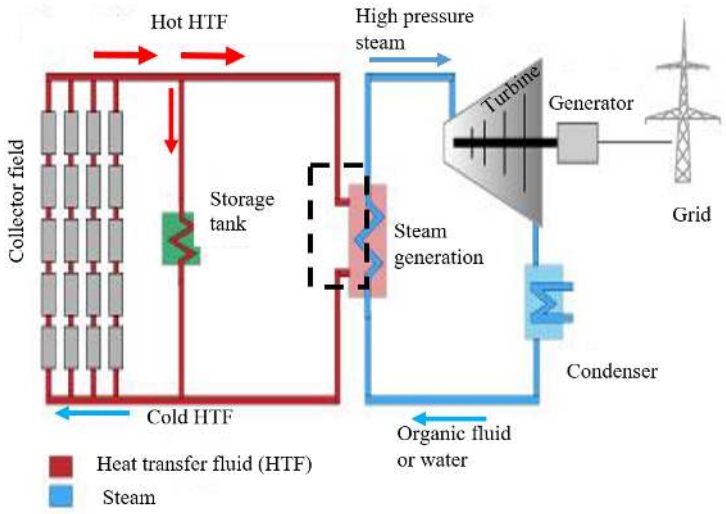

Figure. 1. 21. Solar power plan with storage and Rankin cycle [47].

I.2. Study area

The both cities, Ouagadougou and Agadez are located respectively in Sudano-Sahelian and Sahelian climates.

I.2.1. Study area in Ouagadougou

The landfill site of Ouagadougou city has been chosen for the installation of the weather station. The site has been chosen due to the important emission of methane from waste [218]. According

to Haro et al., the geospatial methane (CH_4) average emission rate from the landfill of Ouagadougou was 657 $mgm^{-2}.h^{-1}$ in 2017 and 1210 mg m^{-2} h^{-1} in 2018 [219] with a concentration ranging between 35% to 60% from one well to another. As the required minimum concentration of methane from the landfill to generation electricity is 35% using microturbine [220], it is obvious that the CTVD has high potential in biogas emission. So, conducting research on CSP potential and the PTC performance assessment under the climate conditions of the CTVD will be a great opportunity to know the possibility of developing a hybridization technology (CSP and biogas) at the landfill of Ouagadougou. The "Centre National de Valorisation et de Traitement de Déchets (CTVD)" is in the North of Ouagadougou at around 5 km away from the city hall and has been subject of several research. The geographical coordinates of the site are 12°25′12" North and 1°30′51" West. The landfill sites for non-hazardous waste produce biogas by anaerobic degradation of the organic fraction of landfilled waste. This biogas is mainly composed of methane (CH4) and carbon dioxide (CO2), two greenhouse gases, represent a major environmental challenge [218].The methane can be recovered by using it as backup to produce an addition heat in a CSP plant reducing the carbon footprint.

Figure. 5. 2 and Figure. 5. 3 illustrate the top view and the location of the landfill respectively in Ouagadougou.

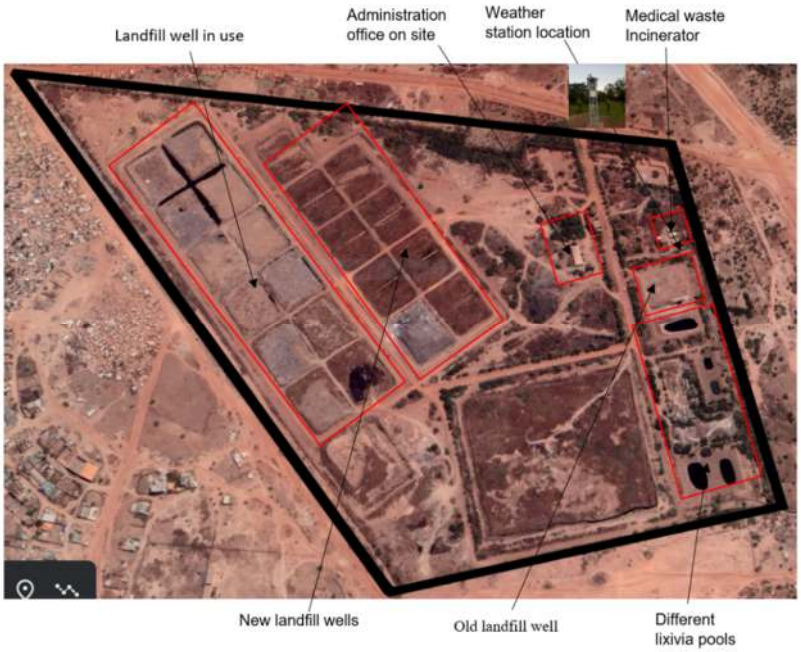

Figure. 5. 2. Top view of the landfill of Ouagadougou.

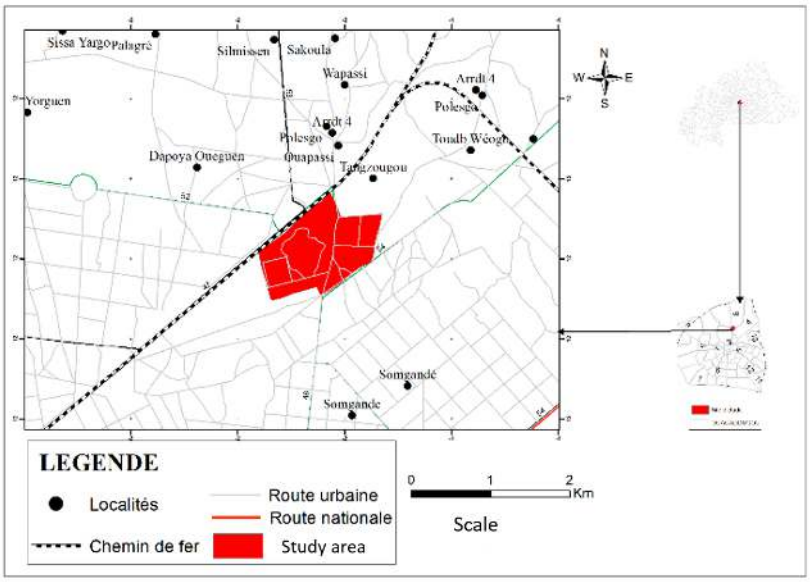

Figure. 5. 3. Location of Polesgo landfill in Ouagadougou city.

Real time DNI data have been collected on the landfill using a weather station funded by Cuomo Foundation and the Intergovernmental Governmental Panel on Climate Change (IPCC).

I.2.2. Weather station description

The station has been supplied by GEONICA company in Madrid from Spain. The station is composed of datalogger, sun tracker, a GPS and the overall mounted on a tower.

I.2.2.1. Data logger.

The datalogger is a METEODATA/HYDRODATA-3008C and 3016C models equipped with 8 and 16 analogue input channels for sensors connexion [221] . Currently, only DNI data is recorded by the station. The energy is supplied to the METEODATA by a PV panel of 100 Wp as illustrated in the figure.5. 7.

I.2.2.2. Sun Tracker-2000

The Model SunTracker-2000 is a lightweight, two-axis completely automatic solar tracker that may be used from any location on Earth's surface to align solar radiation sensors with the Sun's normal incidence. The SunTracker-2000 can be fitted with one or two pyrheliometers to measure direct solar radiation, and a pyranometer to measure global radiation.

The **SunTracker-2000** allows to mount one or two pyrheliometers for the measurement of the Direct solar radiation, as well as one pyranometer for the measurement of the Global radiation. An optional support and shading assembly can also be installed when Diffuse radiation is necessary. Figure. 5. 4 illustrated the associated Datalogger METEODETA 2000/3000

Figure. 5. 4. Associated sun tracker and Datalogger [221]

I.2.2.3. Sun sensor: Pyrheliometer

The pyrheliometer is a Hukseflux model DR15 pyrheliometer is an ISO 9060 spectrally flat Class B (old ISO classification "first class") instrument[222]. It offers the highest accuracy and highest data availability, window heating at low offsets. DR15 is applied in high-accuracy measurements of the solar radiation received by a plane surface from a 5 ° full field of view angle. It is necessary to keep the instrument pointed at the sun by using a two-axis tracker. The DR15 pyrheliometer has a small collimated tube, a thermopile sensor with a black coated surface, and a precisely machined and polished quartz window. It is directly compatible with widely used data logging systems. DR15 just requires 1 W to prevent frost and dew from growing on its window. The external housing of the DR15 pyrheliometer is shown in Figure 5. 5.

Figure. 5. 5. DR15-A1 C/ass 8 pyrheliometer: the externa/ housing [222]

The pyrheliometer is used in tracker-mounted operation. Using DR15 pyrheliometer is easy. It can be connected directly to commonly used data logging systems. The irradiance, E, in W/m^2 **is** calculated by dividing the DRl5 output, a small voltage U, by the sensitivity S. The sensitivity is provided with DR15 on its calibration certificate. The central equation governing DR20 and DRl5 is (5. 1)

$$E= U/S. \quad (5.\ 1)$$

Figure. 5. 6 and Figure. 5. 7 illustrate respectively the connection of the sun tracker and GPS to the datalogger and the weather station after mounting on the tower.

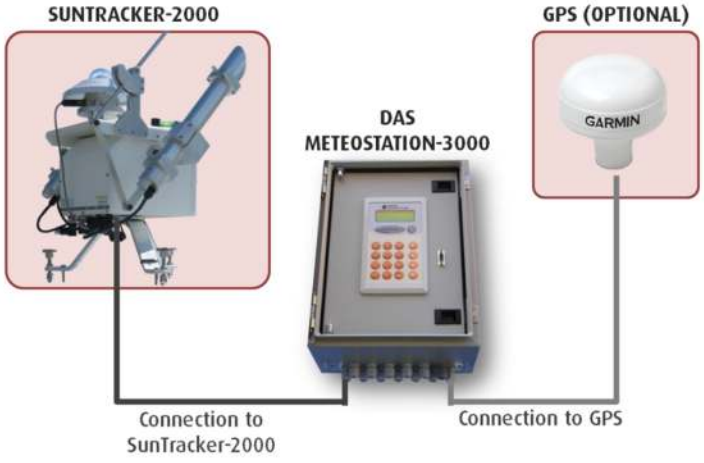

Figure. 5. 6. The data collection system.

Figure. 5. 7. The weather station installed at the Waste management and valorisation centre of Ouagadougou.

I.2.2. Agadez study area

According to the information collected from the Regional Directorate of the Environment of Agadez, the locality of Tchirozérine (study area) is located at about 45 km away from the North-East of the urban commune of Agadez. The study area is located between 17°15'33" North latitude and 7°49'52" East longitude. The site covers an area of 50.539 km². It is located at 517 m above sea level. In addition to the high potential of CSP in the region, the coal bottom ash landfill is located at Tcherirozérine which can be used for TESM development as demonstrated in [53][167]. Moreover, the region has a coal power plant which can be connect to a CSP (use of coal as backup) plant for low carbon transition in this region. But up to now there is no data on CSP technologies performance in Agadez region. If the technology is well mastered, it could help our governments

or donors to take decisions in this direction. Figure. 5. 8 illustrates the study area in the region of Agadez.

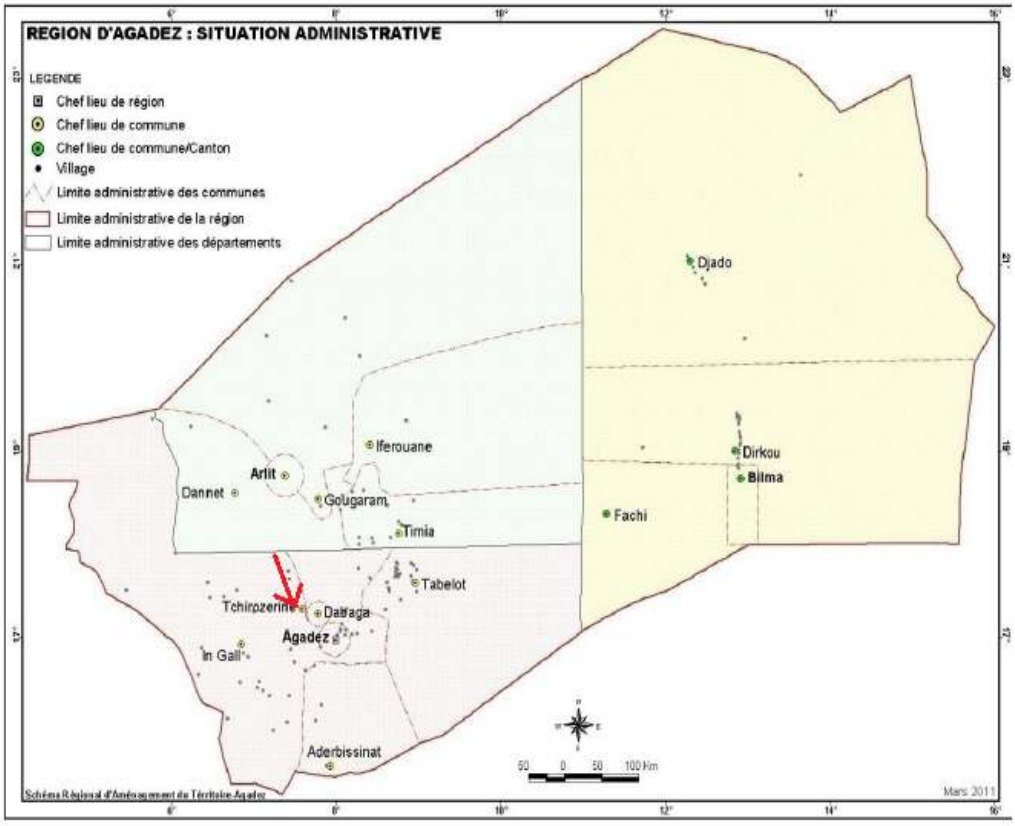

Figure. 5. 8. Location of the study area from Agadez region in Niger.

As said previously DNI data from TCHERIROZÉRINE could be collected using Kasten and Czeplak(1980), model [223].Kasten model cannot take into account the real time weather conditions, but allows to avoid high deviation on the PTC thermal performance analysis when DNI data from this model [15]. To expect more accurate performance of the PTC analysis, daily data have been collected from Photovoltaic Geographical Information system (PVGIS) [224]. Data on solar radiation and photovoltaic (PV) system performance is available for any place in Europe, Africa, and a significant portion of Asia and America through PVGIS. With PVGIS, hourly data can be gathered till 2020.

I.3. Mathematical model of the PTC

I.3.1. Assumption

In this study, various simplifying assumptions were considered and listed below to reduce the complexity of the problem related to heat transfer phenomena.

- The thermal properties of the absorber pipe and the glass of the receiver is assumed to be constant,
- Only heat transfer by radiation is considered between the absorber and the glass,
- The wind speed and ambient temperature are constants with mean value of $3 m.s^{-1}$ and 35°C respectively,
- The regime is quasi-study,
- The fluid is incompressible with unidirectional flowing,
- The repartition of solar radiation over the absorber tube is uniform.
- The temperature distribution within the absorber is linear to limit heat losses,
- The thermophysical properties of the fluids vary according to temperature.

Considering these assumptions, the physical model can be designed as illustrated in

Figure. 5. 9

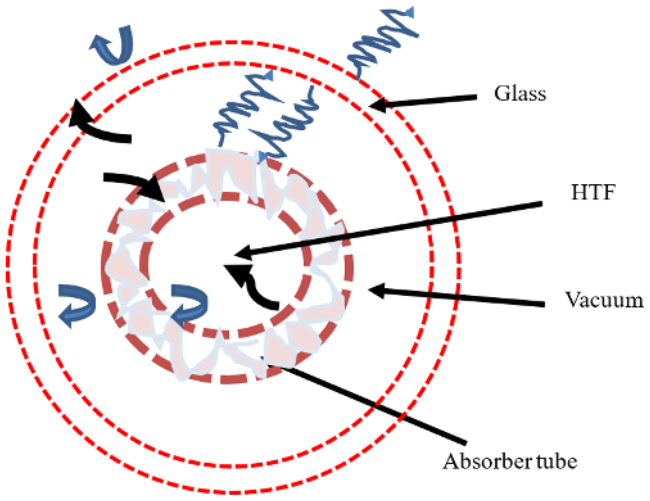

Figure. 5. 9. Cross-section of the receiver model with the various heat transfer phenomena.

I.3.2. Mathematical model

Energy balance equations for the different components of the receiver have been written as follows.

For the heat transfer fluid (HTF) energy balance:

The energy balance equation applied to the transfer fluid contains a stored term, an advective term, an axial diffusion term and a convection term with the absorber tube [225]. The energy balance for the fluid is written in equation (5. 2).

$$\dot{Q}_{store,f} + \dot{Q}_{adv,f} = \dot{Q}_{diff,f} + \dot{Q}_{f\to a} \quad (5.\ 2)$$

$\dot{Q}_{store,f}$ is the quantity of heat store in the oil and can be expressed in equation (5. 2)

$$\dot{Q}_{store,f} = \varepsilon(\rho c_p)_f(\frac{\partial T_f}{\partial t})\ . \quad (5.\ 3)$$

$\dot{Q}_{adv,f}$ is the flux advection flow of the fluid which transports the fluid substance and heat (energy) by bulk motion.

$$\dot{Q}_{adv,f} = \varepsilon(\rho c_p)_f u\frac{\partial T_f}{\partial x} \quad (5.\ 4)$$

$\dot{Q}_{diff,f}$ is the thermal diffusion flux within the fluid expressed in equation (5. 5).

$$\dot{Q}_{diff,f} = \lambda_f \frac{\partial^2 T_f}{\partial x^2} \quad (5.\ 5)$$

$\dot{Q}_{f\to a}$ is the convection flow between the fluid and the absorber and expressed in equation (5. 6).

$$\dot{Q}_{f\to abs} = h_{abs\to f} * \frac{s_{a,f}}{V_f} * \left(T_f - T_a\right) \quad (5.\ 6)$$

The equation (5. 2) becomes equation (5. 7)

$$(\rho c_p)_f(\frac{\partial T_f}{\partial t} + uC_f\frac{\partial T_f}{\partial z}) = \lambda_f[\frac{\partial^2 T_f}{\partial z^2}] + h_{a\to f} * \frac{s_{a,f}}{V_f} * \left(T_a - T_f\right)\ . \quad (5.\ 7)$$

Each term is expressed in watts per cubic meter.

where ρ represents the density, c_p, the heat capacity, s, the cross- sectional area, T, the temperature, u, the HTF velocity, x, the axial distance along the collector, $h_{a\to f}$, the convective heat transfer coefficient inside the pipe.

For the absorber pipe

The energy balance (equation (5. 8) for the absorber tube has similar terms but also includes absorbed solar power, radiation between absorber and glass envelope and conduction losses. Each term is expressed in watts per cubic meter of absorber tube. Conduction heat loss per unit length is neglected because it influences slightly collector efficiency [225].

$$\dot{Q}_{abs,a} = \dot{Q}_{store,a} + Q_{diff,a} + \dot{Q}_{convec,a\to f} + \dot{Q}_{rad,a\to g} \quad (5.\ 8)$$

$\dot{Q}_{abs,a}$ is the energy from sun radiation absorbed by the absorber expressed equation (5. 9)

$$\dot{Q}_{abs,a} = \frac{p_{abs}}{V_a} \quad (5.\ 9)$$

The solar radiation absorbed by the absorber is computed by equation (5.10)

$$P_{abs,a} = \alpha_a \times \tau_g \times \rho_0 \times \gamma \cdot DNI \cdot Acoll \quad (5.\ 10)$$

Where α_{abs} is absorption of the absorber and τ_{glass} transmittivity of the glass envelope, ρ_0 the reflection factor of the reflector and γ the shape factor.

The concentration factor is computed using equation (5. 11)

$$C = \frac{A_{coll}}{A_{receiver}}. \quad (5.\ 11)$$

with C concentration factor.

$$\eta op = \alpha_a \times \tau_g \times \rho_0 \times \gamma \quad (5.\ 12)$$

$\dot{Q}_{store,abs}$ is the quantity of heat stored in the absorber and can be expressed as follows

$$\dot{Q}_{store,abs} = (\rho c_p)_a(\frac{\partial T_a}{\partial t}). \quad (5.\ 13)$$

$\dot{Q}_{diff,abs}$ is the thermal diffusion flux within the absorber expressed in equation (5. 14)

$$\dot{Q}_{diff,a} = \lambda_a \frac{\partial^2 T_a}{\partial z^2} \quad (5.\ 14)$$

$\dot{Q}_{a\to f}$ is the convection flow between the absorber and the fluid expressed in equation (5. 15)

$$\dot{Q}_{convec,a\to f} = h_{a\to f} * \frac{s_{a,f}}{V_a} * \left(T_a - T_f\right) \quad (5.\ 15)$$

$\dot{Q}_{rad,a\to g}$ is the radiative heat flow between the absorber and glass expressed in equation (5. 16)

$$\dot{Q}_{rad,a\to g} = \frac{s_{a,f}}{V_a} \times h_{r(int)} \times (T_a^4 - T_g^4) \ . \quad (5.\ 16)$$

The energy balance for the absorber pipe becomes expressed equation (5. 17)

$$(\rho c_p)_a(\frac{\partial T_a}{\partial t}) = \lambda_a[\frac{\partial^2 T_a}{\partial z^2}] + h_{a\to f} * \frac{s_{a,f}}{V_a} * \left(T_f - T_a\right) + \frac{s_{a,f}}{V_a} \times h_{r(int)} \times (T_g^4 - T_a^4) + \frac{p_{abs}}{V_a} \quad (5.\ 17)$$

Equation (5. 18) can be used to calculate the radiation heat transfer coefficient between the absorber tube and glass envelope.

$$h_{r(int)} = \varepsilon_{int}\sigma * [(T_a + 273)^2 + \left(T_g + 273\right)^2](T_a + T_g + 546) \quad (5.\ 18)$$

ε_{int} the internal emissivity writing in equation (5. 19)

$$\varepsilon_{int} == \frac{(\frac{D_{g(int)}}{D_{a(ext)}})}{\frac{1}{\varepsilon_a} + \frac{1-\varepsilon_g}{\varepsilon_g}} \quad (5.\ 19)$$

Where ε represents emissivity, σ is the Stefan-Boltzmann constant.

The convective heat transfer coefficient was computed using equation (5. 20).

$$h_{a\to f} = \frac{k_f}{Dint_{(a)}} Nu_f \quad (5.\ 20)$$

with k_f fluid thermal conductivity and Nu_f Nussle number.

This number was computed using equation (5. 21)

$$Nu_f = [(3.66)^3 + (0.7)^3 + \left(1.615\sqrt[3]{(Re_f} \times Pr_f \times d\right) - 0.7)^3 + ((\frac{2}{1.22\times Pr_f})^{\frac{1}{6}} \times \sqrt{(Re_f \times Pr_f \times d)})^3]^{1/3}. \quad (5.\ 21)$$

$$Re_f = \rho_f \times \frac{D_{a(int)}}{\mu_f} \times u_f. \quad (5.\ 22)$$

$$u_f = \frac{4\dot{m}_f}{\pi {D_{a(int)}}^2} \ . \quad (5.\ 23)$$

$$h_{(int)} = h_{c(int)} + h_{r(int)} \quad (5.\ 24)$$

The straightforward application of the natural convection relations between two horizontal, concentric cylinders results from the examination of the heat exchanges between the two walls (the glass and absorber).

In this instance, the heat transfer coefficient is provided by equation (5. 25).

$$h_{c(int)} = \frac{2 \times K_{eff}}{D_{a(ext)} \times \ln(\frac{D_{g(int)}}{D_{abs(ext)}})} \quad (5.\ 25)$$

With $K_{eff} = 0.386 \times \lambda_{air} \times (\frac{Pr_{air}}{0.861+Pr_{air}})^{\frac{1}{4}} \times (Rac)^{\frac{1}{4}}$. (5. 26)

$$Ra_c = \frac{(\ln(\frac{D_{glas(in)}}{D_{abs(ext)}})}{L_{eff}{}^3 (D_{ab(ext)}{}^{-\frac{3}{5}} + D_{v(int)}{}^{-\frac{3}{5}})^5} \times Ra_{eff}. \quad (5.\ 27)$$

$$L_{eff} = \frac{D_{g(in)} - D_{ab(ext)}}{2}, \quad . \quad (5.\ 28)$$

$$Ra_{eff} = Gr_{air} \times Pr_{air}. \quad (5.\ 29)$$

Similarly, the energy balance on the glass envelope is computed:

For the glass envelope, there are in addition to the terms of accumulation and axial thermal diffusion a term of losses with the environment at ambient temperature and a term of losses by radiation to the sky. The energy balance in the glass envelope is represented by equation (5. 30) [198],[210],[202] and[220].

$$\dot{Q}_{abs,g} = \dot{Q}_{store,g} + \dot{Q}_{diff,g} + \dot{Q}_{rad,g \to a} + \dot{Q}_{rad,g \to sky} + \dot{Q}_{g \to amb} + \dot{Q}_{g \to \infty} \quad (5.\ 30)$$

$\dot{Q}_{abs,}$ is the energy from sun radiation absorbed by the glass expressed in equation (5. 30).

$$\dot{Q}_{abs,g} = \frac{p_{abs}}{V_g} \times \frac{\alpha_g}{\alpha_a \times \tau_g} \quad (5.\ 31)$$

$\dot{Q}_{store,g}$ is the quantity of heat stored in the glass envelope expressed equation (5. 32).

$$\dot{Q}_{store,g} = (\rho c_p)_g (\frac{\partial T_E}{\partial t}). \quad (5.\ 32)$$

$\dot{Q}_{diff,g}$ is the thermal diffusion flux within the glass expressed in equation (5. 33).

$$\dot{Q}_{diff,g} = \lambda_g \frac{\partial^2 T_g}{\partial z^2} \quad (5.\ 33)$$

$\dot{Q}_{rad,g \to a}$ is the radiative heat flow between the absorber and glass expressed in equation (5. 34).

$$\dot{Q}_{rad,a\to g} = \frac{S_g}{V_g} \times h_{r(int)} \times (T_g^4 - T_a^4) \ . \quad (5.\ 34)$$

$\dot{Q}_{comv,g\to amb}$ is the convective heat flow loss between the glass and ambient air expressed equation (5. 35).

$$\dot{Q}_{conv,g\to amb} = h_{conv(ext)} \times \frac{S_{g,amb}}{V_g} * \left(T_g - T_{amb}\right) \quad (5.\ 35)$$

$\dot{Q}_{g\to\infty}$ is the radiative heat flow between the glass and sky computed by equation (5. 36).

$$\dot{Q}_{g\to\infty} = \sigma \times \varepsilon_E \times \frac{S_{g,amb}}{V_g} (T_g^4 - T_{sky}^4) \quad (5.\ 36)$$

The energy balance for the glass envelope becomes:

$$(\rho c_p)_g(\frac{\partial T_g}{\partial t}) = \lambda_g[\frac{\partial^2 T_g}{\partial z^2}\} + \frac{S_{a,g}}{V_g} \times \frac{\sigma}{\frac{1}{\varepsilon_a}+\frac{1-\varepsilon_g}{\varepsilon_g}\left(\frac{r_{a,o}}{r_{g,i}}\right)} (T_a^4 - T_g^4) + \sigma \times \varepsilon_g \times P_{g,o}(T_{sky}^4 - T_g^4) + h_{conv(ext)} \times \frac{S_{g,amb}}{V_g} * \left(T_{am} - T_g\right) \quad (5.\ 37)$$

The radiation heat transfer coefficient between glass envelope and the sky is computed by equation (5. 38)

$$h_{r(ext)} = \sigma \times \varepsilon_{ext} \times [\left(T_{sky} + 273\right)^2 + \left(T_g + 273\right)^2 + \left(T_{sky} + T_g + 546\right)] \quad (5.\ 38)$$

$$\varepsilon_{ext} = \frac{\sigma}{\frac{1}{\varepsilon_a}+\frac{1-\varepsilon_F}{\varepsilon_g}\left(\frac{r_{A,o}}{r_{glass,i}}\right)} \quad (5.\ 39)$$

$$T_{sky} = 0.0553 * T_a^{1.5} \quad (5.\ 40)$$

$$h_{v(ext)} = C \times Re_{air}^n \times Pr_{air}^m \times (\frac{Pr_{va}}{Pr_{airglout}})^{\frac{1}{4}} \times \frac{k_{air}}{D_{g(ext)}} \quad (5.\ 41)$$

$$h_{v(ext)} = C \times Re_{air}^n \times Pr_{air}^m \times (\frac{Pr_g}{Pr_{air}})^{\frac{1}{4}} \times \frac{k_{air}}{D_{g(ext)}} \quad (5.\ 42)$$

C and m are constants that depend on Reynolds number [210]

$$Re_{air} = \frac{u_{air\times D}}{\mu_{air}} \quad (5.\ 43)$$

$$h_{(int)} = h_{c(int)} + h_{r(int)} \quad (5.\ 44)$$

$$h_{r(int)} = \sigma \times \varepsilon_{int} \times [(T_a + 273)^2 + (T_g + 273)^2 + (T_a + T_g + 546)] \quad (5.\ 45)$$

where sky denotes the temperature of the sky that the system radiates, and air denotes the characteristics of the ambient air.

I.3.3. Boundary and initial conditions

Initial conditions of PTC are given in equations (5. 46) and (5. 47).

$$T_f(t = 0) = T_a \quad (5.\ 46)$$

$$T_g(t = 0) = T_{ambient} \quad (5.\ 47)$$

The boundary conditions only take into account one at the collector's intake and one at its outflow because the numerical models only take into account one-dimensional media. The cold fluid enters the collector from the cold pump, which means inlet temperature and leave the collector from the outlet after being heated up. At the collector inlet boundary conditions were based on equations (5. 48) and (5. 49)

$$T_f(x = 0) = T_L \quad (5.\ 48)$$

$$\frac{\partial T_f}{\partial x}(x = 0) = \frac{\partial T_a}{\partial x}(x = 0) = 0 \quad (5.\ 49)$$

Hot heat transfer fluid leaves the collector, an adiabatic condition for the fluid.

$$\frac{\partial T_f}{\partial x}(x = L_a) = \frac{\partial T_a}{\partial x}(x = L_a) = \frac{\partial T_g}{\partial x}(x = L_g) = 0 \quad (5.\ 50)$$

If DNI is less than the minimum sunshine value to heat up the fluid, the outlet temperature is less than $\boldsymbol{T_{inlet}}$ and is illustrated as illustrates on figure. 5. 10

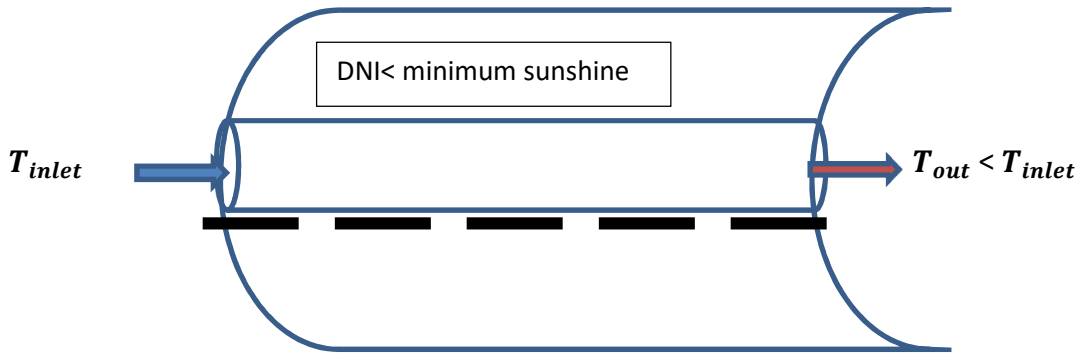

Figure. 5. 10. Solar collector.

II. Development of a controlling model of parabolic trough plant: connection of the collector to the new TES system and dynamic charging

The entire energy system is comprised of more than just the TES system. Therefore, to understand how the storage components interact with the other components of the system, dynamic modelling of the entire system is required (Figure 5. 11). In this chapter, the focus of the simulation is on the TES system and how it is dynamically charged when connecting to the solar field.

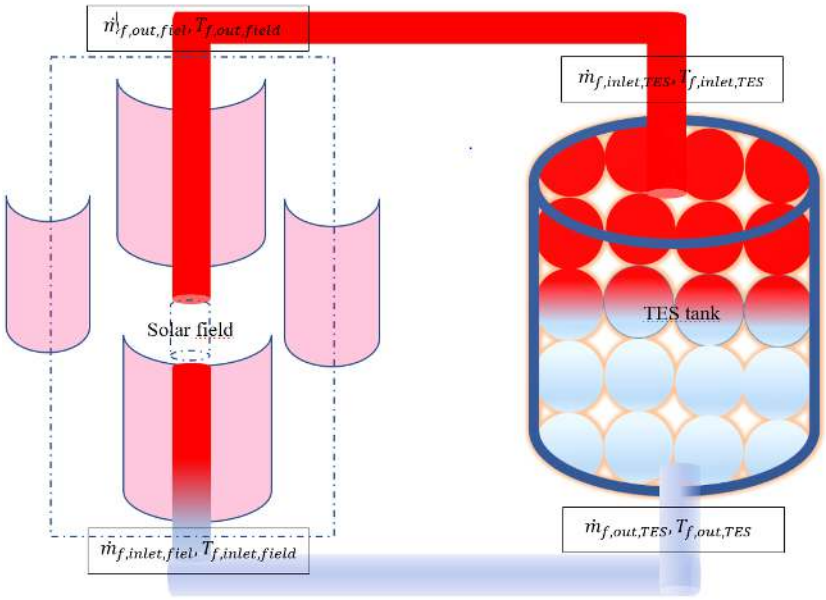

Figure. 5. 11. Overview of the solar field connection to the storage system.

II.1. Mathematical model

For the solar field the energy balance equations for the different component of the collector have been written as follows:

For the heat transfer fluid (HTF) energy balance:

The energy balance equation applied to the transfer fluid contains a stored term, an advective term, an axial diffusion term and a convection term with the absorber tube

absorber tube (Equation (5.51)). Each term is expressed in watts per cubic meter of fluid.

$$(\rho c_p)_f(\frac{\partial T_f}{\partial t} + uC_f\frac{\partial T_f}{\partial x}) = \lambda_f[\frac{\partial^2 T_f}{\partial x^2}] + h_{a\to f} * \frac{S_{A,f}}{V_f} * \left(T_a - T_f\right). \quad (5.\ 51)$$

For the absorber pipe

The energy balance (equation (5. 52)) for the absorber tube has similar terms but also includes absorbed solar power, radiation between absorber and glass envelope and conduction losses through the arms supporting the. Each term is expressed in watts per cubic meter of absorber tube. Conduction heat loss per unit length is neglected because it influences slightly collector efficiency [225] .

$$\left(\rho c_p\right)_a(\frac{\partial T_a}{\partial t}) = \lambda_a[\frac{\partial^2 T_a}{\partial x^2}] + h_{a\to f} * \frac{S_{a,f}}{V_a} * \left(T_f - T_a\right) + \frac{S_{a,f}}{V_a} \times h_{r(int)} \times (T_g^4 - T_a^4) + \frac{p_{abs}}{V_a}$$

(5.52)

The energy balance on the glass envelope is written as follows:

$$(\rho c_p)_g(\frac{\partial T_g}{\partial t}) = \lambda_g[\frac{\partial^2 T_g}{\partial x^2}\} + \frac{S_{a,g}}{V_g} \times \frac{\sigma}{\frac{1}{\varepsilon a} + \frac{1-\varepsilon_g}{\varepsilon_g}\left(\frac{r_{a,o}}{r_{g,i}}\right)}(T_a^4 - T_g^4) + \sigma \times \varepsilon_g \times P_{g,o}(T_{sky}^4 - T_g^4) + h_{conv(ext)} \times$$

$$\frac{S_{g,amb}}{V_g} * \left(T_{am} - T_g\right) \quad (5.\ 53)$$

The energy balance or conservation describing the thermal energy storage system can be writen as follow:

For the liquid phase, the energy balance is written in equation (5. 54)

$$\varepsilon(\rho c_p)_f(\frac{\partial T_f}{\partial t} + u\frac{\partial T_f}{\partial z}) = \lambda_{feff}[\frac{\partial^2 T_f}{\partial z^2}] + h_v\left(T_p - T_f\right) + 4\frac{U_W}{V_{total}}\left(T_{ext} - T_f\right). \quad (5.\ 54)$$

For the solid phase energy balance is:

$$(1-\varepsilon)(\rho c_p)_s(\frac{\partial T_s}{\partial t}) = \lambda_{peff}\frac{\partial^2 T_s}{\partial z^2} + h_v\left(T_f - T_p\right). \quad (5.\ 55)$$

II.2. Boundary and initial conditions

Initial conditions of PTC are:

$$T_f(t=0) = T_a \quad (5.\ 56)$$

$$T_g(t=0) = T_{ambient} \quad (5.\ 57)$$

The boundary conditions only take into account one at the collector's intake and one at its outflow because the numerical models only take into account one-dimensional media. The cold fluid enters the collector from the cold pump, which means inlet temperature and leave the collector from the outlet after being heated up. At the collector inlet

$$\boldsymbol{T_f(x=0) = T_{cold}} \quad (5.\ 58)$$

$$\frac{\partial T_f}{\partial x}(x=0) = \frac{\partial T_a}{\partial x}(x=0) = 0 \quad (5.\ 59)$$

Hot heat transfer fluid leaves the collector to the storage tank. An adiabatic condition for the fluid can be written as follows:

$$\frac{\partial T_f}{\partial x}(x=L_a) = \frac{\partial T_a}{\partial x}(x=L_a) = \frac{\partial T_g}{\partial x}\left(x=L_g\right) = 0 \quad (5.\ 60)$$

Boundary and initial conditions for the TES

Initial conditions of discharge are:

$$T_f(t=0) = T_p = T_{cold}(t=0) \quad (5.\ 61)$$

The boundary conditions during a discharge only take into account one on top and one on bottom of the tank because the numerical models only take into account one-dimensional media. The hot heat transfer fluid from the sun field enters the tank from the top, resulting in an adiabatic condition for the solid and the wall and an inlet temperature and velocity for the fluid conditions. On the bottom:

$$T_f(z=0) = T_{inlet} = T_{outlet,solar\ field} \quad (5.\ 62)$$

$$\frac{\partial T_f}{\partial z}(z=0) = \frac{\partial T_p}{\partial z}(z=0) = 0 \quad (5.\ 63)$$

Hot heat transfer fluid leaves the tank, an adiabatic condition for the solid and for the fluid.

$$\frac{\partial T_f}{\partial z}(z=H) = \frac{\partial T_p}{\partial z}(z=H) = 0 \quad (5.\ 64)$$

II.3. Numerical method

The difference finite method was used to numerically micritized the different equations. The backward differencing scheme was used for the first order derivative term, an implicit scheme was

used for time discretization while the central differencing scheme was used for the second order derivative terms as done in the fourth chapter. The solution was found using an iterative approach based on the Gauss-Seidel computational method to compute simultaneously the three temperatures (fluid, absorber and glass) along the receiver axis. The equations (5. 65) to (5. 67) were used for discretization.

$$\frac{\partial^2 \mathrm{T}}{\partial z^2} = \frac{T_{i+1}^{N+1} - 2 \times T_i^{N+1} + T_{i+1}^{N+1}}{\Delta z^2} \quad (5.\ 65)$$

$$\frac{\partial T}{\partial z} = \frac{T_i^{n+1} - T_{i-1}^{n+1}}{\Delta z} \quad (5.\ 66)$$

$$\frac{\partial \mathrm{T}}{\partial t} = \frac{T_i^{n+1} - T_i^{n}}{\Delta t} \quad (5.\ 67)$$

The convergence criterion was 10^{-3}. The numerical model was coded and computed using an open access software FORTRAN force2.

The figure. 5. 12 and figure. 5. 13 illustrate the flowchart for the PTC and the PTC-TES control model development in FORTRAN.

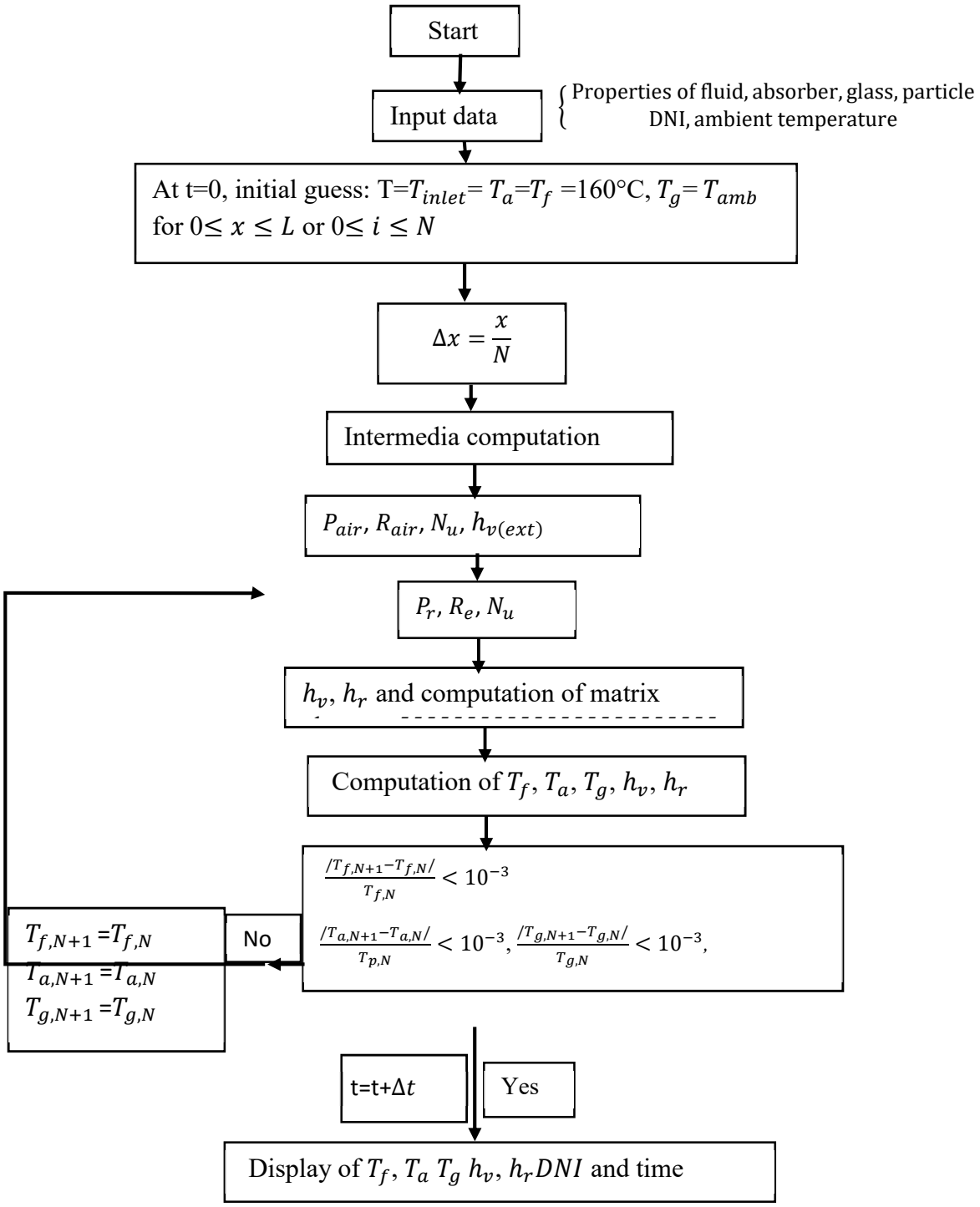

Figure. 5. 12. Flowchart for the PTC control model development in FORTRAN.

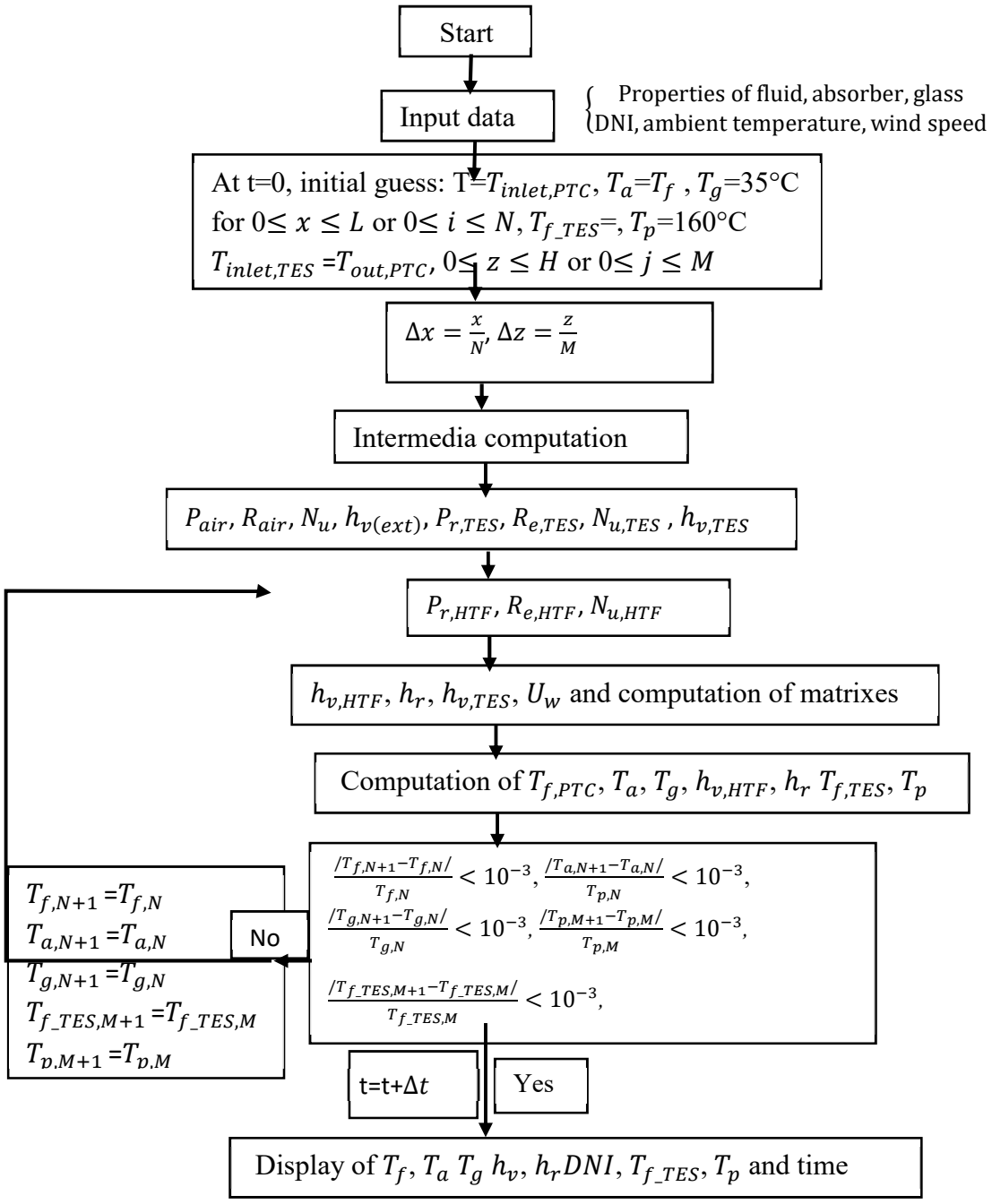

Figure. 5. 13. Flowchart for the PTC pant model development in FORTRAN.

III. Performance analysis method of the PTC

In this study the PTC performance using JCO as HTF was assessed based on instantaneous thermal and daily efficiencies. It is the ratio of the useful energy absorbed by the fluid by the solar energy intercepted by the solar collector aperture area and can be given by equation (5. 68) [225].

$$\eta_{th,inst} = \frac{\dot{m} \times c_{p,f} \times (T_{out} - T_{inlet})}{DNI \times A_{coll}} \quad (5.\ 68)$$

The thermal efficiency of PTC can be computed over the time and is normalized based on equation (5. 69) [210].

$$\eta_{th,norm} = \frac{\int Q_u dt}{A_{coll} \int DNI dt} \quad (5.\ 69)$$

Table 5. 1.Characteristic of the collector module.

Parameters	Characteristics
Absorber length (Labs)	7.8 m
Aperture of the concentrator (W)	5 m
Concentration factor (C)	22.42
Focal length (F)	1.84 m
Aperture angle (∅)	68.38°
Outside diameter of the absorber ($\boldsymbol{D_{a,ext}}$)	0.07
Inner diameter of the absorber ($\boldsymbol{D_{a,in}}$)	0.066
Outer diameter of the glass envelope ($\boldsymbol{D_{g,ext}}$)	0.115
Inner diameter of the glass envelope ($\boldsymbol{D_{g,in}}$)	0.109
Thermal conductivity of the absorber ($\boldsymbol{\lambda_a}$)	$54\ Jkg^{-1}K^{-1}$
Thermal conductivity of the glass envelope ($\boldsymbol{\lambda_g}$)	$1.2\ J.kg^{-1}K^{-1}$
Absorption of the absorber tube ($\boldsymbol{\alpha_a}$)	0.906
Absorption of the envelope ($\boldsymbol{\alpha_g}$)	0.02
Transmittivity of the glass envelope ($\boldsymbol{\tau_g}$)	0.95
Thermal capacity of the absorber ($\boldsymbol{c_{p,abs}}$)	$500\ .kg^{-1}K^{-1}$
Thermal capacity of the glass envelope ($\boldsymbol{c_{p,g}}$)	$1090\ Jkg^{-1}K^{-1}$

Absorber density ($\boldsymbol{\rho_a}$)	$8020\ kgm^{-3}$
Glass envelope density (($\boldsymbol{\rho_g}$)	$2230\ kgm^{-3}$
Emissivity of the absorber ($\boldsymbol{\varepsilon_a}$)	0.14
Emissivity of the glass envelope ($\boldsymbol{\varepsilon_g}$)	0.86
Reflection of the reflector ($\boldsymbol{\rho_0}$)	0.93
Shape factor	0.92

IV. Results and discussions

The modelling of a solar energy conversion chain requires input data characterizing the solar concentrator, the heat transfer fluid and weather data. These data are as follows: DNI, wind speed, fluid inlet temperature and operating fluid flow rate. The characteristics of the collector are presented in Table. 5. 1 [210] and [198]..

IV.1. Model validation

Before any performance analysis, it is important to validate the model, since all the experimental data in the literature are available. To validate the dynamic simulation model, seven simulation have been done using different fluid mass flows and direct normal irradiation used during seven tests done by Sandia National Laboratories in 1992. The simulation results obtained are compared with experimental output data (outlet temperature and difference temperature) obtained at the SNL Laboratory [210] and [216]. The heat transfer fluid is therminol VP-1[216] tested the 16th July 1992. Table. 5. 2 illustrates the outlet temperature results from experimentation and the one simulated from the built model. A maximum deviation of 8.087% has been observed showing that the simulation results are in agreement with the experimental results. The PTC performance analysis model has been furthered in this study compare to the model of Babikir et al., 2021 [210] with an relative error of 8.13%. In addition, in spite of some deviation, the PTC model generally predict the outlet temperature with an acceptable accuracy. Therefore, the present model can be used to simulate the PTC performance at dynamic state.

Table 5. 2.Comparison of the experimental and simulated outlet temperature.

case	DNI ($W.m^{-2}$)	$\dot{m}_f\ (kg.s^{-1})$	T_{inlet} (°C)	T_{out} (°C)	ΔT (model)	ΔT (exp)	Model error (%)

1	937.9	0.6206	297.8	317.46	19.66	19.1	2.932
2	933.37	0.678	102.2	122.237	20.037	21.8	8.087
3	920.9	0.5457	379.5	397.1	17.6	18.5	4.86
4	880.6	0.6205	299	317.27	18.27	18.2	0.38
5	909.5	0.6580	250.7	270.5	19.8	18.7	5.88
6	968.2	0.6536	151	173.35	22.35	22.3	0.224
7	982.3	0.6350	197.5	219.7	22.2	22	0.91

IV.2. PTC performance under Ouagadougou weather condition

The PTC performance in this chapter is assessed using an innovative vegetable oil as a new transfer oil. The thermal properties of this oil are illustrated in table 16 at chapter 4.

IV.2.1. Effect of DNI on PTC outlet temperature and thermal efficiency

The main weather parameters, the PTC need to heat the HTF up is the DNI. The capacity of the PTC to heat the fluid up could depend on the type of fluid, the mass flow, the DNI value and the collector length. The effect of DNI on the PTC performance has been assessed considering the dimension of the collector module with a length of 7.8m and aperture of 5m and JCO mass flow of 1 $kg.s^{-1}$ and inlet temperature of 160°C. The results show the DNI effect on the fluid outlet temperature and PTC thermal efficiency are illustrated on Figure. 5. 14 and Figure. 5. 15. It can be observed that, when the DNI increases the JCO outlet temperature (Figure. 5. 14) and the PTC thermal efficiency (Figure. 5. 15) increase. A minimum DNI value of 50 $W.m^{-2}$ is needed by the PTC module to heat JCO up with outlet temperature of 160.06°C and thermal efficiency of 11.37 %. The outlet temperature increases up to 174.21°C when the DNI increases to 1000 $W.m^{-2}$. The DNI increasing, increases the heat gained by the fluid (Figure. 5. 16) due to the increasing of absorber power. However, from 700 W upwards, the increase in DNI has little effect on the thermal efficiency of the collector, as it increases slightly, while the temperature and heat gain are still rising. The increase in temperature can lead to the increase of heat losses through diffusion, convection and radiation from the receiver to environment. Similar results are presented by Xu et al.,[226] under DNI dramatic variation where the instantaneous thermal efficiency exists between 45% and 20% for a DNI deviation of around 100 $W.m^{-2}$.

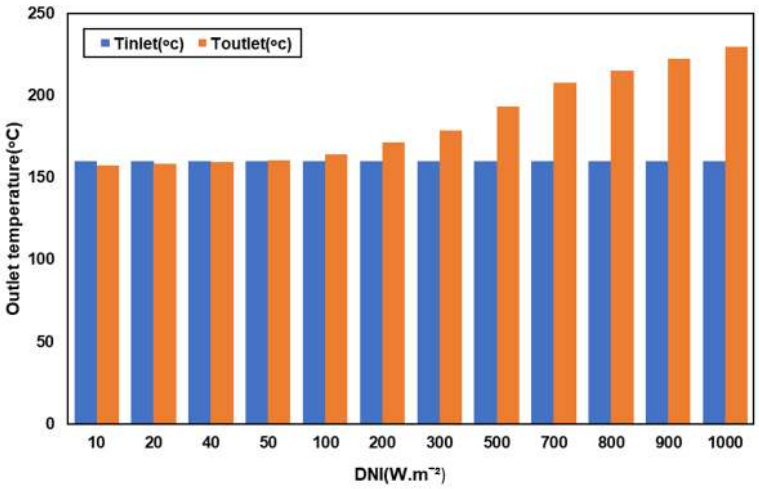

Figure. 5. 14. Effect of DNI on JCO outlet temperature

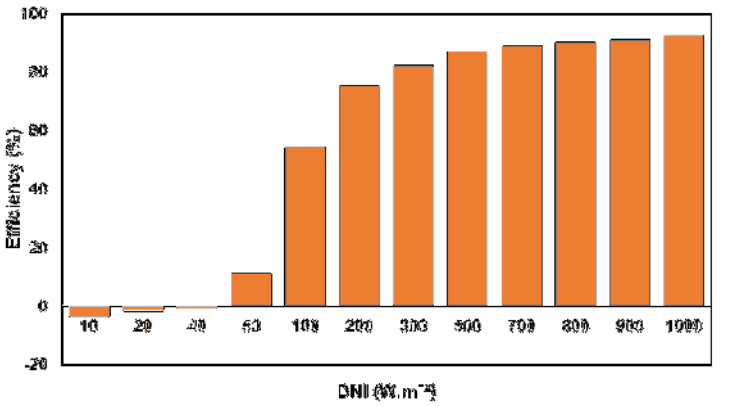

Figure. 5. 15. Effect of DNI on PTC thermal efficiency.

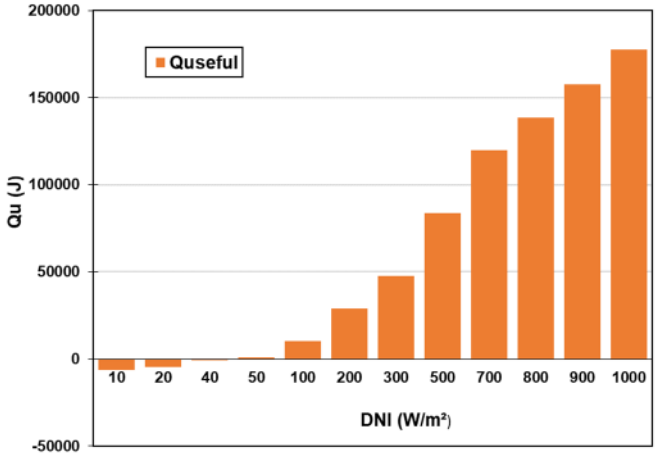

Figure. 5. 16. Effect of DNI on energy gained by the fluid.

IV.2.2. Direct normal irradiation data from July 2022 to January 2023

The DNI and solar height data collected between 6th of July 2022 at February 2023 for some days. After the analysis of the collected data, the 4th of September 2022 was more representative with DNI profile fitting with the median values. So, the PTC thermal performance was analyzed using the DNI data of the 4th of September 2022 (Figure. 5. 17). The other days were randomly chosen to account for dramatic variation of DNI, the month and the maximum DNI reach in the day (figure. 5. 18). For all the days the DNI increases from a lower value at 7:20 to a maximum value at around 13: 00 to and decreases to a lower value around 18:00. The evolution of solar radiation during a day depends on its height, which is almost 0° at sunrise, reaches its maximum at the zenith and decreases to 0° at sunset as illustrated in Figure. 5. 18. But from day to day or month to month, the sun's height varies (Figure 5. 19). Due to its effect on the radiation's optical path, the sun zenithal angle is a significant factor in radiative transfer. The optical path and radiation extinction are inversely correlated with the sun zenithal angle [227]. This can be observed by the Figure. 5. 18 and Figure. 5. 19 where the maximum solar radiation is reached at the lower zenithal angle. Figure. 5. 17 and Figure. 5. 18 show a decreasing of DNI between 7:20 to 8:00. This is due to the shading of the trees around the weather station on the sensor (Pyrheliometer). The trees around the CTVD are tall enough that in the morning their shadow sometimes covers the optical window of the pyrheliometer in the morning. The others fluctuations after this period can be explained by cloud cover.

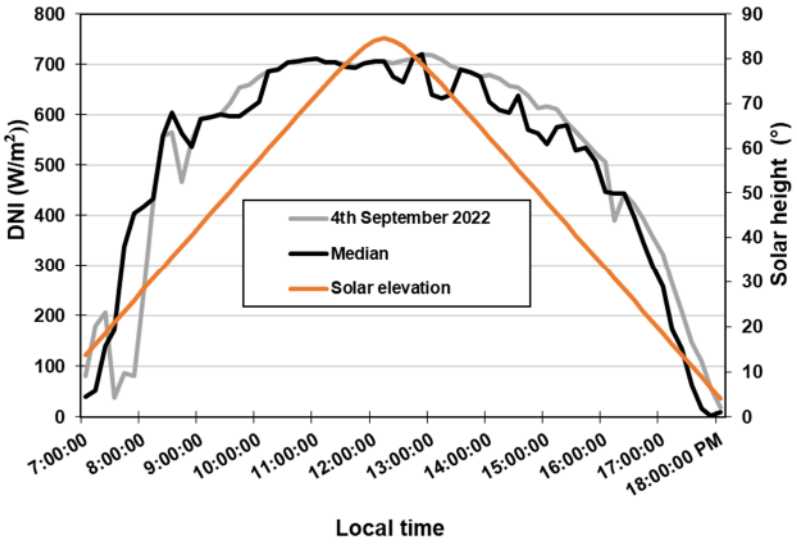

Figure. 5. 17. DNI and solar elevation data of the 4th of September 2022.

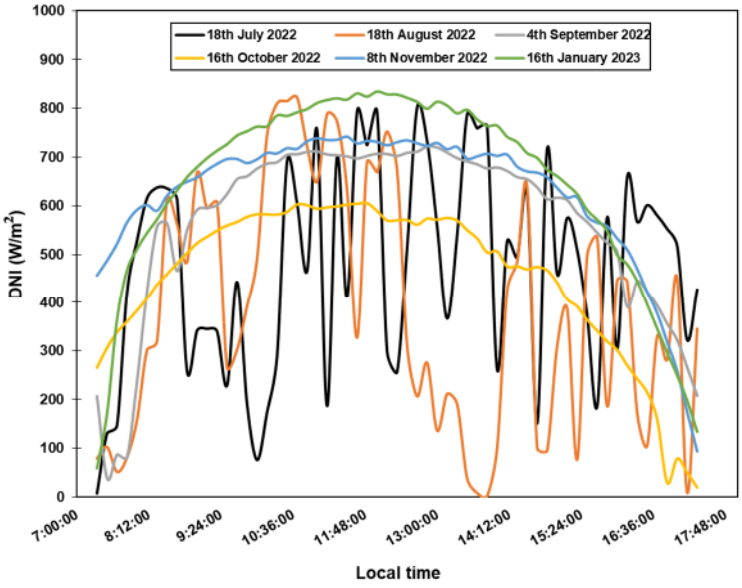

Figure. 5. 18. DNI profile for some days.

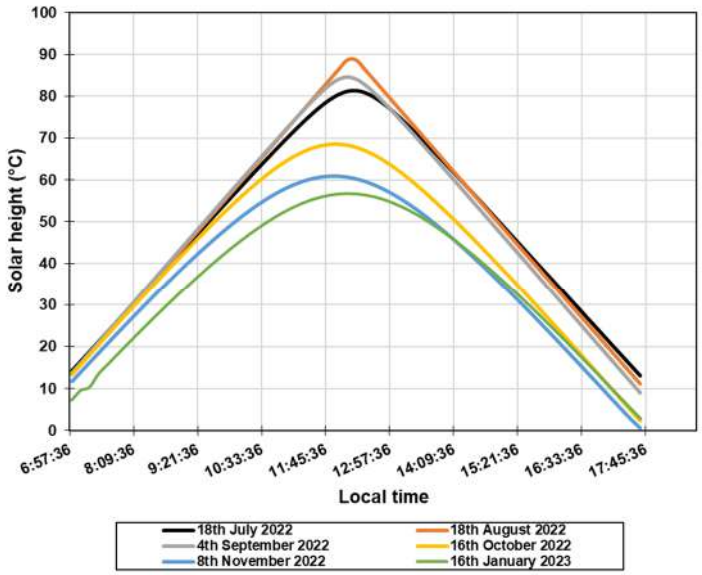

Figure. 5. 19. Solar height data collected at Polesgo for some days using the weather station.

IV.2.2. The effect of JCO mass flow on PTC performance.

To assess the effect of mass flow on the PTC performance, a module with 7.8m length and 5 m width (around 38.33 m^2) was considered. The HTF fluid mass flow ($\dot{m}_{HTF}$) is an important parameter for CSP designing. It is related to the saturated steam flow rate generation in the boiler and can be computed from a steady-state energy balance [66] as written in equation (5. 70)

$$\dot{m}_{HTF} C_{p,HTF} \left(T_{HTF,in} - T_{HTF,out}\right) = \dot{m}_{steam} \times H_{fg} \quad (5.\ 70)$$

$C_{p,HTF}$ is the HTF specific heat capacity, $T_{HTF,in}$ the HTF inlet temperature in the boiler from the solar field or TES system. $T_{HTF,out}$ the HTF outlet temperature from the boiler, $\dot{m}_{steam}$ the stem flow and H_{fg} the enthalpy of vaporization.

In addition it is a parameter which influence highly the fluid outlet temperature [210]. The figure. 5. 20, Figure. 5. 21 and Figure. 5. 22 illustrate respectively the effect of JCO mass flow on its outlet and difference temperature, and the instantaneous efficiency. The results show that whatever the mass flow rate of the JCO the outlet temperature (Figure. 5. 20) and difference temperature (Figure. 5. 21) increase with sun radiation, reach a maximum value at the zenith and decrease when the DNI decrease. This show that, the outlet and difference temperature depend highly on DNI. Higher is the DNI, higher is the heat gain by the JCO and higher are the outlet and difference temperature. Depending on the mass flow rate, the heat effect will be difference driving to different outlet and difference temperature. So, lower is the mass flow rate, higher are outlet and difference temperature. However, with low effect on the PTC thermal efficiency (Figure. 5. 22), a slight increase is observed when the mass flow rate increases. A better outlet and different temperature (maximum values of T_{outlet} =179.667 °C and $\Delta T = 19.667\ °C$ at 13:10 min) are achieved at low mass flow leading to the increasing of heat loss because the lowest average instantaneous efficiency is $83.77\% \mp 16.66\%$ for a mass flow rate $0.5\ kg\ s^{-1}$ against 84.56% for a mass flow rate of $2\ kg\ s^{-1}$. A similar behaviours of the collector is observed from literature [211] and [228]. For mass flow higher than $1\ kg\ s^{-1}$, the efficiency increases slightly of 0.264% when the mass flow increases from $1.5\ kg\ s^{-1}$ to $2\ kg\ s^{-1}$. while an increasing of 0.53% has been observed when the mass frow increase from $0.5 kg\ s^{-1}$ to $1\ kg\ s^{-1}$. This means that the effect of mass flow on PTC performance could be neglected at high mass flow ($\dot{m} > 2\ kg\ s^{-1}$. According to literature, in really working condition the mass flow in a collectors loop (collector in series) range between $0.5\ kg\ s^{-1}$ to $1\ kg\ s^{-1}$ [83] and [229] for small scall power plants. As this model did not considering, the dynamic behaviour of the fluid, a mass flow of $1\ kg\ s^{-1}$ is chosen to assess the effect of collector length on JCO outlet temperature.

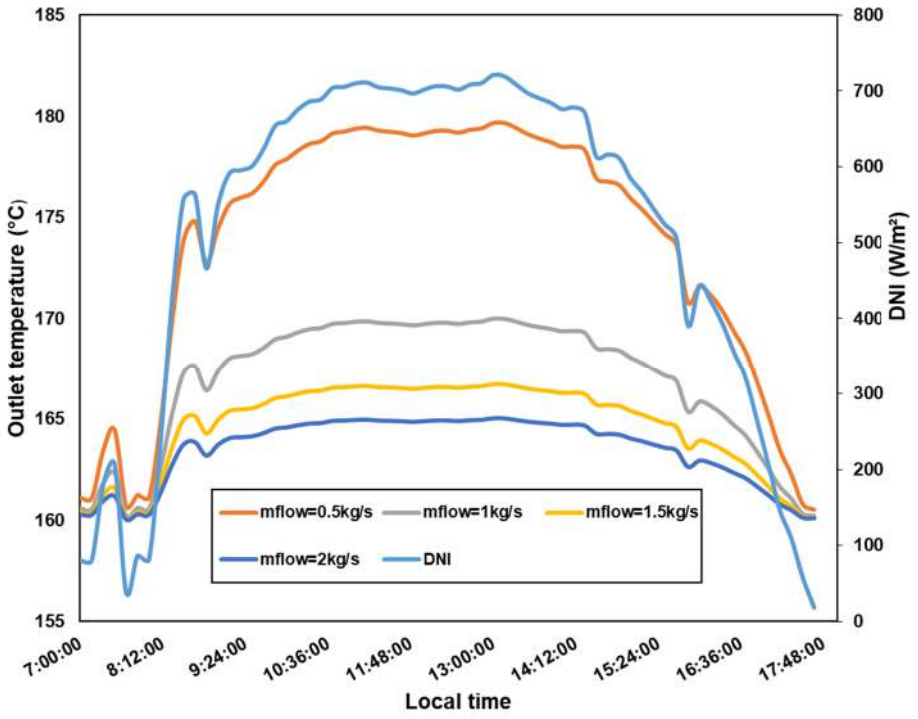

Figure. 5. 20. Effect of JCO mass flow on its outlet temperature.

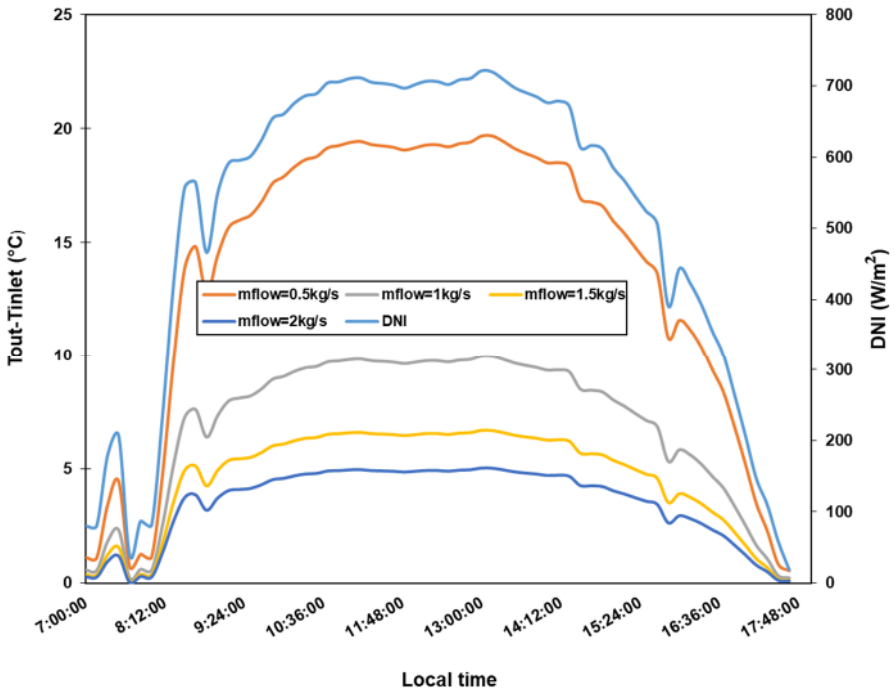

Figure. 5. 21. Effect of JCO mass flow its temperature difference ($T_{outlet} - T_{inlet}$)

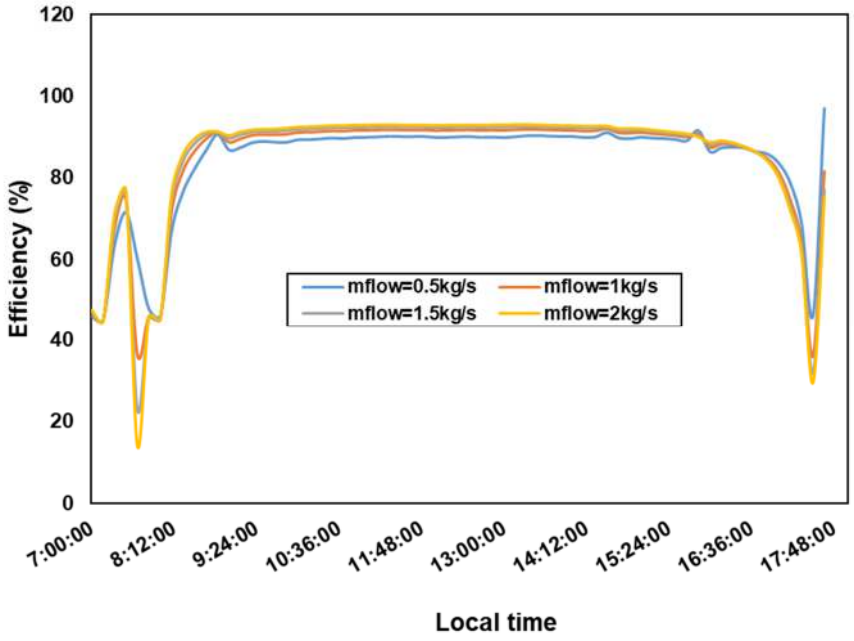

Figure. 5. 22. Effect of JCO mass flow on its outlet temperature.

IV.2.3. Effect of absorber or collector length on the PTC performance

From the assessment of the outlet temperature with one collector module, no mass flow allows to reach the desirable outlet temperature (210 °C). In addition, for a demonstration PTC plant the mass flow should reach at least 1 kgs^{-1} [194], [205], [209]. So, in this study a mass flow rate of at least 1 kgs^{-1} and inlet temperature of 160°C are considered in this section. With a mass flow of 1 kgs^{-1}, the outlet HTF temperature is less 210°C while the objective is to reach a maximum temperature between 210°C to 250°C. To handle this issue, the solution is to put the collector module in series. Figure. 5. 23, Figure. 5. 24 and Figure. 5. 25 illustrate the effect of collector length on the JCO outlet temperature, difference temperature and thermal efficiency. The DNI effect on outlet and difference temperature is the same and was mentioned previously. Figure. 5. 23 and Figure. 5. 24 show that, the outlet temperature and ΔT increases when the collector length increases. The increase of collector length increases the DNI collection area concentrating more sunshine on the absorber which will increase the heat gained by the fluid. For a mass flow of 1 kgs^{-1}, a collector length of 46.8 m is need to achieved outlet temperature of at least 210 °C. As illustrated on Figure. 5. 23 the outlet temperature increases when the DNI is increasing and reach

210 °C at around 9:30. As the sun is still rising the DNI continue increasing and the temperature is risen up to 218.8 °C. This maximum temperature is reached at 13:20 min with difference temperature of 58.8 °C (Figure. 5. 24). From 9:40min a PTC plant can rum at the nominal power when using JCO as heat transfer fluid because the optimum outlet temperature of fluid is reached. As, the HTF outlet temperature defines the working temperature of the plant [230], after 14: 40 min the collector could steal continues to run the power the plant till 15:40 min with mass flow of $1\ kg.s^{-1}$. However, if a storage system is integrated, the storing process has to be cut off or continuing at lower mass flow if the TES system is not full.

Considering the PTC thermal efficiency as illustrated in Figure. 5. 25, it increases when the DNI increases whatever the collector length is increasing and reaches a maximum value at 9:00 and remains constant till around 15:30 and decreases to 40%. Due to DNI fluctuation, unreasonable transient evaluation such as more than 100% instantaneous efficiency is observed between 17:30 and 18:00. This is due to the preheating of the oil in the collector by high levels of solar irradiance and the reduction of DNI to a low value under the effect of cloud cover. Under dramatic DNI fluctuation Xu et al., have observed also instantaneous thermal efficiency of PTC in 2014 with some values reaching 100% [192]. It can be observed that, the instantaneous thermal efficiency decreases when the collector size increases. For the average or normalized thermal efficiency, it decreases from 86.28% to 82.69% when the collector length increases from 7.8 m to 46.8 m (Figure. 5. 26). In addition to that, the required outlet temperature is reached for collector length of 46.8 m leading to the highest heat losses. This confirmed the increasing of heat losses from the PTC when the fluid temperature is increasing. However, when the absorber is longer than 39 m the effect of collector length on the PTC efficiency is neglected. This means that, when the temperature is higher than 200 °C the heat losses are lower.

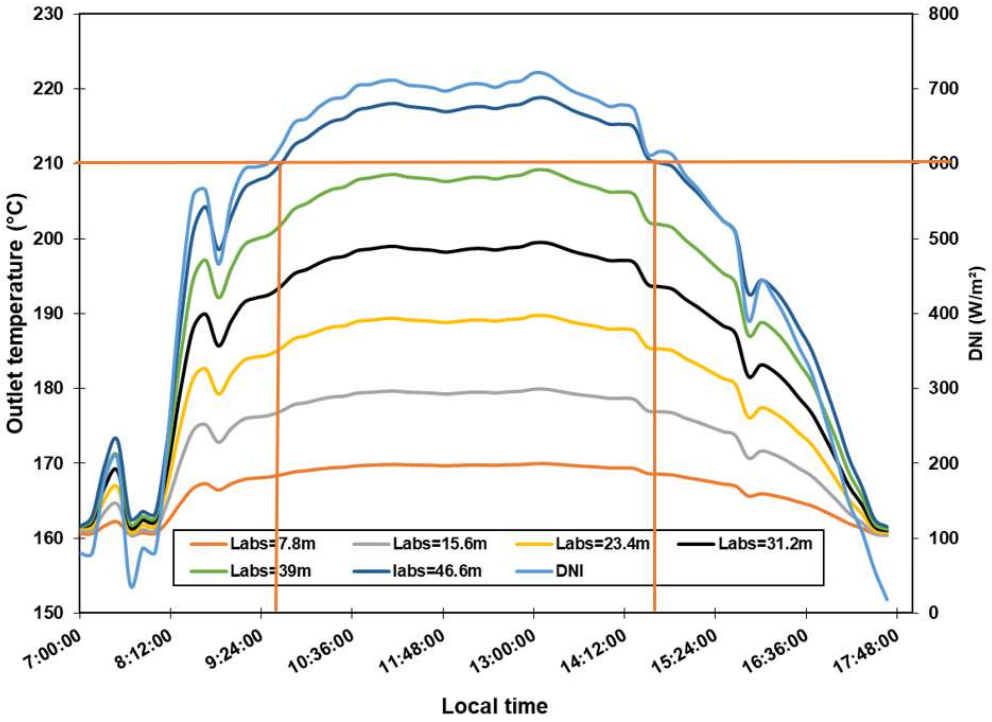

Figure. 5. 23. Effect of collector or absorber length on JCO outlet temperature

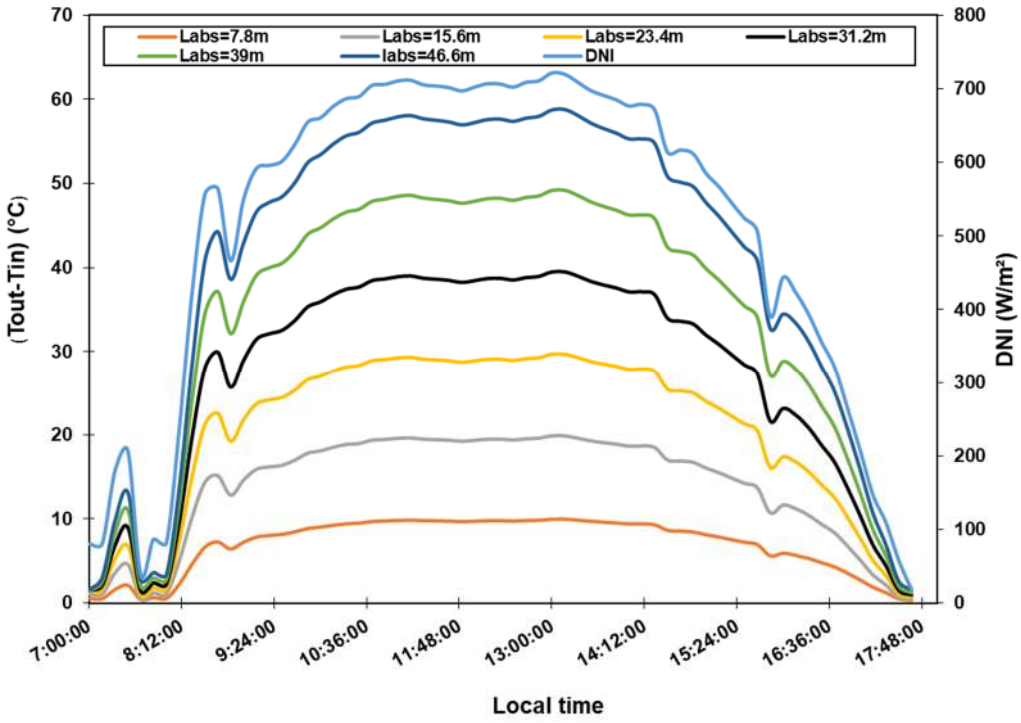

Figure. 5. 24. Effect of collector or absorber length on JCO temperature difference ($T_{outlet} - T_{inlet}$).

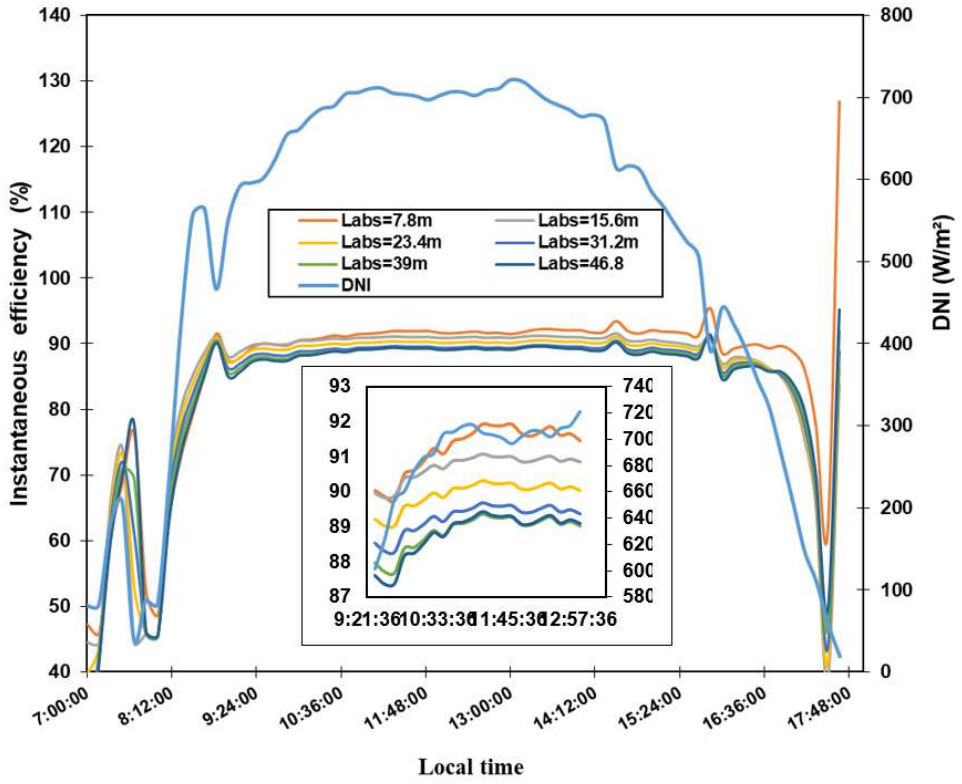

Figure. 5. 25. Effect of absorber or collector length on the PTC efficiency.

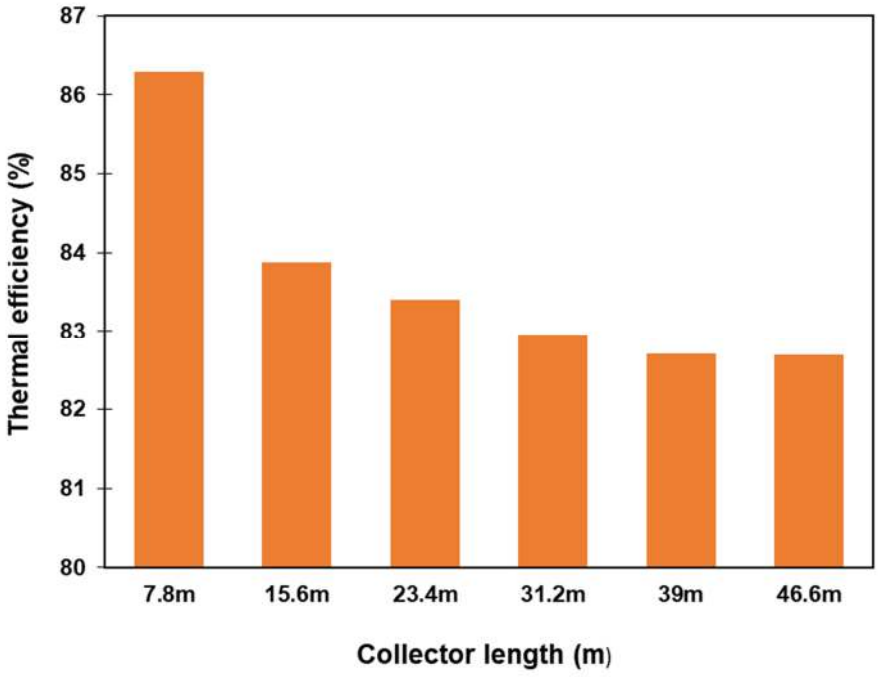

Figure. 5. 26. Effect of collector length on average thermal efficiency.

IV.2.4. The collector performance for different days from July 2022 to January 2023

Six days were chosen ramdomly taking in to account the dramatic fluction of DNI, the low, high and medium extinction of DNI for six months. The aim is to assess the PTC performance under different weather conditions (figure. 5. 30) for a collectors loop of 46.8m or 230 m^2 and JCO mass flow of 1 kg/s. Figure. 5. 27, Figure. 5. 28 and Figure. 5. 29 illustrate the JCO outlet and difference temparatures and the average thermal efficciency of the PTC at Polesgo from 7:20 am to 7:20 pm.The outlet and difference temperature profile depends higly on the weather conditions (DNI conditions). It can be observed in Figure. 5. 27 and Figure. 5. 28 that when the DNI extinction is higher the both JCO outlet and difference temperature are lower. Thus, the lowest JCO outlet temperature is obsered the 16th October 2022 when DNI values are lower and the highest outlet and difference temperature the 16th January when the DNI value are higher. The DNI are extinguished in 16th November to such an extent that the outlet temperature does not reach 210°C throughout the day. This chalenge can be solve by reducing the mass flow rate, but the turbine nominale power output is going to be affected. In addition, high DNI fluctuation (18th July and 18th August, figure. 5. 30) drives to high variation of the oil outlet temperature which impact highly the PTC average thermal efficiency (Figure. 5. 29). The figure. 5. 29 illustrates the effect of different weather conditions on PTC average thermal efficiency. The thermal efficiency is also affected by the weather condition with a better thermal efficiency (88.12%) the 8th November and lower average thermal efficiency (52.5%) in 18th August. It can be observed that, the 8th november 2022 is one of days which has the best weather condition under which the PTC can run effectively with better thermal efficiency reaching 88.12%. The thermal efficiency is 85.41% for the best DNI data (16th January). This low value compare to 88.12% is due heat losses in the PTC at high

temperature. Therefore, JCO can be used as HTF for PTC plant where the DNI can reach 730 W m^{-2} during the day.

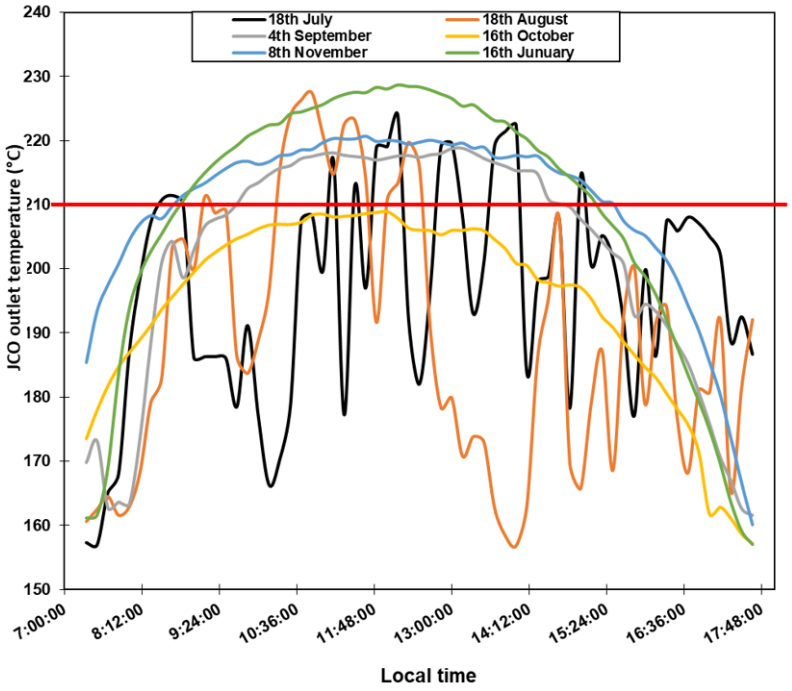

Figure. 5. 27. HTF outlet temperature behaviour under different weather conditions

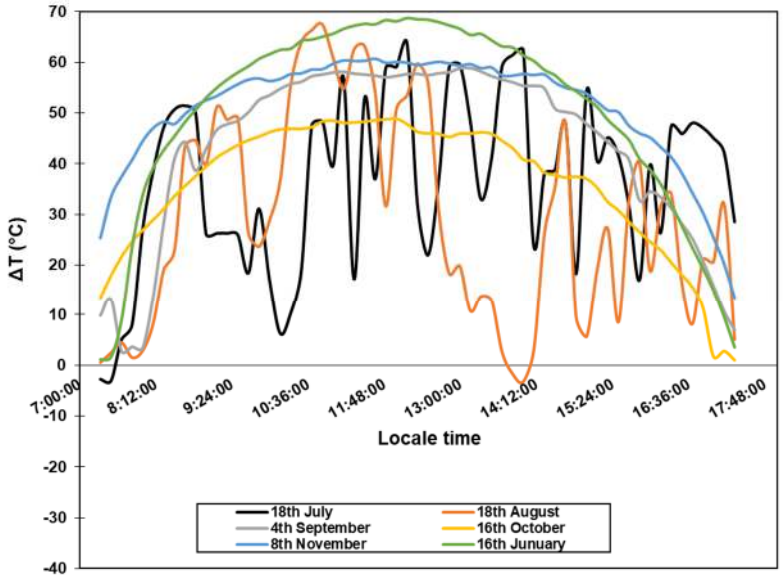

Figure. 5. 28. Temperature difference behaviour under different weather conditions.

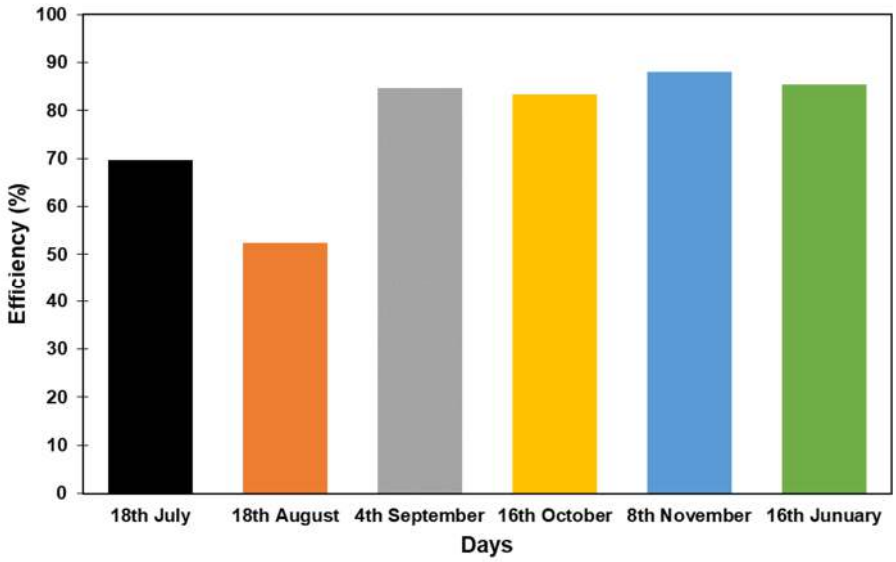

Figure. 5. 29. Collector average efficiency under different weather conditions.

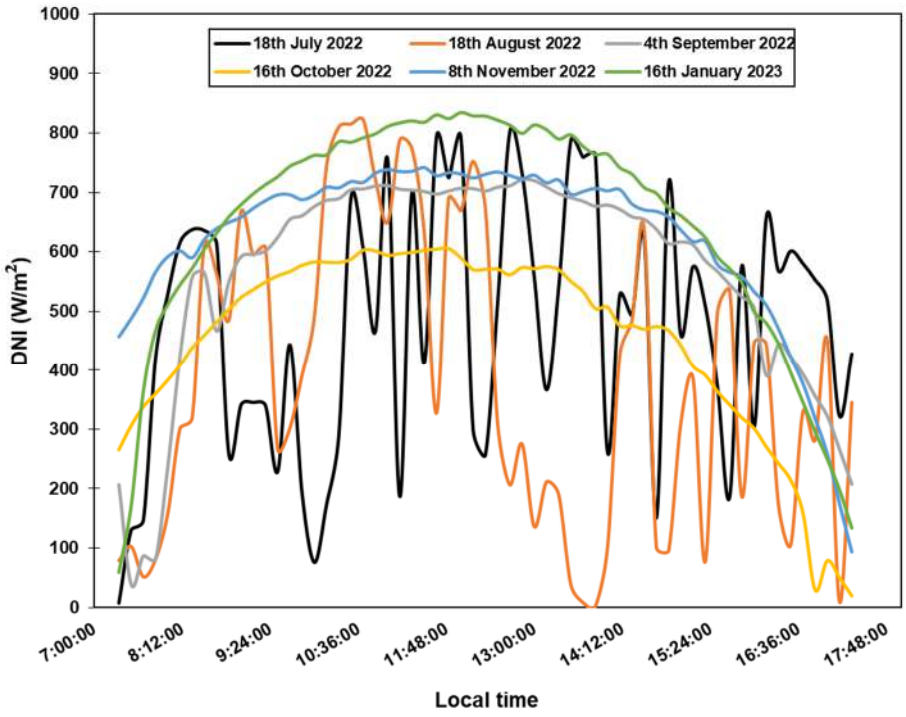

Figure. 5. 30. DNI profile for some days.

IV.3. Performance analysis of PTC under Agadez climate conditions

Figure. 5. 31 illustrates DNI profiles for some days of the year 2020 collected using PVGIS tool [231], [232]. For each month the day was chosen to be around the average day in the month and year [233]. The hourly collected DNI and solar height data are plotted in Figure. 5. 31 and figure. 5. 32. The profile of DNI and solar height from PVGIS is similar to the one obtained with observation data at POLESGO. Assuming that a difference of two years is not going to affect the DNI potential around Agadez, the 4th of September was chosen for PTC performance analysis at TCHIROZERINE (Figure. 5. 33). This will allow having information on the PTC performance under both Ouagadougou and Agadez climate conditions. In addition to that the 4th of September fit with the median with a maximum deviation of 78 W.m^2. The maximum solar radiation is obtained in February and the minimum (Zenithal angle) in June while the solar height is recorded in May and the minimum in December as illustrated in Figure (5.32). This is can be explained by the phenomena of revolution and rotation of the earth around the sun and itself leading the decrease of DNI when the zenithal angle is increasing [227]. The output of the PTC under Agadez climate conditions was analysed for the 4th of September.

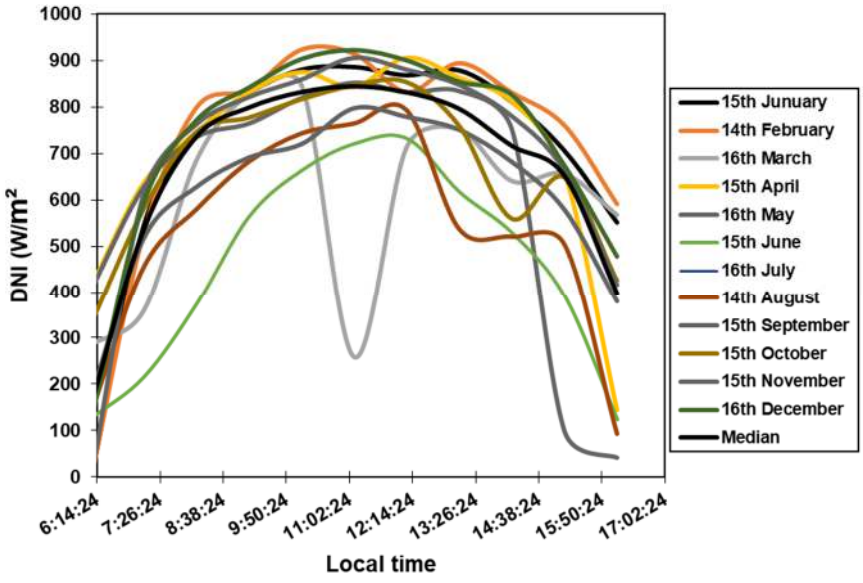

Figure. 5. 31. DNI hourly data for the year 2020 at TCHERIROZÉRINE.

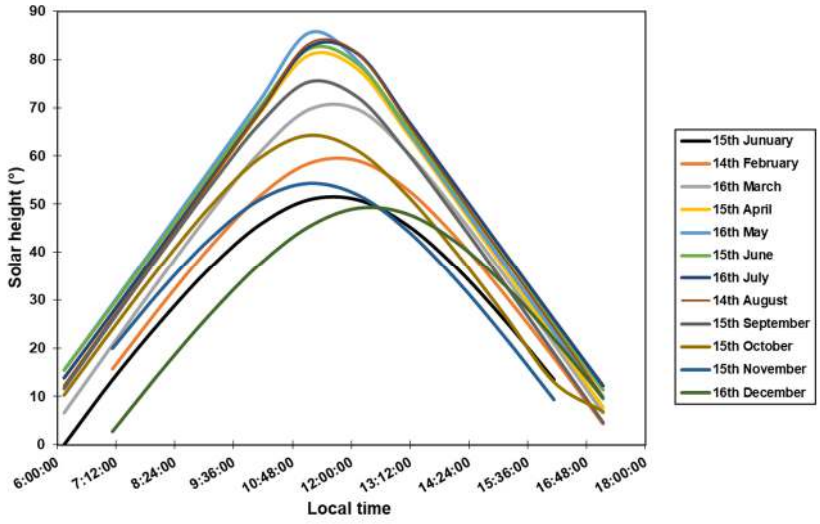

Figure. 5. 32. Solar elevation for some days at TCHERIROZÉRINE.

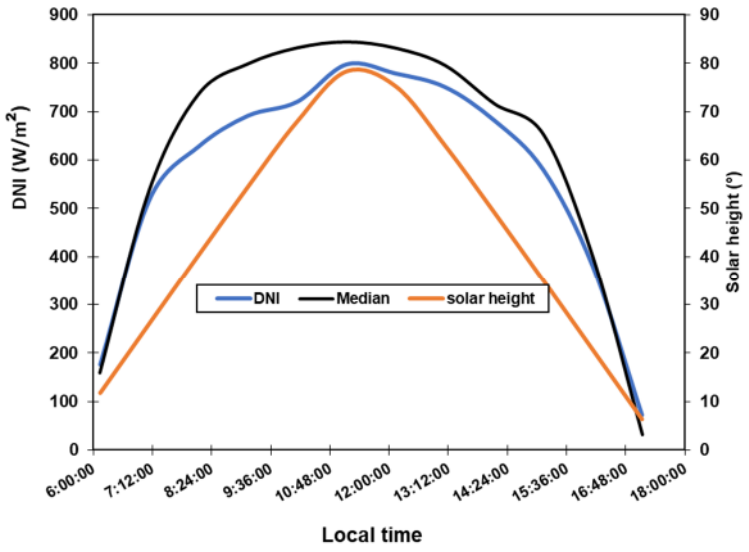

Figure. 5. 33. DNI and solar height profiles for 4th September 2020 at CHIROZERINE.

IV.3.1. Effect of mass flow rate under on the PTC outputs under Agadez climate condition

The figure. 5. 34 illustrates the mass flow rate effect on temperature difference the 4th of September 2020 at TCHERIROZÉRINE. The same evolution of the curves can be observed compare to the one obtained at POLESGO. The difference temperature at the zenith decreases from 21.94 °C to 5.61°C when the mass low rate increases from 0.5 kg. s^{-1} to 2 kg. s^{-1} while the instantaneous

thermal efficiency (Figure. 5. 35) increases from 90.488% to 93.47% at 12 o'clock. At POLESGO, a maximum difference temperature of 19.6678 °C is achieved with a mass flow rate of 0.5 kg. s^{-1} against 5.03 °C for 2 kg. s^{-1} while the thermal efficiency is respectively 90.31% and 92.84% at 13: 30 min. In addition to the mass flow rate, the results show that a high DNI value increases the HTF difference and the outlet temperature. For example, a HTF difference temperature of 21.94 °C against 19.6678 °C respectively for 797.5 W.m^{-2} and 719.2119 W. m^{-2} with a mass flow rate of 0.5 kg. s^{-1} has been observed with a difference of 2.27°C. But when the mass flow rate increases to 2kg.s^{-1} this difference is 0.58°C which is low compared to the one at low mass flow rate.

Figure. 5. 36 illustrates the evolution of the PTC average thermal efficiency with the JCO mass flow rate. The PTC efficiency increases when the mass flow rate increases. The increase of the mass flow decreases the outlet temperature which reduce the PTC heat losses improving the thermal efficiency.

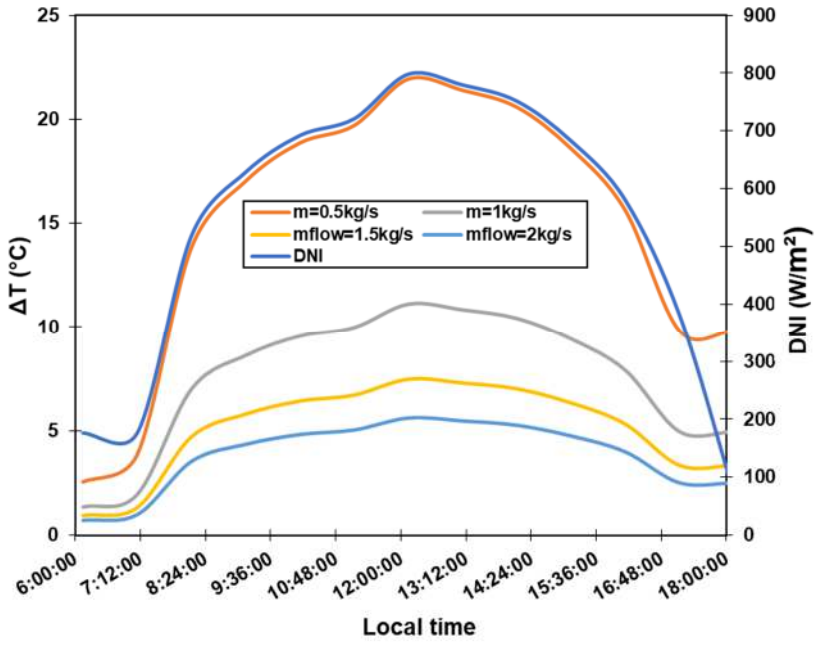

Figure. 5. 34. Effect of mass flow rate on temperature difference.

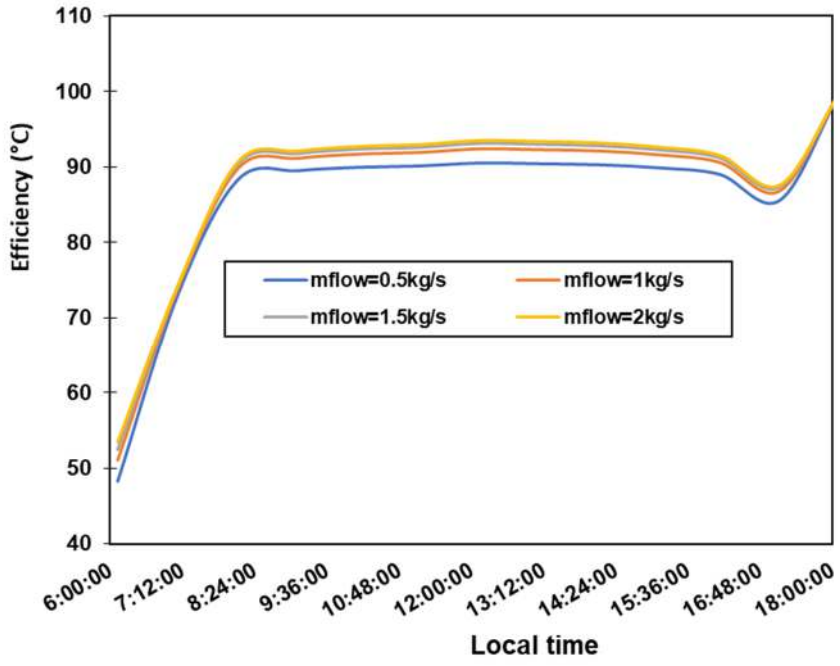

Figure. 5. 35. Effect of mass flow on PTC efficiency.

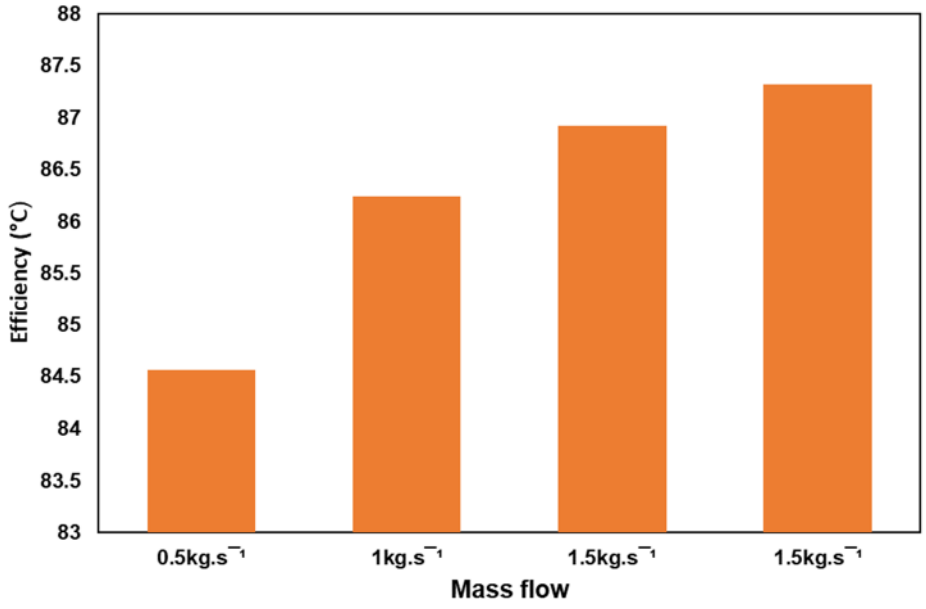

Figure. 5. 36. Effect of mass flow on the PTC thermal efficiency at TCHIROZERINE.

IV.3.2. Effect of collector length on its outputs under Agadez climate condition

As done in IV.2, a mass flow rate of 1 kg. s^{-1} has been considered to assess the effect of the collector loop length on the PTC performance. According to the application, increasing or decreasing of the collector length can help handle the outlets temperature avoiding oversizing or under sizing of the solar field even if a heat controller can be integrated. Figure. 5. 37 shows that, the maximum difference temperature increases from 11.13 °C to 65.59°C when increasing the collector length from 7.8m to 46.8m at inlet temperature of 160°C. For the landfill in Ouagadougou, a maximum difference temperature of 58.80°C was observed for a collector length of 46.8m against 9.96°C for a collector length of 7.8 m. In versus of the mass flow longer collector length affects the temperature output than short collector at difference climate condition or weather condition. Considering the average thermal efficiency, it decreases when the collector length increases (Figure. 5. 38). Compare to Ouagadougou weather condition, Agadez have similar average thermal efficiency (82.6% and 81.76%) for a collector length of 46.8m using JCO as HTF. For a short collector length of 7.8 m an efficiency of 86.28% against 86.23% respectively under Ouagadougou and Agadez weather conditions in September. Therefore, jatropha curcas oil could be more suited than HELISOL XA used in [205] because with a collector surface area of at least 279 m2, a maximum temperature difference of 50°C was obtained for a mass flow rate of at least 1.13 kg.s^{-1} for HELISOL XA while a temperature difference of 58.80°C for a collector surface area of 230.63 m^2 was obtained with a 1 kg. s^{-1} mass flow rate of JCO and a maximum DNI of 720 W.m^{-2}.

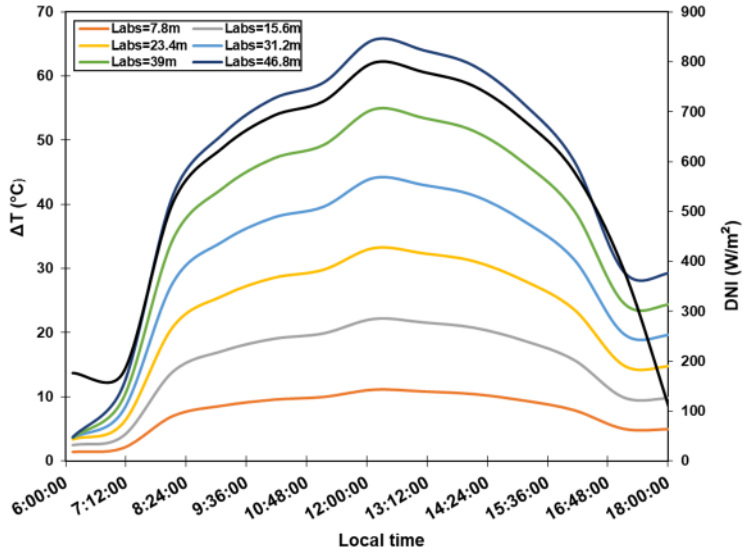

Figure. 5. 37. Effect of collector lengths on difference temperature.

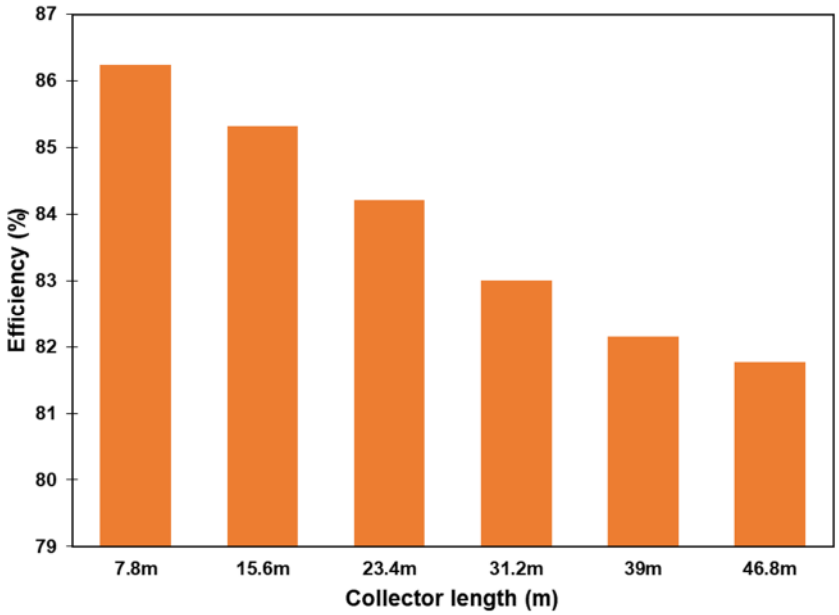

Figure. 5. 38.Effect of collector length on average PTC efficiency.

IV.3.3. Effect of inlet temperature on the PTC output

Figure. 5. 39 and figure. 5. 40 illustrate respectively the JCO inlet temperature effect on its difference temperature and the PTC efficiency. The increasing of the inlet temperature from 80°C to 160 °C drives to the decreasing of the JCO temperature difference from 68.505 °C to 65.598 °C at 12 o′clock. This 2.907 °C drop of the temperature difference reduces the thermal efficiency from 87.97% to 81.76%. This shows that the use of JCO as heat transfer fluid in PTC could be more effective when the inlet temperature is around 80 °C. As illustrated in figure. 5. 41 JCO heat capacity is low for temperatures less than 100°C, increases between 100 °C and 142 °C, and decreases for temperature higher than 142°C. So, increasing JCO inlet temperature from 80 °C increases the outlet temperature reducing its specific heat capacity for temperature higher than 142 °C. Therefore, the average thermal efficiency decreases when the inlet temperature increases. Lower is the outlet temperature higher is the specific heat capacity. Similar behaviour of the PTC was observed by Belos and Christos in 2018 using Syltherm 800 oil as heat transfer fluid [215]. In their study, they have observed a decrease of PTC thermal efficiency from 74.5% to 65.25% when the inlet temperature increases from 300 K to 650 K.

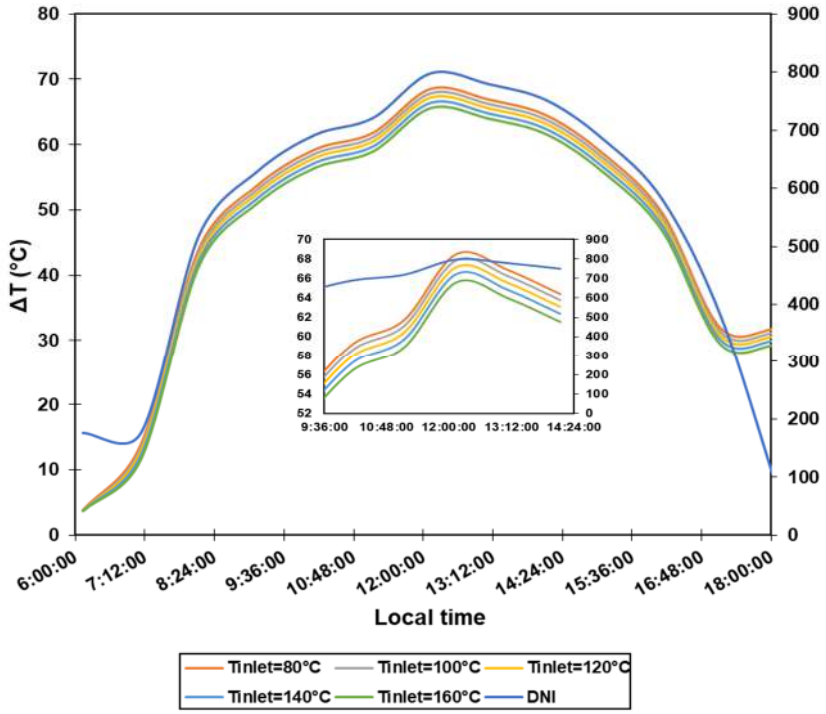

Figure. 5. 39. Effect of HTF inlet temperature on its Temperature difference.

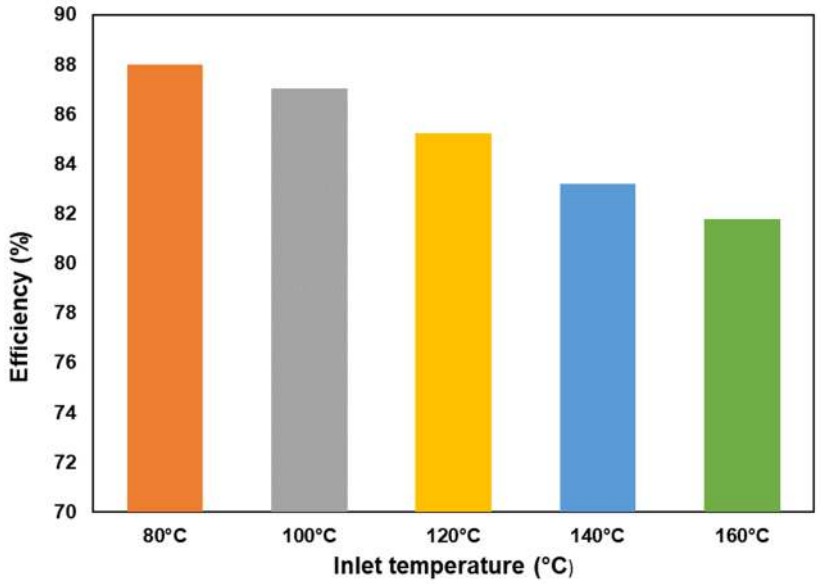

Figure. 5. 40. Effect of HTF inlet temperature on the PTC average thermal efficiency.

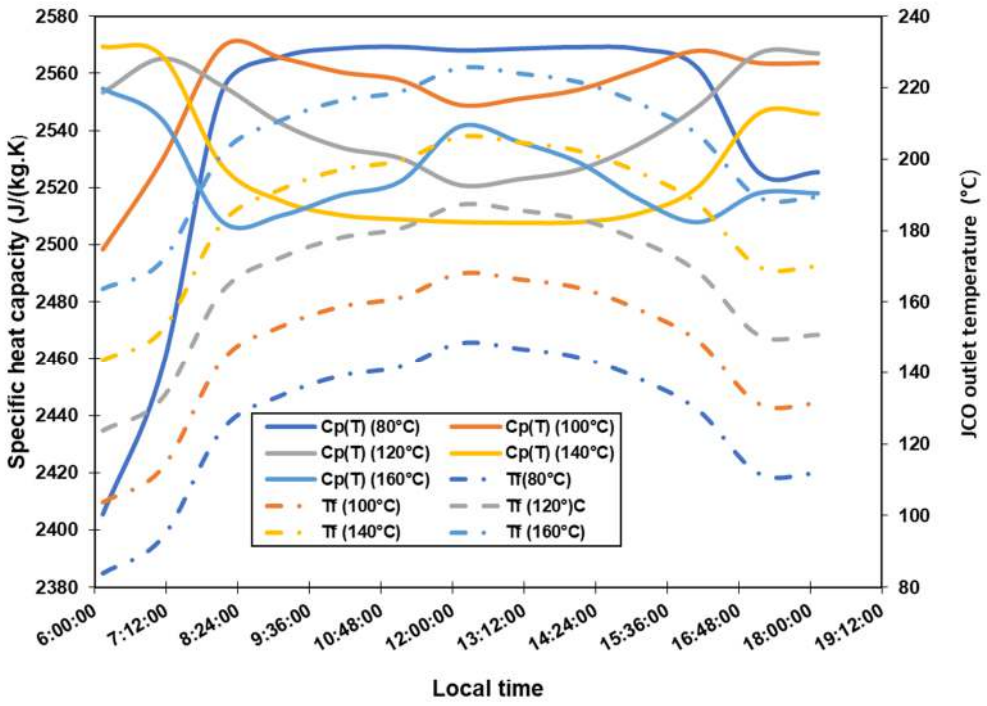

Figure. 5. 41. Effect of inlet temperature on JCO specific heat capacity and outlet temperature.

IV.4. Dynamic behaviour of the solar filed and TES system

In this study, the solar collector was connected directly to the $2\,MWh_{th}$ storage tank after the performance analysis of the two components. The studies conducted previously in IV show that a collector loop length of 46.8 m or collection area of 230 m^2 is needed to have outlet temperature of 210°C around 9:30 for a mass flow rate of 1 kg. s^{-1}. This collector´s loop will be directly connected to the TES system for its performance analysis in real charging condition. So, the mass flow rate of the oil used will be firstly 1kg.s^{-1} and the collection area 230m2. Heat losses or pressure drops between the solar field and TES system are assumed to be negligible ($T_{f\_outlet} = T_{f\_outlet\_DMT}$). Figure. 5. 42 illustrates the evolution of the JCO outlet temperature in the solar field and the its outlet temperature in the thermocline TES system from morning to evening at the study area (Polesgo) on 4th of September 2022. Figure. 5. 43 shows that the storage tank is full at around 14 o´clock considering a maximal charging temperature of 210°C while solar radiation begins to decrease. As the mass flow constant, the fluid outlet temperature from the collector is higher than 210°C at around 9:21min with inlet temperature in the thermocline tank also higher than 210°C after this time as illustrated in Figure. 5. 42. The storage tank is charged with heat at

around 2pm (the outlet temperature is 210°C). At around 3 pm, the JCO inlet temperature in the TES system begins to drop as a result of the reduction in solar radiation. The axial temperature profiles (Figure. 5. 43) in the TES system during a dynamic charging cycle show a large difference compared with the ideal case where the inlet temperature is fixed at 210 °C. This is due to the variation of JCO outlet temperature from the solar field. After 2 pm, if the storage process does not stop, the temperature of the fluid and particles inside the tank will reach 211.34 °C at 3 pm , whereas the inlet temperature is 211.44 °C, leading to an overload (The limit temperature for use of JCO is 210 °C).

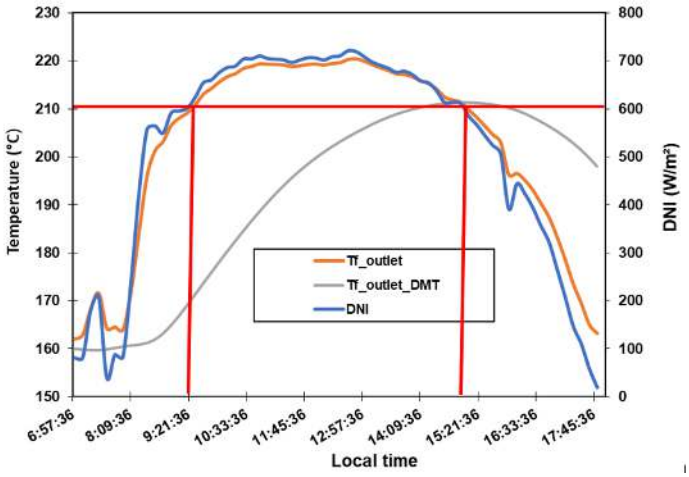

Figure. 5. 42. Dynamic charging of the storage system.

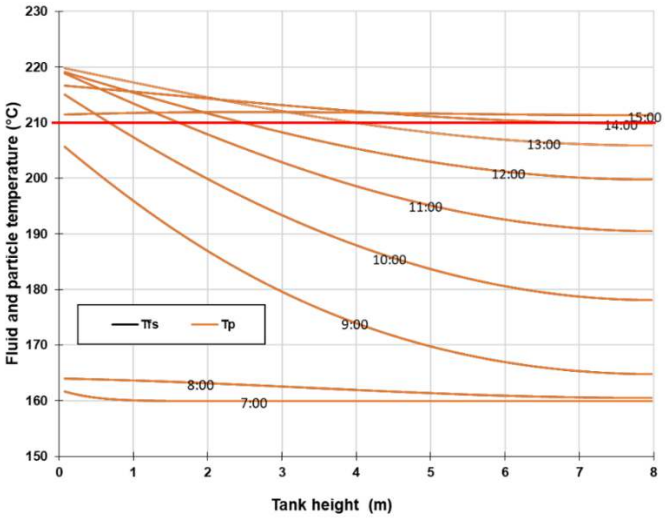

Figure. 5. 43. Fluid and particle temperature profile in the storage system during dynamic charging.

After 3 pm the discharging process is going to start because the solar field outlet temperature decreases to 209 °C. As consequences, it is difficult to obtained the hot and cold zones and intermediate area during dynamic charging, and it can be observed that the dynamic charging gives, results different from ideal one as illustrated in figure. 4. 21. Similar behaviour of the thermocline storage system was observe in [199] and [233].

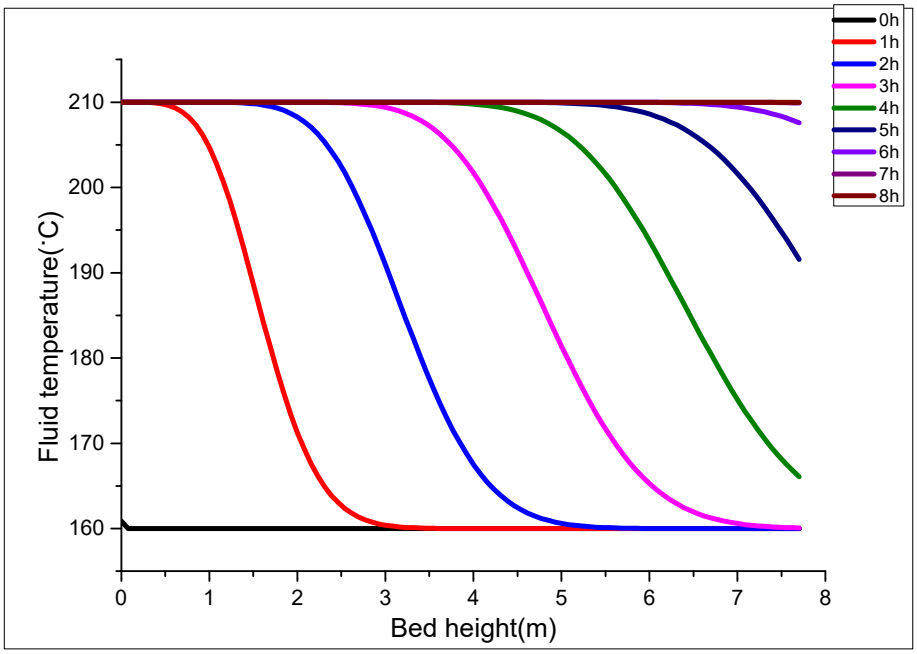

IV.5. Optimization of the TES performances system during dynamic charging

The thermocline thickness and the charging efficiencies are the main parameters studied in this part. The equations (4. 31) to (4. 35) have been used to assess the thermocline thickness. The thermal efficiency during dynamic charging has been assessed based on equation (5. 71).

$$\eta_{chg} = \frac{\int_0^{t_{chg}} \dot{m} C_{p,f} (T_{max} - T_{\min}) dt}{E_{total}} \qquad (5.\ 71)$$

The figure. 5. 44 and figure. 5. 45 illustrate respectively the thermocline thickness and efficiency during dynamic charging. The thermocline thickness increases from 0.88m at 7 am to 5.1m at 9:30 am remains almost constant till 2 pm and decreases to 1.3 m at 3 pm. The thermocline thickness profile shows high values during dynamic charging confirming the issues to create a hot, cold and intermediate zones during the dynamic charging. In addition, the storage efficiency results are not satisfactory for a mass flow rate of 1 kg. s^{-1}. Consequently, the storage efficiency is less than 52%

(figure. 5. 45) at the end of the charging period (2 pm). Similar experimental results were reported by Fasquelle in 2017 with a storage efficiency of 45.5% during dynamic charge of the MicroSol-R plant [198]..

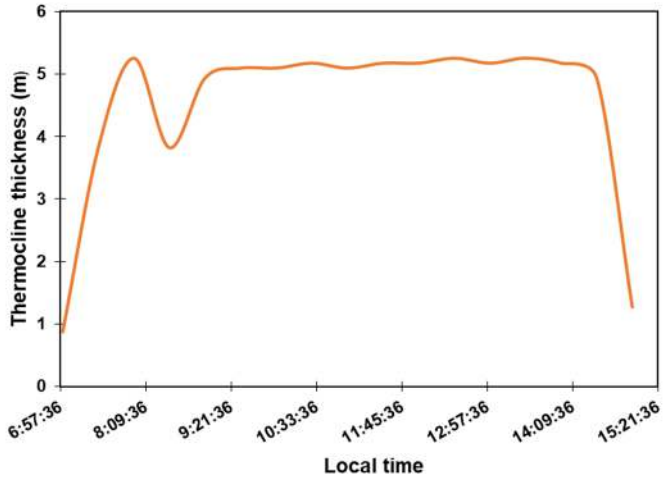

Figure. 5. 44. Thermocline thickness during dynamic charging for ma flow of 1 kg. s-^{1}.

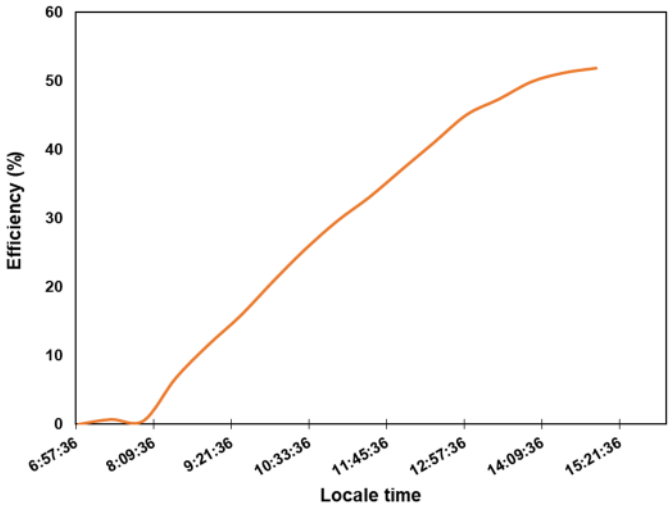

Figure. 5. 45. Thermocline efficiency during dynamic charging for a mass flow of 1 kg. s^{-1}

As the TES charging efficiency (52%) is low with a mass flow rate of 1 kg. s^{-1} and collection area of 230 m^{2}. The effect of mass flow rate on the charging efficiency is assessed in this section to carry out the optmum mass flow rate and loops for an effective charge of the 2 MWh$_{th}$ TES system. Figure. 5. 46 and Figure. 5. 47 illustrate the effect of mass flow on the charging efficiency and thermocline thickness respectively. When the mass flow rate increases from 1 kg. s^{-1} to 2.1872 kg. s^{-1} the thermocline thickness is slightly affected (Figure. 5. 47) while the charging efficiency

increase up to 100 %. For example, the charging efficiency reaches 98% when the mass flow rate is 1.8748 kg/s, whereas it is only 60% for a flow rate of 1.31 kg/s.

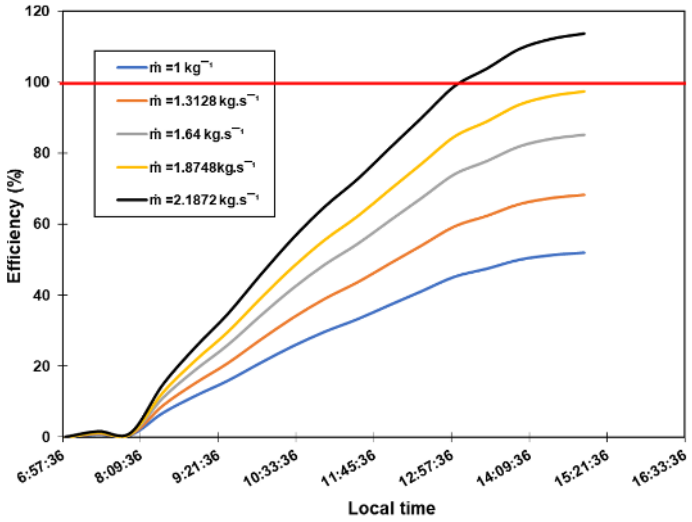

Figure. 5. 46. Effect of mass flow on dynamic charging efficiency.

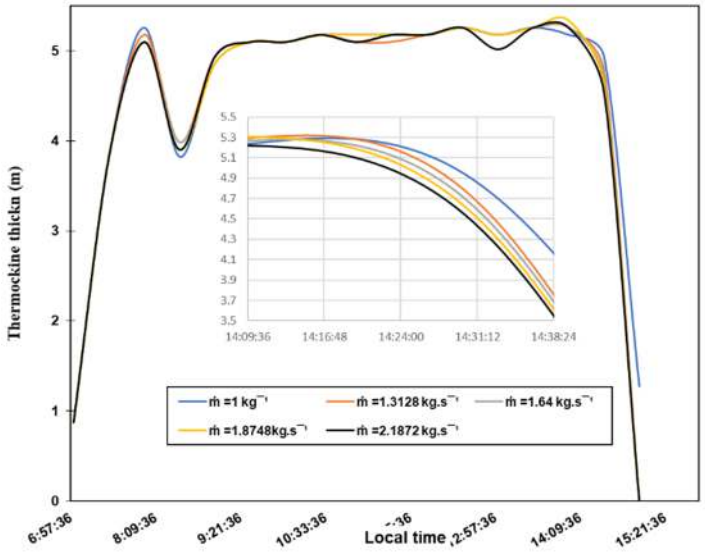

Figure. 5. 47. Effect of mass flow on dynamic charging thermocline thickness.

A mass flow rate of 2 $kg.s^{-1}$ could be used for an optimal charging of the 2 MWh_{th} with around 8 m heigh and 3.2 m dimeter. This required a 2 collector loops of 46.8 m in parallel for the solar field or a collection area of 460 m^2. However, to achieve better thermocline thickness at this mass flow of 2 $kg.s^{-1}$ the inlet temperature has to be controlled at 11 o'clock when the inlet temperature is higher than 210 °C. This can be resolved by increasing the mass flow in the solar field from this

time. So, in addition to develop a control model for the solar field and the storage system it is important to integrate a fluid dynamic model. A design of the PTC field connected to the new TES system can be presented as illustrated in Figure. 5. 48.

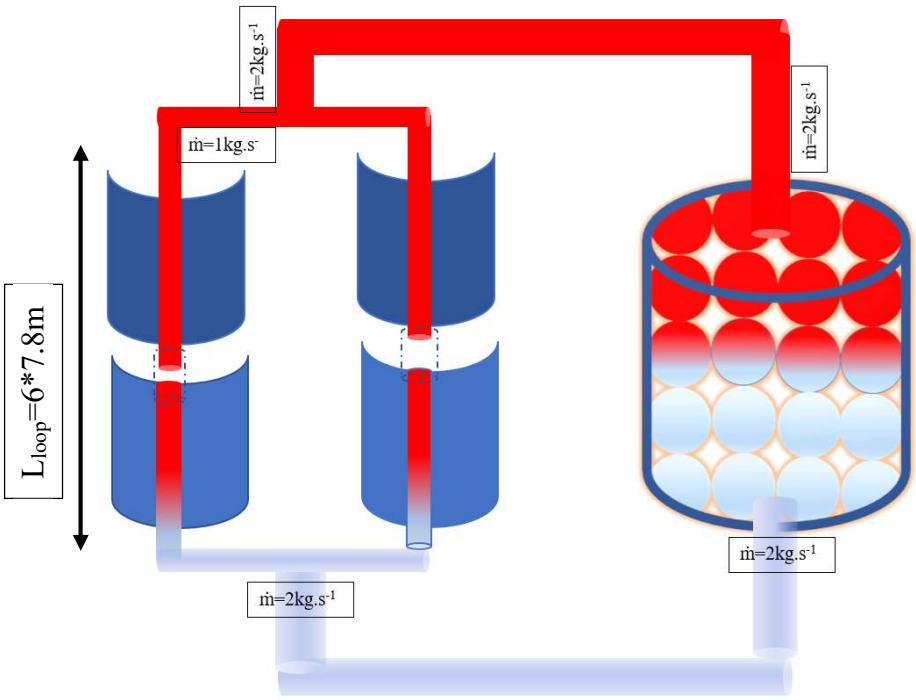

Figure. 5. 48. A design of the PTC and TES system when connecting together.

The power block is supposed to run at any time when sunshine is available and energy is stored in the TES system. So, the sizing of the solar field should be bigger than the one of the power blocks to take into account the storage system. Therefore, the solar multiple should be greater than one. The solar multiple is defined as the factor by which the solar field size is bigger than the size of the power cycle. It can be computed with equation (5. 72).

$$\text{Solar multiple}=\frac{Q_{col,SF}}{Q_{th,PB}} . \qquad (5.\ 72)$$

Where $Q_{col,SF}$ is heat energy collected in the collector field for design point solar irradiance and $Q_{th,PB}$ the power block required thermal energy for the design electrical output.

Conclusion

In this chapter a model has been developed for dynamic performances analysis under Ouagadougou and Agadez climate conditions. The direct normal radiation from the two regions of West Africa were collected using respectively a weather station (instantaneously data) and Photovoltaic geographical Information System (PVGIS) tool (hourly data). After the validation of the model the effect of mass flow, collector length effect on the PTC performance (efficiency) were assessed to choose the corresponding mass flow and absorber length to obtain the requested outlet temperature (>210°C). The results show that more heat loss is observed at low mass flow and longer collector length driving to low instantaneous efficiency at high outlet temperature. For a mass flow of 1.kg. s^{-1} a collector length of 46.8m is required to obtained outlet temperature higher than 210°C from 9:40 am and 9:08 am under Ouagadougou and Agadez climate conditions respectively for the 4^{th} of September 2022 and the 4^{th} of September 2020. The direct connection of the solar collector's loop to the hypothetical 2 MWh_{th} (around 222 kW_{th}) with a mass flow of 1 kg. s^{-1} shows that only the half of the energy can be stored after sunshine declined from 14 o´clock the 4^{th} of September. To handle this issue a solar field with two collectors' loop in parallel with 460m^2 and total mass flow of 2.kg. s^{-1} is required to fully charge the storage with inlet velocity of around 7.6210^{-4} m.$s^{\cdot 1}$ in the storage tank.

General conclusion and perspectives

This work is devoted to the study an appropriate solid materials and fluids for thermal energy storage applications. In essence, without entering into its implementation, a successful heat storage solution must provide a satisfactory balance between the two basic aspects of any TES alternative, the storage material and the implemented technology. Both aspects have been addressed in this thesis work achieving an optimal compromise between the variables governing the cost efficiency, and thermal performance of the heat storage solution.

For the storage material side, the implementation of low-cost solid materials has been proposed. A double approach has been followed in the development of appropriate material candidates. On one hand, natural materials sand, clay, have been selected as raw materials based on their abundance in Burkina Faso and Niger, low ecologic impact and satisfactory thermal properties after firing process. On the other hand, coal bottom ash from Agadez coal power plant incinerator has been identified as suitable raw material for TESM development. The valorization of this industrial waste in the thermal storage frame could represent a win-win approach. It permits an important reduction of waste generation from the electricity generation process from coal and provides a competitive alternative for TES. This waste has been successfully integrated in the ceramic balls developed from sand and clay for TES purpose. For the four different sands used such as, dune sand from Burkina and Niger, mining sand and Natural sand two samples (formulation) are selected as ceramic balls which could meet IEA criteria (based on thermal and mechanical properties) for TESM. These sands have an average grain size of less than 0.93 mm. These formulas are:

- Ceramic balls fired at 1000 °C and 1060 °C with 58 wt.% of dune or mining sand, 12 wt.% and 30 wt.% of green clay and strong clay respectively.
- Ceramic balls fired at 1000 °C and 1060 °C with 40 wt.% of dune or mining sand, 30 wt.% and 30 wt.% of green clay and strong clay respectively.

If the sand means size range between 0.93mm and 1mm only the ceramic balls fired at 1000°C and 1060°C with 40 wt.% of dune or mining sand, 30 wt.% and 30 wt.% of green clay and strong clay meet the requirements of IEA.

With regards to the technological solution able to extract the maximum performance from the developed heat storage materials, the ceramic ball selected were put in contact of a vegetable oil after testing them under atmosphere air during 60 thermal cycles at 610 °C. These balls were stayed with Jatropha curcas oil during 3 months for compatibility study. A complete chemical compatibility analysis has been carried out between the developed and selected TES material and Jatropha curcas oil. This was revealed that a full compatibility is guaranteed with some minor restrictions. The crude oil has to be carefully filtered before its use as HTF and TESM. In addition, the acidity must be truck during real plant operation time to replace the oil when the acidity increases to 25 mgKOH.g^{-1}.

In order to investigate the performance of the developed thermal energy storage materials under a packed bed TES deployment frame, a complete physical model has been developed. This modelling tool accounts for the governing energy, thermal transport (conduction, convection, advection, or dispersion among others) and fluid flow mechanisms, which occur in the packed bed TES arrangement. The presented model represents a successful and innovative modelling strategy since it permits an accurate treatment of heat transport mechanisms together with the possibility of modelling different packing void fraction values. In order to determine the accuracy of the model, two different experiments data reported in the literature have been used as benchmark for the model validation. The calculations carried out showed a very precise agreement between the results obtained from the developed model and the selected experimental results with mean relative error of 3.59°C for the temperature profile in the packed bed.

The physical model developed and validated was used to analyse the thermal behavior of the packed-bed TES. In this regard, a detailed technology implementation analysis has been performed in terms of thermal management of the packed bed TES unit. This study has led to the identification of complete discharge and charge, time-limited partial discharge operation mode with more focus on discharge mode for a hypothetical 2 MWh_{th}. The effect of fluid velocity, tank porosity, particle diameter and particle volumetric heat capacity on the TES performances was carried out. The results analysis showed that low fluid velocity, tank porosity, small particle diameter and good volumetric heat capacity provide better thermal efficiencies, thin thermocline and long discharging time. For the new TESM developed, discharge and storage efficiencies of more than 90% and 70% is reachable with discharge time of at least 9h for fluid velocity less than $6.25.10^{-4}$ m. s^{-1} and tank

porosity less than 45%. However, the fluid velocity should not be below 5.10-4 m. s^{-1} to avoid thermocline extraction challenges.

For dynamic charging of the TES system and design of parabolic trough collector plant under Ouagadougou and Agadez climate conditions, PTC thermal behaviors were assessed when using jatropha curcas oil as heat transfer fluid. Similar to the TES study, a model has been developed on FORTRAN software for PTC thermal behaviors analysis. Seven test data on parabolic trough solar collector from SANDIA (literature) Solar Electric Generating System LS-2 have been used as benchmark for the model validation. The calculations carried out showed an agreement between the results obtained from the developed model and the selected experimental results with maximum error of 8.08%. From the thermal behaviors analysis, the following conclusions can be done:

- Low mass flow and longer collector length increases the collector outlet temperature.
- For a mass flow of 1 kgs^{-1}, a maximum collector length of 46.8 m is required to have HTF (JCO) outlet temperature higher than 210 °C from 9:40 am to 2:50 am and 9:08 am to 2:08 am respectively under Ouagadougou 2022 and Agadez climate conditions the 4^{th} September 2022 and 4^{th} of September 2020 respectively. Around the Zenithal angle, an outlet temperature of 218.80°C and 225.598 °C and average thermal efficiency of 82.69% and 81.76% can be reach under Ouagadougou and Agadez climate conditions with collection area of 230 m^2.
- The connection of the PTC to the TES required two collectors´ loops of 46.8m in parallel to charge a 2 MWh_{th} TES tank under Ouagadougou climate condition before 2 pm.

As perspectives and future work:

- Development of thermocline experimental setup at lab scale using the new developed ceramic balls and JCO for ground data collection.
- A microscopic observation and chemical study of the raw materials and ceramic balls will give better understand of the new energy storage material properties
- In addition the developed ceramic balls can be integrate in solar cooker box to improve the cooking stability during sun radiation fluctuations as addressed by Nebié et al., [235].

- For dynamic performance analysis of the overall PTC plant under Ouagadougou and Agadez climate condition the boiler model should be developed for electricity generation output assessment using the new TESM and HTF. This analysis will provide data for economic study of the plant and its design at commercial level.
- The installation of a demonstration PTC plant at the waste treatment and management site will help to do a hybridization with biogas for low carbon transition (reduction of carbon footprint of the site).
- A techno-economic study of the plant will be an asset to support decision regarding CSP technology integration in the power supply side in West Africa.

References

[1] Inigo Ortega Fernandez, “High Temperature Packed Bed Thermal Energy Storage Systems Based on Low Cost Materials,” 2017. [Online]. Available: https://addi.ehu.es/handle/10810/23629

[2] M. A. Russo, D. Carvalho, N. Martins, and A. Monteiro, “Forecasting the inevitable: A review on the impacts of climate change on renewable energy resources,” *Sustain. Energy Technol. Assessments*, vol. 52, no. PC, p. 102283, 2022, doi: 10.1016/j.seta.2022.102283.

[3] I. E. Agency, “Global Energy Review : CO2 Emissions in 2021 Global emissions rebound sharply to highest ever level INTERNATIONAL ENERGY,” 2021.

[4] T. Esence, A. Bruch, and T. Desrues, “Stockage Thermique Régénératif à Haute Température (300 – 800 ° C) Journées Nationales de l ’ Énergie Solaire,” 2016.

[5] S. Abolhosseini, A. Heshmati, and J. Altmann, “A Review of Renewable Energy Supply and Energy Efficiency Technologies,” *SSRN Electron. J.*, no. 8145, 2021, doi: 10.2139/ssrn.2432429.

[6] J. Mitali, S. Dhinakaran, and A. A. Mohamad, “Energy storage systems : a review,” *Energy Storage Sav.*, vol. 1, no. 3, pp. 166–216, 2022, doi: 10.1016/j.enss.2022.07.002.

[7] A. Ummadisingu and M. S. Soni, “Concentrating solar power - Technology, potential and policy in India,” *Renew. Sustain. Energy Rev.*, vol. 15, no. 9, pp. 5169–5175, 2011, doi: 10.1016/j.rser.2011.07.040.

[8] A. Gil *et al.*, “State of the art on high temperature thermal energy storage for power generation. Part 1-Concepts, materials and modellization,” *Renew. Sustain. Energy Rev.*, vol. 14, no. 1, pp. 31–55, 2010, doi: 10.1016/j.rser.2009.07.035.

[9] J. F. Hoffmann, T. Fasquelle, V. Goetz, and X. Py, “A thermocline thermal energy storage system with filler materials for concentrated solar power plants: Experimental data and numerical model sensitivity to different experimental tank scales,” *Appl. Therm. Eng.*, vol. 100, pp. 753–761, 2016, doi: 10.1016/j.applthermaleng.2016.01.110.

[10] C. Xu, Z. Wang, Y. He, X. Li, and F. Bai, “Parametric study and standby behavior of a

packed-bed molten salt thermocline thermal storage system," *Renew. Energy*, vol. 48, pp. 1–9, 2012, doi: 10.1016/j.renene.2012.04.017.

[11] J. E. Pacheco, S. K. Showalter, and W. J. Kolb, "Solar Energy: The Power to Choose," *Proc. Sol. Forum*, 2001, [Online]. Available: http://infohouse.p2ric.org/ref/22/21032.pdf

[12] IRENA and AfDB (2022), "Renewable Eenergy Market Analysis," www.irena.org/publications, Abu Dhabi and Abidjan., 2022.

[13] W. Bank, "Niger: The World Bank is supporting the strengthening of economic governance and human capital and increased access to energy," WASHINGTON, 2021. [Online]. Available: https://www.worldbank.org/

[14] Y. Azoumah, E. W. Ramdé, G. Tapsoba, and S. Thiam, "Siting Guidelines for Concentrating Solar Power Plants in the Sahel: Case study of Burkina Faso," *Sol. Energy*, vol. 84, no. 8, pp. 1545–1553, 2010, doi: 10.1016/j.solener.2010.05.019.

[15] A. I. Image, H. Sani, D. Nomao, and M. Boukar, "Study of Four (4) Semi-Empirical Models for Estimating Direct Radiation from the Sun and Modeling for Application to the Solar Thermodynamic System," no. August, 2022, doi: 10.14738/aivp.104.12950.

[16] G. . J. and J. J. E. J.T. HOUGHTON, Ed., *The IPCC Scientifc Assessment*. New York. [Online]. Available: https://www.ipcc.ch/site/assets/uploads/2018/03/ipcc_far_wg_I_full_report.pdf

[17] T. R. Gildas and ´, *Réalisation de la Carte d´Ensoleillement Normal Direct (DNI) et de Sites Potentiels pour Implantation de Centrales Solaires Thermodynamiques en Afrique de l´Ouest*. Ouagadougou, 2009.

[18] E. W. Ramdé, Y. Azoumah, A. Brew-Hammond, A. Rungundu, and G. Tapsoba, "Site Ranking and Potential Assessment for Concentrating Solar Power in West Africa," *Nat. Resour.*, vol. 04, no. 01, pp. 146–153, 2013, doi: 10.4236/nr.2013.41a019.

[19] G. S. ATLAS, "Global solar." https://globalsolaratlas.info/

[20] X. Py and Y. Azoumah, "Concentrated Solar Power : Current Technologies , Major Innovative Issues and Applicability to West African countries," vol. 18, pp. 306–315,

2013, doi: 10.1016/j.rser.2012.10.030.

[21] R. Bayón, E. Rivas, and E. Rojas, “Study of Thermocline Tank Performance in Dynamic Processes and Stand-by Periods with an Analytical Function,” *Energy Procedia*, vol. 49, pp. 725–734, 2014, doi: 10.1016/j.egypro.2014.03.078.

[22] H. Grirate, N. Zari, A. Elmchaouri, S. Molina, and R. Couturier, “Life Time Analysis of Thermal Oil Used as Heat Transfer Fluid in CSP Power Plant,” *AIP Conf. Proc.*, vol. 1734, 2016, doi: 10.1063/1.4949096.

[23] LAZARD, *Levelized Cost of Energy Analysis - Version 14.0*, no. October. 2020. [Online]. Available: https://www.lazard.com/media/kwrjairh/lazards-levelized-cost-of-energy-version-140.pdf

[24] C. T. Mark Mehos, J. Jorgenson1, C. H. , Paul Denholm, and and K. Armijo, *Advancing Concentrating Solar Power Technology , Performance , and Dispatchability*, no. May. 2016. [Online]. Available: https://www.nrel.gov/docs/fy16osti/65688.pdf

[25] E. Z. Moya, *Parabolic-trough concentrating solar power systems*, 2nd ed. Elsevier Ltd., 2020. doi: 10.1016/B978-0-12-819970-1.00009-8.

[26] F. A. F. T. HANS MÜLLER-STEINHAGEN, *Concentrating Solar Power,-A Review of the Technology*, no. January 2004. 2020. doi: 10.1201/9781439891209-12.

[27] E. Hakkarainen *et al.*, “Concentrated Solar Power and Circulating Fluidized Bed Power Plant Hybrids: Final Results of the COMBO-CFB project,” Teknologisk a forskningscentrale, 2017. doi: 10.13140/RG.2.2.20145.58722.

[28] N. Tanaka, *Technology Roadmap Concentrating Solar Power*. Paris. [Online]. Available: www.iea.org/about/copyright.asp

[29] S. Gorjian and B. Ghobadian, “Solar Thermal Power Plants : Progress and Prospects in Iran,” *Energy Procedia*, vol. 75, pp. 533–539, 2015, doi: 10.1016/j.egypro.2015.07.447.

[30] V. Sharma, J. K. Nayak, and S. B. Kedare, “Effects of Shading and Blocking in Linear Fresnel Reflector Field,” *Sol. ENERGY*, vol. 113, pp. 114–138, 2015, doi: 10.1016/j.solener.2014.12.026.

[31] D. Barlev, R. Vidu, and P. Stroeve, “Innovation in Concentrated Solar Power,” *Sol. Energy Mater. Sol. Cells*, vol. 95, no. 10, pp. 2703–2725, 2011, doi: 10.1016/j.solmat.2011.05.020.

[32] P. Scalco, J. Copetti, M. H. Macagnan, and J. Diehl de Oliveira, “Linear Fresnel Solar Collector Concentrator - A Review,” no. January, 2021, doi: 10.26678/abcm.cobem2021.cob2021-0132.

[33] A. LOMONACO, *Stockage d´Energie Thermique par Matériaux à Changement de Phase Adapté au Centrales Solaires Thermodynamiques*. Pau, 2015. [Online]. Available: http://www.theses.fr/2015PAUU3012

[34] J. I. Ortega, J. I. Burgaleta, and F. M. Tellez, “Central Receiver System Solar Power Plant Using Molten Salt as Heat Transfer Fluid,” *J. Sol. Energy Eng. Trans. ASME*, vol. 130, no. 2, pp. 0245011–0245016, 2008, doi: 10.1115/1.2807210.

[35] A. Poullikkas, G. Kourtis, and I. Hadjipaschalis, “Parametric Analysis for the Installation of Solar Dish Technologies in Mediterranean Regions,” *Renew. Sustain. Energy Rev.*, vol. 14, no. 9, pp. 2772–2783, 2010, doi: 10.1016/j.rser.2010.07.021.

[36] R. Osuna *et al.*, “PS10, Construction of a 11MW Solar Thermal Tower Plant in Seville, Spain,” in *Solar-PACES Conference, Seville, Spain, June*, 2006, no. January 2006, pp. 20–23. [Online]. Available: https://www.researchgate.net/publication/257128243

[37] I. S. Radonji, D. D. Milosavljevi, and L. S. Panti, “A Review of Concentrating Solar Power Plants in the World and their Potential Use in Serbia,” vol. 16, pp. 3891–3902, 2012, doi: 10.1016/j.rser.2012.03.042.

[38] M. T. Islam, N. Huda, A. B. Abdullah, and R. Saidur, “A Comprehensive Review of State-of-the-art Concentrating Solar Power (CSP) Technologies: Current Status and Research Trends,” *Renew. Sustain. Energy Rev.*, vol. 91, no. April, pp. 987–1018, 2018, doi: 10.1016/j.rser.2018.04.097.

[39] SENER, “The 150 MW Noor Ouarzazate III Solar Tower Power Plant with Storage System Accomplished the First Synchronization.” 2018. [Online]. Available: https://ippjournal.com/update/sener-has-recently-executed-the-start-up-of-the-solar-

receiver-for-the-project

[40] R. S. Matthias Günther, *Advanced CSP Teaching Materials*. 2011. [Online]. Available: https://www.academia.edu/38903309/Solar_Dish_Technology

[41] S. Thermal and E. Storage, "Sensible Thermal Energy Storage," pp. 65–81, 2014, doi: 10.1016/B978-0-12-417291-3.00004-9.

[42] G. Zanganeh *et al.*, "A 3 MWth Parabolic Trough CSP Plant Operating with Air at up to 650°C," pp. 5–10, doi: 10.1109/IRSEC.2014.7059884.

[43] R. Tiskatine *et al.*, "Experimental Evaluation of Thermo-Mechanical Performances of Candidate Rocks for Use in High Temperature Thermal Storage," *Appl. Energy*, vol. 171, pp. 243–255, 2016, doi: 10.1016/j.apenergy.2016.03.061.

[44] C. Xu, X. Li, Z. Wang, Y. He, and F. Bai, "Effects of Solid Particle Properties on the Thermal Performance of a Packed-bed Molten-salt Thermocline Thermal Storage System," *Appl. Therm. Eng.*, vol. 57, no. 1–2, pp. 69–80, 2013, doi: 10.1016/j.applthermaleng.2013.03.052.

[45] T. Laube, L. Marocco, K. Niedermeier, J. Pacio, and T. Wetzel, "Thermodynamic Analysis of High-Temperature Energy Storage Concepts Based on Liquid Metal Technology," *Energy Technol.*, vol. 8, no. 3, 2020, doi: 10.1002/ente.201900908.

[46] P. Brischoux, *Stockage Thermique Saisonnier par Puits Géothermique pour Bâtiments Résidentiels équipés de Panneux Photovoltaïques-Thermiques*. Montréal, 2016. [Online]. Available: https://publications.polymtl.ca/2161/

[47] L. Andre, *Stockage Thermochimique de l ' Energie Solaire Concentrée à Partir de Matériaux Innovants par Réactions Solide-Gaz Réversibles*. Perpignan, 2017. [Online]. Available: https://tel.archives-ouvertes.fr/tel-01806335

[48] D. Laing, D. Lehmann, C. Bahl, and E. Z. Ag, "Concrete Storage For Solar Thermal Power Plant and Industrial Process Heat," 2008, pp. 1–6. [Online]. Available: http://www.stratosolar.com/uploads/5/6/7/1/5671050/26_2008

[49] J. Hoffmann, "Stockage Thermique pour Centrale Solaire Thermodynamique à

Concentration Mettant en Oeuvre des Matériaux Naturels ou Recyclés," Perpignan, 2015. [Online]. Available: https://theses.hal.science/tel-01284834

[50] U. Herrmann, M. Geyer, and D. Kearney, *Overview on Thermal Storage Systems*. 2002. [Online]. Available: https://sftool.gov/Content/attachments/uh_storage_overview_ws030320.pdf

[51] P. Nigay *et al.*, "Structure and Properties of Clay Ceramics for Thermal Energy Storage," *J. Am. Ceram. Soc.*, 2019, [Online]. Available: https://imt-mines-albi.hal.science/hal-01630902

[52] N. Lopez Ferber *et al.*, "Development of a Thermal Energy Storage Pressed Plate Ceramic Based on Municipal Waste Incinerator Bottom Ash and Waste Clay," *Waste and Biomass Valorization*, vol. 11, no. 2, pp. 689–699, 2020, doi: 10.1007/s12649-019-00629-6.

[53] E. S. Kenda, X. Py, K. E. N'Tsoukpoe, Y. Coulibaly, and N. Sadiki, "Thermal Energy Storage Materials Made of Natural and Recycled Resources for CSP in West Africa," *Waste and Biomass Valorization*, vol. 9, no. 9, pp. 1687–1701, 2018, doi: 10.1007/s12649-017-9904-2.

[54] T. Fasquelle, Q. Falcoz, P. Neveu, J. Walker, and G. Flamant, "Compatibility Study Between Synthetic Oil and Vitrified Wastes for Direct Thermal Energy Storage," *Waste and Biomass Valorization*, vol. 8, no. 3, pp. 621–631, 2017, doi: 10.1007/s12649-016-9622-1.

[55] A. C. Iniesta, M. Diago, T. Delclos, Q. Falcoz, T. Shamim, and N. Calvet, "Gravity-fed Combined Solar Receiver/Storage System Using Sand Particles as Heat Collector, Heat Transfer and Thermal Energy Storage Media," *Energy Procedia*, vol. 69, pp. 802–811, 2015, doi: 10.1016/j.egypro.2015.03.089.

[56] M. Diago, A. C. Iniesta, T. Delclos, T. Shamim, and N. Calvet, "Characterization of Desert Sand for its Feasible use as Thermal Energy Storage Medium," *Energy Procedia*, vol. 75, pp. 2113–2118, 2015, doi: 10.1016/j.egypro.2015.07.333.

[57] R. Lalitha Priya, S. Subi, B. Vaishnu, and K. R. M. Vijaya Chandrakala, "Study on Characterization of River Sand as Heat Storage Medium," *Indian J. Sci. Technol.*, vol. 9,

no. 30, 2016, doi: 10.17485/ijst/2016/v9i30/99010.

[58] D. Schlipf, P. Schicktanz, H. Maier, and G. Schneider, “Using Sand and other Small Grained Materials as Heat Storage Medium in a Packed Bed HTTESS,” *Energy Procedia*, vol. 69, pp. 1029–1038, 2015, doi: 10.1016/j.egypro.2015.03.202.

[59] D. Schlipf, E. Faust, G. Schneider, and H. Maier, “First Operational Results of a High Temperature Energy Storage with Packed Bed and Integration Potential in CSP Plants,” in *AIP Conference Proceedings*, 2017, vol. 1850. doi: 10.1063/1.4984445.

[60] R. TISKATINE, *Valorisation Energétique des Matériaux Locaux pour des Applications dans les Centrales CSP et dans le Domaine des Bâtiments*. 2017. [Online]. Available: https://docplayer.fr/113218507-Valorisation-energetique-des-materiaux-locaux-pour-des-applications-dans-les-centrales-csp-et-dans-le-domaine-des-batiments.html

[61] Eastman, “Therminol VP-1, Heat Transfer Fluid.” [Online]. Available: www.eastman.com/locations

[62] E. S. Kenda, K. E. N’Tsoukpoe, I. W. K. Ouédraogo, Y. Coulibaly, X. Py, and F. M. A. W. Ouédraogo, “Jatropha curcas crude oil as heat transfer fluid or thermal energy storage material for concentrating solar power plants,” *Energy Sustain. Dev.*, vol. 40, pp. 59–67, 2017, doi: 10.1016/j.esd.2017.07.003.

[63] A. Gomna, K. E. N’Tsoukpoe, N. Le Pierrès, and Y. Coulibaly, “Thermal Stability of a Vegetable Oil-Based Thermal Fluid at High Temperature,” *African J. Sci. Technol. Innov. Dev.*, vol. 12, no. 3, pp. 317–326, 2020, doi: 10.1080/20421338.2020.1732080.

[64] L. F. Cabeza, I. Martorell, L. Miró, A. I. Fernández, and C. Barreneche, *Introduction to Thermal Energy Storage Systems*. 2020. doi: 10.1016/B978-0-12-819885-8.00001-2.

[65] Y. Konuklu, N. Şahan, and H. Paksoy, “Latent Heat Storage Systems,” *Compr. Energy Syst.*, vol. 2–5, pp. 396–434, 2018, doi: 10.1016/B978-0-12-809597-3.00231-5.

[66] K. M. Powell and T. F. Edgar, “Modeling and Control of a Solar Thermal Power Plant with Thermal Energy Storage,” *Chem. Eng. Sci.*, vol. 71, no. January 2011, pp. 138–145, 2012, doi: 10.1016/j.ces.2011.12.009.

[67] B. Stutz *et al.*, “Storage of Thermal Solar Energy Stockage,” *Comptes Rendus Phys.*, vol. 18, no. 7–8, pp. 401–414, 2017, doi: 10.1016/j.crhy.2017.09.008.

[68] G. Angelini, A. Lucchini, and G. Manzolini, “Comparison of Thermocline Molten Salt Storage Performances to Commercial Two-Tank Configuration,” *Energy Procedia*, vol. 49, pp. 694–704, 2014, doi: 10.1016/j.egypro.2014.03.075.

[69] M. Medrano, A. Gil, I. Martorell, X. Potau, and L. F. Cabeza, “State of the Art on High-Temperature Thermal Energy Storage for Power Generation. Part 2-Case Studies,” *Renew. Sustain. Energy Rev.*, vol. 14, no. 1, pp. 56–72, 2010, doi: 10.1016/j.rser.2009.07.036.

[70] S. Kuravi, J. Trahan, D. Y. Goswami, M. M. Rahman, and E. K. Stefanakos, “Thermal Energy Storage Technologies and Systems for Concentrating Solar Power Plants,” *Prog. Energy Combust. Sci.*, vol. 39, no. 4, pp. 285–319, 2013, doi: 10.1016/j.pecs.2013.02.001.

[71] S. M. Flueckiger, Z. Yang, and S. V. Garimella, “Review of Molten-Salt Thermocline Tank Modeling for Solar Thermal Energy Storage,” *Heat Transf. Eng.*, vol. 34, no. 10, pp. 787–800, 2013, doi: 10.1080/01457632.2012.746152.

[72] U. Herrmann, B. Kelly, and H. Price, “Two-tank molten salt storage for parabolic trough solar power plants,” *Energy*, vol. 29, no. 5–6, pp. 883–893, 2004, doi: 10.1016/S0360-5442(03)00193-2.

[73] Q. Huang, G. Lu, J. Wang, and J. Yu, “Thermal Decomposition Mechanisms of MgCl2·6H2O and MgCl2·H2O,” *J. Anal. Appl. Pyrolysis*, vol. 91, no. 1, pp. 159–164, 2011, doi: 10.1016/j.jaap.2011.02.005.

[74] J. W. Raade and D. Padowitz, “Development of Molten Salt Heat Transfer Fuid with Low Melting Point and High Thermal Stability,” *J. Sol. Energy Eng. Trans. ASME*, vol. 133, no. 3, pp. 1–7, 2011, doi: 10.1115/1.4004243.

[75] S. M. Flueckiger, Z. Yang, and S. V. Garimella, “Thermomechanical Simulation of the Solar One Thermocline Storage Tank,” *J. Sol. Energy Eng. Trans. ASME*, vol. 134, no. 4, 2012, doi: 10.1115/1.4007665.

[76] S. Zunft, M. Hänel, M. Krüger, V. Dreißigacker, F. Göhring, and E. Wahl, “Jülich Solar Power Tower-Experimental Evaluation of the Storage Subsystem and Performance

Calculation," *J. Sol. Energy Eng. Trans. ASME*, vol. 133, no. 3, pp. 1–5, 2011, doi: 10.1115/1.4004358.

[77] C. Mira-Hernández, S. M. Flueckiger, and S. V. Garimella, "Numerical Simulation of Single- and Dual-Media Thermocline Tanks for Energy Storage in Concentrating Solar Power Plants," *Energy Procedia*, vol. 49, pp. 916–926, 2014, doi: 10.1016/j.egypro.2014.03.099.

[78] X. Py and R. Olives, "Thermal Energy Storage for CSP Processes," pp. 1–16, 2010, doi: 10.1002/9781118991978.hces189.

[79] M. A. Abdolyt and D. Rapp, "Theoretical and Experimental Studies of Stratified Thermocline Storage of Hot Water," *Energy Convers*, vol. 22, no. Iii, 1982, doi: https://doi.org/10.1016/0196-8904(82)90053-X.

[80] I. Dincer, "On Thermal Energy Storage Systems and Applications in Buildings," *ENERGY Build.*, vol. 34, no. August 2001, pp. 377–388, 2002.

[81] B. Kurs and K. Okten, "Effect of Rectangular Hot Water Tank Position and Aspect Ratio on Thermal Strati fi cation Enhancement," *Renew. Energy*, vol. 116, pp. 639–646, 2018, doi: 10.1016/j.renene.2017.10.013.

[82] M. Battaglia and M. Haller, "Stratification in Large Thermal Storage Tanks," in *International Solar Energy Society*, 2018, vol. 1. doi: 10.18086/eurosun2018.13.03.

[83] L. G. Radosevich, "Final Report on the Power Production Phase of the 10 MWe Solar Thermal Central Receiver Pilot Plant," SANDIA, 1988. [Online]. Available: https://www.osti.gov/servlets/purl/7132401

[84] C. Odenthal, W. D. Steinmann, and S. Zunft, "Analysis of a Horizontal Flow Closed Loop Thermal Energy Storage System in Pilot Scale for High Temperature Applications – Part I: Experimental Investigation of the Plant," *Appl. Energy*, vol. 263, no. September 2019, p. 114573, 2020, doi: 10.1016/j.apenergy.2020.114573.

[85] E. Faust, D. Schlipf, G. Schneider, and H. Maier, "Flow Modeling of a Packed Bed High Temperature Thermal Energy Storage System," in *AIP Conference Proceedings*, 2018, vol. 2033, no. November, pp. 1–9. doi: 10.1063/1.5067102.

[86] J.-F. Hoffmann, T. Fasquelle, V. Goetz, and X. Py, “A thermocline thermal energy storage system with filler materials for concentrated solar power plants: Experimental data and numerical model sensitivity to different experimental tank scales,” *Appl. Therm. Eng.*, vol. 100, pp. 753–761, May 2016, doi: 10.1016/j.applthermaleng.2016.01.110.

[87] Albert Graells Vilella, *Analysis of Heat Storage with a Thermocline Tank for Concentrated Solar Plants*. 2014. [Online]. Available: https://upcommons.upc.edu/bitstream/handle/2099.1/22101/Project.pdf

[88] K. S. Reddy, V. Jawahar, S. Sivakumar, and T. K. Mallick, “Performance investigation of single-tank thermocline storage systems for CSP plants,” *Sol. Energy*, vol. 144, pp. 740–749, 2017, doi: 10.1016/j.solener.2017.02.012.

[89] T. Esence, *Étude Et Modélisation Des Systèmes De Stockage Thermique De Type Régénératif Solide / Fluide*. 2017. [Online]. Available: https://tel.archives-ouvertes.fr/tel-01714439

[90] T. E. W. Schumann, “Heat transfer: A Liquid Flowing Through a Porous Prism,” *J. Franklin Inst.*, vol. 208, no. 3, pp. 405–416, 1929, doi: 10.1016/S0016-0032(29)91186-8.

[91] P. Klein, T. H. Roos, and T. J. Sheer, “Experimental investigation into a packed bed thermal storage solution for solar gas turbine systems,” *Energy Procedia*, vol. 49, pp. 840–849, 2014, doi: 10.1016/j.egypro.2014.03.091.

[92] A. Bruch, J. F. Fourmigue, R. Couturier, and S. Molina, “Experimental and numerical investigation of stability of packed bed thermal energy storage for CSP power plant,” *Energy Procedia*, vol. 49, pp. 743–751, 2014, doi: 10.1016/j.egypro.2014.03.080.

[93] N. Mahfoudi, A. Moummi, and M. El Ganaoui, “Sand as a Heat Storage Media for a Solar Application: Simulation Results,” *Appl. Mech. Mater.*, vol. 621, no. August, pp. 214–220, 2014, doi: 10.4028/www.scientific.net/AMM.621.214.

[94] T. Esence, A. Bruch, J. F. Fourmigué, and B. Stutz, “A versatile one-dimensional numerical model for packed-bed heat storage systems,” *Renew. Energy*, vol. 133, pp. 190–204, 2019, doi: 10.1016/j.renene.2018.10.012.

[95] A. Mawire, K. Lentswe, R. Lugolole, D. Okello, and K. Nyeinga, “Thermal Stratification

Performance of a Packed Bed Latent Heat Storage System during Charging," in *E3S Web of Conferences 64*, 2018, vol. 1, pp. 1–5. doi: 10.1051/e3sconf/20186403001.

[96] S. A. Zavattoni, M. C. Barbato, A. Pedretti, and G. Zanganeh, "Evaluation of thermal stratification of an air-based thermocline TES with low-cost filler material," *Energy Procedia*, vol. 73, pp. 289–296, 2015, doi: 10.1016/j.egypro.2015.07.691.

[97] J. H. Davidson, D. A. Adams, and J. A. Miller, "A coefficient to characterize mixing in solar water storage tanks," *J. Sol. Energy Eng. Trans. ASME*, vol. 116, no. 2, pp. 94–99, 1994, doi: 10.1115/1.2930504.

[98] I. Ortega-fernández, S. A. Zavattoni, J. Rodríguez-aseguinolaza, B. D. Aguanno, and M. C. Barbato, "Analysis of an Integrated Packed Bed Thermal Energy Storage System for Heat Recovery in Compressed Air Energy Storage Technology," *Appl. Energy*, vol. 205, pp. 280–293, 2017, doi: 10.1016/j.apenergy.2017.07.039.

[99] Z. S. Chang, X. Li, C. Xu, C. Chang, and Z. F. Wang, "The Design and Numerical Study of a 2MWh Molten Salt Thermocline Tank," *Energy Procedia*, vol. 69, pp. 779–789, 2015, doi: 10.1016/j.egypro.2015.03.094.

[100] G. Zanganeh, A. Pedretti, A. Haselbacher, and A. Steinfeld, "Design of packed bed thermal energy storage systems for high-temperature industrial process heat," *Appl. Energy*, vol. 137, pp. 812–822, 2015, doi: 10.1016/j.apenergy.2014.07.110.

[101] M. A. Keilany *et al.*, "Vitrified Asbestos Waste Used as Filler Material in a Thermocline Storage Tank," in *WasteEng2018 Conference*, 2018. [Online]. Available: https://hal-mines-albi.archives-ouvertes.fr/hal-01890815

[102] M. M. Valmiki, W. Karaki, P. Li, J. Van Lew, C. Chan, and J. Stephens, "Experimental investigation of thermal storage processes in a thermocline tank," *J. Sol. Energy Eng. Trans. ASME*, vol. 134, no. 4, pp. 1–9, 2012, doi: 10.1115/1.4006962.

[103] M. Diago, A. C. Iniesta, T. Delclos, A. Soum-Glaude, T. Shamim, and N. Calvet, "Characterization of desert sand as a sensible thermal energy storage medium," *AIP Conf. Proc.*, vol. 1734, 2016, doi: 10.1063/1.4949109.

[104] T. Esence, A. Bruch, J. F. Fourmigué, and B. Stutz, "Extended modeling of packed-bed

sensible heat storage systems," *AIP Conf. Proc.*, vol. 2033, 2018, doi: 10.1063/1.5067101.

[105] A. C. Iniesta, M. Diago, T. Delclos, Q. Falcoz, T. Shamim, and N. Calvet, "Gravity-fed Combined Solar Receiver/Storage System Using Sand Particles as Heat Collector, Heat Transfer and Thermal Energy Storage Media," *Energy Procedia*, vol. 69, no. March, pp. 802–811, 2015, doi: 10.1016/j.egypro.2015.03.089.

[106] C. D. Modi, Anish; Perez-Segarra, "Thermocline Thermal Storage Systems for Concentrated Solar Power Plants : One- Dimensional Numerical Model and Comparative Analysis," *Sol. Energy*, 2014, doi: 10.1016/j.solener.2013.11.033.

[107] T. Esence, A. Bruch, S. Molina, B. Stutz, and J. F. Fourmigué, "A review on experience feedback and numerical modeling of packed-bed thermal energy storage systems," *Sol. Energy*, vol. 153, pp. 628–654, 2017, doi: 10.1016/j.solener.2017.03.032.

[108] A. Bouguila and R. Said, "Performance investigation of a 100-kWhth thermocline packed bed thermal energy storage system: Comparison between synthetic oil and vegetable oil," *Adv. Mech. Eng.*, vol. 12, no. 4, pp. 1–10, 2020, doi: 10.1177/1687814020905746.

[109] L. Geissbühler, A. Mathur, A. Mularczyk, and A. Haselbacher, "An assessment of thermocline-control methods for packed-bed thermal-energy storage in CSP plants, Part 1: Method descriptions," *Sol. Energy*, vol. 178, no. December 2018, pp. 341–350, 2019, doi: 10.1016/j.solener.2018.12.015.

[110] T. Esence, A. Bruch, J. F. Fourmigué, and B. Stutz, "Extended modeling of packed-bed sensible heat storage systems," *AIP Conf. Proc.*, vol. 2033, no. November, 2018, doi: 10.1063/1.5067101.

[111] A. Sharma, V. V. Tyagi, C. R. Chen, and D. Buddhi, "Review on thermal energy storage with phase change materials and applications," *Renew. Sustain. Energy Rev.*, vol. 13, no. 2, pp. 318–345, 2009, doi: 10.1016/j.rser.2007.10.005.

[112] J. T. Van Lew, P. Li, and J. Stephens, "Analysis of Heat Storage and Delivery of a Thermocline Tank Having Solid Filler Material," *Sol. Energy Eng.*, no. April 2016, 2011, doi: 10.1115/1.4003685.

[113] E. S. Kenda, K. E. N'Tsoukpoe, I. W. K. Ouédraogo, Y. Coulibaly, X. Py, and F. M. A.

W. Ouédraogo, “Jatropha Curcas Crude Oil as Heat Transfer Fluid or Thermal Energy Storage Material for Concentrating Solar Power Plants,” *Energy Sustain. Dev.*, vol. 40, pp. 59–67, 2017, doi: 10.1016/j.esd.2017.07.003.

[114] Z. Yang and S. V. Garimella, “Thermal analysis of solar thermal energy storage in a molten-salt thermocline,” *Sol. Energy*, vol. 84, no. 6, pp. 974–985, 2010, doi: 10.1016/j.solener.2010.03.007.

[115] O. Abdelhak, H. Mhiri, and P. Bournot, “CFD Analysis of Thermal Stratification in Domestic Hot Water Storage Tank During Dynamic Mode,” *Build. Simul.*, no. June, 2015, doi: 10.1007/s12273-015-0216-9.

[116] G. Zanganeh, A. Pedretti, S. Zavattoni, M. Barbato, and A. Steinfeld, “Packed-bed thermal storage for concentrated solar power - Pilot-scale demonstration and industrial-scale design,” *Sol. Energy*, vol. 86, no. 10, pp. 3084–3098, 2012, doi: 10.1016/j.solener.2012.07.019.

[117] Q. Mao, N. Liu, and L. Peng, “Numerical Investigations on Charging / Discharging Performance of a Novel Truncated Cone Thermal Energy Storage Tank on a Concentrated Solar Power System,” *Int. J. Photoenergy*, vol. 2019, 2019, doi: https://doi.org/10.1155/2019/1609234.

[118] I. Ortega-fernández, I. Loroño, A. Faik, and I. Uriz, “Parametric Analysis of a Packed Bed Thermal Energy Storage System,” in *AIP Conference Proceedings*, 2017, vol. 080021, no. June. doi: 10.1063/1.4984442.

[119] L. Geissbühler, *Thermocline Thermal Energy Storage: Advances and Applications to CSP, Compressed Air Energy Storage, and Solar Fuels*, no. 24555. 2017. doi: https://doi.org/10.3929/ethz-b-000255795.

[120] S. Roy *et al.*, “High-Flux Solar-Driven Thermochemical Dissociation of CO2 and H2OUsing Nonstoichiometric Ceria,” *Science (80-.).*, vol. 330, no. 6012, pp. 1797–1801, 2010, [Online]. Available: https://science.sciencemag.org/content/330/6012/1797/tab-pdf

[121] A. Nzihou, G. Flamant, and B. Stanmore, “Synthetic fuels from biomass using concentrated solar energy - A review,” *Energy*, vol. 42, no. 1, pp. 121–131, 2012, doi:

10.1016/j.energy.2012.03.077.

[122] E. G. Hertwich and X. Zhang, “Concentrating-solar biomass gasification process for a 3rd generation biofuel,” *Environ. Sci. Technol.*, vol. 43, no. 11, pp. 4207–4212, 2009, doi: 10.1021/es802853g.

[123] J. Felinks, S. Brendelberger, M. Roeb, C. Sattler, and R. Pitz-Paal, “Heat recovery concept for thermochemical processes using a solid heat transfer medium,” *Appl. Therm. Eng.*, vol. 73, no. 1, pp. 1006–1013, 2014, doi: 10.1016/j.applthermaleng.2014.08.036.

[124] E. Koepf, W. Villasmil, and A. Meier, “Pilot-scale solar reactor operation and characterization for fuel production via the Zn/ZnO thermochemical cycle,” *Appl. Energy*, vol. 165, pp. 1004–1023, 2016, doi: 10.1016/j.apenergy.2015.12.106.

[125] B. Boubou *et al.*, “Review on Thermocline Storage Effectiveness for Concentrating Solar Power Plant,” *Energy Power Eng.*, pp. 343–364, 2021, doi: 10.4236/epe.2021.1310024.

[126] G. Zanganeh, M. Commerford, A. Haselbacher, A. Pedretti, and A. Steinfeld, “Stabilization of the outflow temperature of a packed-bed thermal energy storage by combining rocks with phase change materials,” *Appl. Therm. Eng.*, vol. 70, no. 1, pp. 316–320, 2014, doi: 10.1016/j.applthermaleng.2014.05.020.

[127] L. Kocijel, “Conversion of A Medium Heavy Heating Oil Tank into a Heat Storage Tank,” *Heat Mass Transf.*, 2019, doi: https://doi.org/10.1007/s00231-019-02751-6.

[128] I. A. S. Ehtiwesh and A. C. M. Sousa, “Numerical model for the thermal behavior of thermocline storage tanks,” *Heat Mass Transf.*, vol. 54, pp. 831–839, 2017, doi: 10.1007/s00231-017-2181-6.

[129] E. K. Nitedem, *Stockage thermique à base d ’ éco-matériaux locaux pour centrale solaire à concentration : cas du pilote CSP4AFRICA*. 2018. [Online]. Available: https://tel.archives-ouvertes.fr/tel-01753832

[130] K. E. N’Tsoukpoe *et al.*, “Integrated design and construction of a micro-central tower power plant,” *Energy Sustain. Dev.*, vol. 31, pp. 1–13, 2016, doi: 10.1016/j.esd.2015.11.004.

[131] A. Razac *et al.*, “An investigation of the physical , thermal and mechanical properties of fired clay / SiC ceramics for thermal energy storage,” *J. Therm. Anal. Calorim.*, 2019, doi: 10.1007/s10973-019-08964-5.

[132] O. A. Balogun *et al.*, “Experimental Study on the Properties of Fired Sand – Clay Ceramic Products for Masonry Applications,” *J. Mater. Civ. Eng.*, vol. 33, no. 2018, pp. 1–12, 2021, doi: 10.1061/(ASCE)MT.1943-5533.0003532.

[133] F. Motte, Q. Falcoz, E. Veron, and X. Py, “Compatibility tests between Solar Salt and thermal storage ceramics from inorganic industrial wastes,” *Appl. Energy*, vol. 155, pp. 14–22, 2015, doi: 10.1016/j.apenergy.2015.05.074.

[134] Boubou Bagre, “Assessment of Different Sands Potentiallity to Formulate and Effective Thermal Energy Storage Material(TESM),” *Soaphys*, vol. 2, no. 2020, pp. 1–7, 2021, doi: http://dx.doi.org/10.46411/jpsoaphys.2020.01.08.

[135] M. Sawadogo *et al.*, “Formulation of Clay Refractory Bricks: Influence of the Nature of Chamotte and the Alumina Content in the Clay,” *Adv. Mater.*, vol. 9, no. 4, p. 59, 2020, doi: 10.11648/j.am.20200904.11.

[136] A. . Agbo, F. . Anene, and E. . Nnuka, “An assessment of the binding capacity of bentonite and ukpor clay on the foundry properties of river Niger, Onitsha beach sand,” *Int. J. Multidiscip. Res. Dev. www.allsubjectjournal.com*, vol. 4, no. 1, pp. 26–30, 2017, [Online]. Available: www.allsubjectjournal.com

[137] Y. Sawadogo, L. Zerbo, M. Sawadogo, M. Seynou, M. Gomina, and P. Blanchart, “Characterization and use of raw materials from Burkina Faso in porcelain formulations,” *Results Mater.*, vol. 6, no. March, p. 100085, 2020, doi: 10.1016/j.rinma.2020.100085.

[138] N. Savadogo, *Élaboration et caractérisation d ’ un écociment à base de poudre de mâchefer de charbon*. 2017. [Online]. Available: https://theses.hal.science/tel-01626685

[139] A. De Noni, D. Hotza, V. C. Soler, and E. S. Vilches, “Influence of composition on mechanical behaviour of porcelain tile. Part I: Microstructural characterization and developed phases after firing,” *Mater. Sci. Eng. A*, vol. 527, no. 7–8, pp. 1730–1735, 2010, doi: 10.1016/j.msea.2009.10.057.

[140] Y. Choi and R. L. Yuan, “Experimental relationship between splitting tensile strength and compressive strength of GFRC and PFRC,” *Cem. Concr. Res.*, vol. 35, pp. 1587–1591, 2005, doi: 10.1016/j.cemconres.2004.09.010.

[141] A. Ormerod, “Measurement of the tensile strength of brittle materials [1],” *Br. J. Appl. Phys.*, vol. 12, no. 1, pp. 29–30, 1961, doi: 10.1088/0508-3443/12/1/108.

[142] J. C. Jaeger, “Failure of rocks under tensile conditions,” *Int. J. Rock Mech. Min. Sci.*, vol. 4, no. 2, pp. 219–227, 1967, doi: 10.1016/0148-9062(67)90046-0.

[143] Y. H. and OKA, “~,2n 7. I)(2n -77) [a) J,” vol. 4, pp. 363–365, 1966, doi: http://dx.doi.org/10.1016/0148-9062(67)90017-4.

[144] V. Pejchal, Ž. Goran, R. Charvet, C. Dénéréaz, and A. Mortensen, “Compression testing spherical particles for strength : Theory of the meridian crack test and implementation for microscopic fused quartz,” *J. Mech. Phys. Solids*, vol. 99, no. July 2016, pp. 70–92, 2017, doi: 10.1016/j.jmps.2016.11.009.

[145] A. Miserez and A. Mortensen, “Fracture of aluminium reinforced with densely packed ceramic particles: Influence of matrix hardening,” *Acta Mater.*, vol. 52, no. 18, pp. 5331–5345, 2004, doi: 10.1016/j.actamat.2004.07.038.

[146] T. P. A. Hughes, Ifan G., Hase, *Uncertainties in Single-Variable Functions*. 2010. [Online]. Available: https://vtu.academia.edu/AnandS?swp=tc-au-40566592

[147] D. Devices, *KD2 Pro Thermal Properties Analyzer*. 2016. [Online]. Available: www.decagon.com

[148] K. G. Allen, T. W. von Backström, D. G. Kröger, and A. F. M. Kisters, “Rock bed storage for solar thermal power plants: Rock characteristics, suitability, and availability,” *Sol. Energy Mater. Sol. Cells*, vol. 126, pp. 170–183, Jul. 2014, doi: 10.1016/j.solmat.2014.03.030.

[149] A. Bennour, S. Mahmoudi, E. Srasra, S. Boussen, and N. Htira, “Composition, firing behavior and ceramic properties of the Sejnène clays (Northwest Tunisia),” *Appl. Clay Sci.*, vol. 115, no. October, pp. 30–38, 2015, doi: 10.1016/j.clay.2015.07.025.

[150] A. M. F. D. da Silva *et al.*, “Influence of firing temperature on the behavior of clay ceramics incorporated with elephant grass ash,” *Mater. Sci. Forum*, vol. 798–799, no. March 2015, pp. 526–531, 2014, doi: 10.4028/www.scientific.net/MSF.798-799.526.

[151] S. Yilmaz, “Creep of Hard Porcelain during Firing,” *Am. Ceram. Soc. Bull.*, vol. 86, no. 8, 2018, [Online]. Available: http://nek.istanbul.edu.tr:4444/ekos/MAKALE/M5734.pdf

[152] F. Homand-Etienne and R. Houpert, “Thermally induced microcracking in granites: characterization and analysis,” *Int. J. Rock Mech. Min. Sci.*, vol. 26, no. 2, pp. 125–134, 1989, doi: 10.1016/0148-9062(89)90001-6.

[153] R. Bahia, *Evaluation des propriétés réfractaires et cimentaires du kaolin de Djebel Debbagh*. 2013. [Online]. Available: https://theses-algerie.com/static/media/theses-logo.4c577848.png

[154] A. Michot, D. S. Smith, S. Degot, and C. Gault, “Thermal conductivity and specific heat of kaolinite: Evolution with thermal treatment,” *J. Eur. Ceram. Soc.*, vol. 28, no. 14, pp. 2639–2644, 2008, doi: 10.1016/j.jeurceramsoc.2008.04.007.

[155] M. Díaz-Heras, J. F. Belmonte, and J. A. Almendros-Ibáñez, “Effective thermal conductivities in packed beds: Review of correlations and its influence on system performance,” *Appl. Therm. Eng.*, vol. 171, no. May 2019, p. 115048, 2020, doi: 10.1016/j.applthermaleng.2020.115048.

[156] E. Bwayo and S. K. Obwoya, “Coefficient of Thermal Diffusivity of Insulation Brick Developed from Sawdust and Clays,” *J. Ceram.*, vol. 2014, no. 861726, 2014, doi: https://doi.org/10.1155/2014/861726.

[157] A. I. Fernandez, M. Martnez, M. Segarra, I. Martorell, and L. F. Cabeza, “Selection of materials with potential in sensible thermal energy storage,” *Sol. Energy Mater. Sol. Cells*, vol. 94, no. 10, pp. 1723–1729, 2010, doi: 10.1016/j.solmat.2010.05.035.

[158] P. Jacques, “Les Ceramiques Refractaires: De L’Elaboration Aux Proprietes D’Emploi,” *Verres Céramiques Compos.*, vol. 1, no. 2, pp. 28–42, 2011, [Online]. Available: http://revue-vcc.univ-setif.dz/telecharger/Article 3.pdf

[159] J. F. Hoffmann *et al.*, “Temperature dependence of thermophysical and rheological

properties of seven vegetable oils in view of their use as heat transfer fluids in concentrated solar plants," *Sol. Energy Mater. Sol. Cells*, vol. 178, no. July 2017, pp. 129–138, 2018, doi: 10.1016/j.solmat.2017.12.037.

[160] J. F. Hoffmann, T. Fasquelle, G. Vaitilingom, R. Olives, X. Py, and V. Goetz, "Compatibility of vegetable oils with solid filler materials for thermocline thermal energy storage systems," *Sol. Energy Mater. Sol. Cells*, vol. 200, no. January, 2019, doi: 10.1016/j.solmat.2019.109932.

[161] A. Gomna, K. E. N'Tsoukpoe, N. Le Pierrès, and Y. Coulibaly, "Review of vegetable oils behaviour at high temperature for solar plants: Stability, properties and current applications," *Sol. Energy Mater. Sol. Cells*, vol. 200, no. May, p. 109956, 2019, doi: 10.1016/j.solmat.2019.109956.

[162] M. Rafiq *et al.*, "Use of vegetable oils as transformer oils-A review," *Renew. Sustain. Energy Rev.*, vol. 52, pp. 308–324, 2015, doi: 10.1016/j.rser.2015.07.032.

[163] C. Perrier and A. Beroual, "Experimental investigations on insulating liquids for power transformers: Mineral, ester, and silicone oils," *IEEE Electr. Insul. Mag.*, vol. 25, no. 6, pp. 6–13, 2009, doi: 10.1109/mei.2009.5313705.

[164] A. Gomna, K. E. N. Tsoukpoe, and N. Le Pierrès, "Thermal Stability of a Vegetable Oil-Based Thermal Fluid at High Temperature," *African J. Sci. Technol. Innov. Dev.*, vol. 0, no. 0, pp. 1–10, 2020, doi: 10.1080/20421338.2020.1732080.

[165] G. Ferrer, A. Solé, C. Barreneche, I. Martorell, and L. F. Cabeza, "Corrosion of metal containers for use in PCM energy storage," *Renew. Energy*, vol. 76, pp. 465–469, 2015, doi: 10.1016/j.renene.2014.11.036.

[166] R. Martin, *Experiences in service with new insulating liquids*, no. October. Cigre A2-35, 2010. [Online]. Available: https://cigreindia.org/CIGRE Lib/Tech. Brochure/436 New Insulating fluids.pdf

[167] B. Bagre *et al.*, "Development of Sensible Heat Storage Materials Using Sand , Clay and Coal Bottom Ash," *Mater. Sci. Appl.*, vol. 13, no. 12, pp. 603–626, 2022, doi: 10.4236/msa.2022.1312038.

[168] J. F. Hoffmann, T. Fasquelle, G. Vaitilingom, R. Olives, X. Py, and V. Goetz, "Compatibility of vegetable oils with solid filler materials for thermocline thermal energy storage systems," *Sol. Energy Mater. Sol. Cells*, vol. 200, no. May, 2019, doi: 10.1016/j.solmat.2019.109932.

[169] H. Tian and G. Q. Shu, "Organic Rankine Cycle systems for large-scale waste heat recovery to produce electricity," *Org. Rank. Cycle Power Syst. Technol. Appl.*, pp. 613–636, 2017, doi: 10.1016/B978-0-08-100510-1.00017-X.

[170] Y. Grosu, I. Ortega-Fernández, J. M. López del Amo, and A. Faik, "Natural and by-product materials for thermocline-based thermal energy storage system at CSP plant: Compatibility with mineral oil and molten nitrate salt," *Appl. Therm. Eng.*, vol. 136, pp. 657–665, 2018, doi: 10.1016/j.applthermaleng.2018.03.034.

[171] F. K. Tiendrebeogo, N. Sawadogo, R. K. Nanema, and E. R. Traore, "Assessment of genetic diversity of Jatropha curcas L. in Burkina Faso," *Int. J. Innov. Appl. Stud.*, vol. 16, no. 1, pp. 155–165, 2016.

[172] M. Ezeldin Osman, T. F. Sheshko, T. D. Dipheko, N. E. Abdallah, E. A. Hassan, and C. Y. Ishak, "Synthesis and improvement of Jatropha curcas L. biodiesel based on eco-friendly materials," *Int. J. Green Energy*, vol. 18, no. 13, pp. 1396–1404, 2021, doi: 10.1080/15435075.2021.1904943.

[173] L. M. M. Christoph Weber, "Étude de faisabilité sur le Développement de Carburants d´Aviation Durable," 2018. [Online]. Available: https://www.icao.int/environmental-protection/Documents/FeasabilityStudy_BurkinaFasoReportFR-Final-Web-v2.pdf

[174] T. M. I. Riayatsyah *et al.*, "Current Progress of Jatropha Curcas Commoditisation as Biodiesel Feedstock: A Comprehensive Review," *Front. Energy Res.*, vol. 9, no. January, pp. 1–19, 2022, doi: 10.3389/fenrg.2021.815416.

[175] T. F. S. Barros *et al.*, "Fatty acid profiles of species of Jatropha curcas L., Jatropha mollissima (Pohl) Baill. and Jatropha gossypiifolia L.," *Ind. Crops Prod.*, vol. 73, pp. 106–108, 2015, doi: 10.1016/j.indcrop.2015.04.003.

[176] Z. Yaakob, B. N. Narayanan, S. Padikkaparambil, S. Unni K., and M. Akbar P., "A review

on the oxidation stability of biodiesel," *Renew. Sustain. Energy Rev.*, vol. 35, pp. 136–153, 2014, doi: 10.1016/j.rser.2014.03.055.

[177] O. O. Fasina and Z. Colley, "Viscosity and specific heat of vegetable oils as a function of temperature: 35°C to 180°C," *Int. J. Food Prop.*, vol. 11, no. 4, pp. 738–746, 2008, doi: 10.1080/10942910701586273.

[178] C. Nabila, *Détermination de la capacité antioxydant des huiles végétales*. 2013. [Online]. Available: http://dspace1.univ-tlemcen.dz/handle/112/5024

[179] M. H. Gordon, "Factors affecting lipid oxidation," *Underst. Meas. Shelf-Life Food*, pp. 128–141, 2004, doi: 10.1533/9781855739024.1.128.

[180] C. C. Garcia, P. I. B. M. Franco, T. O. Zuppa, N. R. A. Filho, and M. I. G. Leles, "Thermal Stability Studies of Some Cerrado Plant Oils," *J. Therm. Anal. Calorim.*, vol. 87, no. March 2007, pp. 645–648, 2007, doi: https://doi.org/10.1007/s10973-006-7769-x.

[181] C. Paper, M. Alqaydi, T. Delclos, S. Almheiri, and N. Calvet, "Effect of sand and method of mixing on molten salt properties for an open direct absorption solar receiver / storage system," in *AIP Conference Proceedings*, 2017, no. June. doi: 10.1063/1.4984423.

[182] J. Kongkasawan and S. C. Capareda, "Jatropha oil refining process and biodiesel conversion: Mass and energy balance," *Int. Energy J.*, vol. 13, no. 4, pp. 169–176, 2012.

[183] C. Onyema and K. Ibe, "Effects of Refining Processes on the Physicochemical Properties of Some Selected Vegetable Oils," *Am. Chem. Sci. J.*, vol. 12, no. 4, pp. 1–7, 2016, doi: 10.9734/acsj/2016/23290.

[184] J. E. Pacheco, S. K. Showalter, and W. J. Kolb, "Development of a Molten-Salt Thermocline Thermal Storage System for Parabolic Trough Plants," *J. Sol. Energy Eng.*, vol. 124, no. 2, pp. 153–159, May 2002, doi: 10.1115/1.1464123.

[185] F. Avallone, *Modeling of a Thermocline Thermal Energy Storage : application to a Concentrating Solar Power plant*. 2018. [Online]. Available: https://www.politesi.polimi.it/retrieve/a81cb05c-dcd3-616b-e053-1605fe0a889a/Thesis_Avallone.pdf

[186] M. Strasser and R. P. Selvam, “Evaluation of Pressure Drop in Air- and Salt-Based Thermocline Thermal Energy Storage Systems,” 2016, no. November 2015. [Online]. Available: https://www.researchgate.net/publication/301651412%0AEvaluation

[187] A. M. Ribeiro, P. Neto, and C. Pinho, “Mean Prosity and Pressure Drop Measurements in Packed Beds of Monosized Spheres: Side Wall Effects,” *Int. Rev. Chem. Eng.*, vol. 2, no. 1, pp. 40–46, 2010.

[188] F. Andreola, C. Leonelli, M. Romagnoli, and P. Miselli, “Techniques used to determine porosity,” *Am. Ceram. Soc. Bull.*, vol. 79, no. 7, pp. 49–52, 2000.

[189] M. N. Abbas, “Modeling of Porosity Equation for Water Flow Through Packed Bed of Monosize Spherical Packing,” *J. Eng. Dev.*, vol. 15, no. 4, pp. 205–226, 2011.

[190] G. E. Mueller, “Numerically packing spheres in cylinders,” *Powder Technol.*, vol. 159, no. 2, pp. 105–110, 2005, doi: 10.1016/j.powtec.2005.06.002.

[191] G. E. Mueller, “A simple method for determining sphere packed bed radial porosity,” *Powder Technol.*, vol. 229, pp. 90–96, 2012, doi: 10.1016/j.powtec.2012.06.013.

[192] C. Xu, Z. Wang, Y. He, X. Li, and F. Bai, “Sensitivity analysis of the numerical study on the thermal performance of a packed-bed molten salt thermocline thermal storage system,” *Appl. Energy*, vol. 92, pp. 65–75, 2012, doi: 10.1016/j.apenergy.2011.11.002.

[193] J. H. I. Lienhard and J. H. V Lienhard, *A Heat Transfer Textbook, fifth edition*. 2020. [Online]. Available: https://ahtt.mit.edu/

[194] C. J. Visser, *Modelling Heat And Mass Flow Through Packed Pebble Beds: A Heterogeneous Volume-Averaged Approach*, vol. Master, no. April. 2007. [Online]. Available: http://hdl.handle.net/2263/27623

[195] M. Zeneli, A. Nikolopoulos, S. Karellas, and N. Nikolopoulos, “Numerical methods for solid-liquid phase-change problems,” *Ultra-High Temp. Therm. Energy Storage, Transf. Convers.*, vol. 2021, pp. 165–199, 2020, doi: 10.1016/B978-0-12-819955-8.00007-7.

[196] J. F. Hoffmann, T. Fasquelle, V. Goetz, and X. Py, “Experimental and numerical investigation of a thermocline thermal energy storage tank,” *Appl. Therm. Eng.*, vol. 114,

pp. 896–904, 2017, doi: 10.1016/j.applthermaleng.2016.12.053.

[197] X. Zhang, L. Wu, X. Wang, and G. Ju, “Comparative study of waste heat steam SRC, ORC and S-ORC power generation systems in medium-low temperature,” *Appl. Therm. Eng.*, vol. 106, pp. 1427–1439, 2016, doi: 10.1016/j.applthermaleng.2016.06.108.

[198] T. Fasquelle, “Modelisation et Caractérisation Expérimentale d´une Boucle Solaire Cylindro-Parabolique Integrant un Stockage de Type Thermocline,” 2015. [Online]. Available: https://theses.hal.science/tel-01697915/document

[199] F. A. Rodrigues and M. J. S. de Lemos, “Effect of porous material properties on thermal efficiencies of a thermocline storage tank,” *Appl. Therm. Eng.*, vol. 173, no. October 2019, 2020, doi: 10.1016/j.applthermaleng.2020.115194.

[200] Stanislas Sanfo, Serge Dimitri Bazyomo, TizaneDao, and Abdoulaye Ouedraogo, “Study of the Potential for the Solar Concentrating Sector in Burkina Faso,” *J. Energy Power Eng.*, vol. 16, no. 3, pp. 114–120, 2022, doi: 10.17265/1934-8975/2022.03.002.

[201] P. J. Mago, L. M. Chamra, and C. Somayaji, “Performance analysis of different working fluids for use in organic Rankine cycles,” *J. Power Energy*, vol. 221, no. 3, pp. 255–264, 2007, doi: 10.1243/09576509JPE372.

[202] S. Guillot *et al.*, “Corrosion effects between molten salts and thermal storage material for concentrated solar power plants,” *Appl. Energy*, vol. 94, no. JUNE, pp. 174–181, 2012, doi: 10.1016/j.apenergy.2011.12.057.

[203] U. Desideri and P. Elia, “Analysis and comparison between a concentrating solar and a photovoltaic power plant,” *Appl. Energy*, vol. 113, pp. 422–433, 2014, doi: 10.1016/j.apenergy.2013.07.046.

[204] B. Zhao, M. Cheng, C. Liu, and Z. Dai, “An efficient tank size estimation strategy for packed-bed thermocline thermal energy storage systems for concentrated solar power,” *Sol. Energy*, vol. 153, pp. 104–114, 2017, doi: 10.1016/j.solener.2017.05.057.

[205] J. C. Sattler *et al.*, “Dynamic simulation tool for a performance evaluation and sensitivity study of a parabolic trough collector system with concrete thermal energy storage,” *AIP Conf. Proc.*, vol. 2303, no. 2019, 2020, doi: 10.1063/5.0029277.

[206] W. B. Fang, “Performance analysis of solar evacuated tube collector,” *Adv. Mater. Res.*, vol. 712–715, pp. 1605–1608, 2013, doi: 10.4028/www.scientific.net/AMR.712-715.1605.

[207] J. J. C. S. Santos, J. C. E. Palacio, A. M. M. Reyes, M. Carvalho, A. J. R. Freire, and M. A. Barone, “Concentrating Solar Power,” *Adv. Renew. Energies Power Technol.*, vol. 1, no. January 2004, pp. 373–402, 2018, doi: 10.1016/B978-0-12-812959-3.00012-5.

[208] K. Vignarooban, X. Xu, A. Arvay, K. Hsu, and A. M. Kannan, “Heat transfer fluids for concentrating solar power systems - A review,” *Appl. Energy*, vol. 146, pp. 383–396, 2015, doi: 10.1016/j.apenergy.2015.01.125.

[209] P. K. Ktistis, R. A. Agathokleous, and S. A. Kalogirou, “Experimental performance of a parabolic trough collector system for an industrial process heat application,” *Energy*, vol. 215, p. 119288, 2021, doi: 10.1016/j.energy.2020.119288.

[210] M. H. Babikir, D. Njomo, M. Barka, V. S. Chara-dackou, Y. S. Kondji, and M. Y. Khayal, “Thermal modeling of a parabolic trough collector in a quasi-steady state regime Thermal modeling of a parabolic trough collector in a quasi-steady state regime,” vol. 013703, no. February, 2021, doi: 10.1063/1.5145272.

[211] S. Kannaiyan and N. D. Bokde, “Performance of Parabolic Trough Collector with Different Heat Transfer Fluids and Control Operation,” *Energies*, vol. 15, no. 20, pp. 1–23, 2022, doi: 10.3390/en15207572.

[212] M. Bagré, Boubou Boukar *et al.*, “Modelling and Simulation of a Sustainable Thermal Energy Storage System for Concentrating Solar Power (CSP) Plant Using Eco-Materials,” 2023.

[213] M. M. Khan and M. R. Islam, “Investigation of Vegetable Oil as Thermal Fluid in a Parabolic Solar Collector,” in *IMECE2008-69125*, 2017. [Online]. Available: http://www.asme.org

[214] L. Salgado Conrado, A. Rodriguez-Pulido, and G. Calderón, “Thermal performance of parabolic trough solar collectors,” *Renew. Sustain. Energy Rev.*, vol. 67, no. November, pp. 1345–1359, 2017, doi: 10.1016/j.rser.2016.09.071.

[215] E. Bellos and C. Tzivanidis, “Analytical expression of parabolic trough solar collector

performance," *Designs*, vol. 2, no. 1, pp. 1–17, 2018, doi: 10.3390/designs2010009.

[216] E. Dudley, J. Kolb, A. Mahoney, T. Mancini, S. M, and D. Kearney, "Test results: SEGS LS-2 solar collector," 1994. [Online]. Available: https://www.osti.gov/biblio/70756

[217] E. Bellos, C. Tzivanidis, and V. Belessiotis, "Daily performance of parabolic trough solar collectors," *Sol. Energy*, vol. 158, no. October, pp. 663–678, 2017, doi: 10.1016/j.solener.2017.10.038.

[218] K. HARO *et al.*, "Evaluation de l'empreinte carbone d'une Installation de Stockage des Déchets Non Dangereux (ISDND) : Cas du centre traitement et de valorisation des déchets (CTVD) sis à Polesgo (Ouagadougou)," *J. Phys. la SOAPHYS*, vol. 1, no. 1, p. C19A5-1-C19A5-5, 2019, doi: 10.46411/jpsoaphys.19.01.005.

[219] K. Haro *et al.*, "Assessment of CH4 and CO2 surface emissions from Polesgo's landfill (Ouagadougou, Burkina Faso) based on static chamber method," *Adv. Clim. Chang. Res.*, vol. 10, no. 3, pp. 181–191, 2019, doi: 10.1016/j.accre.2019.09.002.

[220] V. Manasaki, I. Palogos, I. Chourdakis, K. Tsafantakis, and P. Gikas, "Techno-economic assessment of landfill gas (LFG) to electric energy: Selection of the optimal technology through field-study and model simulation," *Chemosphere*, vol. 269, p. 128688, 2021, doi: 10.1016/j.chemosphere.2020.128688.

[221] Alejandro Rodríguez, *Solar Energy Measurement System: Sun Tracker 200*. 2017. [Online]. Available: www.geonica.com

[222] A. Rodriguez, *USER MANUAL GEO-DR20-A1 & GEO-DR15-A1*, no. 97. 2019. [Online]. Available: www.geonica.com

[223] M. S. Ahamed, H. Guo, and K. Tanino, "Evaluation of a cloud cover based model for estimation of hourly global solar radiation in Western Canada," *Int. J. Sustain. Energy*, vol. 38, no. 1, pp. 64–73, 2019, doi: 10.1080/14786451.2018.1443934.

[224] E. Commission, "Photovoltaic Geographyical Information System," 2020.

[225] R. V. Padilla, G. Demirkaya, D. Y. Goswami, E. Stefanakos, and M. M. Rahman, "Heat transfer analysis of parabolic trough solar receiver," *Appl. Energy*, vol. 88, no. 12, pp.

5097–5110, 2011, doi: 10.1016/j.apenergy.2011.07.012.

[226] L. Xu, Z. F. Wang, G. F. Yuan, F. H. Sun, and X. L. Zhang, “Thermal Performance of Parabolic Trough Solar Collectors under the Condition of Dramatically Varying DNI,” *Energy Procedia*, vol. 69, pp. 218–225, 2015, doi: 10.1016/j.egypro.2015.03.025.

[227] L. Wald, “Basics in Solar Radiation at Earth Surface -Revised Version,” 2019. [Online]. Available: https://hal-mines-paristech.archives-ouvertes.fr/hal-01676634/document

[228] F. Jamadi, “Experimental Investigation of Effect of Oil Mass Flow Change on Parabolic Trough Collector Efficiency in Solar Water Heater System,” *Int. J. "Technical Phys. Probl. Eng.*, vol. 26, no. 1, pp. 88–94, 2016, [Online]. Available: www.iotpe.com

[229] J. C. Sattler *et al.*, “Dynamic simulation tool for a performance evaluation and sensitivity study of a parabolic trough collector system with concrete thermal energy storage,” *AIP Conf. Proc.*, vol. 2303, 2020, doi: 10.1063/5.0029277.

[230] A. O. Kumar Satish Chand Umrao, “Design and Analysis for 1MWe Parabolic Trough Solar Collector plant based on DSG method,” *(Ijert)*, vol. 2, no. 6, pp. 1–15, 2013, [Online]. Available: www.ijert.org

[231] B. R. Tamuli, S. S. Saikia, S. Nath, and D. Bhanja, “Thermal performance analysis of a co-axial evacuated tube collector with single and two-phase flow consideration under North-eastern India climatic condition,” *Sol. Energy*, vol. 196, no. November 2019, pp. 107–124, 2020, doi: 10.1016/j.solener.2019.11.097.

[232] J. Jamaludin and H. Ohmori, “Solar parabolic trough thermal energy output forecasting based on K-Nearest Neighbors approach,” *IOP Conf. Ser. Earth Environ. Sci.*, vol. 342, no. 1, 2019, doi: 10.1088/1755-1315/342/1/012013.

[233] M. J. Ahmad and G. N. Tiwari, “Study of Models for Predicting the Mean Hourly Global Radiation from Daily Summations,” *Open Environ. Sci.*, vol. 2, no. 1, pp. 6–14, 2008, doi: 10.2174/1876325100802010006.

[234] T. Fasquelle, Q. Falcoz, P. Neveu, F. Lecat, N. Boullet, and G. Flamant, “Operating results of a thermocline thermal energy storage included in a parabolic trough mini power plant,” *AIP Conf. Proc.*, vol. 1850, no. June 2017, 2017, doi: 10.1063/1.4984431.

[235] J. Nébié *et al.*, “Thermal Performance Assessment of a Box-type Solar Cooker with an Inclined Collecting Surface and Kapok Wool Insulation,” *Phys. Sci. Int. J.*, no. January, pp. 29–38, 2021, doi: 10.9734/psij/2021/v25i1030286.